



UNIVERSITÀ
DEGLI STUDI
DI BRESCIA

DOTTORATO DI RICERCA IN
INGEGNERIA MECCANICA E INDUSTRIALE

SSD: CHIM/07

CICLO
XXXVI

TITOLO TESI
MEASUREMENTS OF METAL CONCENTRATION IN AEROSOLS BY LASER-INDUCED
BREAKDOWN SPECTROSCOPY (LIBS) TECHNIQUE

DOTTORANDO
DAVIDE CINIGLIA

SUPERVISORE
LAURA BORGESE

CO-SUPERVISORI
SILVANA DE IULIIS (CNR-ICMATE, Institute of Condensed Matter Chemistry and Technologies for
Energy)
MARIA GRAZIA PERRONE (TCR Tecora Srl, Via delle Primule 16, Cogliate (MB), I-20815)

RIASSUNTO

L'analisi dei metalli pesanti ha grande importanza all'interno della comunità scientifica a causa del loro impatto sulla salute e sull'ambiente, nonché in ambito di economia circolare. Un uso efficiente delle risorse, il riciclo dei rifiuti e il monitoraggio delle emissioni a camino di termovalorizzatori sono questioni importanti da considerare. La normativa di riferimento sulle emissioni di metalli è la EN14385:2004, in cui sono definiti i limiti di emissione a inceneritore di As, Cd, Cr, Co, Cu, Mn, Ni, Pb, Sb, Tl e V. Per monitorare e valutare la concentrazione in emissione di tali elementi è importante un'analisi in loco e in continuo, e la tecnica Laser Induced Breakdown Spectroscopy (LIBS) è promettente per questo scopo, dato che non necessita la preparazione del campione, a differenza di altre tecniche come ICP e TXRF. La tecnica consiste nel focalizzare un opportuno fascio laser producendo un micro-plasma; le specie presenti all'interno del volume di misura vengono vaporizzate ed eccitate. Il segnale LIBS è il risultato dalla radiazione emessa dalla diseccitazione di queste specie. Lo scopo del lavoro di tesi di questo PhD, finanziato da TCR Tecora s.r.l. e dal Consiglio Nazionale delle Ricerche (CNR) all'interno di un progetto Europeo di innovazione (ROP ERDF 2014 – 2020 - F.A.N.G.H.I), è lo studio della tecnica LIBS per sviluppare un prototipo strumentale per condurre misure online di concentrazione di metalli pesanti all'emissione.

È stato sviluppato un apparato sperimentale da laboratorio per misure LIBS su aerosol, successivamente ottimizzato per l'acquisizione del segnale e la seguente analisi. La scelta opportuna dei parametri di raccolta del segnale (ritardo di acquisizione rispetto all'impulso laser e tempo di integrazione del segnale) è importante nella prospettiva di discriminare le linee di emissione atomica rispetto alla radiazione continua di fondo. Le migliori condizioni sperimentali sono state valutate per migliorare la sensibilità del segnale e un appropriato programma di analisi è stato sviluppato in Matlab. In questo contesto, è stato eseguito ed ampiamente discusso un interessante studio sull'effetto matrice dovuto alla presenza di gas o di differenti analiti all'interno del volume di misura.

L'apparato sperimentale da laboratorio è stato riassembleto in una configurazione trasportabile, ottenendo un prototipo adatto alle misure a campo. In queste condizioni sono state costruite le curve di calibrazione degli elementi di interesse e i limiti di rivelabilità ottenuti sono stati descritti e comparati con i dati presenti in letteratura.

Inoltre, con l'obiettivo di ridurre i limiti di rivelabilità, è stato raccolto l'aerosol su filtro per eseguire misure direttamente sul deposito. A tal fine, sono state eseguite delle opportune modifiche al prototipo tanto quanto alle condizioni di acquisizione del segnale, per renderle adatte alle analisi su filtro. Sono state costruite le corrispondenti curve di calibrazione e sono stati valutati i limiti di rivelabilità.

Infine, sono stati presentati differenti casi studio. Sono stati analizzati dei filtri carichi di sedimenti raccolti sulla superficie nevosa della Cordillera Blanca. Questi campioni all'apparenza rossastri, come dimostrato dalle misure LIBS, erano carichi di ferro ossidato, di cui grazie alla calibrazione è stato possibile valutarne la concentrazione superficiale.

Infine, è stato condotto uno studio qualitativo e quantitativo su polveri provenienti dal consumo di freni fornite da TCR Tecora. Le analisi su queste polveri hanno permesso di valutare il contenuto di alcuni metalli.

Gli esempi riportati hanno lo scopo di sottolineare il potenziale della tecnica in diverse applicazioni. Inoltre, il lavoro complessivo condotto durante il periodo di PhD ha raggiunto uno stato di avanzamento con risultati significativi che sono alla base per analisi future su questo tema.

SUMMARY

Heavy metals analysis is of great interest to the scientific community for their impact on human health and the environment, as well as in the framework of circular economy. An efficient use of resources, recycling waste, and emissions monitoring in waste-to-energy plants are challenging issues to be considered. The reference standard on metal emissions is EN14385:2004, which defines the incinerator emission limits of As, Cd, Cr, Co, Cu, Mn, Ni, Pb, Sb, Tl, and V.

In-situ and continuous analysis are important to monitor and evaluate emission concentrations of these metals, Laser Induced Breakdown Spectroscopy (LIBS) technique is promising for this purpose, since no sample preparation is needed compared to other standard techniques, such as ICP or TXRF. The technique consists of focusing an appropriate laser beam producing a microplasma; the species present in the probe volume are vaporised and excited. LIBS signal results from the radiation emitted by the de-excitation of these species.

The aim of this Industrial PhD thesis, financed by TRC-TECORA s.r.l. and the National Council of Research (CNR) within a European project of innovation (ROP ERDF 2014 – 2020 - F.A.N.G.H.I), is the study of the LIBS technique to develop an instrumental prototype to carry out qualitative and quantitative metals emission concentration measurements.

An experimental laboratory apparatus for LIBS measurements on aerosol has been developed and optimized for signal acquisition and processing. In fact, a proper choice of the detection parameters (delay with respect to the laser pulse and integration time of the detector gate) is important in the perspective of discriminating the emission atomic lines with respect to the background continuum emission.

The best experimental conditions have been tested to increase signal sensitivity and a suitable processing Matlab software has been developed for signal analysis. In this context, an interesting study on matrix effects due to gas species and /or concomitant presence of different analytes in the probe volume is also performed and widely described.

The laboratory experimental arrangement has been reassembled in a portable configuration, obtaining a suitable prototype for field measurements. In these conditions, calibration curves of the elements under analysis have been built up, and the results concerning the limit of detection are presented and compared with literature data.

Moreover, to improve the detection limits, an accumulation of aerosol particles on filters was performed for LIBS measurements directly on particles-loaded filters. To this purpose, proper changes in the prototype apparatus have been built as well as in the experimental detection conditions,

resulting more suitable for filter analysis. The corresponding calibration curves have been calculated and the limit of detection retrieved.

Finally, different case studies are presented. Particles-loaded filters obtained from snow superficial sediments of Cordillera Blanca are investigated. These samples exhibited a reddish colour, which was proved to be due to iron oxide thanks to LIBS measurements. Iron was then quantified thanks to a proper calibration.

In the end, a qualitative and quantitative study was carried out on brakes powder supplied by TCR-TECORA in the framework of a field campaign on brakes analysis. LIBS measurements on these powders allow us to evaluate the presence of metals in the powder.

The examples reported are particular and aimed to underline the potential of the technique in different applications. Furthermore, the overall work performed during this PhD period has reached a stage of advancement with significant results that will be the basis of future investigations on this topic.

INDEX

Riassunto	i
Summary.....	iii
Index.....	v
List of tables	vii
List of figures	viii
1 Introduction	1
2 Laser-Induced Breakdown Spectroscopy (LIBS).....	8
2.1 LIBS fundamentals.....	8
2.1.1 Temperature and electron density.....	12
2.2 Qualitative / quantitative analysis	15
2.3 LIBS on aerosols.....	16
2.4 LIBS on filters.....	19
2.5 Comparing LIBS in aerosol and on filters	20
3 Experimental apparatus and methodologies	21
3.1 LIBS set-up on particle aerosol.....	21
3.2 Metal solutions.....	22
3.3 LIBS set-up for filter analysis.....	24
3.4 Data acquisition and processing.....	25
3.4.1 Single spectrum, accumulation and average.....	28
3.4.2 Conditional analysis.....	29
4 Results in aerosol.....	32
4.1 experimental conditions for aerosol analysis	32
4.1.1 Temporal optimization.....	32
4.1.2 Detection gate width analysis	34
4.1.3 Comparative analysis for Cu, Ni, Mn and Cr	35
4.1.4 Fluence evaluation	38
4.2 Calibration curves	41
4.3 LIBS matrix effect study.....	47
4.3.1 Aerosol matrix effect	48
4.3.2 Gas matrix effect.....	54
4.3.3 Combined particles and gas matrix effects	60
5 Results on filter.....	62
5.1 Experimental conditions for filter analysis	62
5.1.1 Calibration curves on filters.....	64

6	Case study.....	71
6.1	LIBS and TXRF measurements comparison (multielement).....	71
6.2	Brake powder study.....	73
6.3	LIBS analysis on filtered deposit on snow.....	76
7	Conclusions	80
	Bibliography.....	82
	Appendix.....	97
	A1 Nebulizers.....	97
	A2 Nebulization analysis via TXRF.....	99
	A3 Suspensions	100
	A4 Brake powder qualitative analysis spectra.....	102

LIST OF TABLES

Table 1. Experimental conditions applied in LIBS on aerosol and on solid [59], [60], [84], [90]. ...	20
Table 2. List of heavy metals under analysis, relative salt used for the solutions production and relative principle analysed line wavelength.	23
Table 3. Hit and Miss number of spectra obtained using SD or SmD selection criteria.	31
Table 4. Power in W, energy in mJ and energy density in mJcm ⁻² measured in correspondence of the number of glass filter used.	38
Table 5. In the table are reported the fitting parameters of aerosol calibration curves: slope, intercept and R ² ; and the calculated LODs.	47
Table 6. In the table are reported the fitting parameters of aerosol deposited on filter calibration curves: slope, intercept and R ² ; and the calculated LODs.	69
Table 7. Sampling time required to reach the surface concentration LODs sampling aerosols at concentrations equal to volume concentration LODs.	69
Table 8. For each element, the related compounds used for the solutions, and the concentration ratio with respect to Cu in the measuring chamber are reported.	48
Table 9. Elements and salts physical parameters.	53
Table 10. Element concentrations inside the measurement chamber.	60
Table 11. LIBS vs TXRF experimental parameters both varying the collection time and sampling repeating with a fixed time: sampling time, element aerosol concentration, element ratio.	71
Table 12. Relative elemental mass detected on deposited brakes wear powder thorough EDS analysis.	74

LIST OF FIGURES

Figure 1. Global average aerosols emission of its principal constituents. Data taken from IPCC report (2013) [2].	1
Figure 2. Size distribution of atmospheric particulate matter.	2
Figure 3. Sketch of a typical LIBS experimental set-up.	8
Figure 4. Sketch of the energy states and related energy transitions [37].	9
Figure 5. Temporal evolution of the plasma emitted radiation [46].	9
Figure 6. Cu emission lines at 324.7 nm and 327.4 nm. The black one collected at 10 μ s of delay time and the red one collected at 30 μ s of delay time, both with a gate aperture of 100 μ s.	10
Figure 7. LIBS laboratory experimental set-up.	21
Figure 8. a) Set-up for the preparation of particles deposited filters. b) LIBS set-up for filter analysis.	24
Figure 9. Sampled iron aerosol spot (right).	25
Figure 10. temporal evolution of the plasma-emitted radiation [93].	26
Figure 11. Example of spectra acquired at four different delay times with the same gate aperture of 5 μ s (a). For clarity spectra at 10, 30 and 50 μ s are shown in (b), (c) and (d).	27
Figure 12. Example of parameters evaluation for the copper emission line.	28
Figure 13. Spectra obtained with different selection criteria. Standard deviation (left) and semi-dispersion (right) multiplied for a factor from 1 to 10 (green scale). In red is reported the averaged spectrum obtained from measurements with no Cu signal.	30
Figure 14. Cu emission lines at 325 nm and 327.6 nm, delay time = 30 μ s, gate width = 1 μ s, 100 accumulated spectra.	32
Figure 15. Cu nitrate solution with molar concentration of 0.01 versus delay time with 1 μ s step until 50 μ s and 5 μ s step until 100 μ s; gate width = 1 μ s.	33
Figure 16. Cu nitrate solution with molar concentration of 0.001 versus delay time with step = 5 μ s until 40 μ s then step = 10 μ s; gate width = 100 μ s.	33
Figure 17. Cu nitrate solution with molar concentration of 0.0005; delay time = 1-60 μ s with step = 5 μ s until 40 μ s then step = 10 μ s; gate width= 100 μ s.	33
Figure 18. P/B values versus gate width (step = 5 μ s). Cu nitrate solution with molar concentration of 0.01; delay time= 20 μ s.	34
Figure 19. Cu nitrate solution with molar concentration of 0.001; delay time = 20 μ s; gate width = 1-100 μ s with step = 5 μ s until 40 μ s then step = 10 μ s.	35

Figure 20. Cu nitrate solution with molar concentration of 0.0005; delay time= 20 μ s; gate width= 1-100 μ s with step = 5 μ s until 40 μ s then step = 10 μ s.	35
Figure 21. Ni chloride solution with molar concentration of 0.01. Left: delay time = 1-60 μ s with step = 5 μ s until 50 μ s then step = 10 μ s; gate = 100 μ s. Right: delay time = 20 μ s; gate = 5-100 μ s with step = 10-15-20 μ s.	36
Figure 22. Mn sulphate solution with molar concentration of 0.005. Left: delay time = 5-100 μ s with step = 5-10-20 μ s; gate = 100 μ s. Right: delay time = 30 μ s; gate = 5-150 μ s with step = 10-15-20-50 μ s.	36
Figure 23. Cr acetate solution with molar concentration of 0.004. Left: delay time = 5-100 μ s with step = 5-10-20 μ s; gate = 100 μ s. Right: delay time = 30 μ s; gate = 5-150 μ s with step = 10-15-20-50 μ s.	37
Figure 24. Cu I (top) and Mn I (bottom) signal evaluation varying the laser pulse energy.....	39
Figure 25. LIBS prototype instrument. (1) Laser; (2) Prism; (3) Measurement chamber; (4) Lens; (5) Optic fibre; (6) Lase controller; (7) Sampling pump;(8) Spectrograph; (9) iCCD camera; (10) Laser power unit.....	40
Figure 26. Example of the calibration curve for LIBS measurements of Vanadium (438.07 nm wavelength emission line).....	42
Figure 27. Left) Cu spectra emission line at different aerosol concentrations. Right) Linear fitting for aerosol copper calibration curve parameters calculation and 95% confidence interval (CI).	43
Figure 28. Left) Ni spectra emission line at different aerosol concentrations. Right) Linear fitting for aerosol nickel calibration curve parameters calculation and 95% confidence interval (CI).	43
Figure 29. Left) Pb spectra emission line at different aerosol concentrations. Right) Linear fitting for aerosol lead calibration curve parameters calculation and 95% confidence interval (CI).	44
Figure 30. Left) Mn spectra emission line at different aerosol concentrations. Right) Linear fitting for aerosol manganese calibration curve parameters calculation and 95% confidence interval (CI).	44
Figure 31. Left) Cr spectra emission line at different aerosol concentrations. Right) Linear fitting for aerosol chromium calibration curve parameters calculation and 95% confidence interval (CI).	44
Figure 32. Left) Cd spectra emission line at different aerosol concentrations. Right) Linear fitting for aerosol cadmium calibration curve parameters calculation and 95% confidence interval (CI). ...	45
Figure 33. Left) Tl spectra emission line at different aerosol concentrations. Right) Linear fitting for aerosol thallium calibration curve parameters calculation and 95% confidence interval (CI).	45
Figure 34. Left) Co spectra emission line at different aerosol concentrations. Right) Linear fitting for aerosol cobalt calibration curve parameters calculation and 95% confidence interval (CI).	45

Figure 35. Left) As spectra emission line at different aerosol concentrations. Right) Linear fitting for aerosol arsenic calibration curve parameters calculation and 95% confidence interval (CI).	46
Figure 36. Left) V spectra emission line at different aerosol concentrations. Right) Linear fitting for aerosol vanadium calibration curve parameters calculation and 95% confidence interval (CI).	46
Figure 37. Typical LIBS spectra of iron (Fe II at 260.1) varying the delay time.	63
Figure 38. Peak, base and Peak (-B) to base ratio of iron LIBS intensity versus delay time.	63
Figure 39. LIBS spectra of iron varying the excitation wavelength (266 nm / 1064 nm) and the filter type (quartz/paper).	64
Figure 40. Self-absorption effect on Mn II 257.9 nm emission line.	65
Figure 41. Left) Cu spectra emission line at different surface concentrations. Right) Linear fitting for deposited copper calibration curve parameters calculation and 95% confidence interval (CI). ..	66
Figure 42. Left) Ni spectra emission line at different surface concentrations. Right) Linear fitting for deposited nickel calibration curve parameters calculation and 95% confidence interval (CI).	66
Figure 43. Left) Pb spectra emission line at different surface concentrations. Right) Linear fitting for deposited lead calibration curve parameters calculation and 95% confidence interval (CI).	66
Figure 44. Left) Mn spectra emission line at different surface concentrations. Right) Linear fitting for deposited manganese calibration curve parameters calculation and 95% confidence interval (CI).	67
Figure 45. Left) Cr spectra emission line at different surface concentrations. Right) Linear fitting for deposited chromium calibration curve parameters calculation and 95% confidence interval (CI). ..	67
Figure 46. Left) Cd spectra emission line at different surface concentrations. Right) Linear fitting for deposited cadmium calibration curve parameters calculation and 95% confidence interval (CI).	67
Figure 47. Left) Tl spectra emission line at different surface concentrations. Right) Linear fitting for deposited thallium calibration curve parameters calculation and 95% confidence interval (CI).	68
Figure 48. Left) Co spectra emission line at different surface concentrations. Right) Linear fitting for deposited cobalt calibration curve parameters calculation and 95% confidence interval (CI). ...	68
Figure 49. Left) V spectra emission line at different surface concentrations. Right) Linear fitting for deposited vanadium calibration curve parameters calculation and 95% confidence interval (CI).	68
Figure 50. Cu I emission spectra (delay time = 30 μ s; gate = 100 μ s) with the addition of Mg chloride (a), Cr acetate (b), Na chloride (c), and Na acetate (d). In each plot, the curves refer to different concentration ratios (with respect to Cu) of the added element.	49
Figure 51. Base intensity (a) and Peak Cu I emission line (b) varying Cu:M ratio. Error bars are added at each point.	50

Figure 52. Enhancement of the 324.7 nm Cu I emission signal with the addition of Mg chloride (a), Cr acetate (b), Na chloride (c), and Na acetate (d).	51
Figure 53. Temporal analysis of the 324.7 nm Cu I emission line from 10 μ s to 60 μ s delay time, with a detection gate aperture of 10 μ s.	51
Figure 54. a) Example of Boltzmann plot (Na:Cu(5:1)). b) Temperature versus delay time. Temperature values are obtained using N I emission lines (delay time: 5–15 μ s; gate: 5 μ s) for pure Cu and 1:5 Cu:M. Na chloride was used for these measurements.....	52
Figure 55. Peak LIBS signal (a), base signal (b), and signal-to-base ratio (P/B) (c) of Cu I emission line at 324.7 nm versus the percentage of He added to air.	55
Figure 56. Peak line emission (a), base (b), and Peak/Base ratio (c) of Cu I emission line at 324.7 nm versus the percentage of Ar added to air.....	56
Figure 57. Peak line emission (a), Base (b), and Peak/Base (c) Cu I emission line at 324.7 nm versus the percentage He added to Ar (35%) and air.....	57
Figure 58. Peak (a), base (b) and P/B ratio (c) behaviour versus delay time in air and in 15% He, 35% Ar and 35% Ar / 15% He mixture in air.	58
Figure 59. peak (a), base (b) and P/B (c) behaviour at different delay times in air and 35% Ar / 15% He.	59
Figure 60. Peak/Base versus delay time of Cu emission line in air, with Ar/He mixture in air, and with the further addition of Cr compound. Concentration ratio of Cu:Cr is 1:5. Error bars are reported in each condition.....	60
Figure 61. Relative quantities of Cu, Ni and Pb measured through LIBS and TXRF with different sampling times. All measurements are compared to the calculated values.	72
Figure 62. Relative quantities of Cu, Ni and Pb measured through LIBS and TXRF in 5 repeated measurements. All measurements are compared to the calculated values.....	72
Figure 63. OPC particles size distribution.	73
Figure 64. Deposited brakes wear powder SEM acquired image (Image Resolution: 512 by 384; Image Pixel Size: 0.07 μ m; Acc. Voltage: 15.0 kV; Magnification: 3500).....	74
Figure 65. 10000 accumulated emission spectra of nebulised water for background analysis and subtraction purposes (black), of brakes powder (blue), and subtraction spectra (red). Regions of evaluation: Cu (top-left), Cr (top-right), Mn (bottom).....	75
Figure 66. Aerosol concentrations results for Cu, Cr and Mn and relative errors, obtained with LIBS and ICP measurements.....	75
Figure 67. Single spectrum collected with a delay time of 500 ns and a gate aperture of 100 ns from the emission of a single laser pulse discharge operating at 23 mJ/pulse.	77

Figure 68. Theoretical emission spectrum composed by the emission lines of Si I, Fe I and Fe II calculated by means of the NIST LIBS database tool [141].	77
Figure 69. Calibration curve of Fe II emission line at 260.1 nm. It is clearly visible a linear relation between surface concentration and signal up to 30 $\mu\text{g}/\text{cm}^2$, and then a plateau up to 80 $\mu\text{g}/\text{cm}^2$.	78
Figure 70: Left) Fe signal detected from the 3 filters (F1, F2 and F3), each spectrum is an average of 3 spectra collected from 3 different areas of the filter. Right) calculated surface concentration for F1, F2 and F3 by evaluating the signals with the calibration curve.	78
Figure A1. left) TSI Constant Output Atomizer; right) HUDSON UP-DRAFT Nebulizer.	97
Figure A2. 180 repetitions of solution consumption measured during the nebulization; TSI (left) and HUDSON (right).	98
Figure A3. Mean consumption value calculated over the 180 repetitions and related standard deviation.	99
Figure A4. Experimental set-up for aerosol nebulization study.	99
Figure A5. Procedure steps for suspension production. 1) loaded filter; 2) filter immersion in pure water; 3) ultrasonic bath for particles detachment and suspension; 4) suspension; 5) nebuliser tank filling; 5) aerosolization in ultrasonic bath.	101
Figure A6. Brakes powder qualitative spectra.	103

1 INTRODUCTION

Overview

Nowadays air pollution represents a very important health, environmental, social, and economic issue. Aerosols play a central role in environmental challenges, such as global warming and air quality [1]. It is only relatively recently that there has been increased awareness of the possible health effects of vehicular pollution, and in particular submicron particles. The presence of aerosol in atmosphere is characterised by a great background due to natural sources such as volcanoes, dust winds, bubble bursting and erosion, and an addition of particulate matter (PM) originated by anthropogenic activities emissions, which are the focus for pollution studies. Such PM arises prevalently from different source categories such as combustion of hydrocarbons, industrial processes, dust suspension and transportation activities with cars, ships, airplanes, and other vehicles. Therefore, anthropogenic aerosols contain sulphate, ammonium, black carbon, biomass burning aerosols, non-methane volatile organic compounds (NMVOCs) and primary organic aerosol (POA), but also nitrate, trace metals, and water [2]. In Figure 1 the percentage contributions of the principal constituents in aerosol emission are reported.

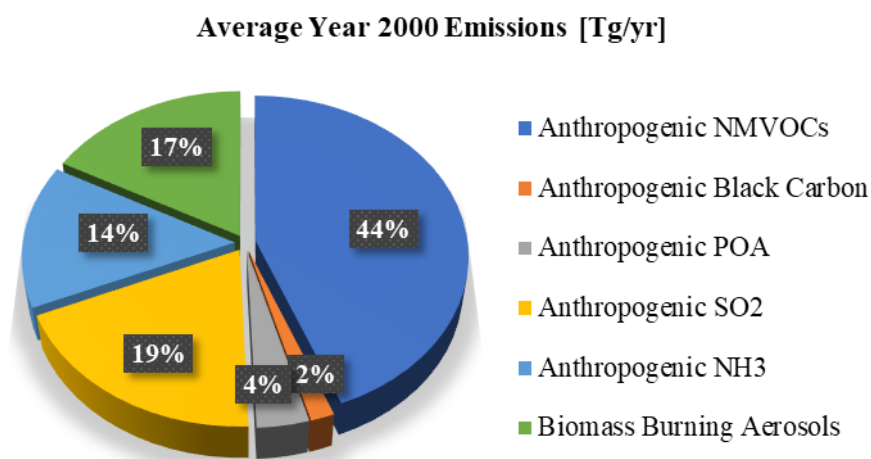


Figure 1. Global average aerosols emission of its principal constituents. Data taken from IPCC report (2013) [2].

In order to fulfil EU standards and World Health Organization guidelines [3], in recent decades many improvements have been made to reduce anthropogenic aerosol emissions both in industry and transportation. Although in this way air quality in Europe has generally improved, air pollution levels still exceed these limits in many places. PM is among the six primary pollutants in air, which thresholds are set by the European Air Quality standards [4,5].

Technically, the definition of aerosol is a stable suspension of liquid or solid in a gas [1]. Aerosols dimensions span from 0.001 μm to 100 μm , with the particle size covering several orders of magnitude, from molecular sizes up to macroscopic.

According the U.S. Environmental Protection Agency (EPA) [6], atmospheric particles can be classified as follows:

- Ultrafine: particles with an aerodynamic diameter lower than 0.1 μm ;
- Fine: particles with an aerodynamic diameter in the range 0.1 – 2.5 μm such as those found in smoke and haze;
- Coarse: particles with an aerodynamic diameter in the range 2.5 – 10 μm , such as those found near roadways and dusty industries;
- Supercoarse: particles with an aerodynamic diameter higher than 10 μm .

A further classification of particles performed by EPA is given as:

- Total Suspended Particulate Matter (TSP): particles ranging in size from 0.1 μm to about 30 μm ;
- PM₁₀: particulate matter with an aerodynamic diameter less than or equal to 10 μm ;
- PM_{2.5}: particulate matter with an aerodynamic diameter less than or equal to 2.5 μm ;
- Nanoparticles: particles with diameters below 50 nm.

In Figure 2 the size distribution of the atmospheric PM is reported with the classification in the size classes described.

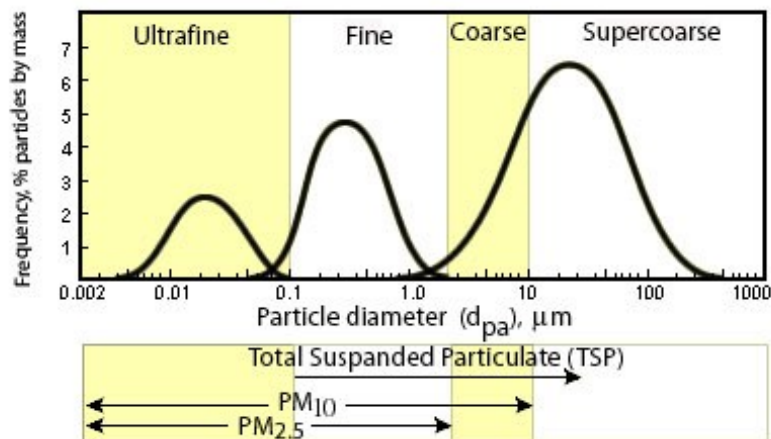


Figure 2. Size distribution of atmospheric particulate matter.

It is important to highlight that the properties of the aerosol are strictly related to the dimension of the particles present, spanning from properties similar to large gas molecules to properties described by Newtonian physics.

Aerosols present in the atmosphere can be subdivided in primary or secondary aerosol. Primary aerosols are composed by particles that are directly emitted into the atmosphere, while secondary

aerosols consist of particles resulting from several complex chemical-physical processes, such as reactions with sulphur dioxides and nitrogen oxides or in situ aggregation / nucleation from gas-phase molecules [1]. Atmospheric particles can be originated from combustion processes, re-suspensions of soil materials (for example by the wind or the traffic) or secondary formations from chemical-physical processes in the atmosphere.

As already observed, the interest of the scientific community in the study of PM is essentially due to environmental aspects and adverse effects on human health. Considering climate effects, due to scattering or absorbing solar radiation, a change in cloud properties can result, which causes rain or snow fall. Over the past decades different studies suggest that by increasing the air pollution in the urban area, an increasing of respiratory and cardiovascular mortality is observed [7]. In particular, ultrafine particles are dangerous as they present a higher predicted pulmonary deposition, greater potential to induce pulmonary inflammation, large surface area, and enhanced oxidant capacity.

Aerosol particles physicochemical properties, such as chemical composition, particle size, and absolute particle mass density, strongly depend on the origins of the PM emissions as well as the surrounding environment and transport conditions.

Among the wide range of pollutants heavy metals are of significant interest for their toxicity which impacts on human health and environment. Monitoring Pb, Hg, As, Cd, and Ni is crucial, being parts of long-range transboundary air pollution [4,5,8]. Moreover, other heavy metals are classified as hazardous, persistent, or bio-accumulative (e.g., Cr, Cu, Zn, Pt, Rh) [9].

The interest in heavy metals analysis is becoming more stringent in the framework of a circular economy approach. In this context, it is of primary importance an efficient use of available resources and, at the same time, recycling waste. The management of removal and recycling of these waste materials, as well as energy recovery from the emission in exhaust ducts of power plants, can have a significant impact on the environment. Due to the lack of raw material in Italy, the possibility of reusing waste, for example in substitution of natural minerals, is fundamental. In particular, the Lombardy production of sewage is around 800 thousand tons, 500 of which are wastewater [10]. Combustion of this waste material, however, is very critical, because of the emission in ambient air, through Municipal Solid Waste (MSW) incinerator stack, of different polluting materials. Among these polluting materials, one of the most important contributions is given by metals, and especially heavy metals, because of their toxicity, as already mentioned [11]. For this reason, it turns out to be very important to have diagnostic tools and instruments able to measure in real-time the concentrations of pollutants at the exhaust and, at the same time, able to separate, pick up and then recycle metals.

Context and motivation

Regarding metals emission and in particular concerning short term monitoring, the regulation EN14385:2004 has to be followed [12], in which a reference manual method is specified for the determination of the mass concentration of specific elements emitted by incinerators of urban waste. The regulated elements are As, Cd, Cr, Co Cu, Mn, Ni, Pb, Sb, Tl, and V. On the other hand, concerning long term monitoring of metals emission, different techniques are categorized as Multi-Metal CEMs (Continuous Emission Monitoring). These techniques have to respect PS-10 criteria [13] such as response time (the CEMs shall continuously sample the stack effluent), quality assurance standard, and relative accuracy (it must be no greater than 20 percent of the mean value of the reference method test data in terms of units of the emission standard for each metal, or 10 percent of the applicable standard, whichever is greater). Furthermore, a multi-metals CEMs must be able to accurately report the concentrations of at least two metals. This can be performed by extracting a representative sample of stack effluent and capturing the metal analytes of interest on a medium. The CEMs must have a cycle time that is less than one third the period of the applicable standard. The range of the instrument must be from 10 % to at least 400% of the applicable regulation as determined by field campaigns or laboratory tests. Finally, the instrument or operator must be able to perform daily upscale, blank, and flow quality assurance checks to ensure the accuracy, precision, and stability of the instrument and its data [14]. In order to test the measurements of the instrument, the reported CEMs concentration have to be plotted together with the concentration reported by the same analysis carried on following EPA directives or a suitable alternative [15], and then compare them with a linear regression analysis. This is the correct procedure for a CEM validation.

Different CEMs instruments have been developed and commercially available based on Atomic Absorption Spectroscopy (AAS), Inductively Coupled Plasma (ICP) or X-Ray Fluorescence Spectroscopy (XRF) techniques [16–18]. AAS technique consists in evaluating the absorption of light by free metallic atoms. Each element has a typical pattern of absorbed lines through which can be recognised [19]. ICP technique consists in vaporising and ionizing the sample inside a plasma and then recognizing the elements through a mass spectrometer (ICP-MS) or through characteristic atomic emission lines due to decays (ICP-AES) [20]. For AAS and ICP proper samples preparation procedures are needed. PM is collected onto particular filters, like quartz, PTFE, PC, cellulose [21], which are then dissolved in strong acids. Such process could lead to contamination and material loss [22] and could also require the use of dangerous and pollutants chemicals. XRF is a promising alternative multi-element technique that is quicker, less expensive, more environmentally friendly, sustainable, and non-destructive compared to AAS and ICP [23–25]. The technique consists of the emission of characteristic fluorescent X-rays from a material excited by high energy X-rays.

However, its application to PM analysis is still challenging. Total reflection XRF (TXRF) is known for achieving higher sensitivities due to the instrument geometrical configuration that enhances the fluorescence emissions and collection. This technique has proved high potential for the analysis of PM collected on quartz reflector [26] and quartz fibre filters [27].

The XRF technique has been used by the Cooper Environmental Services to build different commercial instruments able to measure metals emitted by exhaust ducts. The XCEM (X-Ray Fluorescence-Based Multi-Metal Continuous Emission Monitor [28]) extracts a sample of stack gas and concentrates the metals of interest on a filter tape, then an XRF instrument is used to determine metal mass concentration. This system is able to give concentration measurements every 10 to 20 minutes up to 19 elements. After testing this instrumentation, the XCEM met the proposed PS-10 requirements for sampling and response time and quality assurance but satisfied the required relative accuracy only for 5 out of 9 elements tested (Pb, Cd, Cr, Sb, and Ba). Another XRF based instrument developed by the Cooper Environmental Services is the XACT® 640 Multi-metals monitor. This system uses reel-to-reel filter tape sampling and non-destructive energy dispersive X-ray fluorescence (EDXRF) analysis to monitor stack HAP (Hazardous Air Pollutant) metal emissions. An isokinetic sub-sample of stack gas passes through the stilling chamber and it is drawn through a chemically reactive filter tape. Vapor phase metals, including mercury (Hg), are deposited along with the particulate matter (PM) on the filter tape. It can identify and measure 23 elements simultaneously and it is a near real-time instrument. It can provide analysis every 15, 30, 60, and 120 minutes.

There are other CEMs based on the ICP technique, but only one of the ICP units, developed by Thermo Jarrell Ash Corporation, has been successful in meeting the relative accuracy (RA) criteria of the PS-10. The ICP technique is based on the use of a plasma that atomize and ionize the sample and it is used in order to detect metals in the liquid sample even in the condition of low concentrations. However, since preliminary preparation is needed, no real time information about pollutant emissions can be obtained. In this context, Laser Induced Breakdown Spectroscopy (LIBS) is a promising technique for real-time qualitative and quantitative analysis of pollutant elements. As an optical diagnostic tool, it is an interesting technique for in-situ and not intrusive analysis, which can be performed for monitoring the presence of metals at the chimney stack and particularly of measuring their concentration when emitted in the open air. While LIBS-based instruments are proposed in the literature and commercially available to measure element concentration on liquids and/or solids [29–32], very few can be found for aerosol measurements [33–36].

The technique is based on focusing a laser pulse in or on a target material, which can be a gas, liquid, aerosol, or solid, to form a micro-plasma. The material in the probe volume is atomized and excited, and the resulting spectral emission is collected and analysed by a detector [37]. The technique is

particularly suited for aerosol analysis due to its capability to simultaneously detect different elements, which aligns with the significant chemical heterogeneity present in aerosols.

The aim of this PhD thesis is the application of the LIBS technique to carry out online qualitative and quantitative measurements of stack heavy metal concentration. This work is financed in the framework of an innovation project (F.A.N.G.H.I) of European funding ROP ERDF 2014 – 2020, whose main goal is the study and development of new technologies for the sewage treatment. In particular, the project aims to optimise the management of removal, usage and the energetic recovery of raw materials and to evaluate health and environmental impacts of different technological solutions.

In this context, one of the objectives of this innovative project is the main goal of this thesis work. More specifically, it is the development of an innovative instrumentation for measurements at the exhaust of combustion systems and in a challenging prospective for monitoring atmospheric polluting emissions and air quality. In particular, the instrumentation developed thanks to research laboratory activity should be able to detect metals concentration with a reasonably low limit of detection in order to meet the requirement imposed by EU Directives and National law for exhaust measurements.

The laboratory work will be mainly based on the implementation and development of the experimental apparatus for LIBS measurements. With the purpose of recreating in laboratory the same conditions present at the smokestack of a combustion plant, an aerosols generator will be used. Moreover, both direct and indirect approaches are considered. Direct real time measurements are applied when the elements concentration in the probe volume is higher than the detection limit. Otherwise, in low concentration conditions, below the limit of detection of the analyte in direct analysis, an indirect approach is proposed. In this case, PM is collected on filters for an off-line subsequent LIBS analysis. [38].

Another interesting objective pursued in this thesis work concerns the fundamental critical analysis of LIBS measurements in the context of gas and elements/compounds matrix effects. On one side, this effect is proved to significantly affect LIBS signal for calibration/quantitative analysis, on the other end it can be fruitful for signal enhancement. Moreover, different case studies are performed, whose results are extensively presented and discussed, with interesting comparison with ICP and TXRF measurements.

Finally, an interesting goal of the doctorate project has been the implementation of a LIBS instrumental prototype for in-situ analysis. To this purpose ad-hoc components and appropriate apparatus set-up have been realized.

Structure of the manuscript

This PhD work is composed of 8 Chapters described extensively in the following.

- In Chapter 1 the fundamentals of the LIBS technique are reported with particular emphasis on the specific physical parameters involved and affecting the analysis. LIBS measurements on aerosols and on particle-deposited filters are considered.
- In Chapter 2 the experimental arrangement for aerosol and particle-deposited filters are deeply described, with details on each experimental part and in particular on the solutions prepared.
- In Chapter 3 the acquisition approach implemented is described differently for in-situ/ex-situ analysis, namely averaging versus conditional analysis mode.
- In Chapter 4 the measurements and results obtained in aerosol are presented. In particular, the choice of the experimental detection conditions for aerosol is motivated thanks to a parametric study on time-scale, detection gate, delay time and laser fluence. Then, the calibration curves are reported for each element under analysis.
- In Chapter 5 the corresponding study and calibration curves for particle-deposited filters is presented. Moreover, the substantial differences are underlined in the experimental detection conditions applied to aerosol and particle-deposited filters.
- In Chapter 6 matrix effects study due to gas and / or concomitant presence of other elements/compounds in the probe volume is performed trying to highlight possible application for enhancing LIBS signals. Moreover, different case studies are presented aimed to underline the potential of the technique in different applications.

In particular, considering the last chapter, measurements on brakes powder and impurities detected on ice samples are considered and discussed as interesting applications.

2 LASER-INDUCED BREAKDOWN SPECTROSCOPY (LIBS)

The development of LIBS follows a few years after the birth and development of the first lasers [39,40]. Starting in 1958 with the idea by Schawlow and Townes [41] to extend the maser to optical radiation and the first working ruby laser by Maiman in 1960 [42,43] arriving to the first air discharge generated by a laser, obtained by Maker, Terhune and Savage in 1964 [44]. Immediately, researchers dealt with the acquisition timing, in order to resolve the different emission lines. From the beginning it was clear the strong presence of physical and chemical matrix effect which could not be neglected for quantitative analysis. In the late 1970s aerosols analysis started to be object of research [37]. In later decades with the technology improvement in situ studies and more reliable quantification measurements and methods have been developed. In Figure 3 a sketch of a typical experimental set-up for LIBS measurements is reported.

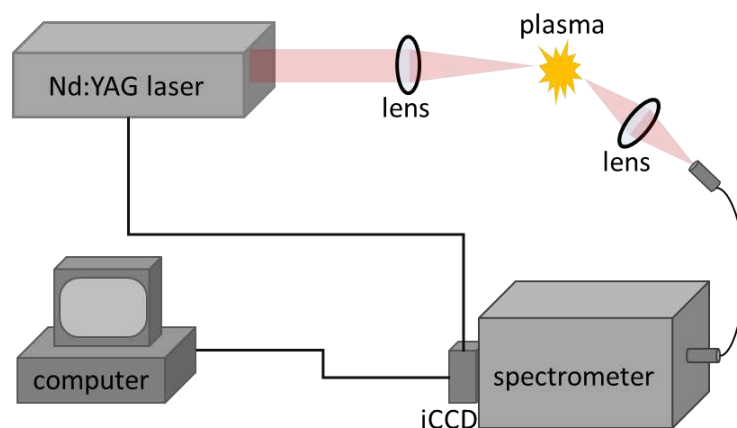


Figure 3. Sketch of a LIBS experimental set-up.

2.1 LIBS FUNDAMENTALS

The basis for the study of the LIBS technique starts from a definition of plasma: a plasma is a local assembly of atoms, ions, molecules, and free electrons, overall electrically neutral, in which the charged species often act collectively [37]. In LIBS technique the plasma is produced by focusing a pulsed laser beam of a relatively high pulse energy. The radiation emitted from the plasma consists of well-defined spectral lines and a continuum bremsstrahlung emission.

Generally, the process involved in the generation of the continuum emission which is the bremsstrahlung emission which is due to the deceleration of electrons deflected by the electrical fields of the atoms. In Figure 4 is reported a sketch of the energetic transitions occurring between different states after energy absorption.

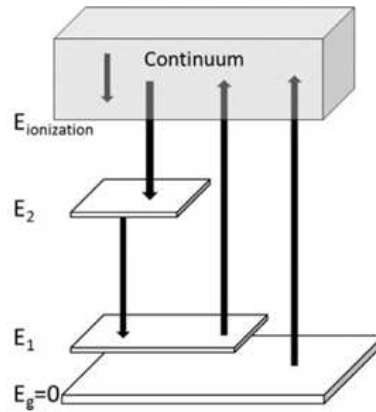


Figure 4. Sketch of the energy states and related energy transitions [37].

The frequencies of free-bound transitions are obtained as [45]

$$h\nu = \xi - E_j + \frac{1}{2}mv^2 \quad (1)$$

where $\frac{1}{2}mv^2$ is the kinetic energy of the free electron and ξ is ionization energy of the atom. In this context, the bremsstrahlung originates from the deceleration of the electrons, which is a free-free emission transition occurring with kinetic energy losses of electrons.

In Figure 5 the typical time scale of the phenomena occurring after laser pulse is shown.

In the first hundreds of nanoseconds, ionic emission can be detected above the strong continuous spectrum previously described. Atomic emission starts to be observed in the first microseconds, followed by molecular emission in the scale of hundreds of microseconds.

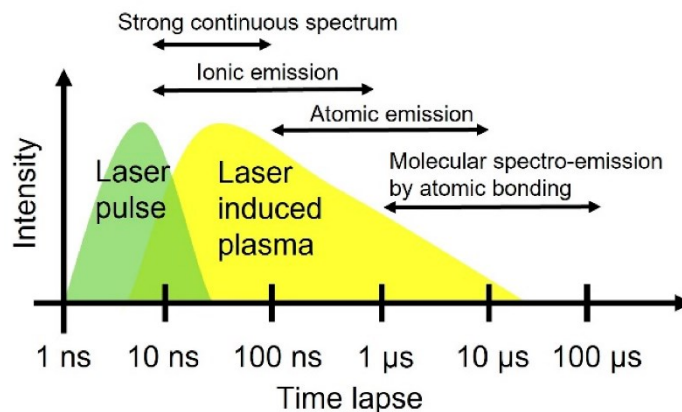


Figure 5. Temporal evolution of the plasma emitted radiation [46].

The key point of LIBS technique is to collect the radiation emitted from the plasma with a correct timing, in order to discriminate each analyte signal against the background. Choosing a correct time

setting is of crucial importance since, as can be observed in the Figure 5, at early time the intensity of the continuous spectrum is strong.

Then, when the plasma starts cooling down, the background decreases with time. At this point the intensity of the emission lines becomes to be visible. This is the correct time window for analytical analysis.

As an example, in Figure 6 are reported Cu emission lines, generated from the same sample, collected into two different temporal windows, 10 μs and 30 μs respectively. The difference in the background intensities and in the lines prominence above the continuum signal is evident. The temporal evolution of LIBS signals is also dependent on laser energy, environment pressure, analyte state (gas, liquid, solid or aerosol) and also on the element under investigation, since each element exhibits a specific decay time.

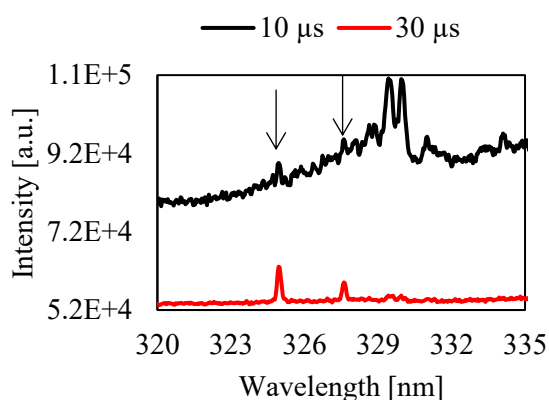


Figure 6. Cu emission lines at 324.7 nm and 327.4 nm. The black one collected at 10 μs of delay time and the red one collected at 30 μs of delay time, both with a gate aperture of 100 μs .

In fact, changing the laser energy, a significant change in the plasma conditions occurs, related to different physical and chemical processes involved [47].

The laser pulse energy is the amount of energy that is delivered to the sample in each laser pulse. The higher the laser pulse energy, the more material is evaporated and the larger is the plasma. This results in a stronger emission signal, which can improve the sensitivity and accuracy of the LIBS signal. The repetition rate is the number of laser pulses that are emitted per second, and it defines the maximum measurement frequency for LIBS. The higher the repetition rate, the faster the analysis can be performed. However, the repetition rate is also limited by the time it takes for the plasma to cool down between pulses. Typical laser pulse energies for LIBS range from 1 to 1000 mJ, depending on the application. The repetition rate is typically 10–100 Hz for flashlamp-pumped Nd:YAG lasers with electro-optical Q-switching. The optimal laser pulse energy and repetition rate for LIBS will vary depending on the specific application. The irradiance is the power of the laser per unit area. Typical

breakdown thresholds are $>10^7$ W/cm² for solids and $>10^{11}$ W/cm² for gases. The irradiance depends on the pulse energy, the pulse width, the beam diameter, and the beam quality at the location of interaction with the sample.

Another important parameter is the pulse width. Usually, for LIBS analysis nanoseconds or femtoseconds lasers are employed. The principal difference is that for nanosecond pulses the plasma generation starts while the laser irradiation still persists, resulting in an interaction between laser beam and plasma: the plasma can absorb energy from the pulse after its formation and can be furtherly heated. On the contrary, in femtosecond pulses no interaction between laser and plasma occurs and this results in a weaker and shorter line emission. Moreover, for solids there is a well-defined crater formation. Generally, for aerosol LIBS analysis nanoseconds lasers are more suitable.

The interaction between laser and analyte depends also on the wavelength of the laser radiation. The wavelength coupled with the material can lead to a more or less energy absorption, which can affect the measurement sensitiveness [48–50]

As already reported, the laser beam is focused to increase the irradiance to values greater than 10^7 W/cm². The materials, solids, liquids or gases, exposed to these values of irradiance will be transformed in the plasma state within a few nanoseconds. For this reason, the focusability of laser radiation is of great importance and it depends on the beam quality and wavelength. In the ideal case of a Gaussian beam, the laser beam can be focused by a lens in the following beam waist radius [47]

$$w_0 = \frac{2f\lambda}{\pi D} \quad (2)$$

where w_0 is the radius of beam waist, f is the focal length of the lens, λ is the wavelength of the laser radiation, and D is the diameter of the lens. A real laser beam is different from an ideal Gaussian beam, and this difference is described by the standardized beam propagation ratio M^2 [47]

$$M^2 = \frac{\pi d \theta}{\lambda} \quad (3)$$

where d is the diameter of the laser beam, and θ is the beam divergence angle of the laser beam. The smallest possible value of M^2 is 1. However, for real laser beams M^2 is always greater than 1. For the average irradiance at the location of the beam waist is valid the relation [47]

$$I_f = \frac{E_L}{\tau_L \pi W_0^2} = \frac{\pi E_L D^2}{4 \tau_L f^2 \lambda^2 M^4} \quad (4)$$

where E_L is the energy of the laser pulse, τ_L is the temporal width (FWHM, full width at half maximum) of the laser pulse. For typical values ($E_L = 80$ mJ, $D = 10.8$ mm, $L = 20$ ns, $f = 200$ mm, $\lambda = 1064$ nm, $M^2 = 2.8$), an average irradiance of $I_f = 10^{11}$ W/cm² is obtained [47].

The intensity of spectral lines is typically dependent on two parameters: the transition probability, that is the probability of a certain transition between two atomic levels (an intrinsic property of the atom), and the excitation condition. This last parameter refers to the energy involved in the process, the physical and chemical properties of the analyte, and the related environment. Generally, a line is easily detectable when the medium is in condition to be optically thin, this means that the emitted photons have low chance to be re-absorbed. In particular cases, these conditions are not fulfilled, and a phenomenon called self-absorption can occur. For example, resonance lines generally generated from the transition from the lowest excited levels to ground state, emit light that have a very large probability to be reabsorbed before leaving the plasma. The typical effect of self-absorption is a broadening of the line profile, as described extensively in the following, and, in some cases, the flattening of the LIBS peak with possible intensity dip in the centre of the peak.

2.1.1 Temperature and electron density

The spectral emission lines intensity relevant in spectroscopic studies, is dependent on the specific environment considered. Ideally for free atoms the emission lines are described by a Lorentzian trend [45]

$$I(\nu) = \frac{I_0 (\gamma/4\pi)^2}{[(\nu - \nu_0)^2 + (\gamma/4\pi)^2]} \quad (5)$$

where I_0 is the intensity at the centre of the peak at a wavenumber ν_0 , and γ is the radiation damping constant. The Lorentzian spreading is the natural spread around the theoretical emission line. Two different effects can contribute to the line broadening: the Doppler and the Stark effects.

- Doppler effect. In this case, the line broadening is generated by the random thermal motion of the emitting atom and is represented by a Gaussian shape.
- Stark effect. This effect occurs in a dense plasma, where the interaction of the atom and the electric field has to be considered.

In this last case, a splitting and shifting of the atom energy levels can occur. The Stark effect could be linear, for hydrogen-like atoms, and quadratic for the other atoms. The linear one exhibits a

symmetrical broadening without any shift, while the quadratic one generates an asymmetrical broadening and shifts the centre of the line.

The emitted intensity is also strongly dependent on the plasma opacity [37]. The emitted radiation has to pass through the plasma without undergoing significant absorption and scattering. In this case, the plasma is optically thin. The emission intensity can be described by the following relationship [37]

$$I(\lambda) = [\varepsilon(\lambda)/\alpha(\lambda)](1 - e^{-\alpha(\lambda)L}) \quad (6)$$

where $\varepsilon(\lambda)$ is the emissivity, $\alpha(\lambda)$ is the absorption coefficient, and L is the plasma length along the detection line. In conditions of optical thin plasma, $\alpha(\lambda) \ll \varepsilon(\lambda)$, this relationship becomes

$$I(\lambda) \sim \varepsilon(\lambda)L. \quad (7)$$

If this condition is not respected, self-absorption effect can manifest.

Once the emitted radiation is collected, the spectral analysis can give information about the composition of the plasma as well as its physical properties.

There are three main physical parameters that are useful to characterize and describe a plasma: the temperature (T), the degree of ionization and the electron density (n_e). As already seen, in normal conditions the width of emission lines is affected by the Stark effect. The Stark broadening can be used to retrieve the electron density in the plasma. To this purpose, sometimes, hydrogens lines are used. In fact, generally high intensity lines could suffer from self-absorption and in hydrogen or hydrogenic ions, to first approximation, the Stark effect is linear. In this context we can use a simple relationship which links the electron density with the spectral line width, $\Delta\lambda_S$, [51]:

$$n_e [cm^{-1}] = C(n_e, T)(\Delta\lambda_S)^{1.5} = 8.02 \times 10^{12} (\Delta\lambda_{1/2}/\alpha_{1/2})^{1.5} \quad (8)$$

where the coefficient $\alpha_{1/2}$ is a weak function of temperature and pressure tabled by Griem [52], $\Delta\lambda_{1/2}$ is the FWHM in Å. Due to the energy level shift introduced by the Stark effect, Griem showed two expressions relating the shift, d_{total} , and line width to the electron density in non-hydrogenic ions [37]

$$w_{total} \sim [1 + 1.75A(1 - 0.75r)](n_e/10^{16})w \quad (9)$$

$$d_{total} \sim [d/w + 2.00A(1 - 0.75r)](n_e/10^{16})w \quad (10)$$

where w_{total} is the measured HWHM (half width at half maximum), A is a parameter that accounts for the ion contribution, r is the ratio of the mean distance between ions and the Debye radius (radius such that the emitting atom is shielded from the effects of all charged particles located at distances greater than or equal to the Debye radius [37]), and w is the HWHM due to Stark effect caused by the electron density.

The other important parameter for the physical characterization of the plasma is the temperature, affecting the relative population of energy levels and the particles speed distribution. A correct interpretation of the temperature can be obtained only when the plasma under analysis is in thermodynamic equilibrium. According to this the concept of local thermodynamic equilibrium (LTE) as an approximation is used. LTE condition is reached with plasma thermalization, which occurs after a sufficient number of collisions. However, not all species may be simultaneously in thermodynamic equilibrium. Generally, atoms and ions equilibrate in a different moment than electrons, being the first heavier than the electrons. In order to verify that the plasma LTE conditions are fulfilled, the McWhirter criterion can be applied [53], given by the following relationship between electron density (n_e) and temperature (T)

$$n_e > 1.6 \times 10^{12} T^{1/2} (\Delta E)^3 \quad (11)$$

where ΔE is the energy of the upper level above the ground state. This simple criterion for LTE can be evaluated after experimental measurements of n_e and T are carried out. However, in some cases when plasma could not be assumed homogeneous and stable this criterion is not sufficient and further analysis needs to be considered [54].

If the experimental conditions are supposed to generate an LTE plasma, there are two principal methods to calculate the experimental plasma temperature. The first method exploits the ratio between two line intensities of two lines. The line intensity emitted by an analyte [37] is given as

$$I[Wsr^{-1}] = \frac{h\nu AN}{4\pi} = \left(\frac{hcN_0 gA}{4\pi\lambda Z} \right) e^{-\frac{E}{kT}} \quad (12)$$

where h is the Planck constant, ν is the frequency of the emission line, A is the Einstein coefficient, N is the number density, c is the speed of light, N_0 is the total species population, g is the statistical

weight of the level, λ is the wavelength of the line, Z is the partition function, E is the energy of the level, and k is the Boltzmann constant. So, if two emission lines are taken into account the ratio will be expressed by [37]

$$I'/I = (\lambda g' A' / \lambda' g A) \exp[-(E' - E)/kT] \quad (13)$$

This is called the two line method [37] and allows to retrieve the temperature measuring the intensities of two lines with known parameters. A second way to calculate the plasma temperature, which may result in a more accurate measurement is a graphical analysis. Considering the logarithm of Eq. (1), the following relationship can be obtained [37]

$$\ln(I\lambda/gA) = -E/kT - \ln(4\pi Z/hcN_0) \quad (14)$$

By plotting the left quantity in the equation (on the y axis) versus the energy E (on the x axis), a straight line is obtained whose slope ($1/kT$) directly gives the temperature T .

2.2 QUALITATIVE / QUANTITATIVE ANALYSIS

Considering a specific compound present in the probe volume, which is involved inside the plasma generated by the laser breakdown, it is broken into its elements which are then excited. The resulting emission consists of spectral lines of different intensities, related to each element under analysis. The number of lines decreases if the amount of the element involved in the discharge is more diluted. Only a few lines of that element, which are also the lines of highest intensity, persist. Therefore, the qualitative analysis can be carried out by looking at the persistent lines of that element. If these lines are absent, it can be assumed that the analyte concentration is below the limit of detection of the technique. In a general case several lines of different elements will be present simultaneously. Each line or group of lines can be identified by the use of available databases [55].

After the identification of the analyte species, quantitative analysis can be performed consisting in associating a quantity, in concentration [ppm, $\mu\text{g}/\text{m}^3$, $\mu\text{g}/\text{cm}^2$ or else] or amount [ng or else], to the emitted lines detected. In the context of LIBS emission spectra analysis, quantification is possible both without the need of calibration, calibration-free LIBS (CF-LIBS) and with a calibration, depending on the plasma conditions.

CF-LIBS is based on the measurement of the emission line intensities of all the analytes present in the probe volume as well as the knowledge of plasma parameters, such as electron density and temperature and is applicable only when the plasma is in LTE conditions [54,56–58]. The acquisition

time required to obtain an optimal LIBS signal for the analysis of low-concentration aerosols generally exceed tens of microseconds for direct measurements and hundreds of nanoseconds for particle-deposited filter, as described in the following. For the direct analysis, this time is too long for a reliable analysis of plasma parameters such as electron density and temperature. Therefore, the CF-LIBS approach is not applicable for this type of direct aerosol measurements and calibration is needed. Generally, calibration curves are obtained by keeping the same experimental conditions for all the measurements considered. In this context, some issues have to be taken into account, i. e. laser variation shot by shot, electronic noise due to the instrumentation, gas matrix effect, chemical matrix effect, linearity of the response, and uniformity of the sample are the principal ones.

2.3 LIBS ON AEROSOLS

Laser-Induced Breakdown Spectroscopy applied to aerosols represents a notably effective technique for aerosol analysis. In particular, real-time insights into the composition and quantification of constituent elements within the specific aerosol under analysis can be readily obtained. This spectrum of analysis spans from environmental contaminants to the evaluation of emissions originating from expansive production and incineration facilities. Notably, the implementation of LIBS technique obviates the need of sample pre-processing, since the plasma can be instantaneously generated within a measurement cell, where the sample under analysis is directly conveyed, thus avoiding any extraneous sampling artefact. A compact instrumentation could be developed for continuous and in-situ monitoring [35,59–61].

In aerosol LIBS, the breakdown threshold is closely related to the gas matrix in which the particles are suspended. In comparison to solid or liquid samples, the breakdown threshold presents distinctive characteristics. The formation of plasma in a neutral gas primarily follows some overlapping steps over time. Initially, there is plasma ignition, involving a rapid increase of the number of free electrons and ions subsequent to the initial interaction between the naturally present free electrons and photons of the incident laser beam. Under common working conditions, that are ambient pressure and laser wavelength of 1064 nm, breakdown occurs through the process of inverse bremsstrahlung, or free-free absorption, leading to cascade generation of electrons. While the initiation of breakdown depends on the production of the first electrons, the irradiation threshold is governed by the cascade growth of ionization, fed by the absorption of laser radiation. In fact, electrons in a laser field gain energy to ionize and multiply through inverse bremsstrahlung interactions. Subsequently, the plasma continues to expand and interact with the laser beam, sustaining photoionization processes. Finally, following the end of the laser pulse, the plasma extinguishes due to the diffusion and conduction of thermal

energy, and ion and electron recombination, gradually returning to a neutral and equilibrium state with the external environment.

The presence of particles within the gaseous matrix affects the absorption of laser radiation and the threshold value for breakdown [62,63]. As soon as the focused laser pulse interacts within the measurement volume with the particles, they absorb the radiation and begin to heat up, undergoing phase changes until vaporization, which can be either complete or partial. This process is not uniform within the probe volume but depends on the distribution of particles within the gaseous matrix. For each individual particle, it also depends on its morphology and constituent components. Thus, various hotspots can be created, corresponding to different particles or even different positions within the same particle. In these hotspots, since the absorption of laser radiation is higher, initiation points for plasma formation can occur: the particles heat up and lose some of their energy through vaporization and interaction with the surrounding gas. These processes lead to the breakdown of the surrounding gas, producing an increase in temperature and additionally in the number of free electrons. Moreover, free electrons can be produced by different mechanisms such as the initial breakdown in the evaporated particles, thermionic emission, electrons photoemission, and tribo-electrons. These processes are responsible for a lowering in plasma formation threshold. In air, this threshold decreases from approximately 10^{11} W/cm² to around 10^7 W/cm². Apart from the presence of particles, the breakdown threshold also depends on other parameters such as pulse length, laser beam frequency, and particles size [64–71].

In the context of spectral analysis applied to an aerosol sample, careful consideration must be given to the discrete nature of both the dispersed particulate matter within the gaseous matrix and the laser pulses generated at a specific frequency. This intrinsic nature gives rise to two distinct analytical regimes for spectra processing. One regime concerns the scenarios characterized by high analyte concentrations. In such cases, a uniform composition in aerosol of the analyte under analysis can be considered, ensuring that the plasma generated by each laser pulse effectively interacts with the analyte species.

Conversely, the other regime corresponds to scenarios wherein the analyte is present in significantly low concentrations within the gaseous matrix. In this context, due to the sparse nature of the analyte dispersion, not all laser pulses can hit the analyte.

In the first scenario, the approach employed for analysis involves the averaging of a great number of individual spectra. This method allows enhancing signal-to-noise ratio and reducing any LIBS signal fluctuation originating from plasma fluctuations, detector noise, and intensifier-related noise [72]. Generally, under conditions where the particulate concentration is sufficiently high to ensure a substantial number of induced plasma events interacting with the analyte, averaging is performed

across hundreds of spectra. Beyond this point, a reduction in analyte signal proportional to the inverse of the sampling rate would occur [45].

Usually in building up the calibration curve for quantitative analysis, instead of considering the simple LIBS signal, the signal to background ratio is considered. In fact, since the background depends on laser intensity, this ratio allows correcting the LIBS signal for laser pulse-to-pulse fluctuations.

Another critical point to take under consideration is the occurrence of complete vaporization of the particles under analysis. This ensures a linear response of the signal. The threshold for complete vaporization depends on the specific experimental conditions and the particles size, ranging from a few micrometres in diameter to approximately ten micrometres [59,73–75]. Lastly, in the pursuit of analysing the ensemble-averaged spectra, careful attention must be devoted to the establishment of an appropriate calibration curve. This necessitates maintaining concentrations within a range that permits a favourable sampling rate and guarantees complete vaporization of particle sizes.

In the second scenario, a statistical approach must be considered. Considering the discrete nature of the interaction of a laser pulse with the analyte, the probability of interaction is well represented by a Poisson distribution [45,76,77]

$$P_n = \frac{\mu^n}{n!} e^{-\mu} \quad (15)$$

where μ is the average number of mass-equivalent particles in the plasma volume, considering that the detected signal is the sum of contribution given by all the particles involved in the plasma formation. In this way the particles sampling rate (PSR) is given by [76]

$$PSR = 1 - e^{-\mu}. \quad (16)$$

In the case of low PSR, an approach called conditional analysis can be applied, in order to enhance the analyte LIBS signal response [77]. The standard procedure consists in separating the collected spectra into two classes, one containing the so called “*hits*”, which means spectra in which the analyte LIBS signal is evident, the other one called “*misses*”, in which spectra with no signals are detected. Only *hits* spectra are considering in the average procedure. By using the calibration curve, concentration measurement is derived corresponding to this average LIBS signal. Finally, this value is corrected by the experimental PSR obtained as the ratio of the *hits* spectra and the total acquired spectra in order to retrieve the analyte concentration.

Of crucial importance is the choice of the threshold criteria for the distinction between *hits* and *misses*, as reported in the literature.[77–79]. A different approach can be applied if a further analyte peak is detected in the same LIBS spectrum. In this case, the selection threshold can be lowered by considering the control performed on this second LIBS signal.

2.4 LIBS ON FILTERS

In the condition of extremely low concentrations of the analyte, the direct application of LIBS for aerosol analysis is not straightforward. A notable example is the evaluation of pollutants' effects within polar or high-altitude environments, where analyte levels are inherently low [80]. Additionally, circumstances wherein the generation of a plasma poses safety hazards, such as when assessing particulate matter within a gaseous matrix containing flammable gases, pose challenges for the direct application of LIBS. In response to these difficulties, an alternative approach that has proved to be of considerable utility involves the collection of atmospheric particulate onto a filter substrate [74,81–84].

While this approach loses the advantage of real-time analysis, it presents distinct merits over other measurement techniques, for example in contrast to Inductively Coupled Plasma (ICP) methods, as it obviates the need for prior sample pre-treatment [85–88]. By manipulating filtration flow rates and selecting optimal sampling durations in a proper way, it becomes feasible to collect a higher concentration of analyte particles onto the filter substrate, thereby substantially enhancing the possibility for detecting the analytes of interest.

Conversely, for environments marked by potential hazards, the practice of gathering particulate matter onto a filter substrate prior to conducting a secure LIBS analysis subsequent to the aerosol sampling. To ensure the efficacy of this approach, particular attention must be dedicated to the degree of filter loading. This consideration safeguards against the problem of signal saturation, a phenomenon that may arise due to filter saturation, detector saturation and strong self-absorption. Moreover, there is the potential risk of incomplete vaporization of the analyte, leading to an underestimation of its concentration. Furthermore, the accurate calibration of laser power and the tuning of signal acquisition timing should be well organised before in order to optimize the analysis. Undoubtedly, the selection of an appropriate filter medium stands as a paramount issue. The specific kind of sampling environment and the nature of the analyte of interest lead the choice of filter. When sampling is undertaken within exhausts of combustion systems, the filter must exhibit robust thermal resilience to overcome elevated temperatures. For scenarios involving the evaluation of environmental impacts, particularly concerning the presence of heavy metal contaminants, the filter should exhibit minimal levels of such pollutants as contaminants, to ensure measurement accuracy.

Additionally, the filter efficiency in collecting airborne particulate assumes great significance. This efficiency, ideally approaching 100%, should be finely tuned to fulfil the specific aerosol size fraction of the aerosol under analysis.

Another approach usually employed in the literature to determine the multi-elemental composition of solid samples is the double pulse configuration [89]. The use of the second pulse absorbed by the plasma (produced by the first pulse) can be very effective in improving the detection limit and the sensitivity because of the re-excitation of the ablated matter by the first laser pulse by the second laser pulse.

2.5 COMPARING LIBS IN AEROSOL AND ON FILTERS

Comparing LIBS measurements performed on aerosol with the ones on particle-loaded filter, different experimental conditions have to be taken into account.

As for measurements on aerosol, it is already observed that an energy threshold has to be considered, above which breakdown and plasma condition can occur. In this case, relatively high value of laser energy is employed, resulting in high density energy in the probe volume. The resulting time evolution of the physics is the one already considered in the previous section.

The experimental conditions are completely different in the case of LIBS performed on solid samples. In this case, the threshold for plasma formation is lower. In fact, first of all this high laser energy would interact with the substrate where the particles are deposited and can eventually destroy it. Moreover, the presence of the filter with the particles deposited can substantially reduce the breakdown threshold, even down to very low pulse energy (less than 50 mJ). Moreover, as a result of relatively low laser energy employed, LIBS emission line can be collected in completely different time scale after the laser pulse, compared to the signal detected from particles aerosol.

For thoroughness, in Table 1 the main experimental conditions normally applied in LIBS measurements on aerosol and on solid samples are reported.

Table 1. Experimental conditions applied in LIBS on aerosol and on solid [59,60,84,90].

	LIBS on Aerosol	LIBS on solid
Pulse laser	> 200 mJ/pulse	Few mJ/pulse
Delay time	> 10 μ s	< 30 μ s
Gate width	100s μ s	< 10 μ s

3 EXPERIMENTAL APPARATUS AND METHODOLOGIES

In this Section the experimental apparatus developed and employed for LIBS measurements is presented and extensively described. In this context it is worthwhile to stress that the main goal of this work is the time resolved analysis and measurements of metal concentration at the exhaust of combustion system. To this purpose, two different experimental set-ups are described: one for LIBS measurements in particle aerosol and the other on powder-deposited filter. Moreover, details on the measurement's methodologies employed are also reported.

3.1 LIBS SET-UP ON PARTICLE AEROSOL

In Figure 7 the experimental apparatus for LIBS measurements performed on aerosols is shown.

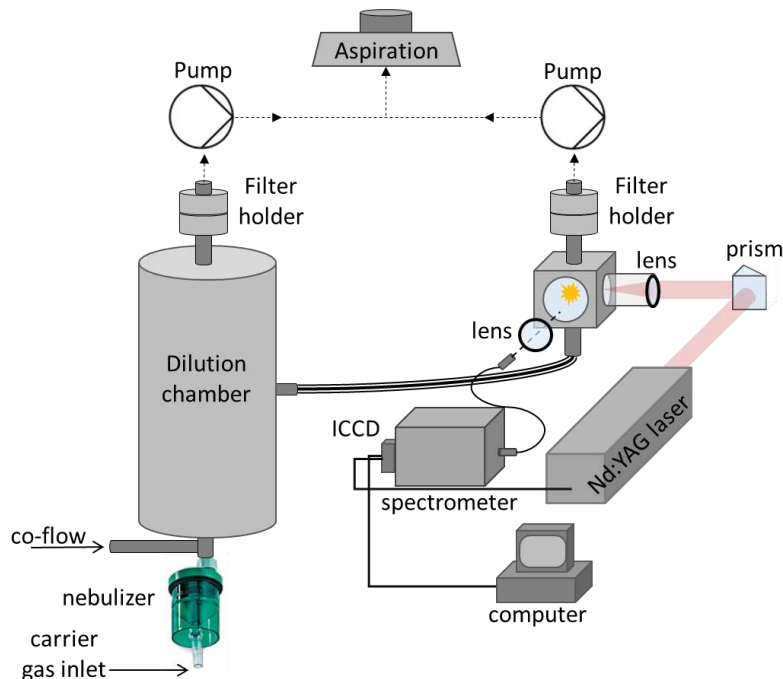


Figure 7. LIBS laboratory experimental set-up.

It is essentially composed by two main parts. The first part involves the spectroscopic section, which includes the laser that ignites the plasma, the measuring chamber, the collecting optical system and the detection and measurements apparatus. In this work a Q-switched flashlamp-pumped Nd:YAG laser (Quantel-Lumibird Q-Smart 450) working at its fundamental wavelength (1064 nm) is used. The laser operates at 10 Hz repetition rate, with a pulse duration of 6 ns. Nominally each pulse has an energy of 450 mJ. The generated laser beam is then deflected by a prism, losing part of its energy and assessing to 370 mJ/pulse, and directed towards a 20 mm focal length adjustable lens, which is positioned at the entrance of the measurement chamber. The average irradiance, I , at the location of the beam waist can be calculated using Eq. (4). In this experimental set-up $E_L = 370$ mJ, $D = 0.7$ cm,

$\tau_L = 6 \text{ ns}$, $f = 20 \text{ mm}$, $\lambda = 1064$ and $M^2 = 2$. Using these parameters an irradiance of $1.3 \cdot 10^{14} \text{ W/cm}^2$ is obtained, resulting well above the air breakdown threshold of 10^{11} W/cm^2 [45].

The atmospheric pressure sample chamber comprises a PTFE six-way cell equipped with four optical windows. The chamber internal volume is 15 cm^3 , and the aerosol inlet and outlet have a diameter of 4 mm. As reported previously, one of the chamber windows is substituted by the 20 mm focal length lens to generate the plasma in the centre of the chamber, directly in the aerosol flow. As for the optical collection system, a double convex lens is used to collect the emitted radiation from the plasma within a certain solid angle and focusing it on an optic fibre. This fibre is connected to a Czerny–Turner spectrograph (Shamrock 500i, Andor Technology) coupled with an iCCD (iStar 320 T, Andor Technology) camera, which allows the analysis of the collected data. The spectrograph is equipped with a three gratings turret, namely 300 grooves/mm, 1200 grooves/mm, and 1800 grooves/mm, and with a blaze at 300 nm wavelength.

Through the coupling between the spectrometer and the camera, it is possible to select the spectral region to be analysed, which will be wider or narrower depending on the resolution of the selected grating. To detect atomic lines, a high-resolution spectrograph grating is used (1200 grooves/mm) resulting in a 25 nm spectral window. The intensified CCD detector is synchronized with the Q-switch laser to change the delay time of the detection gate with respect to the laser shot.

The second part of the instrumental setup involves aerosol production. In a laboratory configuration, this is accomplished using an aerosol production line consisting of a nebulizer, connected to a flowmeter that allows controlling the compressed air flow rate needed for the aerosol droplets production. In particular, two different nebulizers are used, namely the TSI Constant Output Atomizer model 3076 or a medical nebulizer (UP-DRAFT Nebuliser, Hudson RCI). The previous one was used for preliminary measurements, while the medical nebulizer was implemented for calibrations and the case studies under analysis. More details about the two nebulizers are given in the Appendix A1.

In order to dry the droplets, a dilution chamber (40 l volume) is connected to the nebulizer outlet. Here 5 l/min wet aerosol flow is mixed with 20 l/min dry air flow obtained by pumping at 25 l/min with an aspiration system (Edwards, E2M2). For LIBS measurements, by using another pumping system (DDS Aero, Tecora), 1 l/min flow rate of aerosol is isokinetically sampled from the dilution chamber and sent into the measuring chamber. The particles are then collected on a glass fibre filter positioned before the pump.

3.2 METAL SOLUTIONS

The availability of controlled and well characterized aerosols and the implementation of specific quantification procedures are fundamental to perform LIBS instrumental calibration [60,91,92]. For

this reason, two different nebulizers were tested, as described in Appendix (A1). Their consumption was monitored over time to verify the stability and repeatability of the measurement conditions. A detailed study of the spray emitted from the medical nebulizer was also conducted in dependence of the solution level, nebulizer positioning and sampling position in the nebulised spray, Appendix (A2).

Table 2. List of heavy metals under analysis, relative salt used for the solutions production and relative principle analysed line wavelength.

Metal	Salt		Reference wavelength [nm]
	Chemical Formula	Name	
Copper	$\text{CuN}_2\text{O}_6 \cdot 3\text{H}_2\text{O}$	Copper(II) nitrate trihydrate	325.03
Nickel	$\text{CL}_2\text{Ni} \cdot 6\text{H}_2\text{O}$	Nickel(II) chloride hexahydrate	352.72
Lead	$\text{C}_4\text{H}_6\text{O}_4\text{Pb} \cdot \text{H}_2\text{O}$	Lead diacetate monohydrate	406.02
Manganese	$\text{MnO}_4\text{S} \cdot \text{H}_2\text{O}$	Manganese sulfate monohydrate	279.74
Chromium	$\text{C}_6\text{H}_9\text{CrO}_6 \cdot n\text{H}_2\text{O}$	Chromium(III) acetate	358.11
Cadmium	$\text{CdCl}_2 \cdot \text{H}_2\text{O}$	Cadmium chloride monohydrate	229.08
Thallium	CITl	Thallium(I) chloride	535.22
Cobalt	$\text{CoSO}_4 \cdot 7\text{H}_2\text{O}$	Cobalt(II) sulphate heptahydrate	345.63
Arsenic	AsNaO_2	Sodium (meta)arsenite	228.94
Vanadium	NaVO_3	Sodium (meta)vanadate	438.07
Antimony	$\text{Sb}_2(\text{SO}_4)_3$	Antimony(III) sulfate	231.17

In Table 2 the elements under analysis in this work, the related compounds employed, and the related main emission line wavelength analysed are listed. As already observed, in fact, aerosol particles are produced by nebulizing solutions of these salts. It is important to observe that the preparation of proper solutions is the starting point for the aerosol measurements. To this purpose, ultra-pure

distilled water was used as a solvent, in which these salts were dissolved with known molar concentrations. Values changing from about 0.1 molar to about 0.000001 molar were used, in order to obtain aerosol concentrations ranging from hundreds of nanograms per cubic meter to hundreds of micrograms per cubic meter, and, in some cases even up to a few milligrams per cubic meter in less sensitive cases. More details in molar concentrations and mass concentrations will be given in the calibration curves construction.

3.3 LIBS SET-UP FOR FILTER ANALYSIS

Indirect analysis of the aerosol collected on filters was carried out in order to increase the detection limit of the heavy metal concentration for possible application on air quality monitoring. In this context, in order to obtain reasonably time-resolved measurements, the collection time was kept relatively low (about 30 minutes for concentrations of about hundreds of ng/m^3 , more details are reported in the results chapter). Moreover, such approach also allows performing a comparison of this technique with Total X-Ray Fluorescence (TXRF) and Ionised Coupled Plasma (ICP) technique. The experimental set-up used for these analyses was slightly different from the one described in the set-up employed for aerosol LIBS measurements. In order to prepare the filter sample, the aerosol generation part was separated from the LIBS apparatus: it was directly used for generating the aerosol of interest and collect it on a filter. In Figure 8 the set-up for depositing the particles on the filter for subsequent LIBS measurements are shown, respectively.

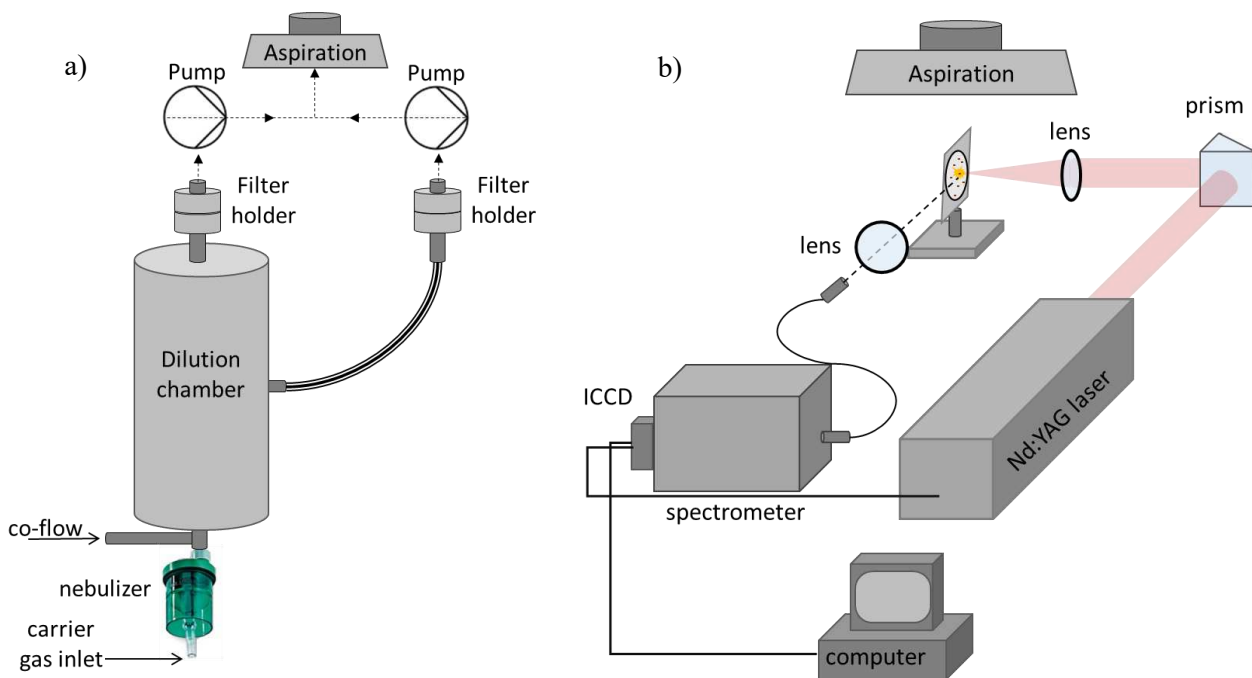


Figure 8. a) Set-up for the preparation of particles deposited filters. b) LIBS set-up for filter analysis.

For the aerosol generation, the same medical nebuliser was used, working with a flow rate of 5 l/min and generating droplets with a diameter of 3 μm . The aerosol particles flowing in the dilution chamber (aspiring 24 l/min air) are pumped out by means of an aspirating pump. To prepare the filter sample, 1 l/min flow rate of aerosol is isokinetically sampled from the dilution chamber and sent on a paper filter positioned in a proper filter holder. In order to increase the LIBS signal sensitivity, the particles were channelled in a 4 mm diameter tube resulting in a particle-collection area of 4 mm of diameter. In Figure 9 a picture of the filter area is reported.

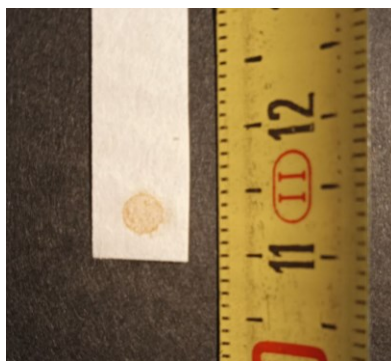


Figure 9. Sampled iron aerosol spot (right).

LIBS indirect analysis can be then performed on the sampled filter. This spectroscopic section is the same as the one described for the direct analysis in all the optical path, from the generation of the laser pulse to the acquisition of the spectra, except for the focusing lens and the measurement chamber, as reported in Figure 8 (b). In fact, this last part is replaced by a larger quartz double convex lens (focal length of 115 mm) and by a movable filter holder. As extensively reported in the previous section, the experimental conditions normally applied in LIBS measurements performed on solid samples are completely different than the ones in aerosol. In fact, the presence of matrix element in solid sample measurements results in higher plasma temperature and electron density even at low laser energy. This results also in different temporal behaviour of the LIBS signal. For the experimental conditions employed, details are given in the next Sections.

3.4 DATA ACQUISITION AND PROCESSING

The methodology for acquiring spectra is of fundamental importance for the analysis of LIBS signals. As described previously, the LIBS signal is collected and analysed thanks to the coupling of a spectrometer and an iCCD camera. For that, for optimal signal acquisition, it is necessary to set the delay time and gate width to be opened appropriately starting from the laser pulse, as depicted in Figure 10.

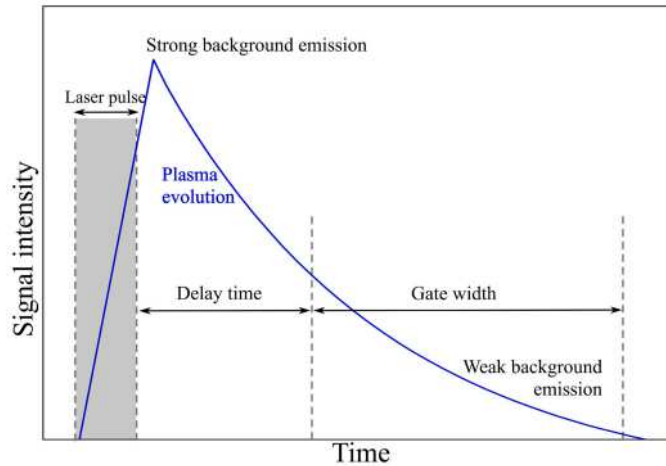


Figure 10. temporal evolution of the plasma-emitted radiation [93].

As previously described, the signal is predominantly due to the bremsstrahlung just after the formation of the plasma. With the cooling of the plasma, the contributions due to emission from the elements within the plasma also begin to become evident.

As an example of the temporal evolution of the signal, the graphs representing the emission signal generated by copper aerosol are shown in Figure 11. These spectra are acquired at four different delay times, namely 5 μs , 10 μs , 30 μs , and 50 μs , with a gate width of 5 μs .

As a first analysis, in all the spectra reported there is a constant background at the edges of each spectrum, with the same intensity independently of the signal acquisition times. Actually, the sensor is not completely covered by the intensifier: the sensor is rectangular in shape (27 mm x 7 mm), while the circular intensifier is 18 mm in diameter. Consequently, this background is the electronic noise of the camera and the intensifier.

Comparing these spectra, it is possible to note a decrease in the overall signal with increasing delay time. The spectrum acquired at a delay time of 5 μs has a significantly higher background than the other spectra, due to the emission from the still hot plasma. Increasing the delay time, with a colder plasma, the contribution to the background decreases more and more, making the emission lines of the elements more pronounced.

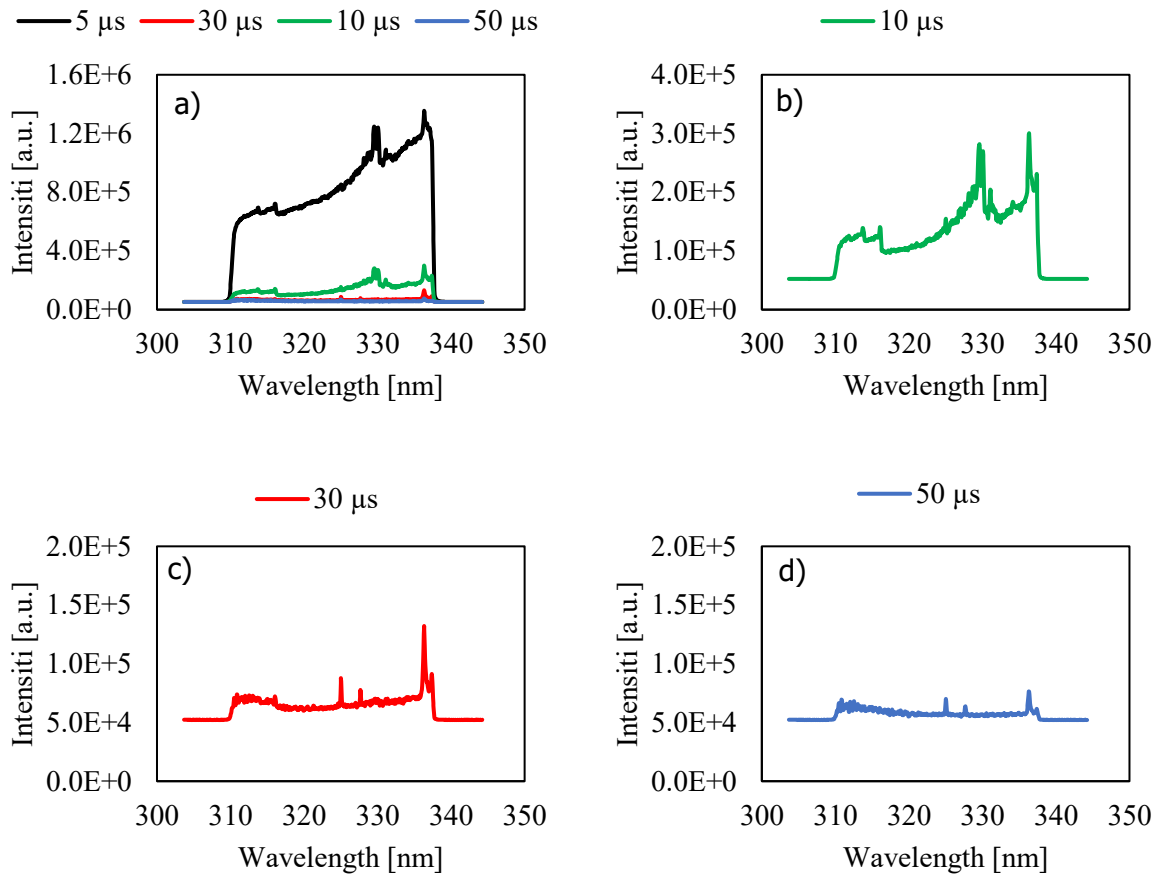


Figure 11. Example of spectra acquired at four different delay times with the same gate aperture of 5 μs (a). For clarity spectra at 10, 30 and 50 μs are shown in (b), (c) and (d).

To summarise, for each specific conditions and analyte the variation of following parameters is properly investigated: Delay time (of the detection gate width with respect to the laser shot occurrence)

- Detection gate width
- Laser energy/pulse

The main goal is to maximize the peak-to-base value. This analysis has been performed both on aerosol and particle-deposited filters as it will be deeply described in the results sections.

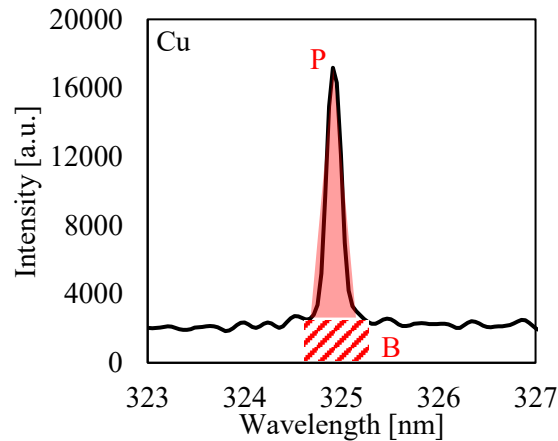


Figure 12. Example of parameters evaluation for the copper emission line.

Taking into account the typical emission line of Cu analyte, reported in Figure 12, the parameters considered for LIBS measurements are:

- The peak area P, which refers to the integral of the prominent peak of LIBS emission line subtracted for the background.
- The base B, which is the background area evaluated as the area in the same region of the analyte's peak without the analyte.
- Consequently, P/B refers to the peak-to-base ratio.

3.4.1 Single spectrum, accumulation and average

In order to process a large number of spectra, different data acquisition methodologies have been performed, namely single shot, accumulation, or averaging of acquired signals depending on the experimental conditions under analysis and in particular on the type of analyte to be studied, specifically aerosol versus particle-deposited filter and its concentration.

- Single shot measurements. This methodology has been applied on particulate matter collected on filters. In particular, the acquisition of a spectrum generated by a single pulse may be sufficient to provide a reliable signal for the analysis. Moreover, at low concentration, the analysis has been performed by mapping the entire filter surface with single shot LIBS measurement. A global analysis of the sampled aerosol has been obtained by averaging the resulting LIBS signals from this mapping.
- Accumulation mode. This methodology of signal acquisition has been applied in low-concentration aerosols, but still above the detection limits. This strategy consists of accumulating the spectrum collected from multiple spectra (tens, hundreds, or even thousands), in order to reduce background noise and emphasize the signal of the analyte of interest.

In this context, it is important to emphasize the accumulation mode cannot be applicable in the case of particulate matter deposited on a filter. In this condition, in fact, the first laser shot can produce a shock wave responsible for a removal of the particles from the filter and sometimes responsible for a crater formation around the laser spot.

To overcome this problem, as already described, an average of single shot spectra acquired at different spatial location on the filter can be performed in order to increase signal-to-noise ratio.

3.4.2 Conditional analysis

Due to the discrete nature of the plasma volume combined with the discrete nature of aerosol particles, typical LIBS spectra could not contain the spectral lines related to the species under analysis. This problem is particularly effective at low concentration measurements. For this reason, conditional analysis has been applied in the case studies reported in this thesis, consisting in extracting only the spectra containing the line emission of the metal of interest and rejecting the others [76,79,94,95]. Compared to the averaging approach applied at low concentration measurements, this methodology allows the improvement of the signal-to-noise ratio and the investigation of single-shot LIBS spectra corresponding to individual aerosol particles emission. This method consists in the following steps.

- A series of 5000 single spectra were collected (in kinetic mode)
- The eventual occurrence of the specific line emission in each spectrum was evaluated. To this purpose, a well-defined criterium for selecting the “hit” spectra was considered, tested and subsequently applied to the data.
- Once the “hit” spectra were selected, an average value was obtained from which equivalent concentration was calculated by applying the related calibration.
- The effective analyte mass was finally estimated taking into account the sampling rate.

The number of the series chosen for the application of conditional analysis is strictly dependent on the concentration under analysis: the lower is the concentration the higher should be the number of spectra collected. The value of 5000 has been selected after different preliminary measurements on the analyte under analysis as a compromise between the signal acquisition time and the signal improvement.

Considering the selection criterion, this parameter results to be of crucial importance. Since the LIBS spectrum is very noisy and includes numerous structures that can hide the emission peak of the analyte of interest, it was necessary to select spectra for which this peak can be clearly noticed above the background structures.

Two kinds of analyses are considered for the best selection criterion. The first strategy is to evaluate the variability of signal intensity in the region adjacent to the peak by calculating the standard deviation (SD). Specifically, a certain number of channels is considered, symmetrically distributed

around the peak. The mean of this signal intensity is also evaluated on the same channels, which was used as a reference value for the background. The choice of the number of channels is strictly dependent on the specific spectral region under analysis and possible interference with other line emission. For this reason, particular attention has to be paid to analyse nearby peaks falling within these selected areas. In these cases, it is appropriate to modify the analysis area and choose a clean one that refers exclusively to the background.

A second mathematical tool that can be used to establish a selection criterion is the evaluation of the semi-dispersion. In this case, the mean of the background signal and the related semi-dispersion are also calculated in the same channels indicated previously. The semi-dispersion (SmD) will be used as a discriminant threshold to establish the presence or absence of the analyte of interest.

In both cases, SD or SmD evaluation, the selection of the hit spectrum is carried out by applying the following criterion:

$$Signal > mean + n * (SD \text{ or } SmD) \quad (17)$$

In brief, the emission line can be taken in the analysis if the intensity is higher than a certain number n of SD or SmD.

In Figure 13 a direct comparison of SD or SmD choice is shown. The red curve refers to a “clean” spectrum (not containing the analyte under analysis), obtained averaging 1000 *miss* spectra, which is considered as a reference in the conditional analysis. In Table 3 the number of *hit* against *miss* spectra is reported varying the multiplicative factor n .

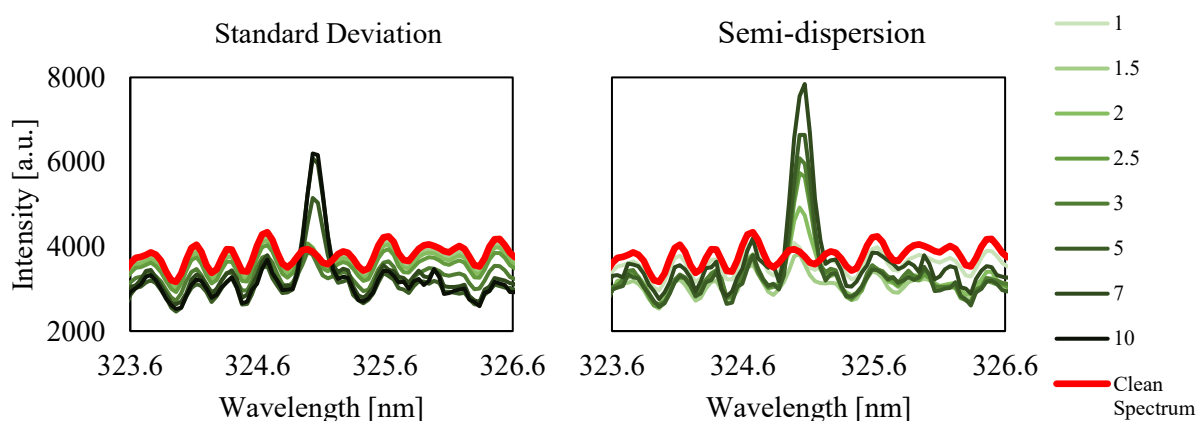


Figure 13. Spectra obtained with different selection criteria. Standard deviation (left) and semi-dispersion (right) multiplied for a factor from 1 to 10 (green scale). In red is reported the averaged spectrum obtained from measurements with no Cu signal.

Table 3. Hit and Miss number of spectra obtained using SD or SmD selection criteria.

Multiplicative factor	SD		Semidispersion	
	Hit	Miss	Hit	Miss
1	2867	2133	485	4515
1.5	1727	3273	45	4955
2	900	4100	11	4989
2.5	386	4614	6	4994
3	138	4862	5	4995
5	8	4992	3	4997
7	5	4995	2	4998
10	4	4996	0	5000

It is clear that taking a single SD or a single semi-dispersion, many spectra are selected, with the mean signal very close to the reference spectrum.

Considering in the same figure the SD approach, a notable hit spectrum can be obtained starting from the multiplicative factor 5. However, using the SD multiplied factor 5 is a very strong assumption considering the mathematical nature of the standard deviation. Considering the non-Gaussian structure behaviour of the background, SD cannot be considered a good choice. Analysing the graphs reported in Figure 13, it is clear that the signal used for the background evaluation (certain number of channels around the peak considered) exhibits a peculiar feature, which cannot be attributed to a statistical noise, rather to well-defined structures. For this reason, the use of semi-dispersion seems more suitable to be considered for the threshold evaluation. In fact, a detectable signal is obtained with a multiplicative factor of 2, which can be representative of the whole background signal amplitude. For that, 2 times the semi-dispersion will be used as discriminant criterion.

4 RESULTS IN AEROSOL

4.1 EXPERIMENTAL CONDITIONS FOR AEROSOL ANALYSIS

4.1.1 Temporal optimization

In this section the role of the delay time of the detection gate width on LIBS signal is presented with the aim to choose the best detection conditions for LIBS signal enhancement. Copper was chosen as the primary element for testing these experimental conditions.

A typical LIBS spectrum of copper is reported in Figure 14, where the two copper peaks at 325 nm and 327.6 nm wavelengths are shown, respectively.

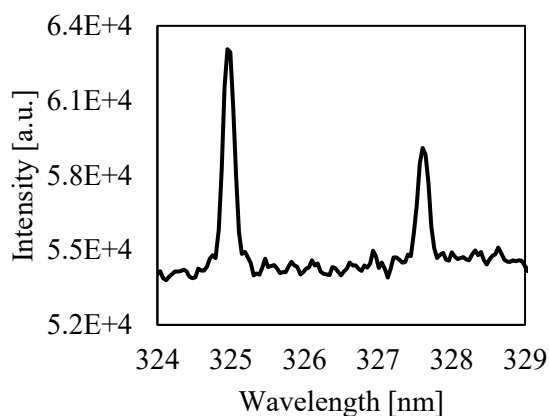


Figure 14. Cu emission lines at 325 nm and 327.6 nm, delay time = 30 μ s, gate width = 1 μ s, 100 accumulated spectra.

Solutions of copper nitrate with molar concentrations of 0.01, 0.001, and 0.0005 were employed. Keeping constant the aspiration and the nebulization flows, thereby operating at a constant concentration, an assessment of the delay time was performed by varying it from 1 μ s to 100 μ s. In this analysis, the detection gate width was fixed at 1 μ s and 100 μ s for the solution with molar concentration of 0.01 and for the other two solutions (0.001 and 0.005), respectively. In Figure 15 the P/B signal versus delay time is reported in the configuration under analysis. While the analysis with 1 μ s gate width was performed up to 100 μ s delay time, in the other configurations, the analysis was limited up to 60 μ s due to the longer gate aperture (100 μ s). In fact, after 150 μ s the plasma emission decays substantially.

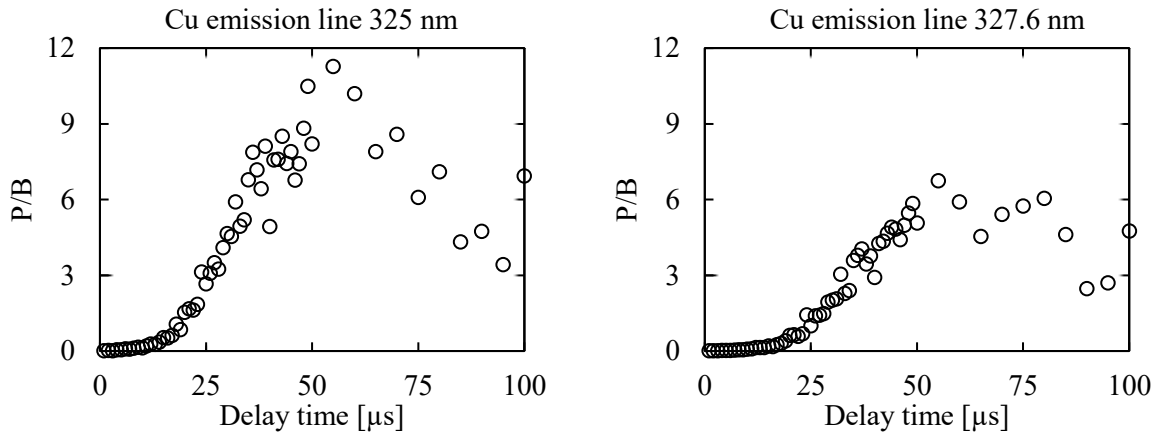


Figure 15. Cu nitrate solution with molar concentration of 0.01 versus delay time with 1 μs step until 50 μs and 5 μs step until 100 μs ; gate width = 1 μs .

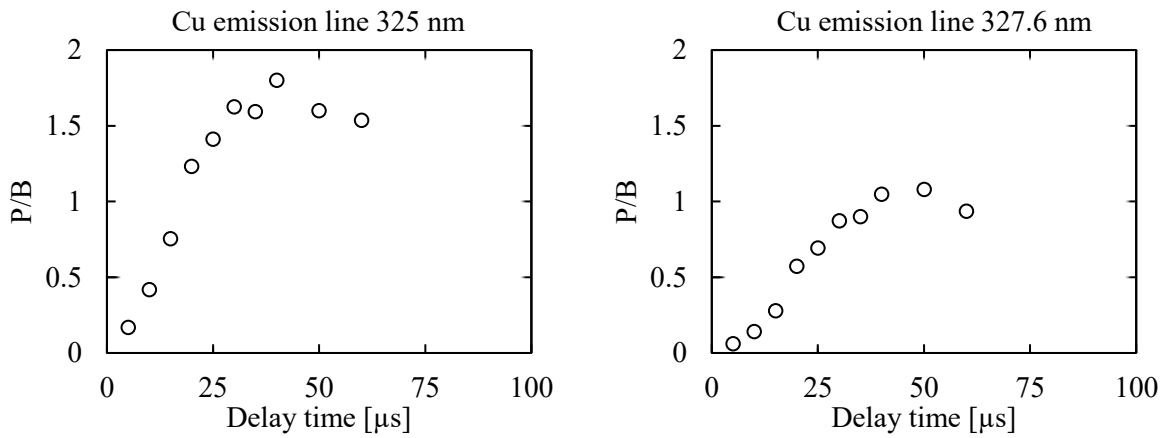


Figure 16. Cu nitrate solution with molar concentration of 0.001 versus delay time with step = 5 μs until 40 μs then step = 10 μs ; gate width = 100 μs .

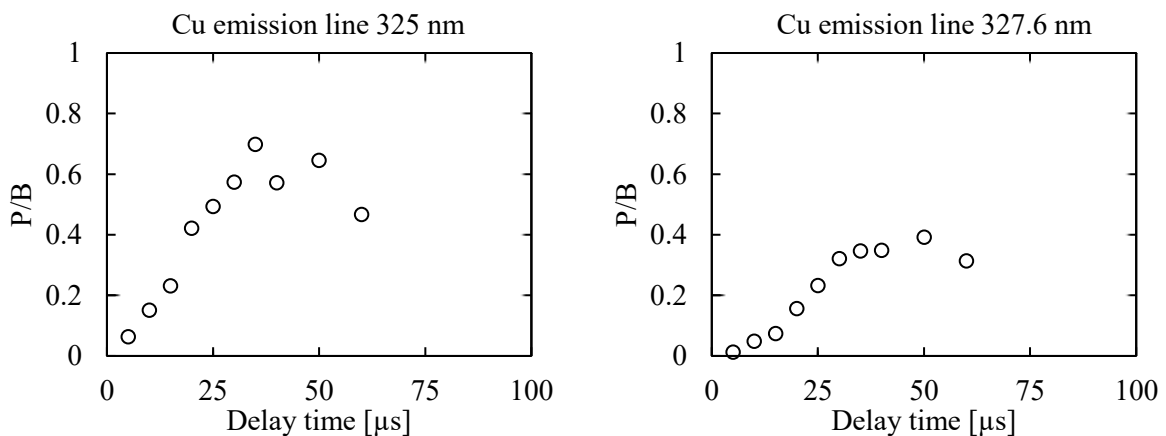


Figure 17. Cu nitrate solution with molar concentration of 0.0005; delay time = 1-60 μs with step = 5 μs until 40 μs then step = 10 μs ; gate width = 100 μs .

These results highlight how a more punctual variation mapping of the delay time, coupled with a short gate width of 1 μs , results in a more efficient detection in data variability. In this configuration, the peak signal is achieved for delay times ranging between 45 μs and 60 μs for both analysed peaks at 325 nm and 327.6 nm. Moreover, for values higher than 50 μs , there is a pronounced increase in signal variability, attributed to a more distinct variability effect of the peak compared to the baseline. This is particularly relevant for longer delay times when the plasma has nearly cooled completely, causing the peak variability to have a greater impact due to the proximity of the baseline to the background noise. Comparing the LIBS measurements performed on copper nitrate with molar solution concentrations of 0.001 and 0.0005 respectively and delay time intervals of 5 μs , (see Figure 16 and Figure 17) a significant reduction in the signal spreading is detected due to averaging effects. Correspondingly, also a reduction in the P/B values are obtained.

In any case, a value of delay time around 30 μs , where the maximum of P/B value is obtained, is considered in the following for our LIBS measurements on aerosol.

4.1.2 Detection gate width analysis

In this section the dependence of the LIBS signal on the detection gate width is investigated while maintaining a fixed delay time at 20 μs . The analysis was carried out using the same three solutions with varying molar concentrations of copper nitrate as the ones employed in the previous paragraph for delay time study. In Figure 18, Figure 19 and Figure 20 the results obtained in the different conditions under analysis are reported.

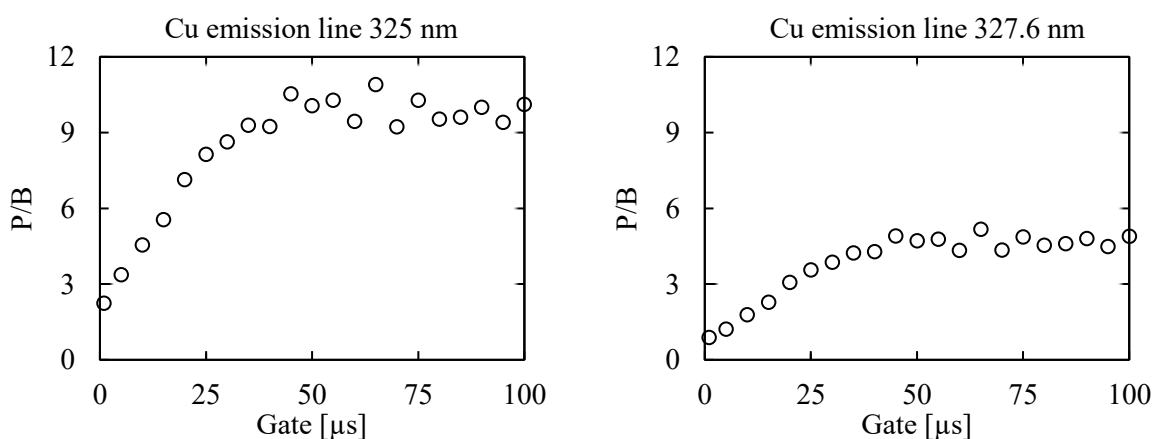


Figure 18. P/B values versus gate width (step = 5 μs). Cu nitrate solution with molar concentration of 0.01; delay time = 20 μs .

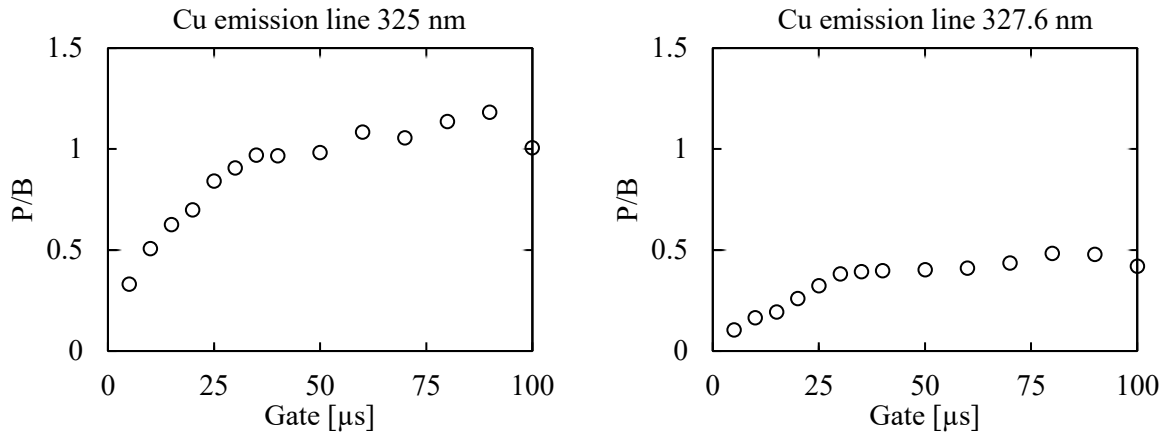


Figure 19. Cu nitrate solution with molar concentration of 0.001; delay time = 20 μs; gate width = 1-100 μs with step = 5 μs until 40 μs then step = 10 μs.

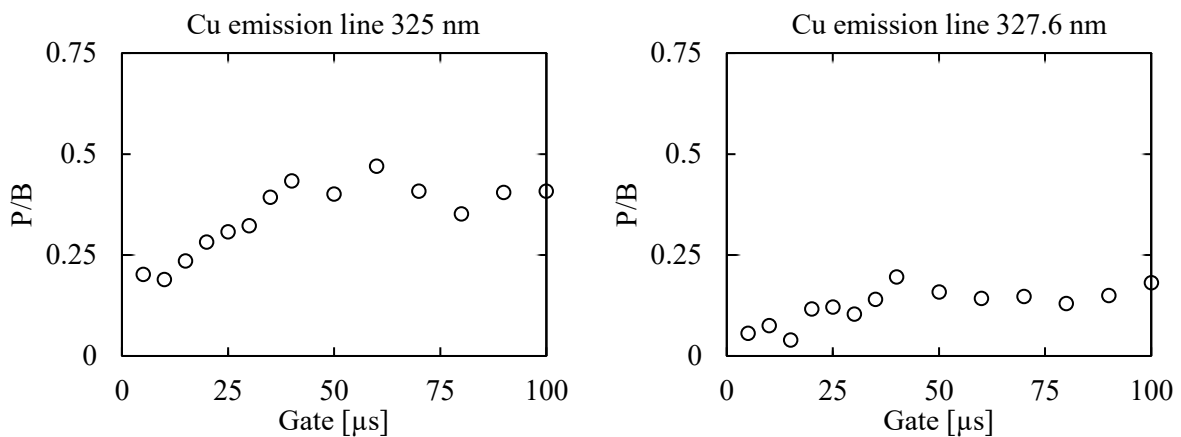


Figure 20. Cu nitrate solution with molar concentration of 0.0005; delay time = 20 μs; gate width = 1-100 μs with step = 5 μs until 40 μs then step = 10 μs.

In all conditions, starting from a gate aperture of 35 – 40 μs, the signal reaches a plateau and remains stable until 100 μs aperture, consistently with a stable value of the peak. Considering the timeframes employed for acquiring these spectra, it can be inferred that beginning from approximately 55-60 μs (20 μs of delay time plus 35-40 μs of gate width) after the discharge, the signal contribution computed as P/B remains constant. This persistence is actually due to a reduction of both the LIBS signal and the base. Such behaviour can be essentially attributed to globally less plasma emitted radiation.

4.1.3 Comparative analysis for Cu, Ni, Mn and Cr

In order to extend this temporal evaluation to a generic unknown element that may be a constituent of a real aerosol analysis, the same evaluations were performed on three additional elements: nickel, manganese, and chromium. These elements were chosen as representative examples to assess temporal differences, with the aim of subsequently determining optimal acquisition conditions that include favourable temporal settings for elemental analysis in a general context. In Figure 21, Figure

22 and Figure 23, Ni, Mn and Cr analysis concerning the delay time and the detection gate width are reported.

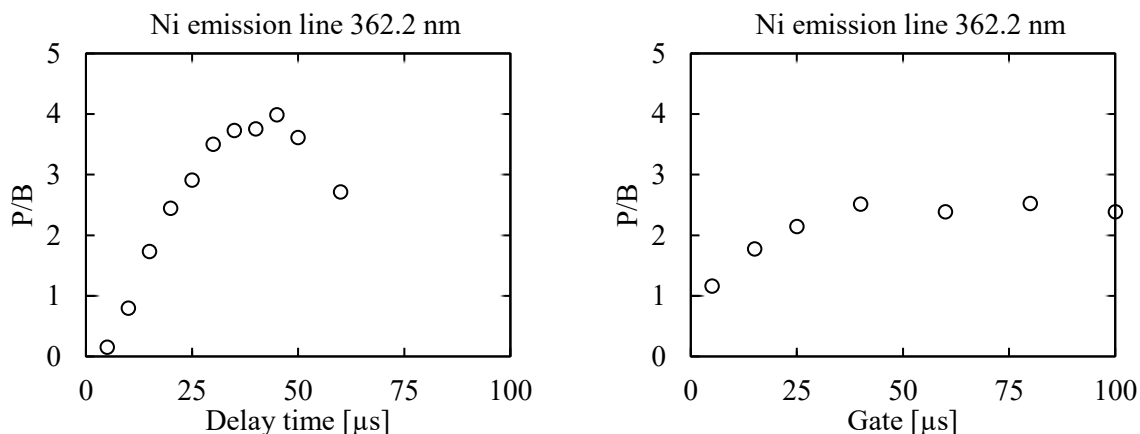


Figure 21. Ni chloride solution with molar concentration of 0.01. Left: delay time = 1-60 μs with step = 5 μs until 50 μs then step = 10 μs ; gate = 100 μs . Right: delay time = 20 μs ; gate = 5-100 μs with step = 10-15-20 μs .

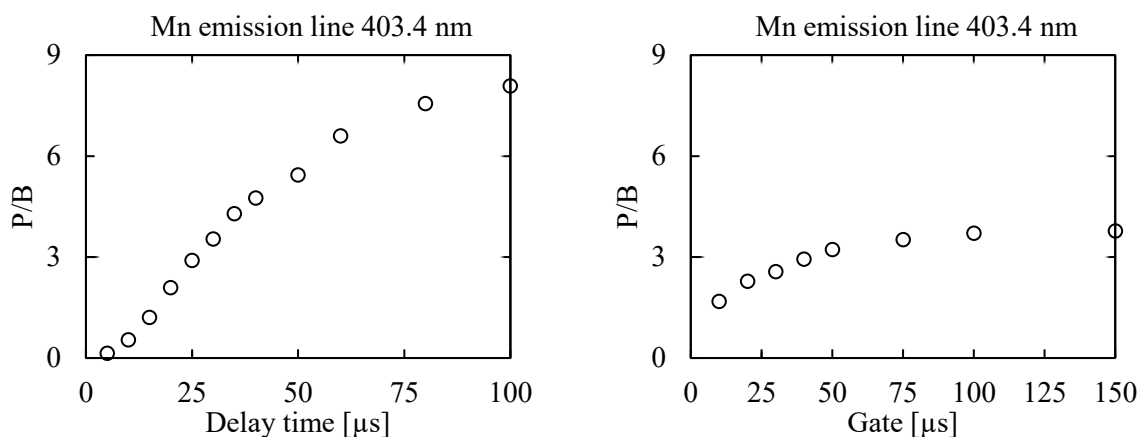


Figure 22. Mn sulphate solution with molar concentration of 0.005. Left: delay time = 5-100 μs with step = 5-10-20 μs ; gate = 100 μs . Right: delay time = 30 μs ; gate = 5-150 μs with step = 10-15-20-50 μs .

Regarding nickel analysis, a nickel chloride solution with a molar concentration of 0.01 was used. The emission signal was evaluated at the peak centred at 362.2 nm wavelength. As reported in Figure 21, it is evident that with a fixed gate aperture of 100 μs , the signal reaches its maximum within delay time intervals of 35 μs to 50 μs . Moreover, when the delay time is set at 20 μs , the signal achieves its maximum value at a gate aperture of 40 μs , maintaining a plateau until 100 μs gate width.

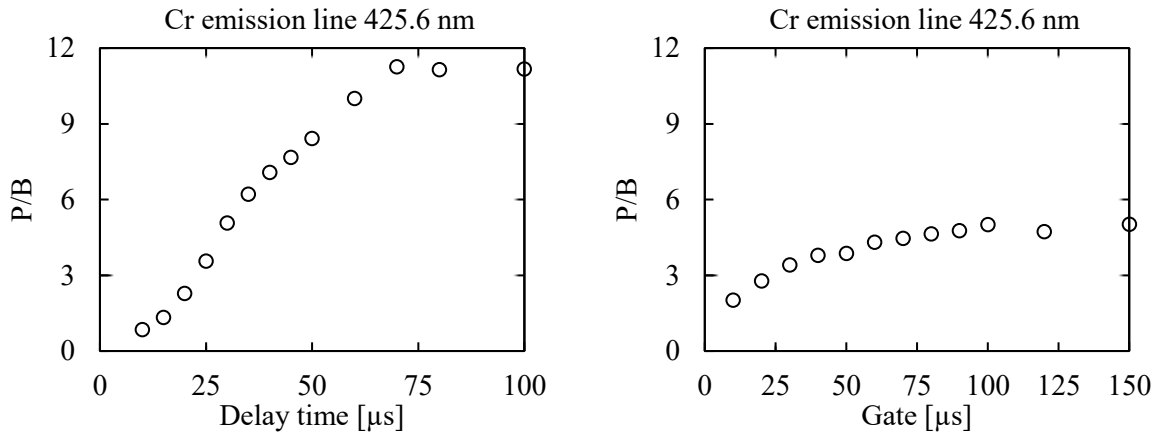


Figure 23. Cr acetate solution with molar concentration of 0.004. Left: delay time = 5-100 μs with step = 5-10-20 μs ; gate = 100 μs . Right: delay time = 30 μs ; gate = 5-150 μs with step = 10-15-20-50 μs .

For manganese analysis, a manganese sulphate solution with molar concentration of 0.005 was nebulised, and the emission line centred at 403.4 nm was acquired. The evaluation of the signal concerning variations in delay time and gate settings, as shown in Figure 22, highlights a constant signal increase as the delay time is extended, while keeping the gate fixed at 100 μs . The maximum value is obtained at a delay time of 100 μs , which however is the last delay time considered. In contrast, by fixing the delay time at 30 μs , the optimal gate aperture for signal maximization is 100 μs , and the signal remains stable up to 150 μs . Lastly, for the analysis of the final element, a solution of chromium acetate with molar concentration of 0.004 was nebulised. The analysed emission line was centred at 425.6 nm wavelength. From the graphs in Figure 23, it is evident that with a fixed gate aperture of 100 μs , the signal reaches its peak value at 70 μs and remains constantly at a plateau level until a delay time of 100 μs . Moreover, with a delay time set at 30 μs , the variation in gate aperture reveals that the maximum of the signal is achieved starting from a gate aperture of 90 μs .

Considering the comparative analysis of the temporal responses exhibited by the four distinct elements under analysis, it is evident that Cu and Ni exhibit similar temporal behaviour. In particular, with these two analytes, the LIBS signal changes more significantly at longer delay time than Mn and Cr. On the contrary similar trend is obtained for the gate width in all conditions under analysis.

Taking into account these comparative evaluations, a set of acquisition parameters to be applied for all the not a priori known elements were chosen, which are a delay time of 30 μs and a gate aperture of 100 μs . The motivation behind this is to ensure that the beginning of signal acquisition is aligned with temporal windows where the maximum intensity signal occurs for elements characterized by short temporal emissions. Furthermore, the gate width of 100 μs allows also to detect the maximum intensity of LIBS signal for elements with a slower temporal emission. The choice to avoid extending the gate aperture beyond the 100 μs threshold is due to an average consideration. This perspective

takes into account the potential signal suppression due to such an extension, since the spectra obtained for both element typologies (with a rapid / slower emission) could result in a general lowering of P/B, due to the addition of lower global intensity to the spectrum.

4.1.4 Fluence evaluation

The energy available for the generation of the plasma for LIBS measurements primarily depends on the type of laser used, as well as from the energy dissipation along the optical path. Generally, the higher is the pulse energy generated by the laser, the larger are the dimensions and costs of the laser. In the perspective of creating a compact instrument for the measurement of heavy metal aerosols using LIBS technology, it is necessary to find the best compromise between costs and dimensions. For this reason, the signal was analysed for different laser pulse energies. This study was carried out on the same two copper emission lines used in the previous paragraphs (324.7 nm and 327.4 nm wavelengths), and on the manganese peak (403.1 nm wavelength) to find the lower limit of pulse energy that allows the emission to be reliably analysed.

Table 4. Power in W, energy in mJ and energy density in mJcm-2 measured in correspondence of the number of glass filter used.

# glass filters	Power [W]	Energy [mJ]	Energy density [mJ/cm ²]
0	3.65	365	1100
1	3.11	311	937
2	2.45	245	738
3	2.19	219	660
4	1.92	192	579
5	1.61	161	485
6	1.35	135	407
7	1.14	114	344
8	0.93	93	280
9	0.81	81	244
10	0.67	67	202
11	0.59	59	178
12	0.52	52	157
13	0.45	45	136
14	0.39	39	118
15	0.30	30	90

To perform this analysis, calibrated glass windows were used, in order to change the laser pulse energy, which was then measured by using a power meter (ThorLabs). Taking into account the laser working frequency of 10 Hz and the laser beam diameter of 6.5 mm, the pulse energy and the energy density were calculated. Is reported in Table 4 the power in Watt, the pulse energy in mJ and the energy density in mJ/cm^2 , changing the number of calibrated glass filters used.

Analysing the copper emission signal at 324.7 nm wavelength is possible to notice that the highest peak intensity values are obtained for laser pulses energies between 2 W and 3 W, which means between 200 mJ and 300 mJ of energy per pulse. On the contrary, for the 327.4 nm the maximum peak intensity is obtained with the maximum pulse energy. This highlights that the energy range in which is possible to have the maximum P/B is quite wide and spans from 200 mJ/pulse to more than 300 mJ/pulse. Moreover, a different response to the variation of energy is obtained for the two Cu emission lines (at 324.7 nm and 327.4 nm), because the higher intensity of the 324.7 nm line highly reflected the measurement fluctuation.

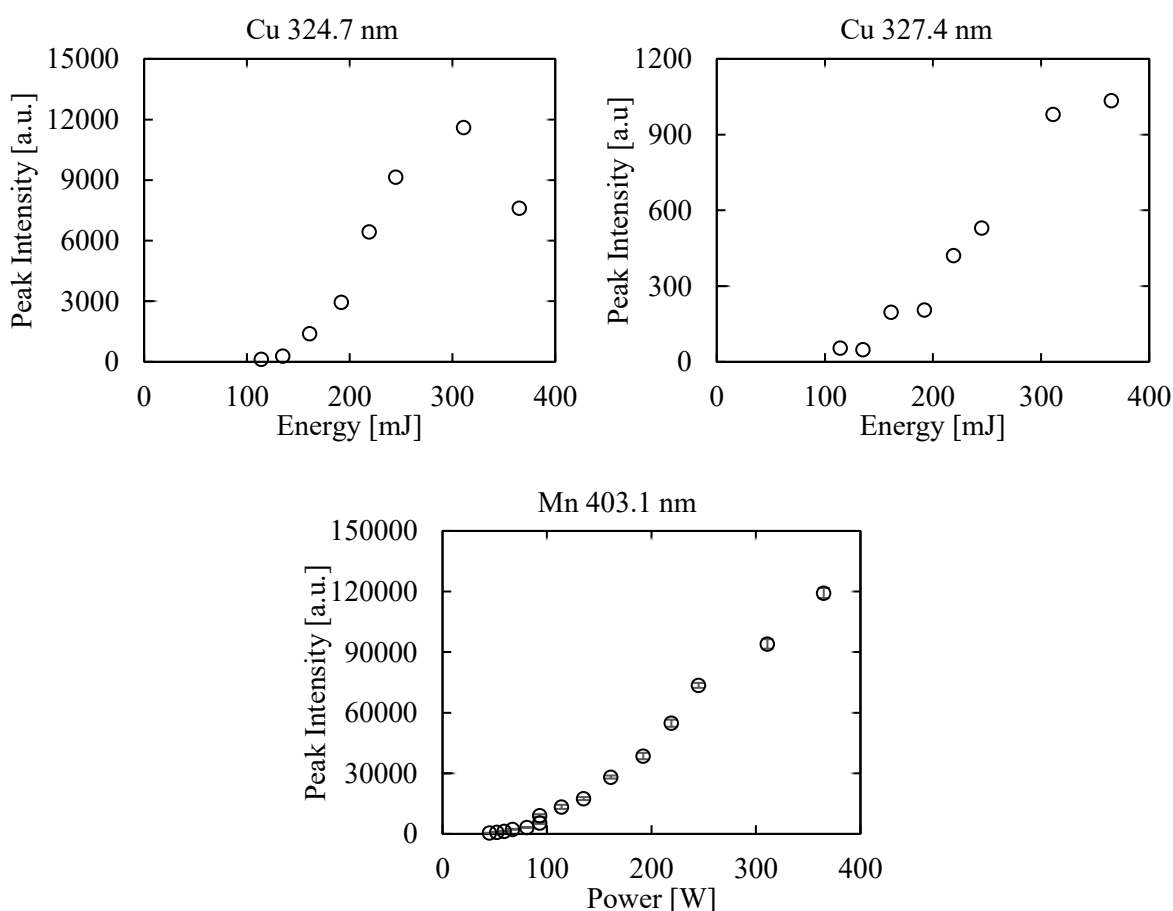


Figure 24. Cu I (top) and Mn I (bottom) signal evaluation varying the laser pulse energy.

Nebulizing a manganese salt solution, it was possible to get an insight on the variation of the signal with different pulses energies with more detail. In particular, starting from the nominal laser shot energy, (that is 450 mJ/pulse before the prism deflection), measurements were carried out varying the

laser energy, in the range from 365 mJ/pulse to 30 mJ/pulse. As reported in Figure 24 is evident that for laser energies below 100 mJ/pulse the peak intensity is comparable with zero. This occurs since, reducing the laser energy, the peak becomes less evident, and comparable with the background signal. Moreover, decreasing the laser pulses energy the number of laser shots that do not generate breakdown becomes greater and greater. Such condition is more significant for the lower energy values (with 14 and 15 glass windows). In fact, measurements taken at 20 mJ/pulse and 39 mJ/pulse are not reported in the graph, because the majority of accumulated shots have no signal, leading to a zero-signal background. In these experimental conditions it would be correct to consider 70 mJ/pulse as the inferior energy per pulse threshold. Looking at the signal with low variability, it is highlighted that also for manganese the maximum signal is obtained with the maximum of energy per pulse. The best experimental conditions defined in this preliminary analysis have been applied for the LIBS prototype developed in this work, which is shown in Figure 25. It consists in a compact arrangement of the experimental laboratory apparatus, with a laser beam of 450 mJ/pulse nominal output power which is deflected by a prism to be sent into the measurement chamber. Actually, the data obtained from this study suggest that it is possible to optimize the size of the instrument by using a laser with a nominal pulse energy of approximately 100 mJ. Calibration curves were then obtained on this instrument so that it could then be employed for real-time aerosol measurements, as shown in the following chapters.

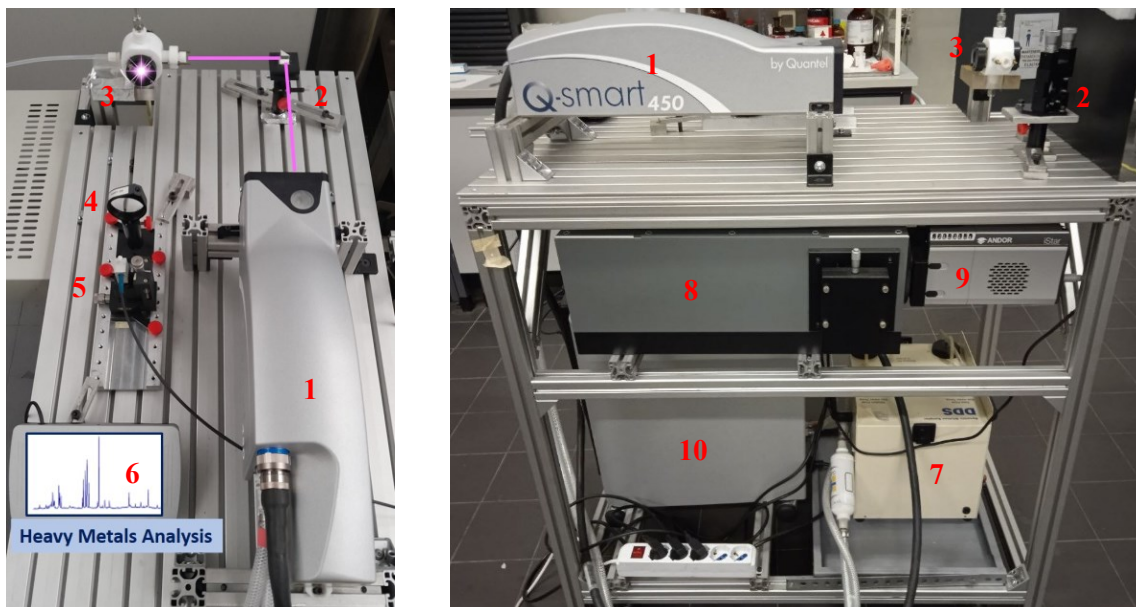


Figure 25. LIBS prototype instrument. (1) Laser; (2) Prism; (3) Measurement chamber; (4) Lens; (5) Optic fibre; (6) Lase controller; (7) Sampling pump; (8) Spectrograph; (9) iCCD camera; (10) Laser power unit.

4.2 CALIBRATION CURVES

Once the experimental conditions are fixed and the optical alignment to maximize the collected incoming radiation was carried out, a calibration procedure was developed to perform quantitative analysis on unknown aerosols. It is therefore necessary the construction of calibration curves for the elements under analysis. In the evaluation of the calibration curve, particular attention has to be paid to the self-absorption phenomenon, which is responsible for a loss of linearity occurring at high concentrations. In the direct measurement configuration, although a low analyte density is present inside the plasma, the presence of a wide number of cold atoms along the optical path in the direction of the collecting optics is responsible for significant self-absorption of the LIBS emission signal. As reported theoretically, different lines are affected with different strength by self-absorption. The radiation emitted by an atom due to its decay from an excited to the ground state is more probably reabsorbed by cold atoms because of the resonance phenomenon. Of course, with the increase number of cold atoms the probability of radiation absorption in favour of resonance transition increases as well [96,97,106,98–105].

For each element, different solutions were prepared with different molarities to generate increasing aerosol concentrations, from a few micrograms up to about a thousand per cubic meter. Each solution was nebulised, and the resulting aerosol was sent into the measurement chamber where 5000 LIBS spectra were acquired for each concentration.

In this way, a series of signals, each associated with its own concentration, were recorded. As for the concentration C , it is evaluated according to the following equation:

$$C = \frac{MA \cdot M \cdot c}{Q} \quad (18)$$

where MA is the elemental atomic mass, M is the salt molar concentration dissolved in the aqueous solution, c is the solution consumption inside the nebuliser and Q is the air flow rate inside the mixing chamber and is expressed in l/min .

In Figure 26 a typical example of calibration curve of vanadium (detected at 438.07 nm) is shown, where the P/B value is reported versus the concentration, as described in the previous paragraph. As it can be seen, the first two points exhibit a similar P/B value, which is due to a reduction in sensitivity, assuming value very close to the spectrum noise. Moreover, above a certain value of concentration (about $300 \mu g/m^3$ in the figure) a loss in linearity is detected related to signal saturation.

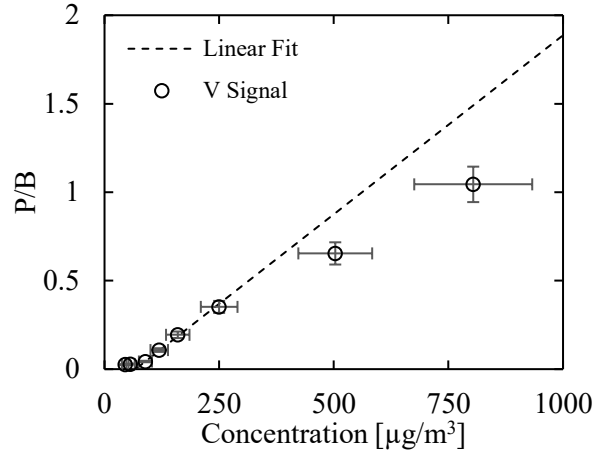


Figure 26. Example of the calibration curve for LIBS measurements of Vanadium (438.07 nm wavelength emission line).

For these reasons for each element the calibration curve is computed in the range of concentrations where P/B values exhibit a linear trend, eliminating values at too low concentrations for which sensitivity was lost and at too high concentrations for which the self-absorption occurred. The resulting calibration curve is then obtained by means of a linear fitting. The strength of the self-absorption effect is dependent on the element and in particular on the detected line.

An error was associated with both the concentrations (x-axis) and the signals (y-axis). The error on the concentrations was evaluated by applying the error propagation theory to the relationship reported in Eq.(18) and resulting in an uncertainty of 16%. The main contribution to this error is due to the variability of the consumption in the nebuliser, as described in the Appendix A1. As for the signal error, 9.6% of the relative error with respect to the mean signal was evaluated.

It is worthwhile to stress that the linear fitting performed by using the Origin software is obtained taking into account both the uncertainties on x and y axis. In addition, the slope of the linear fitting was used in order to calculate the limits of detection (LOD) of the element under analysis according to the equation [107–110]:

$$LOD = \frac{3[\sigma_B^2 + \sigma_i^2 + (i/s)^2 \sigma_s^2]}{s} \quad (19)$$

where s is the slope of the linear calibration curve, σ_B is the standard deviation accounting for the background variability, i is the intercept and σ_i is the intercept error. This parameter was calculated on 10 spectra averaged over 1000 acquisitions each and acquired from aerosol without the analyte of interest. Moreover, the error on the LODs was evaluated by applying the error propagation to Eq.(19), in which the only contribution to the error is considered.

In the following, for each analyte, an example of the emission line and the related calibration curve is reported in Figure 27-Figure 36 for Cu, Ni, Pb, Mn, Cr, Cd, Tl, Co, As and V, respectively. As for the emission line, the different peaks (red line reported in Figure 27 for example) and the related lateral bases are highlighted. As for the calibration curve, the linear fitting is reported and the 95% confidence area from the linear fit is highlighted between two dotted lines.

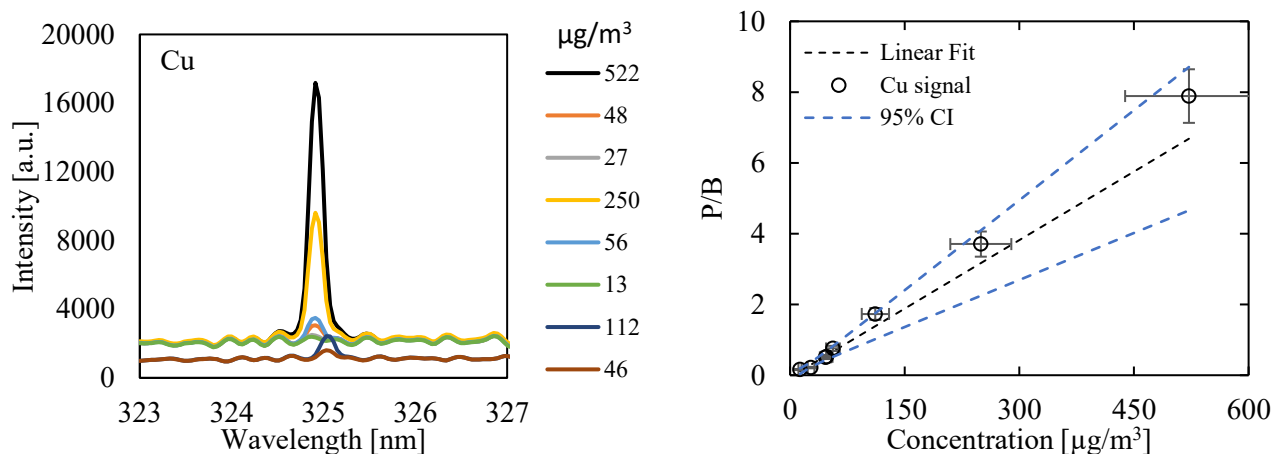


Figure 27. Left) Cu spectra emission line at different aerosol concentrations. Right) Linear fitting for aerosol copper calibration curve parameters calculation and 95% confidence interval (CI).

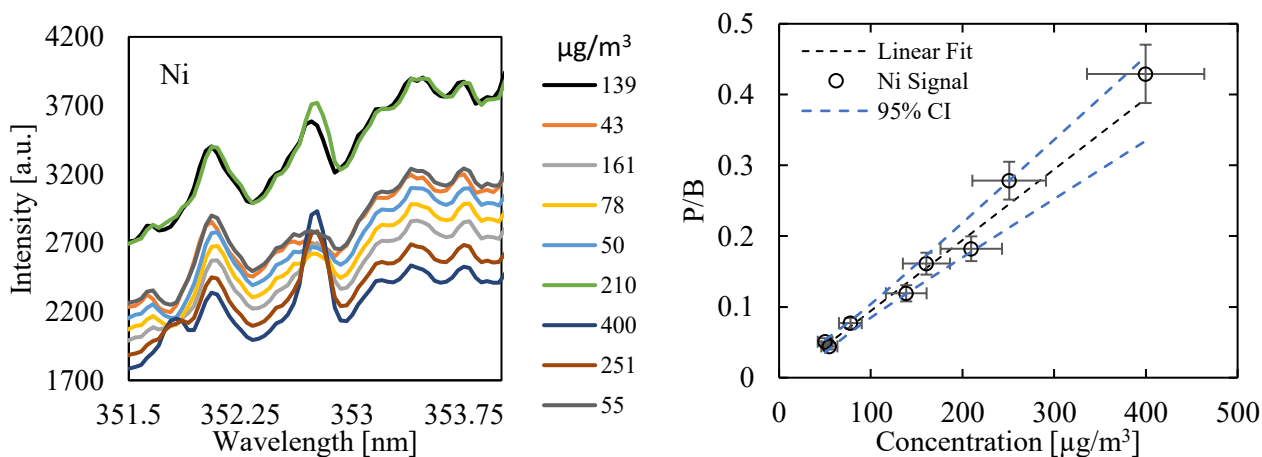


Figure 28. Left) Ni spectra emission line at different aerosol concentrations. Right) Linear fitting for aerosol nickel calibration curve parameters calculation and 95% confidence interval (CI).

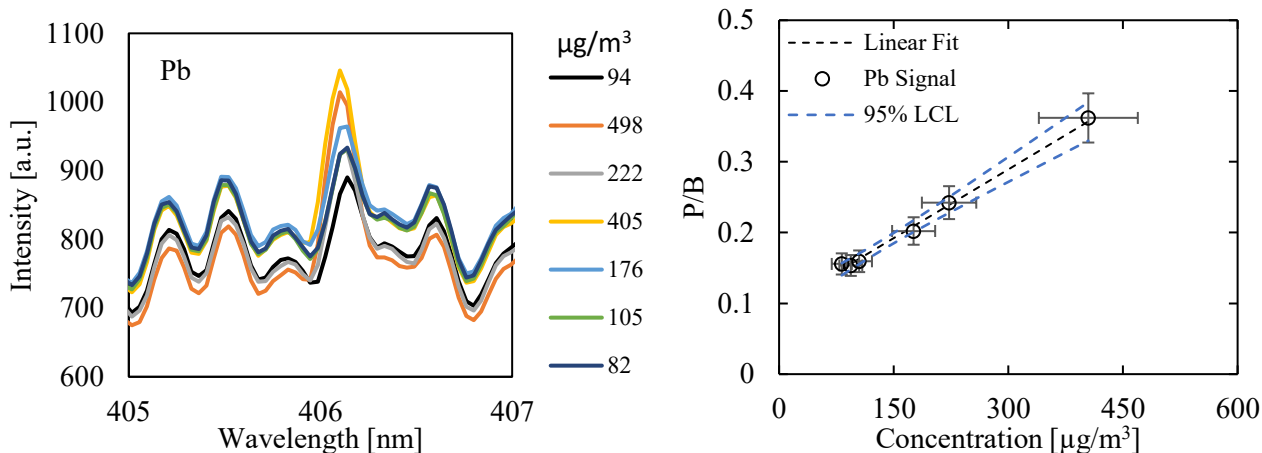


Figure 29. Left) Pb spectra emission line at different aerosol concentrations. Right) Linear fitting for aerosol lead calibration curve parameters calculation and 95% confidence interval (CI).

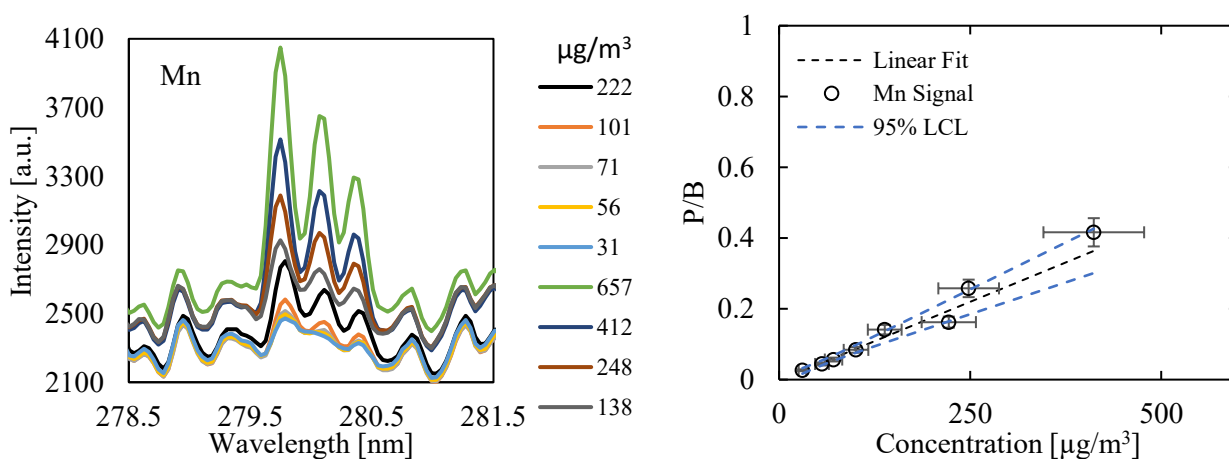


Figure 30. Left) Mn spectra emission line at different aerosol concentrations. Right) Linear fitting for aerosol manganese calibration curve parameters calculation and 95% confidence interval (CI).

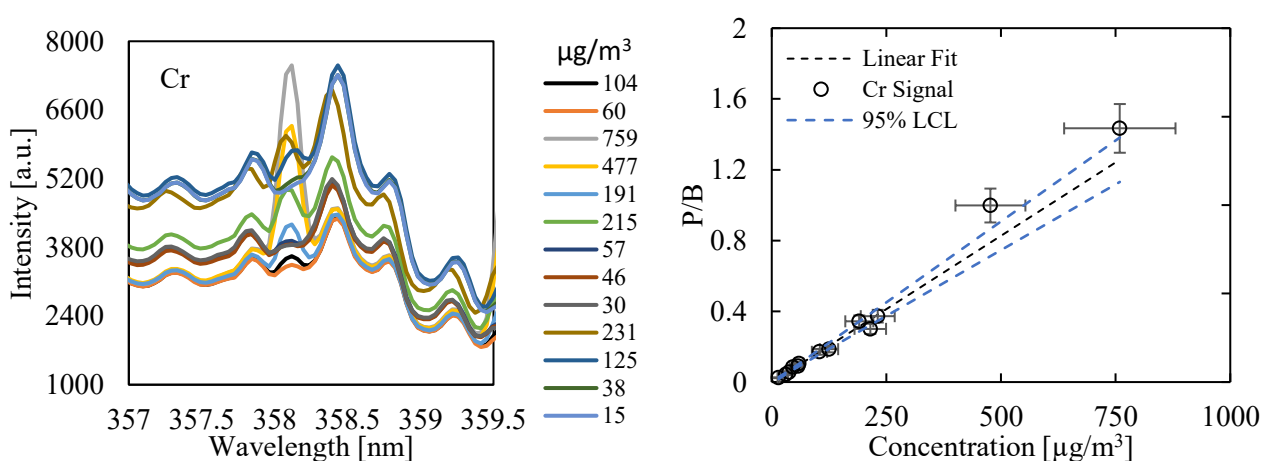


Figure 31. Left) Cr spectra emission line at different aerosol concentrations. Right) Linear fitting for aerosol chromium calibration curve parameters calculation and 95% confidence interval (CI).

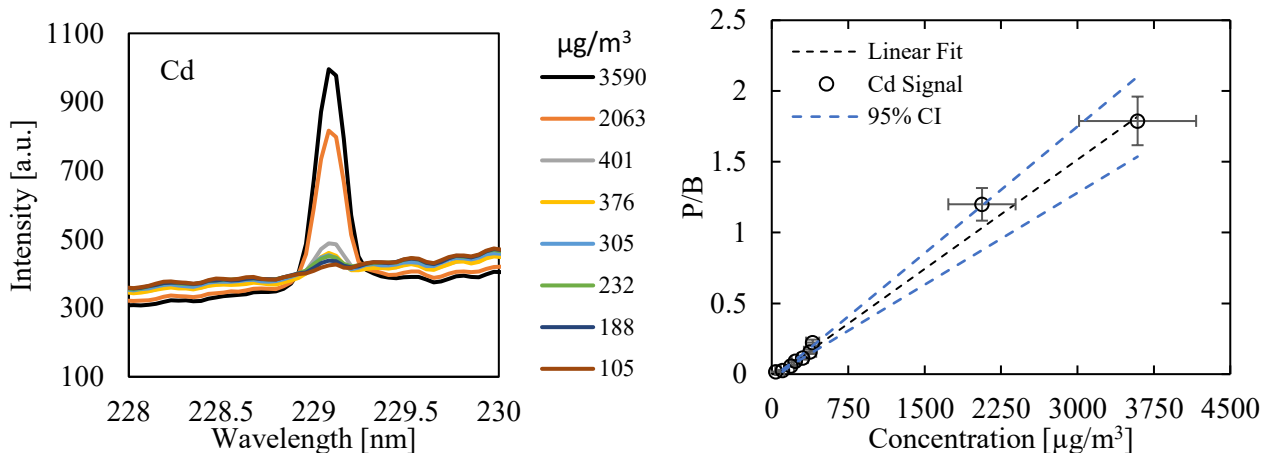


Figure 32. Left) Cd spectra emission line at different aerosol concentrations. Right) Linear fitting for aerosol cadmium calibration curve parameters calculation and 95% confidence interval (CI).

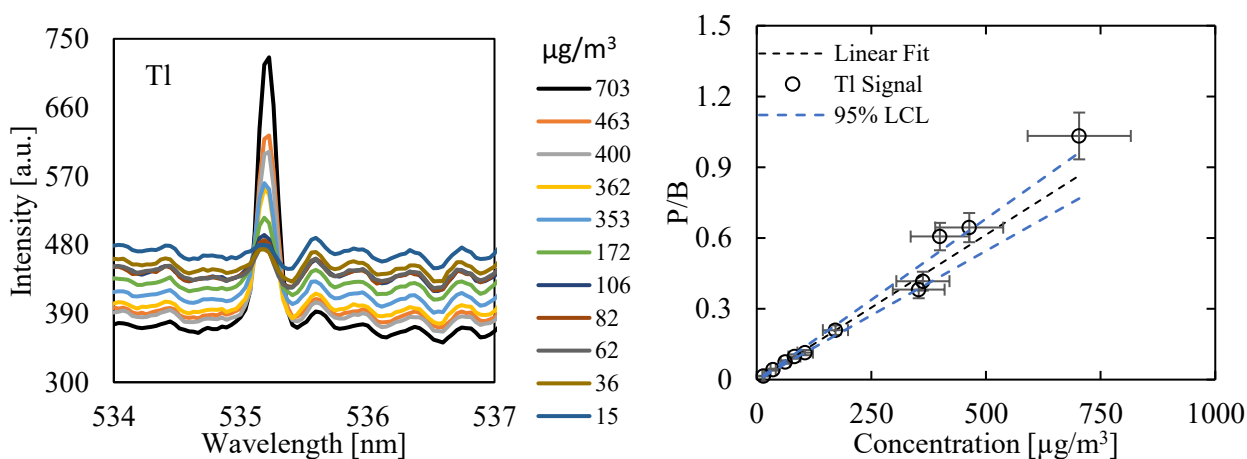


Figure 33. Left) Tl spectra emission line at different aerosol concentrations. Right) Linear fitting for aerosol thallium calibration curve parameters calculation and 95% confidence interval (CI).

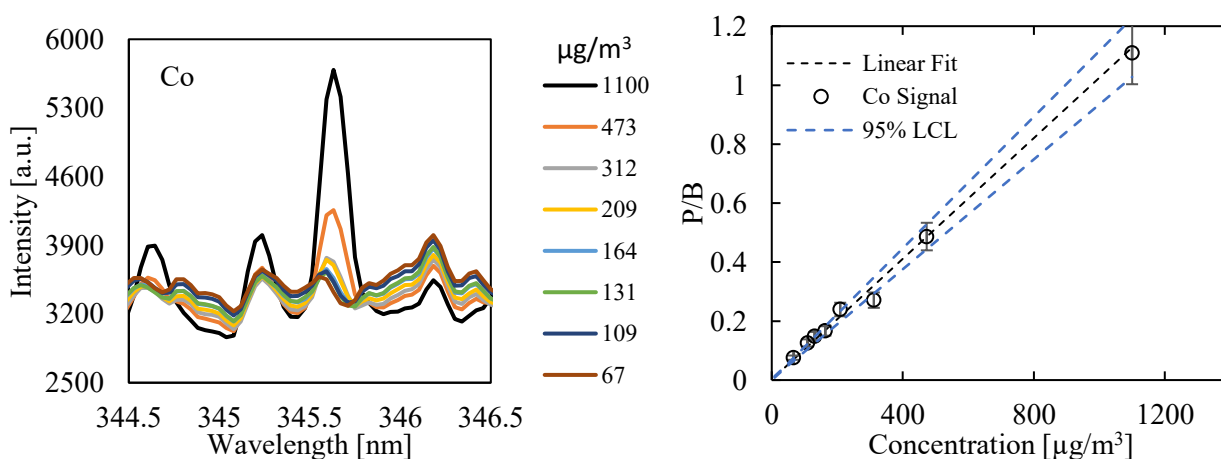


Figure 34. Left) Co spectra emission line at different aerosol concentrations. Right) Linear fitting for aerosol cobalt calibration curve parameters calculation and 95% confidence interval (CI).

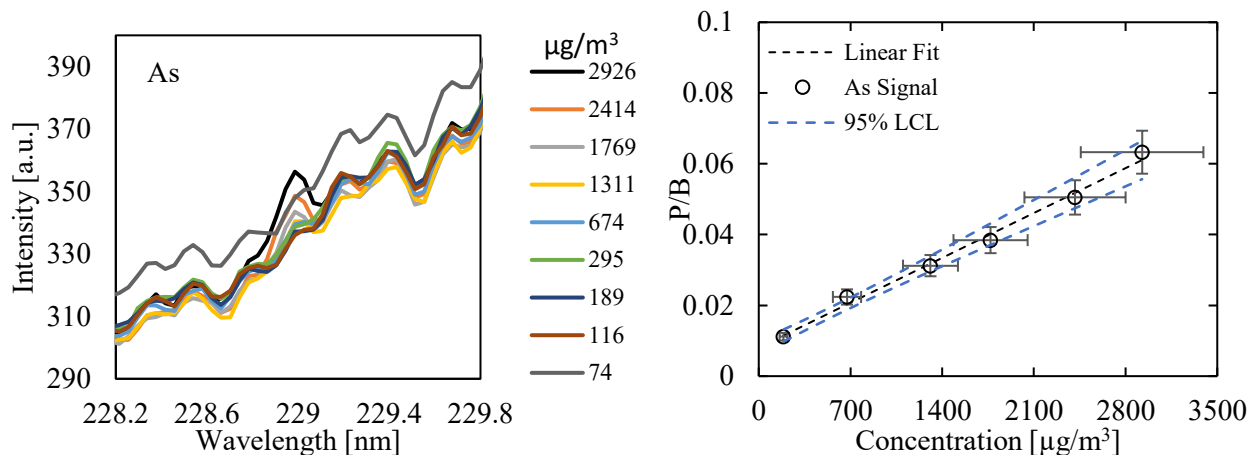


Figure 35. Left) As spectra emission line at different aerosol concentrations. Right) Linear fitting for aerosol arsenic calibration curve parameters calculation and 95% confidence interval (CI).

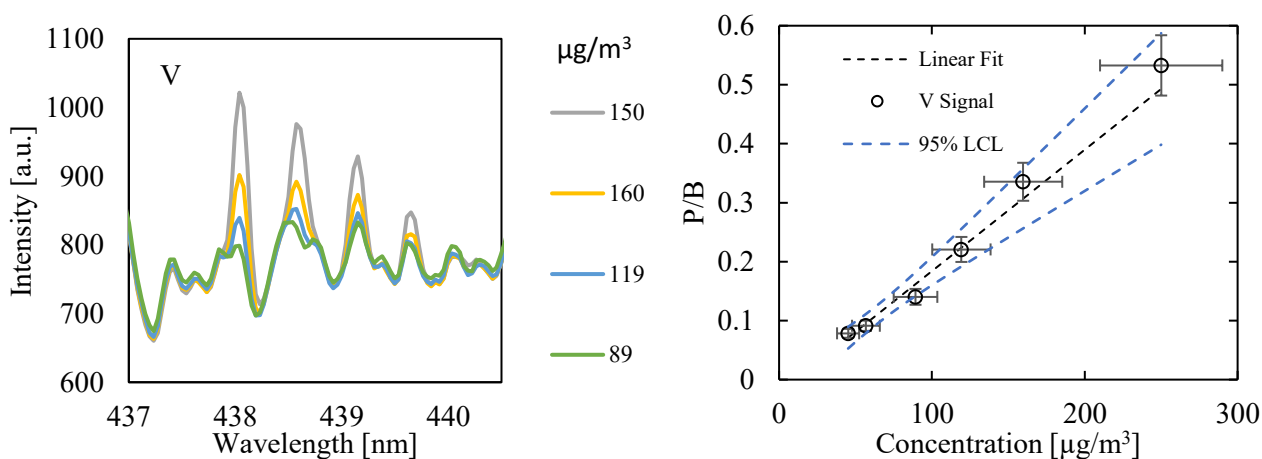


Figure 36. Left) V spectra emission line at different aerosol concentrations. Right) Linear fitting for aerosol vanadium calibration curve parameters calculation and 95% confidence interval (CI).

Finally, for all analytes, Table 5 reports the parameters of the calibration curves obtained, slope and intercept, R^2 values as an index of the goodness of the fitting, together with the calculated LODs and the corresponding ones found in the literature.

As for antimony, it was not possible to perform an accurate analysis and therefore to build a calibration curve, since the experimental set-up was not enough sensitive to the Sb emission lines at concentrations below one milligram per cubic meter. Moreover, high concentrated aerosols were difficult to be produced due to the poor solubility of the antimony salt available.

As also reported in Table 5, a good improvement in detection limits was achieved in comparison to the values reported in previous literature works.

Table 5. In the table are reported the fitting parameters of aerosol calibration curves: slope, intercept and R^2 ; and the calculated LODs.

Metal	Slope	Intercept	R^2	LOD [$\mu\text{g}/\text{m}^3$]	Literature LOD [$\mu\text{g}/\text{m}^3$]
Cu	$1.3 \cdot 10^{-2}$	-0.181	0.99	12 ± 4	15 [59]
Ni	$8.9 \cdot 10^{-4}$	0.035	0.98	19 ± 6	-
Pb	$4.9 \cdot 10^{-4}$	0.102	0.98	37 ± 12	155 [111]
Mn	$8.1 \cdot 10^{-4}$	0.033	0.99	16 ± 5	-
Cr	$2.1 \cdot 10^{-3}$	0.116	0.95	10 ± 3	30 [112]
Cd	$5.2 \cdot 10^{-4}$	-0.029	0.97	48 ± 16	60 [112]
Tl	$1.2 \cdot 10^{-3}$	0.006	0.97	7 ± 2	-
Co	$6.1 \cdot 10^{-4}$	-0.037	0.98	9 ± 3	-
As	$1.6 \cdot 10^{-5}$	0.004	0.92	254 ± 85	400 [112]
V	$2.0 \cdot 10^{-3}$	-0.137	0.99	20 ± 7	-

Taking into account the LODs obtained for the other metals and comparing them with the directive that regulates emissions from incinerators (2010/75/UE [113]), the analytes can be divided into two groups. One group consists of Cd and Tl, and the other group consists of the remaining metals (Cu, Ni, Pb, Cr, Co, Mn, V, As and Sb). According to the directive, which refers to a minimum sampling time of 30 minutes and a maximum of 8 hours, Cd and Tl can be emitted with a total maximum concentration of $50 \mu\text{g}/\text{m}^3$, while for the other elements the total emission allowed is $500 \mu\text{g}/\text{m}^3$. From the LODs obtained, we have a total LOD for Cd and Tl of $55 \mu\text{g}/\text{m}^3 \pm 18 \mu\text{g}/\text{m}^3$ and a total LOD for the remaining metals of $377 \mu\text{g}/\text{m}^3 \pm 125 \mu\text{g}/\text{m}^3$. Since the sum of the detection limits is below or compatible within the error with the regulated emission limit value it is possible to state that the instrument so calibrated is able to monitor the emission level of this list of heavy metals despite of the lack in antimony contribution.

4.3 LIBS MATRIX EFFECT STUDY

An important issue to face for the interpretation of the LIBS signal is the matrix effect, which is essentially related to the specific matrix considered (e.g. the presence of other solid/gas-phase elements in the probe volume) or also the different experimental conditions under analysis (e.g., temperature) [91,92,122,114–121]. These specific parameters are responsible for a change in the line intensity of the analyte under study, which affects its calibration curve. Although matrix effect in gas

phase results to be significantly lower than in solid [123], the change in the line intensity due to specific gas matrix used has to be considered for a correct interpretation of LIBS signals in the quantitative analysis. Different works are reported in the literature concerning the study of matrix effects in LIBS measurements performed on aerosol particles or gas phase [91,92,125,114–120,124].

4.3.1 Aerosol matrix effect

The role of the concomitant mass present in the probe volume on the physics of the particle vaporization as well as on the plasma conditions has been investigated, which results in a change in the response of the analyte under analysis [126]. It is evident that for a deep comprehension of the matrix effects, the chemical and physical processes occurring in the plasma must be considered. For example, the heat and mass diffusion rates within laser-induced plasma could be responsible for the presence of locally perturbed areas (in correspondence with the analyte) inside the bulk plasma. The works reported in the literature and the interpretation of the data obtained, underline the complexity of the processes involved in the laser-induced plasma, which are strictly related to the chemical and physical properties of the elements present in the probe volume and their combinations [127–131]. Here the effects of the concomitant mass present in the probe volume on the Cu I (324.7 nm) emission line were studied in order to stress the role of the physical properties of the elements involved in the plasma. To this purpose, Mg, Cr, and Na were used as matrix elements, as obtained from different salt solutions: nitrate, chloride, and acetate. The effect on the signal was investigated by increasing the loading of these elements with respect to copper concentration. Moreover, the effect on Cu I emission line was investigated due to the specific matrix compounds. To this purpose, Na chloride and Na acetate were used, and the effect was evaluated by increasing their loading in the probe volume. In Table 10 for each element, the related compound and the concentration ratio of this element with respect to copper concentration are reported.

Table 6. For each element, the related compounds used for the solutions, and the concentration ratio with respect to Cu in the measuring chamber are reported.

Element	Compound	Element mass concentration Ratio
Cu	Cu(NO ₃) ₂ ·3H ₂ O	
Na	NaCl C ₂ H ₃ NaO ₂	1:1 – 1:3 – 1:5
Mg	MgCl ₂ ·6H ₂ O	
Cr	C ₆ HCrO ₆	

Samples were prepared by mixing 7.5 ml Cu 0.001 M solution with 7.5 ml matrix solution of different molar concentrations, resulting in $400 \mu\text{g}/\text{m}^3$ Cu concentration and varied matrix mass concentrations in the measuring chamber. The molar concentrations of the matrix solutions were properly prepared in order to obtain the mass concentration ratios reported in Table 6. In particular, 1:1, 1:3, and 1:5 refer to the Cu: (Mg, Cr, Na) mass concentration ratio.

In Figure 37, LIBS spectra referring to Cu emission lines in the presence of different concentrations of Mg (a), Cr (b), and Na obtained from chloride (c) and acetate (d) salts are reported. Spectra were collected with a detection gate of $100 \mu\text{s}$ and a delay time of $30 \mu\text{s}$ with respect to the laser occurrence, and resulted from an average over 3000 single shots. As it can be seen, a change in the peak and base is detected in the presence of other elements added to copper. In particular, the base decreases, while the emission line intensity exhibits different behaviour depending on the specific element considered.

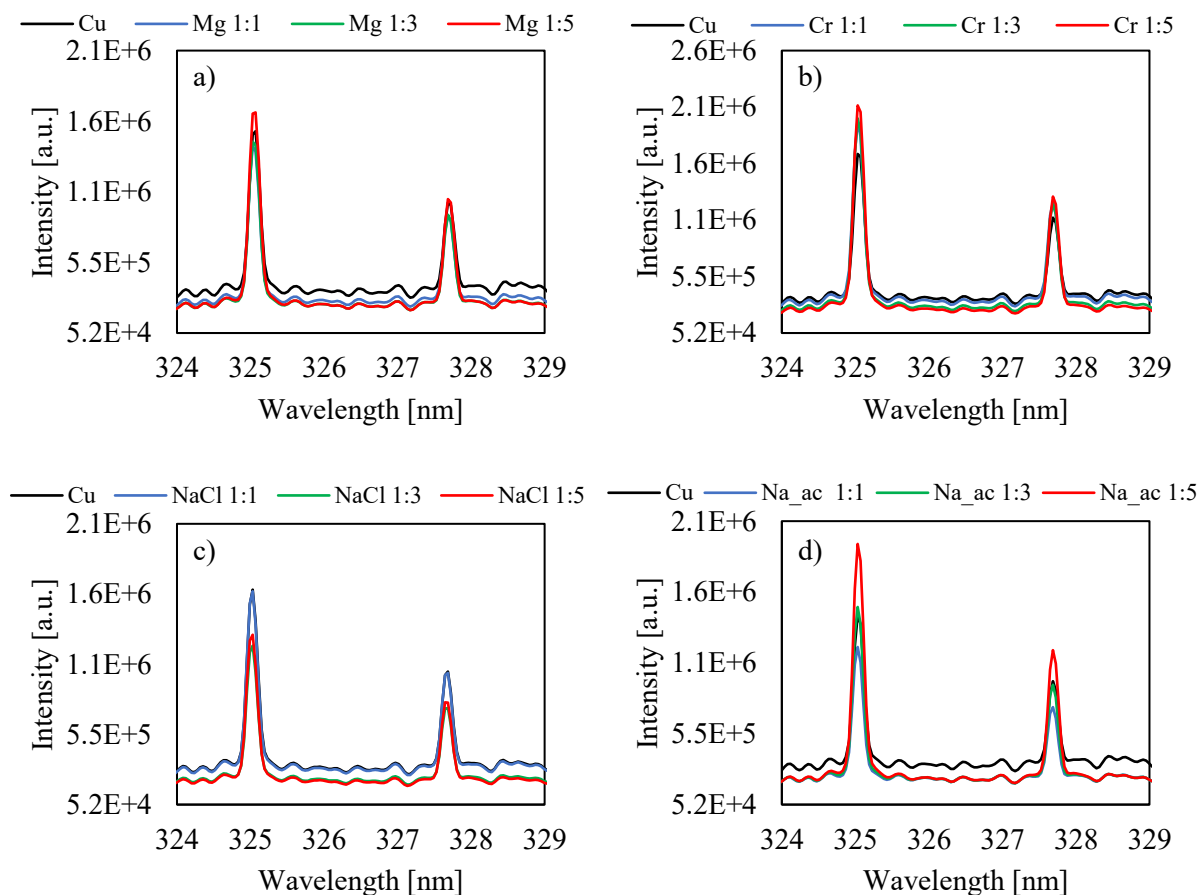


Figure 37. Cu I emission spectra (delay time = $30 \mu\text{s}$; gate = $100 \mu\text{s}$) with the addition of Mg chloride (a), Cr acetate (b), Na chloride (c), and Na acetate (d). In each plot, the curves refer to different concentration ratios (with respect to Cu) of the added element.

To deeply explore such effects, the base and the peak are separately considered changing the loading of the different matrix element under analysis. In Figure 38, these values are reported versus the Cu:matrix concentration ratio (Cu:M in the figure). In the figures the uncertainties are also reported

as error bars, referring to a relative error of 9.6% for LIBS signal and 4.2% for the base. These errors were evaluated considering the semi-dispersion of five Cu line intensities obtained in pure Cu aerosol. In this way, the variabilities due to the laser energy, the nebulization, and dilution flow rate conditions are considered.

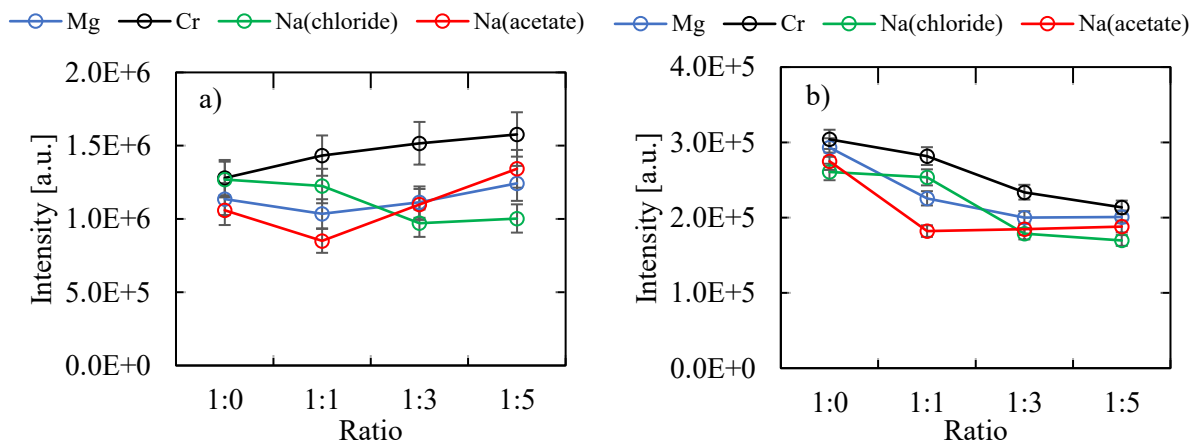


Figure 38. Base intensity (a) and Peak Cu I emission line (b) varying Cu:M ratio. Error bars are added at each point.

The base exhibits a global decreasing trend with loading, which is different for the matrix elements under analysis (Figure 38(a)). However, close Cu base signals are reached at 1:5 Cu:M ratio in all cases. On the contrary, Cu peak values are differently affected by each matrix element (Figure 38(b)). It is worth noticing that Cr addition always promotes an enhancement of the Cu LIBS signal with loading. Starting from the base and the peak, the P/B value can be obtained for the Cu LIBS signal in all conditions. In order to underline such effect, a Cu signal enhancement is considered, defined as the ratio of Cu emission line with and without the matrix element addition.

In Figure 39, the P/B enhancement (as percentage unit) is reported versus Cu:M ratio showing a significant loading effect of matrix elements on P/B Cu value. A progressive enhancement is obtained increasing the concentration, related to the element and compound considered. The addition of chromium acetate exhibits the highest matrix effect, reaching an enhancement of 75% with 1:5 loading. Moreover, from a direct comparison of Na Chloride and Na acetate matrix compounds, we can see that the addition of Na acetate is more effective in the enhancement produced.

By considering the results reported in Figure 38 and Figure 39, we can infer that the increase in P/B with Cu:M is mostly due to the decrease in the base, although the entity of the enhancement is dependent on the matrix element.

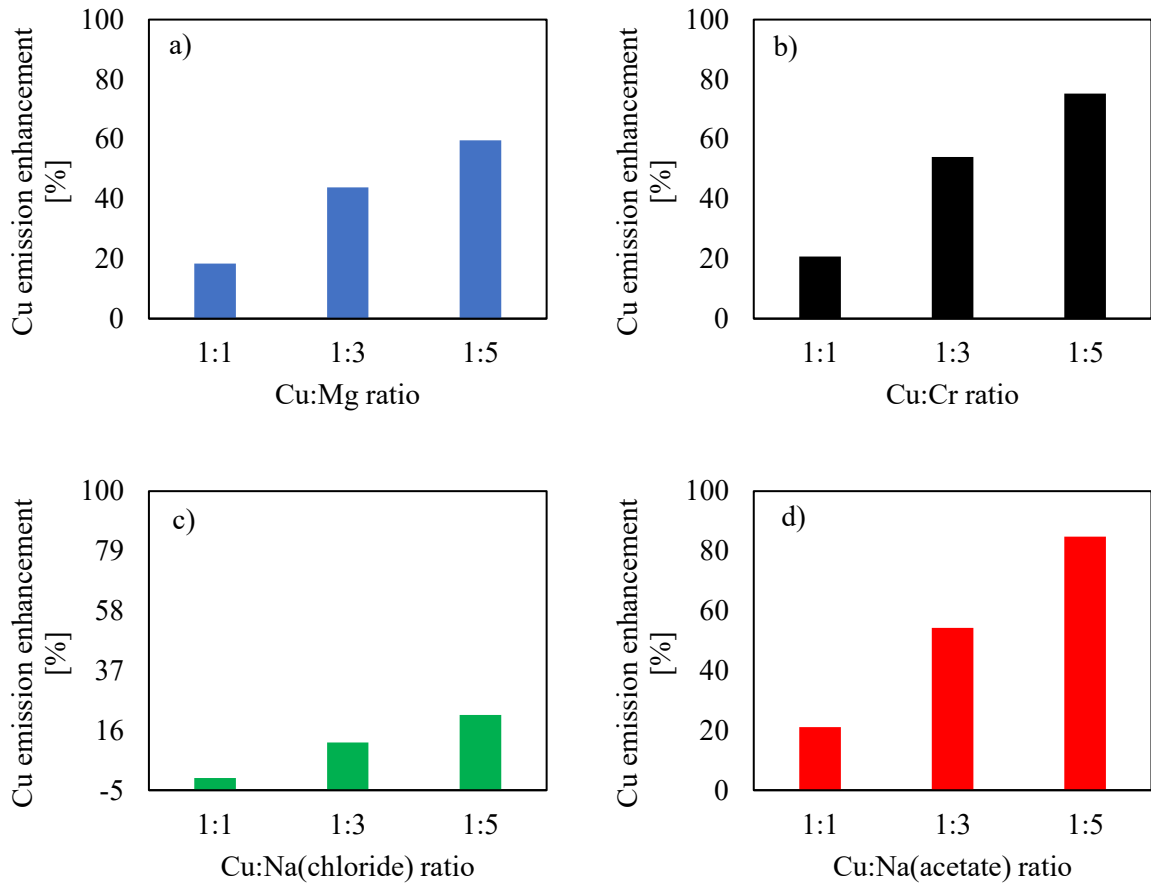


Figure 39. Enhancement of the 324.7 nm Cu I emission signal with the addition of Mg chloride (a), Cr acetate (b), Na chloride (c), and Na acetate (d).

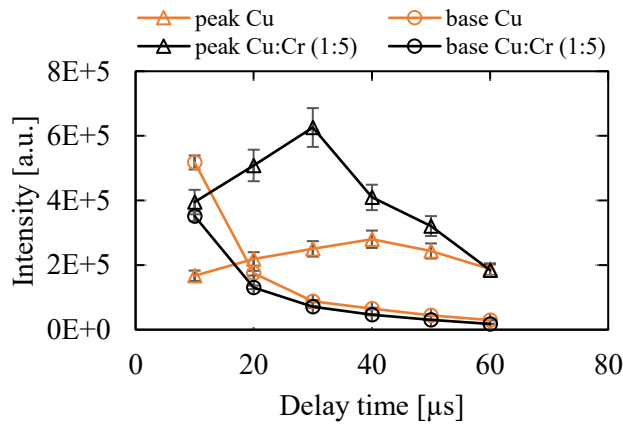


Figure 40. Temporal analysis of the 324.7 nm Cu I emission line from 10 μs to 60 μs delay time, with a detection gate aperture of 10 μs.

To further explore the impact of matrix compounds on plasma conditions, time-resolved LIBS measurements were performed for pure Cu and 1:5 Cu:Cr, which corresponds to the highest enhancement investigated. In Figure 40 the base and the peak of Cu without and with Cr are reported versus delay time. We can see that the base with Cr addition is lower than pure Cu, especially at early

delay times (from 10 μs to 20 μs), which is consistent with the previous analysis reported in Figure 38. As for the peak, with Cr addition, an increase in the Cu emission line is detected, with the maximum shifted from 40 μs delay time (for pure Cu) to 30 μs delay time (with Cr addition). The behaviour observed, namely the decrease in the background and the corresponding increase of the emission line at short delay times, accounts for a change in plasma conditions essentially due to plasma cooling.

Interestingly, at 60 μs , the peak values are close, suggesting that the matrix effect can be considered negligible at long delay time.

As a further analysis, the plasma temperature is evaluated from the slope of the Boltzmann equation (14). The analysis was performed on pure Cu and 1:5 Cu:M conditions. Unfortunately, with our experimental set-up only two Cu lines can be detected, which, belonging to the same doublet, are not sufficient for temperature measurements. Therefore, N I lines are considered, namely 410.0, 410.9, 746.8, 821.1 and 821.6 nm. Due to the substantial decrease of N I lines with delay time and the necessity to be in LTE conditions, these measurements are carried out from 5 μs to 15 μs delay times. In Figure 41 (a), a typical example of Boltzmann plot is shown, with the related linear fitting used to retrieve the temperature value. In Figure 41 (b) this temperature is reported versus delay time for pure Cu and Cu:M conditions. In presence of matrix elements, a decrease in plasma temperature is detected in the range of delay time considered. This is consistent with the base behaviour previously reported in Figure 38 (b), although in the previous analysis data are collected at longer (30 μs) delay time.

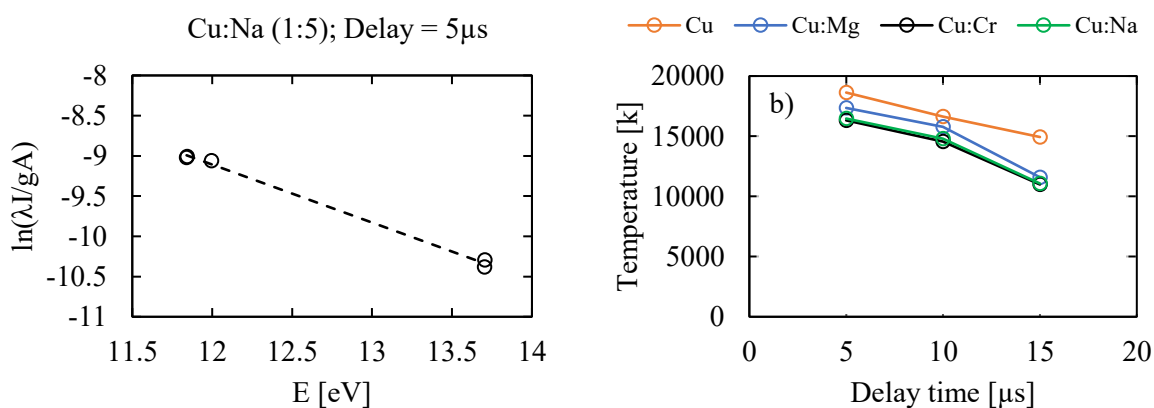


Figure 41. a) Example of Boltzmann plot (Na:Cu(5:1)). b) Temperature versus delay time. Temperature values are obtained using N I emission lines (delay time: 5–15 μs ; gate: 5 μs) for pure Cu and 1:5 Cu:M. Na chloride was used for these measurements.

The decrease in plasma temperature can be related to an enhancement in collisions and subsequent recombination between electrons and ions. As a result of these processes, an increase in Cu LIBS neutral lines can be obtained. Such behaviour can be attributed to the chemical and physical properties

of the elements and/or compounds involved [132,133]. The combination of the heat of vaporization (HV), binding energy (BE), and ionization energy (IE), these last related to the volatility are crucial in the comprehension of the different behaviour observed.

For clarity, in Table 7 HV, BE and IE values are reported for the species (elements and compounds) under analysis as taken from literature.

Table 7. Elements and salts physical parameters.

	HV [kJ/mol]	BE [eV]	IE [eV]
Na(acetate)	34 [134]	8.58 [135]	-
Na(chloride)	284 [135]	7.98 [135]	8.92 [135]
Na	98 [135]	-	5.14 [135]
Mg(chloride)	33 [136]	-	-
Mg	128 [135]	-	7.65 [135]

Considering Figure 38-Figure 39, similar trend can be detected for MgCl₂ and Na acetate, in the base and the LIBS peak signal, as well as in the loading enhancement. This trend can be attributed to their close heat of vaporization (of the compounds and atoms) and volatility (see Table 7, HV_{Mg(chloride)} = 33 kJ/mol [136]; HV_{Na(acetate)} = 34 kJ/mol [134]; HV_{Mg} = 128 kJ/mol [135]; HV_{Na} = 98 kJ/mol [135]). Comparing the two sodium compounds (chloride vs acetate), the relative binding energy and heat of vaporization accounts for the different effect on Cu LIBS signal. In fact, although both the compounds have similar binding energies (see Table 7, BE_{Na(chloride)} = 7.98 eV [135]; BE_{Na(acetate)} = 8.58 eV [135]) Na acetate has HV = 34 kJ/mol [134], which is much lower than the value of NaCl (HV = 284 kJ/mol [135]). In this case, a large part of the energy is needed to break the molecular bond and only a small quantity is left for ionization (IE_{Na} = 8.92 eV [135]). Therefore, few free electrons are available for the recombination with Cu ions, resulting in a slight change in the atomic line intensity.

These measurements highlight the complex mechanisms at the basis of the matrix effect. Matrix physical properties affect plasma conditions, changing temperature and plasma temporal evolution, substantially affecting the LIBS signal. As a final remark, in line with these observations, performing LIBS measurements at a relatively long delay time, when these chemical and physical processes triggered by matrix effects are quenched, could be a possible strategy to be adopted.

The data reported in this paragraph are collected in a paper published in *Spectrochimica Acta part B*, reported at the end of this thesis.

4.3.2 Gas matrix effect

As already observed, several works can be found in the literature, concerning the role of different gas matrices on LIBS signal collected in different experimental conditions. In particular, the investigation of oxygen effects was performed by different authors and the quenching effect of oxygen species on different analytes is well known [116,137–139]. In the works [91,92], LIBS measurements performed on Cu analyte were carried out, by comparing measurements in N₂ and air carrier gas. Two competitive phenomena have been observed in presence of oxygen: an enhancement of the LIBS signal at short delay time and a signal quenching at long delay time. Since no significant differences are detected in the plasma temperature and electron density, the authors excluded the role of thermal effects and attributed the behaviour detected to chemical kinetic mechanisms triggered by oxygen in the carrier gas.

In this thesis work, Helium and Argon are used as dilution gases and the effect on Cu I emission line at 324.7 nm is investigated. For this analysis it was used the solution containing copper nitrate and He flow rate was varied between 0.1 l/min and 0.7 l/min and Ar flow rate between 0.2 l/min and 0.6 l/min.

LIBS measurements were collected at 30 μ s delay time and 100 μ s detection gate width. Since the addition of He or Ar results in a dilution effect on the analyte under analysis, measurements are corrected for the related dilution ratio. In Figure 42 the peak (P), base (B) and corresponding peak-to-base ratio (P/B) are shown versus the percentage of He added to air. The peak signal refers to the maximum LIBS line intensity after subtracting the base signal.

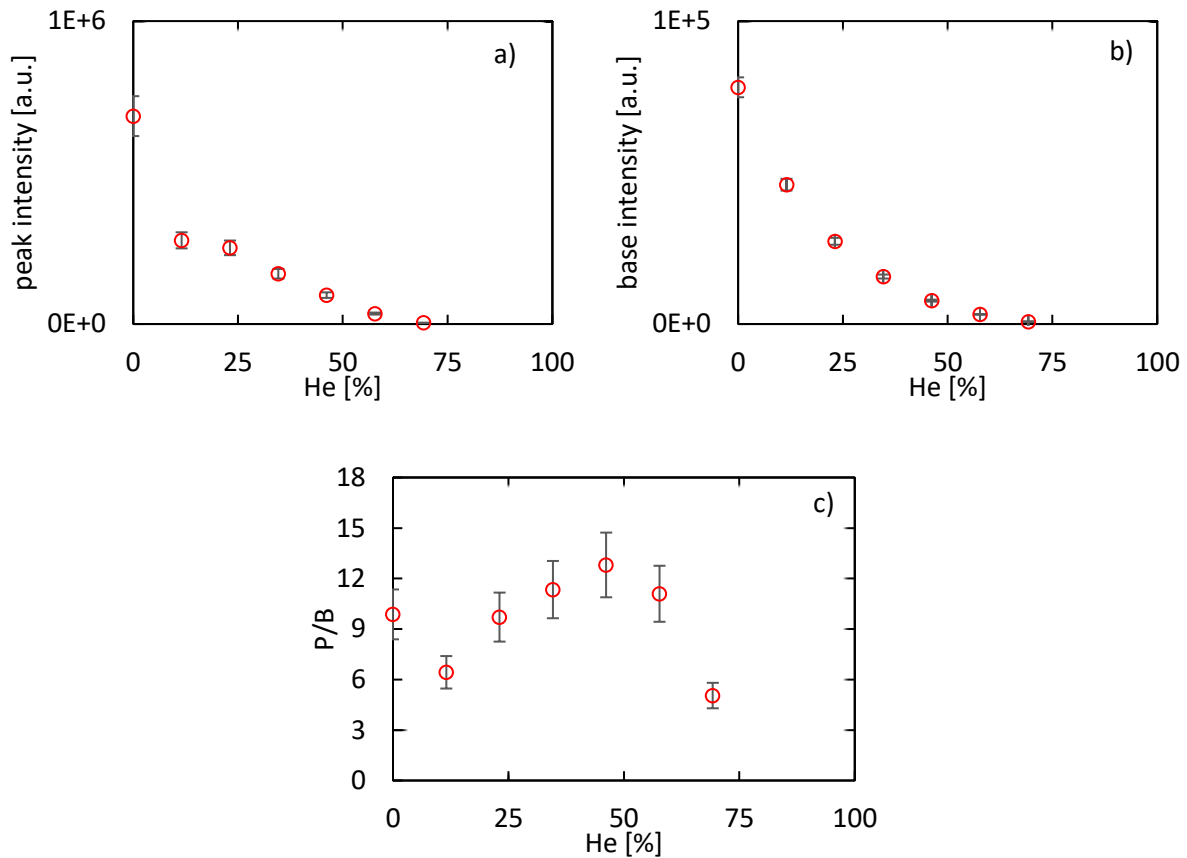


Figure 42. Peak LIBS signal (a), base signal (b), and signal-to-base ratio (P/B) (c) of Cu I emission line at 324.7 nm versus the percentage of He added to air.

As can be seen in the figure, a fast decrease of the peak intensity is observed with a minor addition of He (12%). However, with the further increments of the gas percentages, the rate of decrease becomes more gradual. As for the base, a uniform decrease is observed in increasing He percentage. Such behaviour of the base highlights the fast-cooling effect of the plasma due to He addition [137]. This is confirmed by an evident change in the plasma shape as also highlighted by a muffled acoustic signal. The combination of the slightly different decreasing behaviour of peak and base with He addition results in a bell-like shape in the peak/base trend, with a maximum value occurring at about 40% He. The same analysis was carried out with the addition of argon, as reported in Figure 43. As for the peak, the presence of Ar in the percentage between 30% and 50% range results in an increase of this value compared to the signal in air. Different behaviour is obtained for the base: the values with Ar addition are almost comparable with the ones in air.

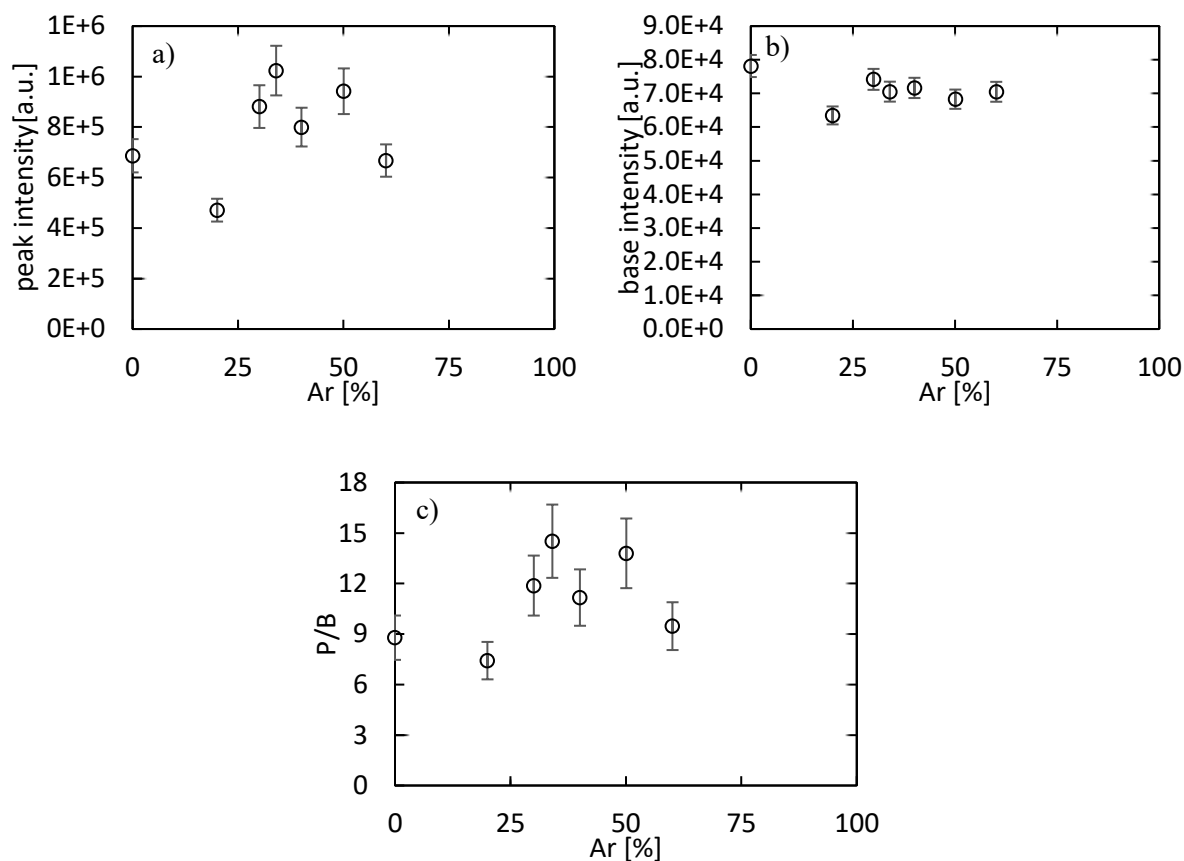


Figure 43. Peak line emission (a), base (b), and Peak/Base ratio (c) of Cu I emission line at 324.7 nm versus the percentage of Ar added to air.

Combining the two behaviours in the P/B ratio an enhancement for Ar addition above 30% is obtained.

To study the combined effect of the two gases, we fixed the Ar percentage at 35% and we vary the He percentage. Such value of Ar percentage was chosen to avoid a further increase in the dilution for He addition in the measurement volume.

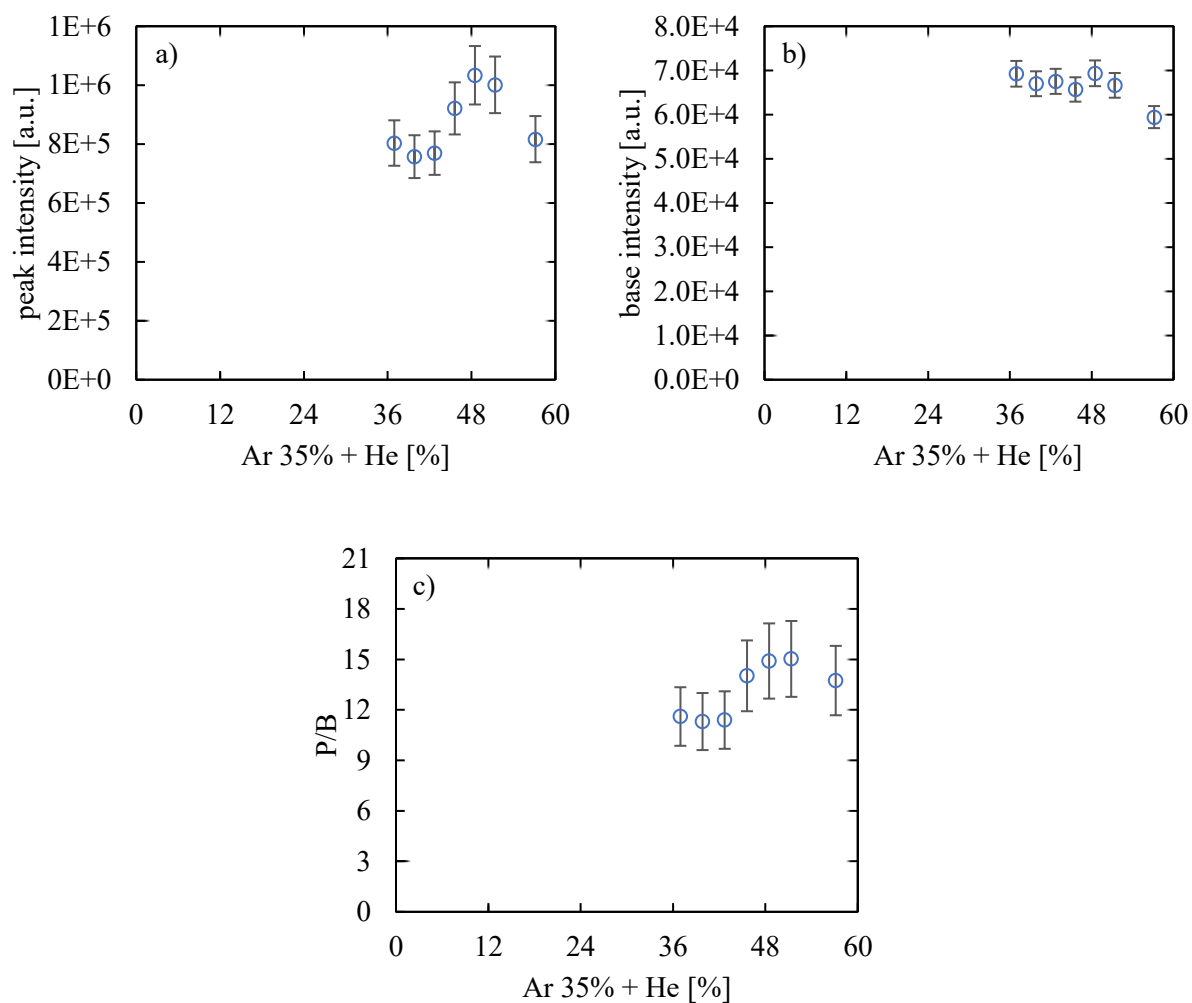


Figure 44. Peak line emission (a), Base (b), and Peak/Base (c) Cu I emission line at 324.7 nm versus the percentage He added to Ar (35%) and air.

In Figure 44 peak, base and peak/base are reported versus He percentage, keeping constant Ar at 35% in air. While the base signal is not affected by He addition, the peak line emission exhibits a slight increase, which results in a corresponding increase in P/B ratio. The maximum enhancement was obtained with the following conditions: 35% of Ar and 15% of He in air.

A time-resolved LIBS signal study was performed with the different gases under analysis in the probe volume, namely with 15% of He, 35% of Ar, and the mixture 35% Ar / 15% He. In Figure 45 peak, base and peak/base are reported versus delay time. The same trend is detected for all gas conditions: increasing the delay time, a significant decrease of both peak and base is detected, which corresponds to an increase in peak/base ratio.

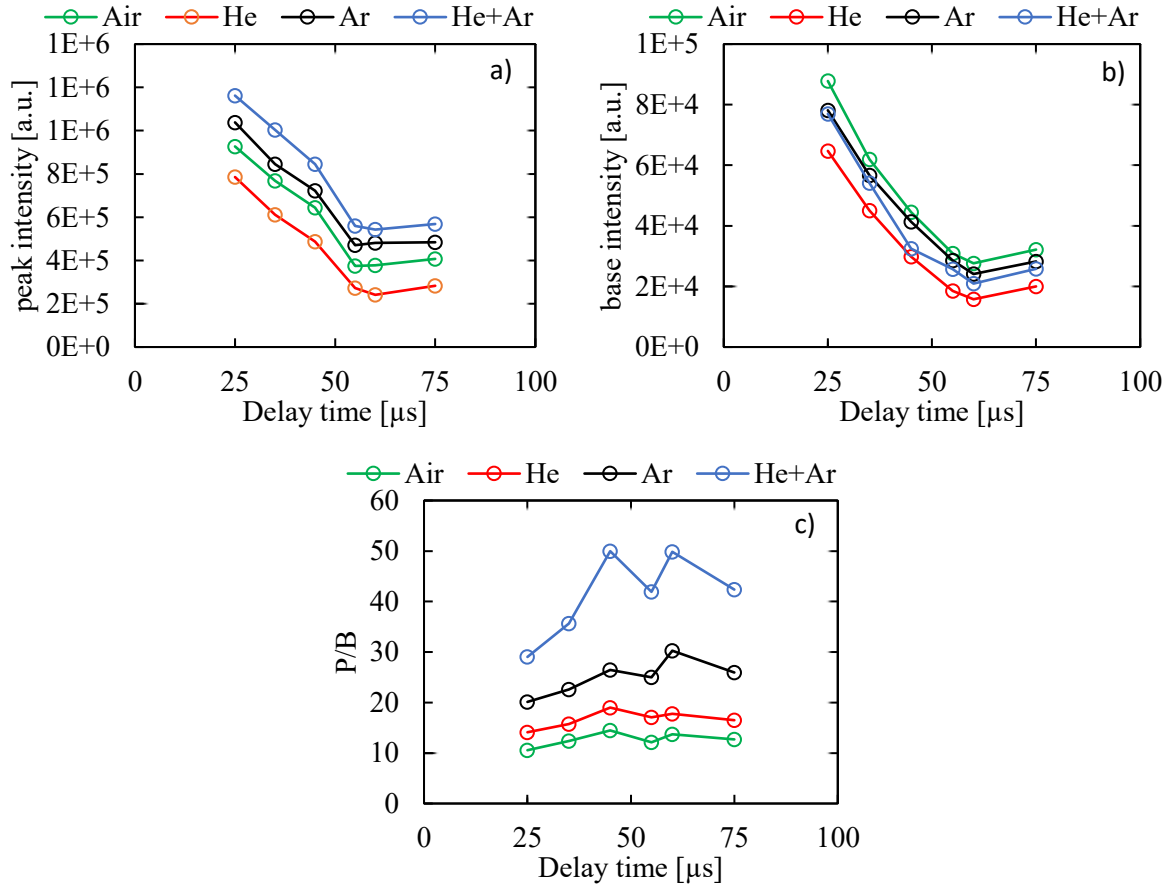


Figure 45. Peak (a), base (b) and P/B ratio (c) behaviour versus delay time in air and in 15% He, 35% Ar and 35% Ar / 15% He mixture in air.

For all delay times, the peak and the base are lower with He addition than in the other configurations. This effect is due to the expansion of the plasma and the resulting faster cooling in the He environment [140]. Moreover, the significant decrease in the base accounts for an increase in P/B compared to the values in air. Different behaviour is detected with the other gases, Ar, He +Ar mixture and pure air. While the base exhibits almost the same values at any delay time, an increase in the peak is observed with the addition of Ar and 35% Ar / 15% He mixture to air. This corresponds to an enhancement in the P/B value in the presence of Ar especially with Ar + He. As shown before this behaviour can be attributed to a faster cooling in He atmosphere and a corresponding slower cooling in Ar atmosphere (with respect to pure Air) [140,141]. The mixture of the two gases results in a more evident enhancement thanks to the background suppression observed in He atmosphere, and emission line enhancement due to Ar. A more detailed temporal analysis of the mixture configurations is reported in Figure 46, where it is highlighted a higher peak intensity and a lower base at all delay times in presence of the mixture of gases compared to the values in air.

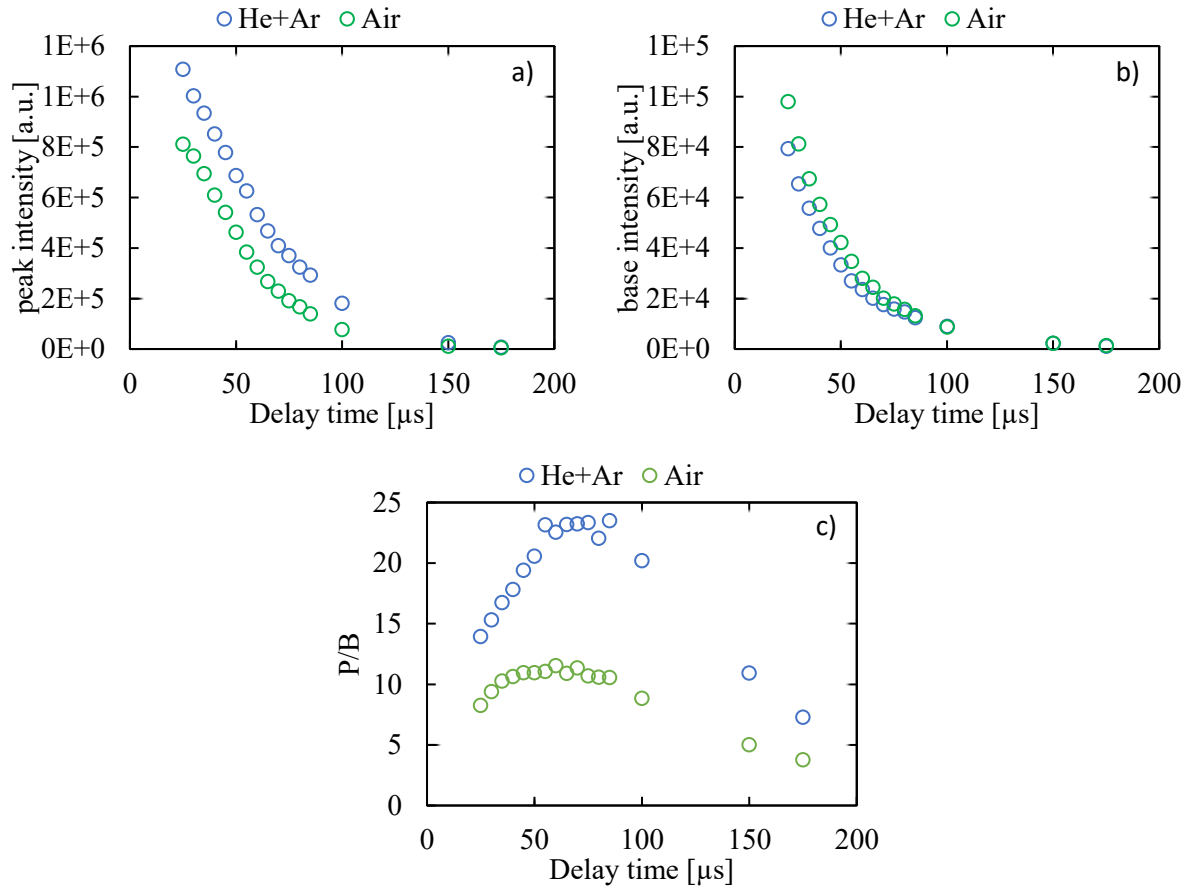


Figure 46. peak (a), base (b) and P/B (c) behaviour at different delay times in air and 35% Ar / 15% He.

Moreover, in the case of gas mixture configuration P/B trend exhibits a maximum higher than the value in air of about 50% and shifted at a longer delay time (occurring at 55 μs vs 45 μs in air). This P/B value continues to be significantly higher in the He / Ar mixture than in air up to about 200 μs. These results might suggest an interesting approach to apply for enhancing the LIBS signal, which is extending the integration time (detection gate width) to a longer delay time in the He/Ar mixture condition compared to air condition. Such behaviour can be attributed to some properties of Ar and He such thermal conductivities and ionization potentials [140]. In brief:

- the higher value of He increases the cooling rate, which reflects in a reduction in the spectral noise level.
- The enhancement in the LIBS signal with Ar addition can be attributed to a slight increase in the thermal conductivity of Ar with respect to air, and also to the substantial reduction of oxygen percentage in the probe volume, and consequently to the reduction in the quenching effect of O₂ on LIBS signal [92,116].

4.3.3 Combined particles and gas matrix effects

To investigate the combined effect of the gas matrix and the concomitant presence of another element in the probe volume, the presence of Cr in the probe volume was also considered on the Cu LIBS emission line. In Table 8 the concentration used for Cu and Cr are shown, where the Cu:Cr ratio of about 1:5 is considered due to the highest enhancement detected.

Table 8. Element concentrations inside the measurement chamber.

Element	Concentration [$\mu\text{g}/\text{m}^3$]
Cu	500
Cr	2700

In Figure 47 the time-resolved trend of the peak/base value related to the Cu emission line is shown in air, with the addition of Ar/He mixture to air, and with the further addition of the Cr compound.

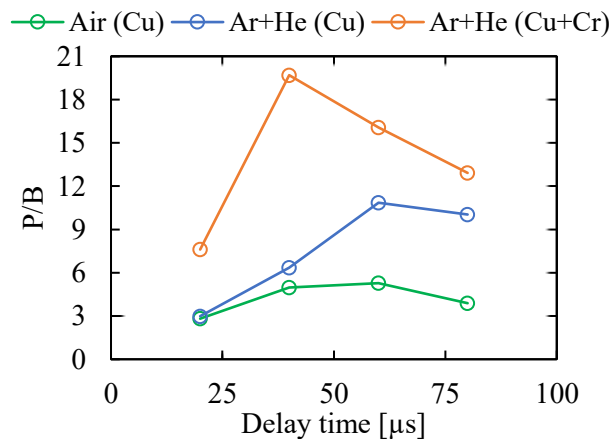


Figure 47. Peak/Base versus delay time of Cu emission line in air, with Ar/He mixture in air, and with the further addition of Cr compound. Concentration ratio of Cu:Cr is 1:5. Error bars are reported in each condition.

In this figure it is evident the concomitant effect of the mass and gases matrix on Cu analyte in the probe volume.

- The addition of the He/Ar mixture results in an increase in the maximum P/B value and in a shift of this maximum occurrence at a higher delay time, which is the same trend already shown in Figure 46.
- The further addition of Cr in the probe volume is responsible for a further enhancement of P/B value and a shift of this peak to lower delay time.

As it can be seen in the measurements reported in Figure 47, the concentration of Cu analyte is half than the value shown in Figure 46. This choice is due to the need of further adding Cr compound for this specific study.

We can conclude that the effect of the concomitant mass present in the probe volume is independent from the effect of the gas matrix and actually, the two contributions can be considered in the final P/B trend of the Cu emission line.

These data are presented in a paper which is being prepared for submission on a peer review journal.

5 RESULTS ON FILTER

In order to improve the detection limits and thus be able to perform measurements at lower concentrations, an accumulation of aerosol particles on filters is performed for subsequent LIBS measurements directly on the particulate collected on the filter, as shown in the experimental setup reported in the previous section.

5.1 EXPERIMENTAL CONDITIONS FOR FILTER ANALYSIS

In this section, the experimental conditions employed for LIBS analysis on filter are reported, underlining their significant difference from those used for direct aerosol analysis. To this purpose, the experiment set-up reported in the previous section is used where the aerosol with the element under analysis is deposited on 3 mm diameter spot filter. Differently from aerosol measurements, lower laser energies are sufficient to achieve breakdown, and acquisition times are significantly reduced. In this case, the laser energy was set at 23 mJ/pulse, which was the upper limit of energy before the filter was damaged by the laser pulse. Moreover, a significant damaging also in the region outside the area under analysis is obtained, more important with higher laser energy. Decreasing the laser energy and consequently limiting the ablation area, multiple LIBS measurements were carried out on the same deposit avoiding possible interferences between close measurements. The analyses were initially performed using a laser beam with a wavelength of 266 nm, in order to explore possible differences in employing different laser wavelength. The laser pulse parameters (energy and wavelength) were fixed and the gate width for signal acquisition was set at 100 ns, since the LIBS signal was no longer visible for shorter gates and tended to background noise for too long gates. Five measurements were performed on iron aerosol deposited on a paper filter, varying the signal acquisition delay time at the values of 200 ns, 300 ns, 500 ns, 750 ns, and 1000 ns, as shown in Figure 48. In particular, Fe II emission line at 260.1 nm is reported.

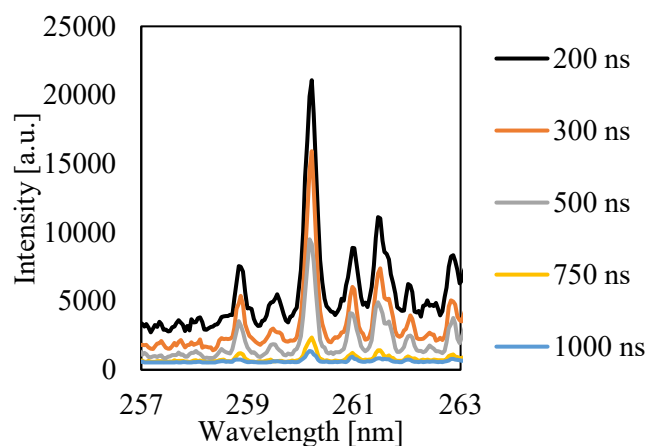


Figure 48. Typical LIBS spectra of iron (Fe II at 260.1) varying the delay time.

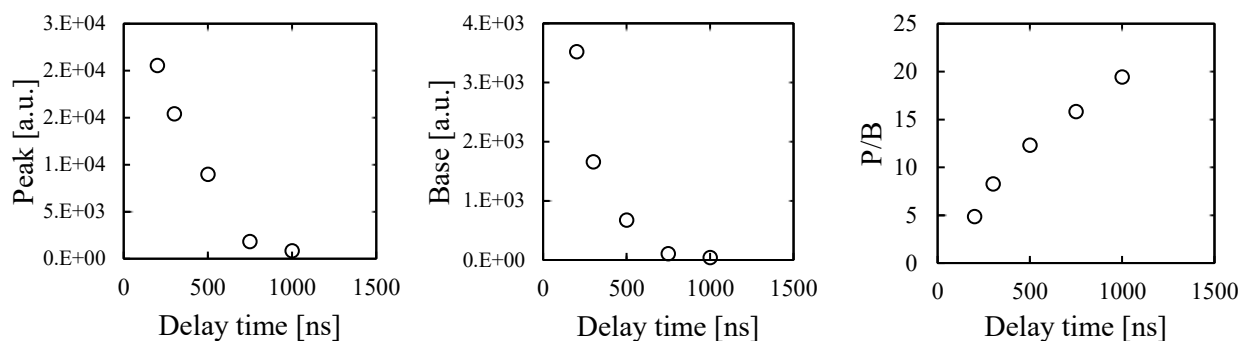


Figure 49. Peak, base and Peak (-B) to base ratio of iron LIBS intensity versus delay time.

It is evident that, although peak and base decrease with increasing delay time, a resulting enhancement in P/ B is obtained. However, at delay times of 750 ns and 1000 ns, base values very close to the electronic background noise are detected, indicating the occurrence of a cold plasma, far from LTE conditions. For this reason, in this work 500 ns was chosen as delay time for LIBS measurements on particle-loaded filter.

In order to investigate the effect of the use of different excitation wavelength or different filter type in LIBS measurements, in Figure 50 I report a comparison of the iron LIBS spectra obtained at 1064 nm and 266 nm excitation wavelength and paper/quartz filter. In particular, measurements are performed with 500 ns delay time and 100 ns gate width.

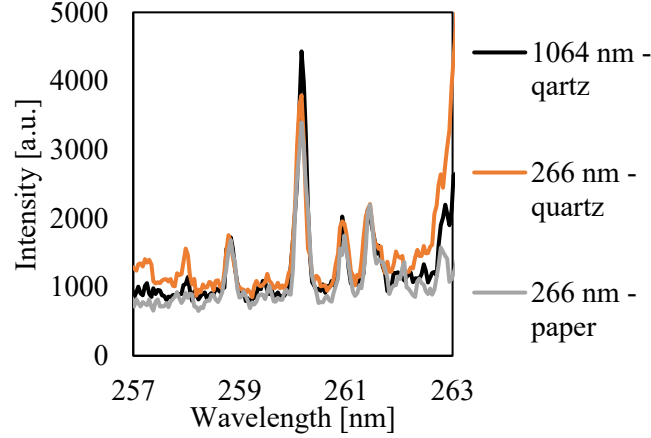


Figure 50. LIBS spectra of iron varying the excitation wavelength (266 nm / 1064 nm) and the filter type (quartz/paper).

As highlighted in this figure, using the same laser pulse energy and performing measurements on deposits with the same surface concentration, very similar spectra are obtained, showing that the excitation wavelength effect and the filter matrix effects can be considered negligible. According to these analyses, 1064 nm laser beam with an energy of 23 mJ and samplings performed on quartz fibre filters are considered for the analysis reported in the following.

5.1.1 Calibration curves on filters

For the calibration, single shot measurements were carried out varying the probe volume position on the filter spot. In particular, 9 different points in the spot were considered and the LIBS signal was evaluated by averaging on these 9 single shot measurements. The corresponding surface particle concentration C_s was calculated as follows:

$$C_s = \frac{m}{A} = \frac{Q_s \cdot t \cdot C}{A} \quad (20)$$

where m is the elemental mass deposited on the filter, A is deposited surface spot, Q_s is the sampling flow rate, t is the sampling time and C is the aerosol concentration expressed in $\mu\text{g}/\text{m}^3$. Each surface concentration was associated with an error derived by applying the error propagation theory to Eq.(20). The relative errors of A and Q_s result to be less than 1 % each, which can be considered negligible compared to the relative error of the aerosol concentration C measurement which is assessed to 16 %. Therefore, 16 % results to be also the relative error of the surface concentration. In this case, no error is associated to the signal because the variability in single shots is mostly due to inhomogeneity of the pollutants' concentration onto the filter more than intrinsic measurement errors.

Differently from aerosol measurements, for filter analysis other lines are employed for manganese and cadmium, both referred to ion emission lines. In particular, Cd emission line was detected at 223.7 nm wavelength, and Mn emission line at 257.9 nm wavelength. These ion lines, in fact, allowed a better signal evaluation and consequently a better limit of detection.

Theoretically, this collecting procedure allows the measurement of any concentration of a given analyte by simply adapting the collection times to the related aerosol concentration. For this reason, filters with different surface concentrations of the analyte were sampled, and by performing LIBS measurements, the calibration curves were obtained. In Figure 51 a typical example of the calibration curve for manganese is shown, where the P/B is reported versus the surface concentration. While at low surface concentration, a linear trend can be detected, a loss in linearity is present above a certain surface concentration threshold, which is different for each element. This effect is due to self-absorption effect, which is particularly evident when comparing the calibration curves of lead and manganese. It is important to stress that the line emitted by manganese (Mn II 257.9 nm) results from the decay to the ground state, while the line emitted by lead (Pb I 406.2 nm) comes from a decay to a higher energy level, only slightly more than 1 eV. As described previously, the radiation emitted by a decay to the ground state exhibits a significant probability of being absorbed by resonance by another atom of the same species, while this probability decreases for radiation emitted from decays on other energy levels. This is confirmed in our measurements: for high surface concentrations, there is no evident filter or detector saturation on lead, while in the case of manganese this phenomenon starts already at $10 \mu\text{g}/\text{cm}^2$, with a loss in linearity between the mass of the analyte and the intensity of the emitted signal. In this case as well, the calibration lines for the different elements were calculated in the range of linearity between surface concentration and collected LIBS signal.

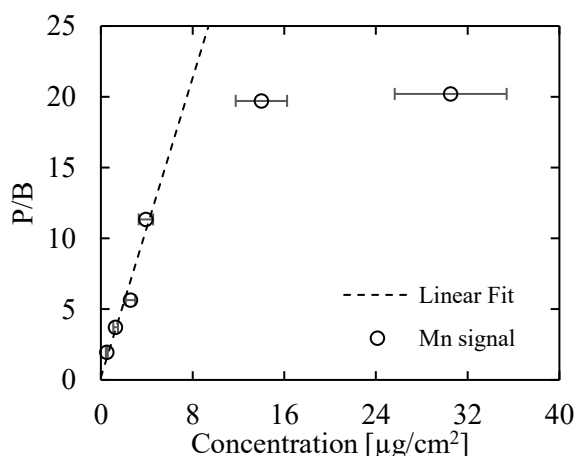


Figure 51. Self-absorption effect on Mn II 257.9 nm emission line.

In Figure 52-Figure 60 results obtained for Cu, Ni, Pb, Mn, Cr, Cd, Tl, Co and V are shown respectively. In particular, for each element the spectra are reported at each concentration on the left,

while on the right the corresponding calibration plot. These calibration curves are obtained by means of a linear fit, with 95% confidence area highlighted using two dotted lines.

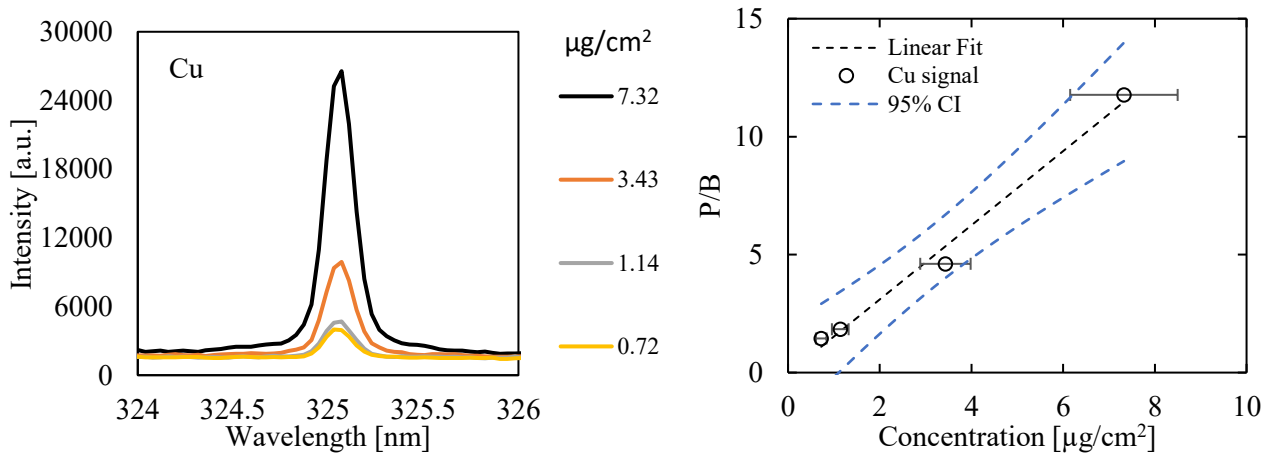


Figure 52. Left) Cu spectra emission line at different surface concentrations. Right) Linear fitting for deposited copper calibration curve parameters calculation and 95% confidence interval (CI).

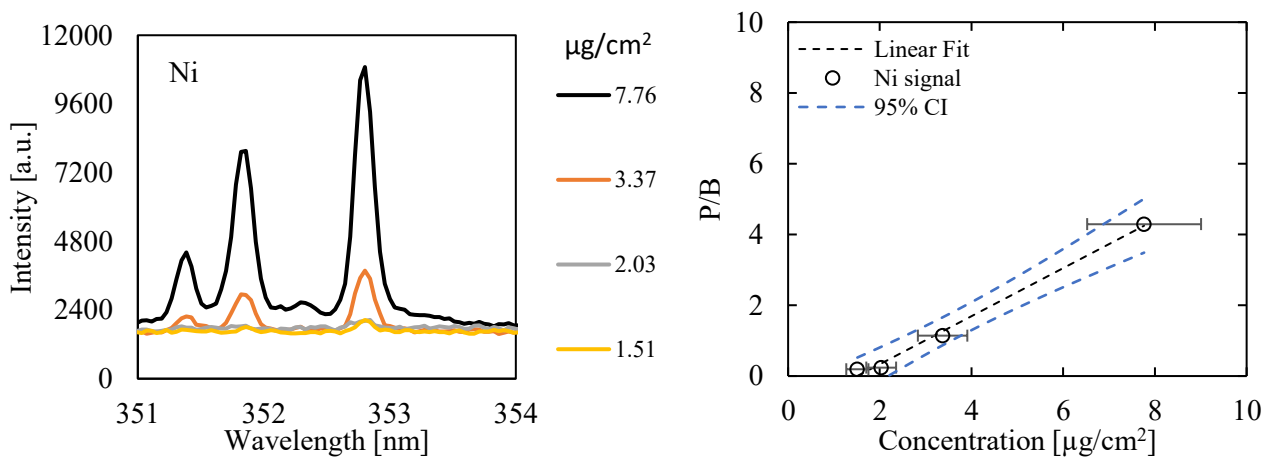


Figure 53. Left) Ni spectra emission line at different surface concentrations. Right) Linear fitting for deposited nickel calibration curve parameters calculation and 95% confidence interval (CI).

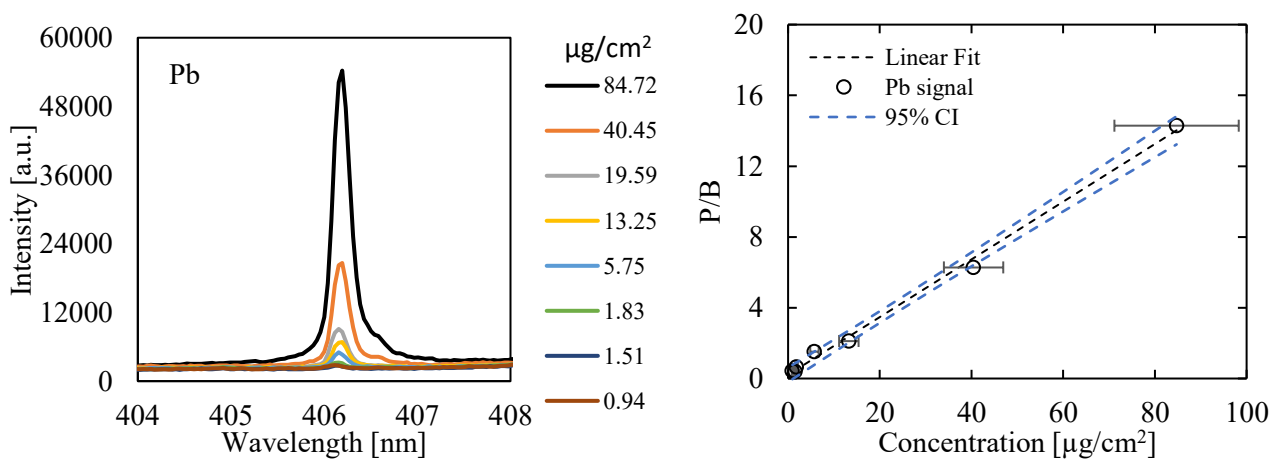


Figure 54. Left) Pb spectra emission line at different surface concentrations. Right) Linear fitting for deposited lead calibration curve parameters calculation and 95% confidence interval (CI).

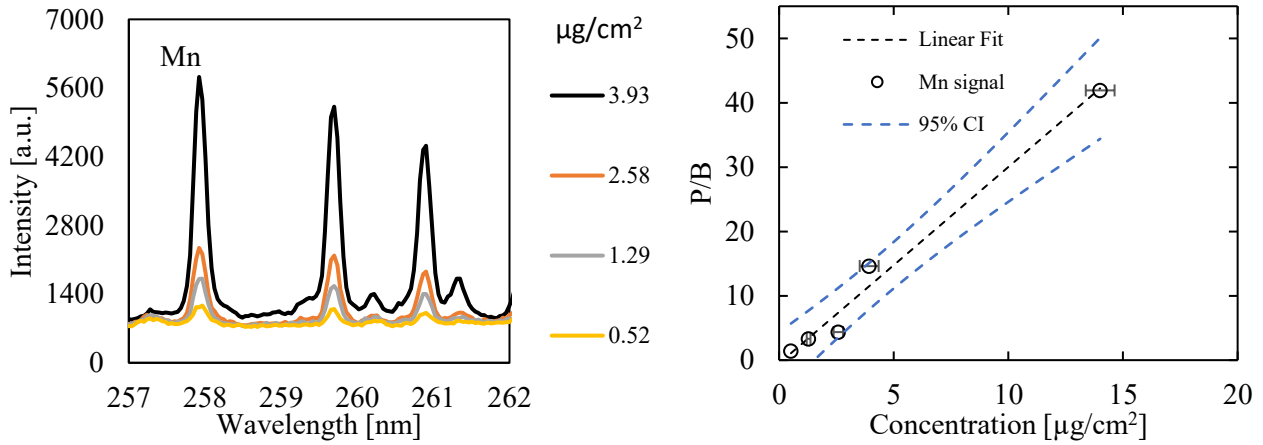


Figure 55. Left) Mn spectra emission line at different surface concentrations. Right) Linear fitting for deposited manganese calibration curve parameters calculation and 95% confidence interval (CI).

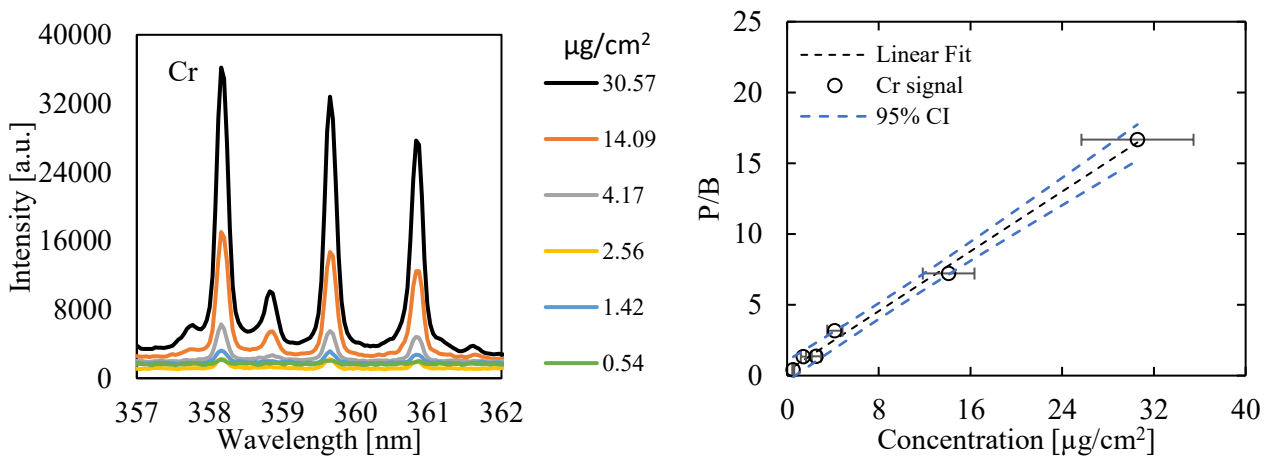


Figure 56. Left) Cr spectra emission line at different surface concentrations. Right) Linear fitting for deposited chromium calibration curve parameters calculation and 95% confidence interval (CI).

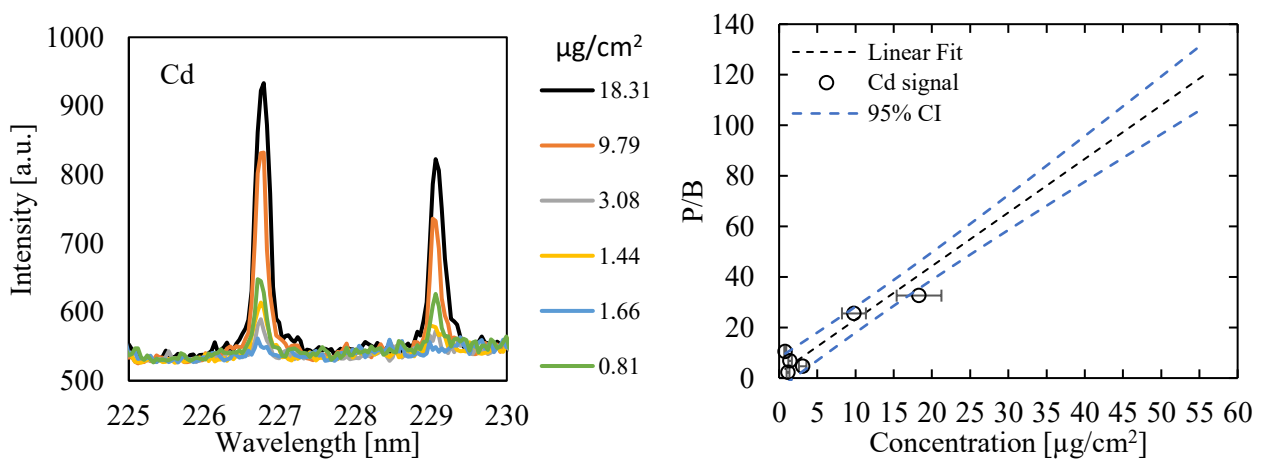


Figure 57. Left) Cd spectra emission line at different surface concentrations. Right) Linear fitting for deposited cadmium calibration curve parameters calculation and 95% confidence interval (CI).

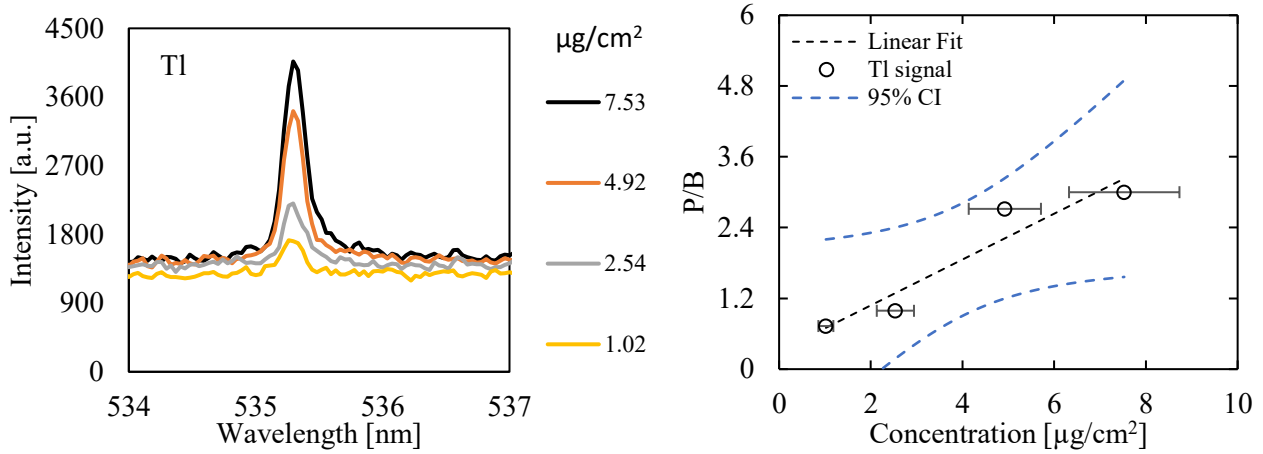


Figure 58. Left) Tl spectra emission line at different surface concentrations. Right) Linear fitting for deposited thallium calibration curve parameters calculation and 95% confidence interval (CI).

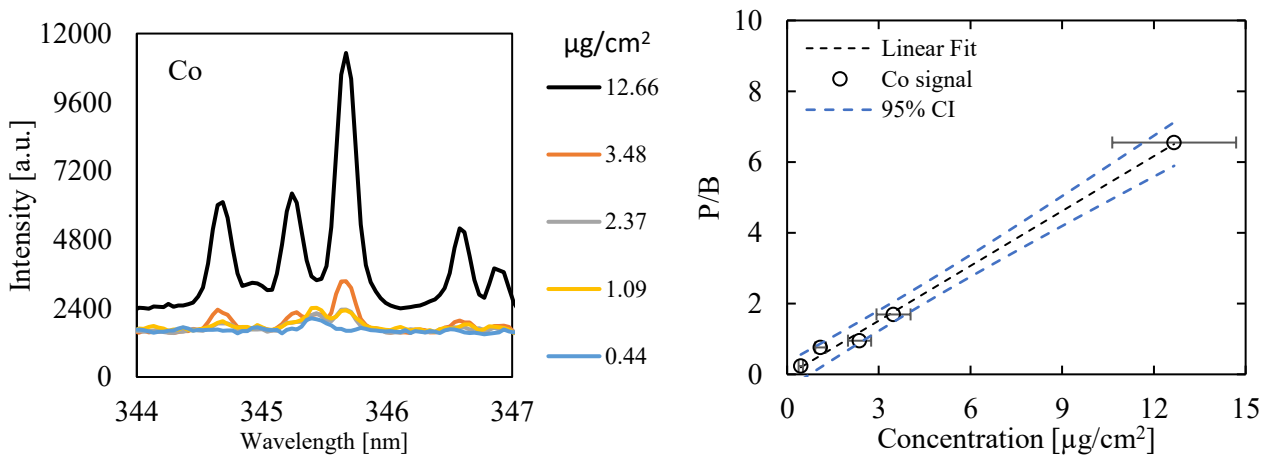


Figure 59. Left) Co spectra emission line at different surface concentrations. Right) Linear fitting for deposited cobalt calibration curve parameters calculation and 95% confidence interval (CI).

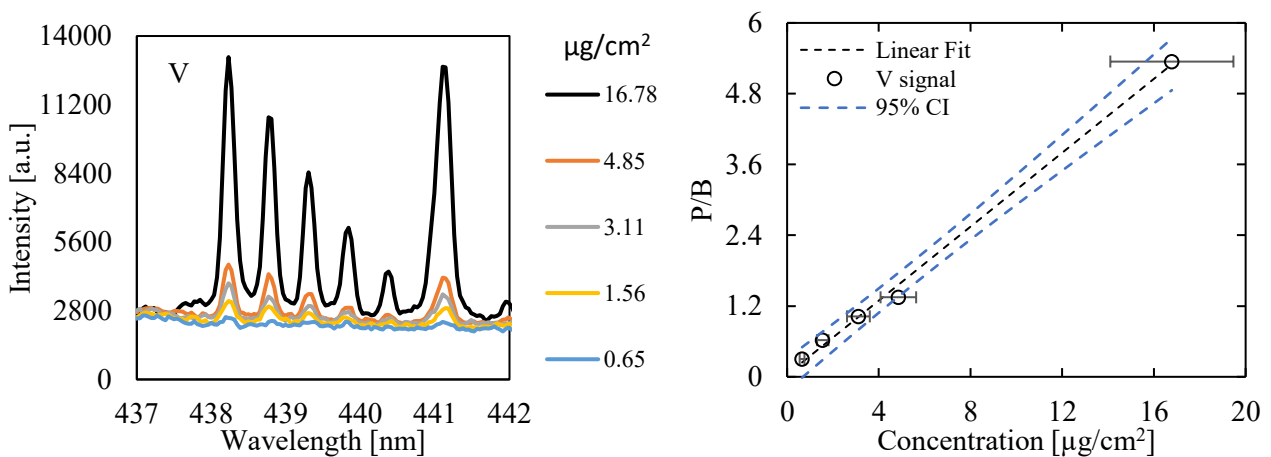


Figure 60. Left) V spectra emission line at different surface concentrations. Right) Linear fitting for deposited vanadium calibration curve parameters calculation and 95% confidence interval (CI).

No LIBS signal was detected for arsenic, which was instead reported for direct aerosol measurements. In fact, even at high concentrations and long deposition times, no emission signal was obtained. The problem is likely due to a combination of factors, including a weak instrumental response in that wavelength range and a weak sensitivity of the analyte to the LIBS technique.

Table 9 reports the parameters of the calibration curves obtained, slope and intercept, the R^2 as an index of the goodness of the fitting, and the calculated LODs.

Table 9. In the table are reported the fitting parameters of aerosol deposited on filter calibration curves: slope, intercept and R^2 ; and the calculated LODs.

Metal	Slope	Intercept	R^2	LOD [$\mu\text{g}/\text{cm}^2$]
Cu	1.93	0.86	0.99	0.05 ± 0.02
Ni	0.98	-1.35	0.99	0.9 ± 0.3
Pb	0.20	0.01	0.99	1.4 ± 0.5
Mn	2.64	0.17	0.92	1.6 ± 0.5
Cr	0.57	0.73	0.99	1.5 ± 0.5
Cd	0.89	6.33	0.69	4 ± 1.2
Tl	0.31	0.36	0.92	3.4 ± 1.1
Co	0.29	0.48	0.99	1.0 ± 0.3
As	-	-	-	
V	0.30	-0.20	0.99	1.0 ± 0.3

In order to relate the LODs obtained from direct and indirect measurements, a table of the minimum sampling time required to obtain the same analyte concentration on samples as the one corresponding to LODs in aerosol is shown in Table 10. In particular, these time values refer to a sampling flow rate of 1 L/min and a spot area of 0.07 cm^2 .

Table 10. Sampling time required to reach the surface concentration LODs, sampling aerosols at concentrations equal to air concentration LODs.

Metal	Cu	Ni	Pb	Mn	Cr	Cd	Tl	Co	V
Time [min]	0.3	3.3	2.7	7.1	10.6	5.9	34.3	7.9	3.5

Considering direct aerosol measurements obtained with 5000 acquisitions and working with a laser shot repetition rate of 10 Hz, it takes approximately 9 minutes for a single measurement. Therefore, in conditions of concentrations close to the LODs in air for elements such as Cr and Tl, a direct

measurement is convenient in terms of time, while for the others an indirect measurement is preferred. Obviously, in the case of higher concentrations, the collection times would be reduced for all elements. On the other hand, for air concentrations below the LODs obtained for direct measurements, it would be mandatory to perform samplings of longer duration than the times reported in Table 10, depending on the presumed concentration.

Considering as standard a sampling of 5 min at 1 l/min flow rate, the above superficial LODs span from 1 $\mu\text{g}/\text{m}^3$ for Cr to 48 for Cd $\mu\text{g}/\text{m}^3$. Comparing these values with literature [36,59,84,142], they are generally higher, this because a prevalent improvement of the instrument for direct on-line measurements, but these values can be lowered by extending the sampling time or increasing the sampling flow-rate.

6 CASE STUDY

In this chapter matrix effects study due to gas and / or concomitant presence of other elements/compounds in the probe volume is performed trying to highlight possible application for enhancing LIBS signals. Moreover, different case studies are presented aimed to underline the potential of the technique in different applications.

6.1 LIBS AND TXRF MEASUREMENTS COMPARISON (MULTIELEMENT)

It is important to stress that these analyses were performed with known elemental percentages. In this paragraph a direct comparison between LIBS and TXRF measurements were performed for calibration purposes.

Table 11. LIBS vs TXRF experimental parameters both varying the collection time (1st to 5th columns) and sampling repeating with a fixed time (6th to 10th columns): sampling time, element aerosol concentration, element ratio.

Time [min]	Conc. [$\mu\text{g}/\text{m}^3$]	Ratio [%]			Time [min]	Conc. [$\mu\text{g}/\text{m}^3$]	Ratio [%]			Element
		Calc.	LIBS	TXRF			Calc.	LIBS	TXRF	
	99	10	5	10		239	10	23	18	Cu
12	792	78	89	77	45	726	54	58	52	Pb
	124	12	6	13		370	28	18	29	Ni
	109	10	7	10		217	10	19	19	Cu
20	875	78	86	77	45	660	54	64	50	Pb
	137	12	7	13		336	28	18	31	Ni
	97	10	6	10		217	10	20	18	Cu
30	780	78	88	77	45	659	54	62	51	Pb
	122	12	7	13		335	28	18	30	Ni
	101	10	6	10		223	10	20	19	Cu
45	823	78	87	77	45	676	54	61	49	Pb
	129	12	7	13		344	28	19	32	Ni
						219	10	19	19	Cu
					45	664	54	62	48	Pb
						338	28	19	33	Ni

Using LIBS as a real-time monitoring technique, several filters were sampled and subsequently analysed by TXRF. In particular, relative concentrations of multi-element samples, namely copper,

nickel, and lead obtained with the two techniques were compared. Two different series of samplings were performed following the parameters reported in Table 11.

It is important to stress that these analyses were performed with known elemental percentages. In this paragraph a direct comparison between LIBS and TXRF measurements were performed for calibration purposes.

Table 11 are also shown in Figure 61 Figure 62, where different and the same acquisition time was used respectively. The relative quantities of elements measured by LIBS are within 10% of the calculated values, while the relative values obtained by TXRF are within 5%. Considering the relative nature of these measurements, since no absolute concentration value was associated with the signal obtained, these results highlight a fair calibration of the LIBS instrumentation. In fact, it was possible to assign the correct weight to each element signal to obtain relative quantities that are comparable to both the calculated values and the values obtained by TXRF.

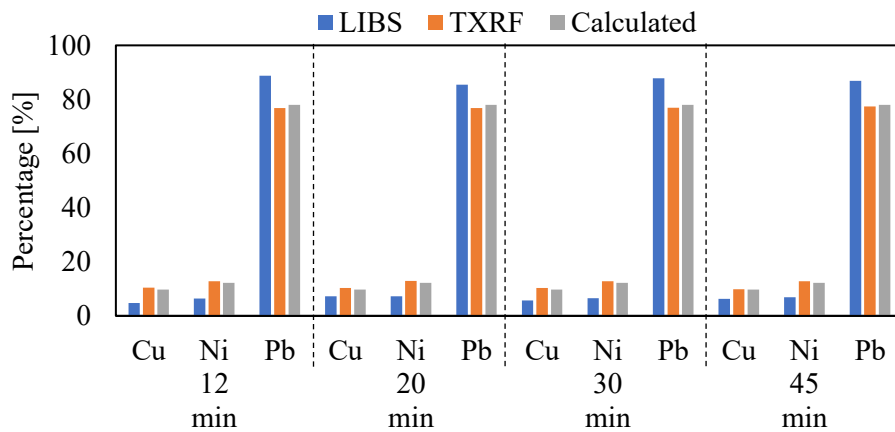


Figure 61. Relative quantities of Cu, Ni and Pb measured through LIBS and TXRF with different sampling times. All measurements are compared to the calculated values.

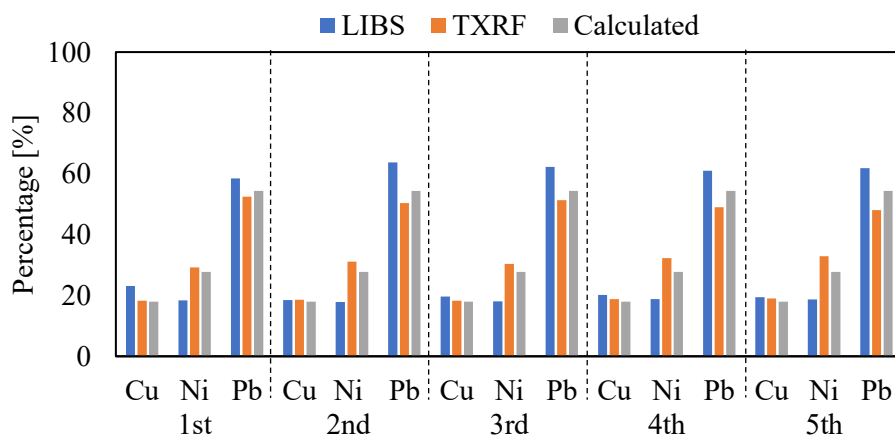


Figure 62. Relative quantities of Cu, Ni and Pb measured through LIBS and TXRF in 5 repeated measurements. All measurements are compared to the calculated values.

These results were presented at the conference PM2022 as a poster contribution.

6.2 BRAKE POWDER STUDY

LIBS measurements on real aerosol generated with brake wear powders were performed. To this purpose particulate matter was used collected on filters provided by TCR Tecora s.r.l. in collaboration with Istituto di Ricerche Farmacologiche Mario Negri-IRCCS which sampled break wear dust. In order to perform the analysis on aerosol, such powder was again resuspended in ultrapure distilled water using an ultrasonic bath to be further nebulized inside the LIBS analysis sampling circuit as described in Appendix A3.

A preliminary analysis on the aerosol produced is performed in order to investigate the size distribution of particles considered. To this purpose, an Optical Particles Counter (OPC) (Portable GRIMM Dust Monitor 1.107) is used, through which the particulate matter can be subdivided into 31 dimensional classes from 0.25 μm to 32 μm .

A copper oxide powder (CuO) was considered as particles dimension reference, consisting of particles with 3 μm maximum diameter. In Figure 63 the size distribution of these particles as well as the brakes powder are shown, revealing in both cases a bimodal distribution. In the case of CuO particles, particles diameter up to 3 μm are detected, with values approaching zero for the channels at 3.5 μm and 4 μm . On the contrary, for brakes powder a wider dimensional distribution compared to copper oxide is obtained. In fact, the second mode of the distribution is shifted towards higher particle size, up to 10 μm , this analysis reveals the ability of the system to aerosolize particles larger than 3 μm in diameter.

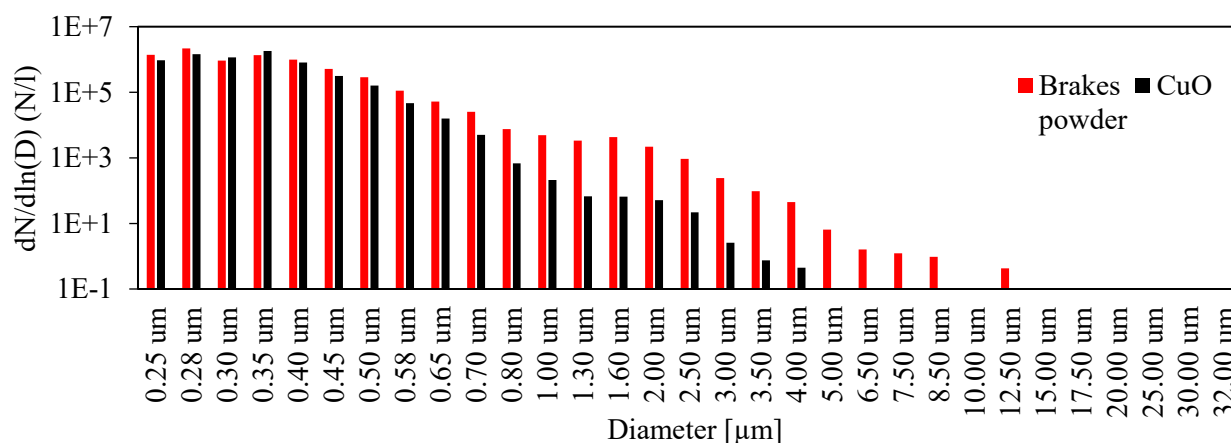


Figure 63. OPC particles size distribution.

In Figure 64 Scanning Electron Microscope (SEM) image of brake powder is reported, where it is possible to note the presence of particles with diameters greater than 5 μm , although in a smaller number than smaller particles. This is consistent with the low number of particles detected using OPC with diameters greater than 5 μm . These analyses confirm a good aerosolization of the powders without the risk of losing most of the powders before measurements.

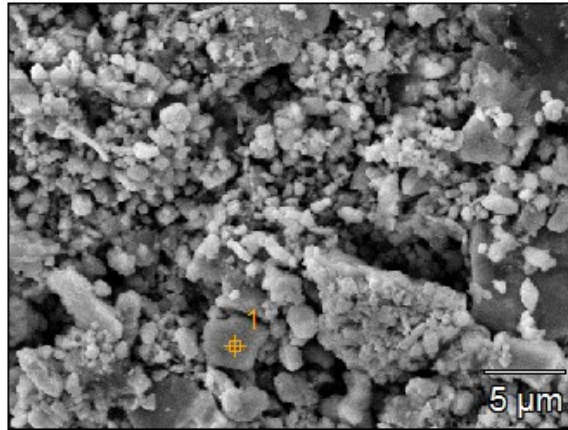


Figure 64. Deposited brake wear powder SEM acquired image (Image Resolution: 512 by 384; Image Pixel Size: 0.07 μm ; Acc. Voltage: 15.0 kV; Magnification: 3500).

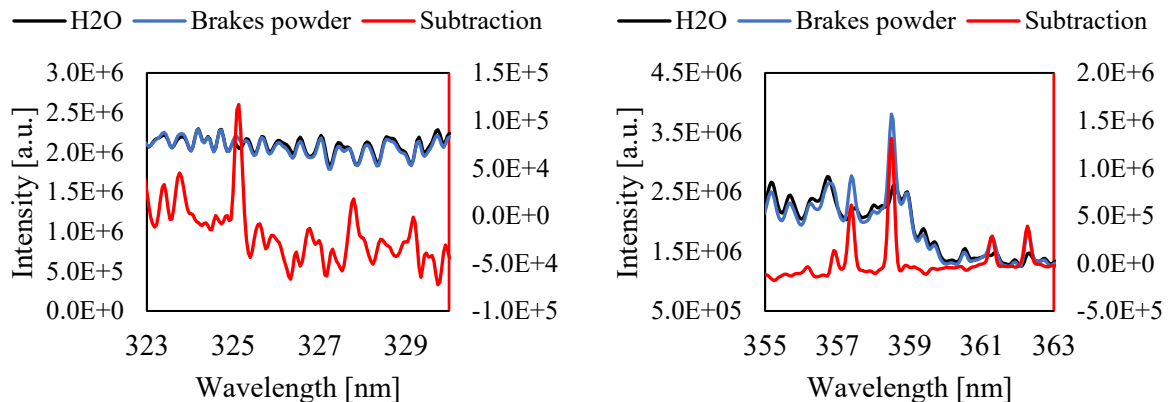
As a first analysis qualitative LIBS measurements were carried out in order to check the presence of the metals under regulation. A wide scan from 200 nm up to 500 nm was performed, subdividing the acquisition into 12 spectral windows of 25 nm wide each. For each acquisition 10000 spectra are accumulated. This qualitative analysis was performed in conjunction with Energy Dispersive X-Ray Spectroscopy (EDS) analysis on the same powders. In Table 12 the relative

Table 12

Table 12. Relative elemental mass detected on deposited brake wear powder thorough EDS analysis.

	O	Mg	Al	Si	Ca	Cr	Mn	Fe	Cu	Zn	Mo
Weight [%]	26.32	0.17	9.27	3.93	0.33	0.09	0.67	58.20	0.28	0.31	0.43

In this context, Cu, Cr and Mn are considered and the related emission lines are reported in Figure 65. While the emission lines of copper and the triplet of manganese are perfectly resolved, for chromium, interferences with very intense emission lines from iron are evident. All the other scanned regions are reported in appendix A4.



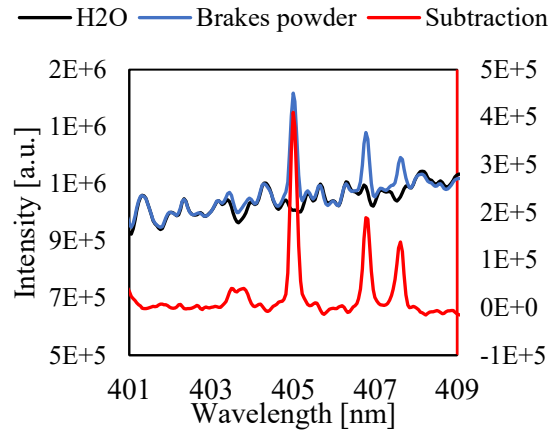


Figure 65. 10000 accumulated emission spectra of nebulised water for background analysis and subtraction purposes (black), of brakes powder (blue), and subtraction spectra (red). Regions of evaluation: Cu (top-left), Cr (top-right), Mn (bottom).

For the quantitative analysis, a series of 10000 single spectra for each region of interest were recorded at 30 μ s of delay time and with a gate width of 100 μ s. Then, the conditional analysis was applied on these series of spectra. Measurements at four different concentrations loadings were performed, one at “high concentration” and three at lower concentration, called “low concentration”, obtained diluting the original suspension. Moreover, considering Cr analysis, particular attention was given in the conditional analysis in order to avoid overestimation for the presence of high iron signals. In order to validate LIBS measurements, the aerosol measured directly with LIBS was sampled on quartz filters at the exit of the measurement chamber for subsequent analysis via ICP technique. In Figure 66 a direct comparison of the concentrations obtained with ICP and LIBS measurements is shown. In particular, we refer to the four measurements as F7, F11, F14 and F17, where F14 was the highest concentration measurement. The analysis of Cu concentration levels obtained with LIBS measurements points out the presence of low concentration for F7, F11 and F17 and a higher concentration for F14, which is in agreement with the sample preparation.

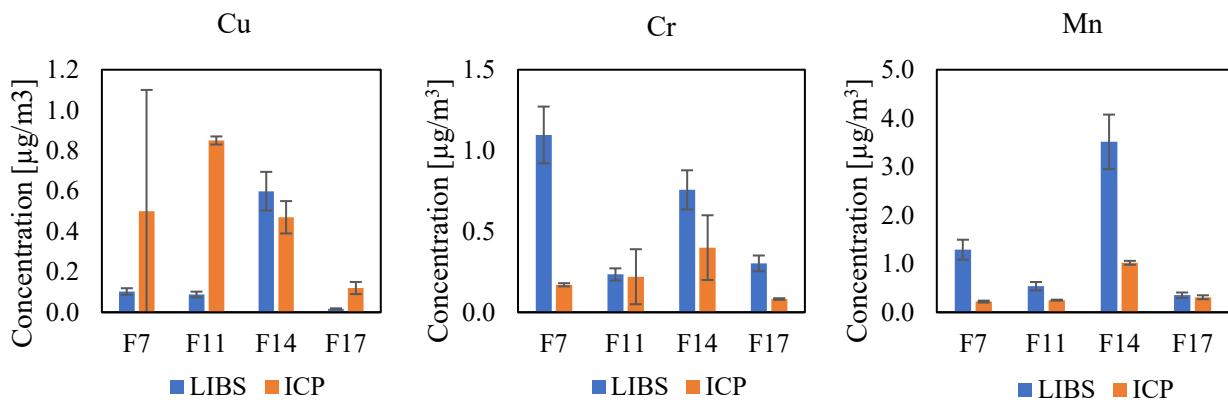


Figure 66. Aerosol concentrations results for Cu, Cr and Mn and relative errors, obtained with LIBS and ICP measurements.

There is not accordance with ICP results for F7 and F11, also due to a low sensitivity to Cu of the ICP instrumentation employed. Focusing on Cr and Mn results, for the measurements F11, F14 and F17 is highlighted the high concentration for F14 and the low concentration for the other two filters. The sample F7 was evaluated as low concentration by ICP while, especially for Cr, was higher in LIBS results. This anomaly can be due to the presence of a greater number of Fe spectra in F7, resulting in an overestimation of Cr. On the contrary, F7 for Mn in LIBS was measured at 280 nm despite the other measurements at 403 nm, and this led an interference with Mg, that was rejected from analysis but as for the Fe interference can lead to an overestimation of Mn emission line.

As a final remark, concentrations obtained with LIBS were expected to be slightly higher than those with ICP, because of a possible loss of particle along the path before reaching the filter and also due to the collection efficiency of the filter itself.

The data were presented to an International Conference (LIBS 2022) as a poster contribution, reported at the end of this thesis.

6.3 LIBS ANALYSIS ON FILTERED DEPOSIT ON SNOW

Indirect LIBS analysis on filters was implemented to analyse three quartz filters on which materials from snow superficial sediments, coming from the Cordillera Blanca in Perú, were collected. These sampled filters were provided by Stefania Gilardoni, CNR-ISP. In this context, the aim of this analysis is to evaluate the presence of iron in the powder collected. A preliminary qualitative analysis to verify the presence of this element was accompanied by a more detailed quantitative analysis after appropriate instrumental calibration. All the spectra, both for qualitative and quantitative measurements, are acquired using the laser in a configuration able to generate pulses of 23 mJ each, and the spectrometer set to register the signal with a delay time of 500 ns and a gate time of 100 ns, parameters chosen after some tests on quartz fibre filter analysis.

In Figure 67, a typical example of emission intensity of LIBS signal is reported, while in Figure 68 the theoretical spectrum computed with an on-line NIST tool is shown [143].

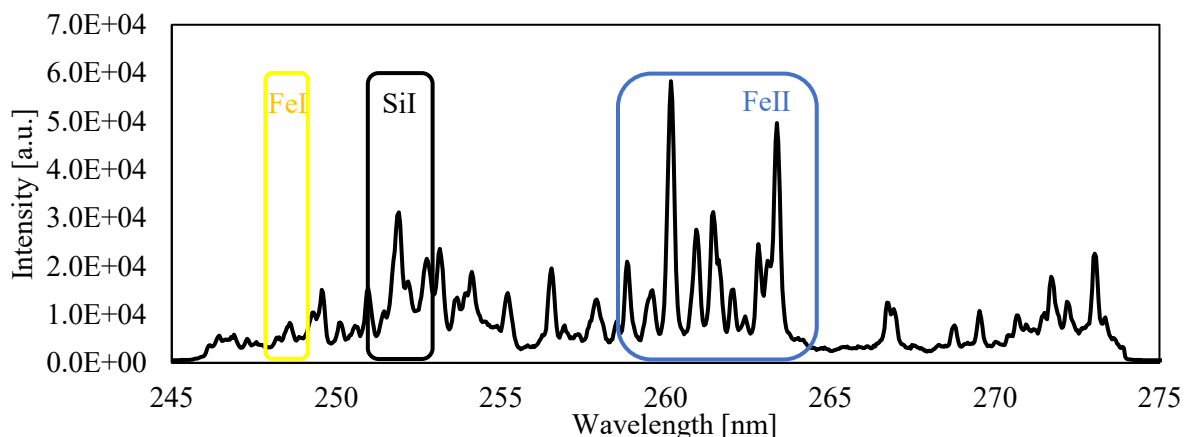


Figure 67. Single spectrum collected with a delay time of 500 ns and a gate aperture of 100 ns from the emission of a single laser pulse discharge operating at 23 mJ/pulse.

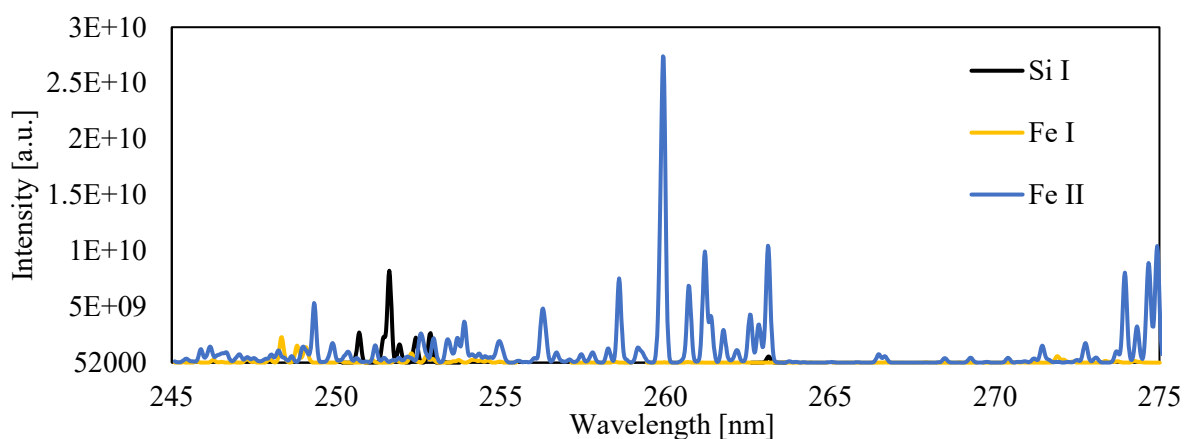


Figure 68. Theoretical emission spectrum composed by the emission lines of Si I, Fe I and Fe II calculated by means of the NIST LIBS database tool [143].

Comparing the two graphs reported in Figure 67, a single shot LIBS spectrum, and Figure 68, it is possible to establish the presence of iron from two groups of emission lines, which can be attributed prevalently to Fe II ion emission. The pattern of the 5 emission lines at wavelengths of 260.1 nm, 260.9 nm, 261.4 nm, 262.8 nm, and 263.3 nm are all attributable to Fe II, as are the lines at 256.5 nm, 258.8 nm, and 273.0 nm, and all these lines are present in both graphs, the experimental one and the theoretical one. Only the line at 248.5 nm is visible as an emission line from neutral Fe atoms. In addition, two emission lines from neutral silicon at 250.9 nm and 251.9 nm are also clearly visible, which are due to emission from the quartz filter matrix as well as the presence of natural sediments within the deposited powders. The presence of Si lines emitted by the filtering matrix proves of the ability of measure through the whole layer of deposited particles with a single laser shot without

saturation problems due to the particles amount. After the qualitative elemental identification, the second step was to construct a proper calibration curve in order to have a quantification of the iron deposited on the filter. For this reason, filters with six different surface concentrations have been employed. As reported in the graph displayed in Figure 69 a good linear relationship is highlighted at lower concentrations, up to $30 \mu\text{g}/\text{cm}^2$, corresponding P/B, reaching a value of 12. Using the obtained relationship is possible to evaluate the quantity of iron deposited onto the 3 filters (F1, F2 and F3).

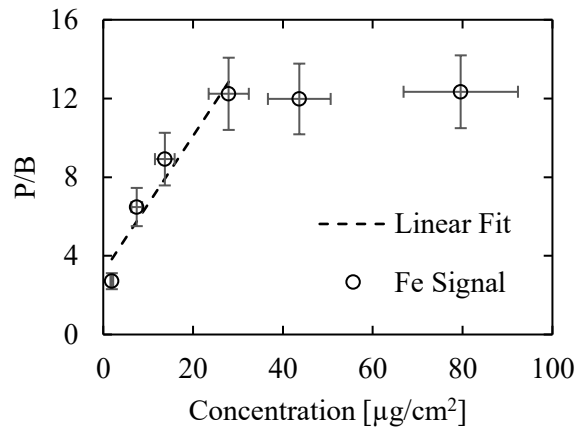


Figure 69. Calibration curve of Fe II emission line at 260.1 nm. It is clearly visible a linear relation between surface concentration and signal up to $30 \mu\text{g}/\text{cm}^2$, and then a plateau up to $80 \mu\text{g}/\text{cm}^2$, due to filter saturation.

As shown in the graphs of Figure 70, for each filter a representative spectrum has been obtained by averaging three spectra collected from LIBS measurements in three different points of each filter.

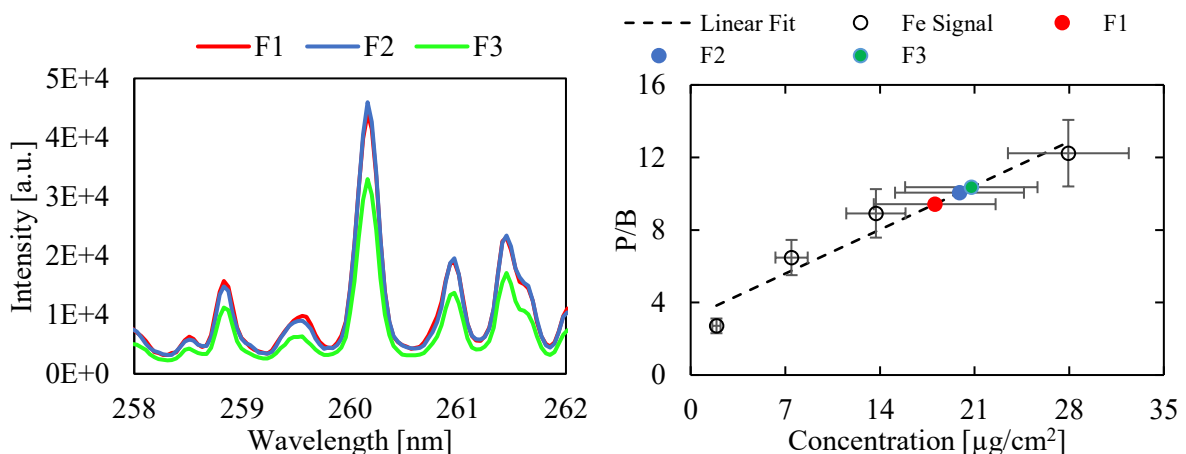


Figure 70: Left) Fe signal detected from the 3 filters (F1, F2 and F3), each spectrum is an average of 3 spectra collected from 3 different areas of the filter. Right) calculated surface concentration for F1, F2 and F3 by evaluating the signals with the calibration curve.

By using the calibration curves, concentration measurements are obtained, that are $18 \pm 5 \mu\text{g}/\text{m}^2$ for F1, $20 \pm 5 \mu\text{g}/\text{m}^2$ for F2, and $21 \pm 5 \mu\text{g}/\text{m}^2$ for F3. Here, the errors have been calculated by propagating the errors of the curve parameters. As highlighted from the left graph in Figure 70, the 3 signals are within the linear peak response, making possible the use of this calibration curve for the concentration evaluation.

7 CONCLUSIONS

The main goal of this PhD work has been the design and development of an instrumental prototype capable to perform real-time monitoring of heavy metal emissions at the chimney of industrial combustion systems/plants. In particular, the focus has been set on regulated heavy metals, namely Cu, Ni, Pb, Cr, Mn, Cd, Co, Tl, V, As and Sb with the aim of performing their simultaneous detection. To this purpose, the LIBS technique has been adopted, being this diagnostic tool very sensitive to metal detection and especially suitable for real-time monitoring since it does not require sample preparation. However, being the metals of interest dispersed in very low concentration in aerosol phase, effort has been spent in the optimization of the experimental condition, in particular the data collection and processing strategy, in order to increase the signal-to-noise ratio and thus reduce the detection limits. Moreover, the experimental apparatus has been designed to be compact and robust for effortless employment in field campaigns other than for being more versatile, thus suitable for different applications.

The resulting prototype has been properly calibrated for each heavy metal, in the $\mu\text{g}/\text{m}^3$ concentration range, individually. Thus, the corresponding limit of detection has been retrieved, resulting to be lower than the LOD values reported in the literature for metals measurements in aerosol. Therefore, this prototype can be considered a valuable asset in atmospheric heavy metal monitoring.

The complexity of the aerosol samples (different types of particles + gases) also required a fundamental study concerning the effect of a specific matrix on the LIBS signal evaluation. According to the matrix nature (particle vs gases) different effects has been observed, which can be summarized as follows:

- the concomitant presence of other elements in the probe volume generally produces a LIBS peak intensity enhancement;
- the entity of the enhancement strictly depends on the element loading and the chemical-physical properties of all the species in the probe volume.
- the effects of gas addition on LIBS signal is mostly related to the thermal conductivity of the species considered;
- He addition promotes a rapid plasma expansion and cooling, resulting in a reduction in the signal background;
- Ar tends to limit the expansion of the plasma and to maintain higher temperatures causing a global increasing of the emission signal.

- in general, the effect of the concomitant mass present in the probe volume is independent from the effect of the gas matrix and actually, the two contributions can be added to improve the peak intensity.

Therefore, if experimentally feasible, an environment with a controlled atmosphere of He and Ar or the addition of a known element in the probe volume can be used to increase the LIBS emission signal of the metal of interest, especially for those elements with a relatively high detection limit.

Another option for reducing the limit of detection is to accumulate the aerosol particles on a filter and then perform LIBS measurements on the particle-loaded filter. This approach has been also tested in the present PhD work and it required a modification of the prototype design to accommodate the particle-loaded filter in the probe volume as well as a new optimization of the data collection procedure (laser fluence, detection gate and width) and analysis. For sampling time of the order of a few-minutes, which make these measurements comparable with the ones in the aerosol phase, the LOD obtained on particles-loaded filters are slightly higher than the corresponding values reported in the literature but generally lower than LODs obtained in aerosol. However, the LOD of metal-loaded filters via LIBS can still be improved by properly tuning the sampling time or the sampling flow rate and can be considered a valuable alternative to aerosol measurements for all those elements which are present in very low concentration in the aerosol phase.

To emphasize the potentiality of the technique, LIBS analysis on specific applications are also performed, as for example on brake powder in aerosol.

To conclude, it is worth underling that the application of LIBS technique for heavy metals detection and concentration measurements in aerosol is a valuable and suitable tool for the analysis at the chimney of industrial combustion plants. However, such application in aerosol is still challenging to be performed for air quality monitoring. The employment of the analysis on particle-loaded filter (obtained with relatively short-time collection) as tested in this work has proved to overcome in part this limitation for real time monitoring.

BIBLIOGRAPHY

- [1] I. Colbeck, M. Lazaridis, *Aerosol Science: Technology and Applications*, John Wiley & Sons Inc, 2014. <https://onlinelibrary.wiley.com/doi/book/10.1002/9781118682555>.
- [2] O. Boucher, D. Randall, P. Artaxo, C. Bretherton, G. Feingold, P. Forster, V.-M. Kerminen, Y. Kondo, H. Liao, U. Lohmann, P. Rasch, S.K. Satheesh, S. Sherwood, B. Stevens, X.Y. Zhang, Clouds and Aerosols, in: T.F. Stocker, D. Qin, G.-K. Plattner, M. Tignor, S.K. Allen, J. Boschung, A. Nauels, Y. Xia, V. Bex, P.M. Midgley (Eds.), *Clim. Chang. 2013 Phys. Sci. Basis. Contrib. Work. Gr. I to Fifth Assess. Rep. Intergov. Panel Clim. Chang.*, Cambridge University Press, Cambridge, United Kingdom and New York, NY, USA, 2013: pp. 571–657. https://www.ipcc.ch/site/assets/uploads/2018/02/WG1AR5_Chapter07_FINAL-1.pdf.
- [3] WHO global air quality guidelines: particulate matter (PM_{2.5} and PM₁₀), ozone, nitrogen dioxide, sulfur dioxide and carbon monoxide, 2021.
- [4] European Parliament; European Council, Directive 2008/50/EC on ambient air quality and cleaner air for Europe, *Off. J. Eur. Communities*. 152 (2008).
- [5] EU, Directive 2004/107/EC of the European Parliament and of the Council of 15/12/2004 relating to arsenic, cadmium, mercury, nickel and polycyclic aromatic hydrocarbons in ambient air, *Off. J. Eur. Union*. L 23 (2004).
- [6] U.S. Environmental Protection Agency, U.S. Environmental Protection Agency, (n.d.). <https://www.epa.gov/environmental-topics/air-topics>.
- [7] D.C. Chalupa, P.E. Morrow, G. Oberdörster, M.J. Utell, M.W. Frampton, Ultrafine particle deposition in subjects with asthma, *Environ. Health Perspect.* 112 (2004) 879–882. <https://doi.org/10.1289/ehp.6851>.
- [8] E. Taurino, A. Bernetti, A. Caputo, M. Cordella, R. De Lauretis, I. D’Elia, E. Di Cristofaro, A. Gagna, B. Gonella, F. Moricci, E. Peschi, D. Romano, M. Vitullo, *Italian Emission Inventory 1990 - 2018*, 2020.
- [9] J. Briffa, E. Sinagra, R. Blundell, Heavy metal pollution in the environment and their toxicological effects on humans, *Heliyon*. 6 (2020). <https://doi.org/10.1016/j.heliyon.2020.e04691>.
- [10] Regione Lombardia, *Da rifiuti a risorsa con “FANGHI”, grazie a tecnologie e riutilizzi innovativi*, (n.d.).

<https://www.openinnovation.regione.lombardia.it/it/b/635/darifiutiarisorsaconfanghigrazieatecnologieeriutilizziinnovativi>.

- [11] L. Järup, Hazards of heavy metal contamination, *Br. Med. Bull.* 68 (2003) 167–182.
<https://doi.org/10.1093/bmb/ldg032>.
- [12] European Standards, EN 14385:2004 Stationary source emissions. Determination of the total emission of As, Cd, Cr, Co, Cu, Mn, Ni, Pb, Sb, TI and V, (2004). <https://www.en-standard.eu/bs-en-14385-2004-stationary-source-emissions-determination-of-the-total-emission-of-as-cd-cr-co-cu-mn-ni-pb-sb-ti-and-v/>.
- [13] U.S. Environmental Protection Agency, PERFORMANCE SPECIFICATIONS FOR MULTI-METALS CEMS PERFORMANCE SPECIFICATION 10, (1996).
<https://www.epa.gov/emc/emc-performance-specifications>.
- [14] J.A. Cooper, K. Petterson, B.E. Johnsen, C.A. Yanca, M. Nakanishi, D. Barth, Performance Specification YY: Specifications and Test Procedures for X-Ray Fluorescence Based Multi-Metals Continuous Emission Monitoring Systems at Stationary Sources, (2005).
<https://www3.epa.gov/ttnemc01/prelim/otm16.pdf>.
- [15] U.S. Environmental Protection Agency, Method 29 - Metals Emissions from Stationary Sources, (2017). <https://www.epa.gov/emc/method-29-metals-emissions-stationary-sources>.
- [16] K.F. Kapiamba, W. Hao, S. Adom, W. Liu, Y.W. Huang, Y. Wang, Examining Metal Contents in Primary and Secondhand Aerosols Released by Electronic Cigarettes, *Chem. Res. Toxicol.* 35 (2022) 954–962. <https://doi.org/10.1021/acs.chemrestox.1c00411>.
- [17] A. Kashani, J. Mostaghimi, Aerosol characterization of concentric pneumatic nebulizer used in inductively coupled plasma-mass spectrometry(ICP-MS), *At. Sprays.* 20 (2010).
<https://doi.org/10.1615/AtomizSpr.v20.i5.40>.
- [18] S.E. Maestre, J.L. Todolí, J.M. Mermet, Evaluation of several pneumatic micronebulizers with different designs for use in ICP-AES and ICP-MS. Future directions for further improvement, *Anal. Bioanal. Chem.* 379 (2004). <https://doi.org/10.1007/s00216-004-2664-4>.
- [19] A. Zettner, Principles and Applications of Atomic Absorption Spectroscopy, in: H. Sobotka, C.P.B.T.-A. in C.C. Stewart (Eds.), Elsevier, 1964: pp. 1–62.
[https://doi.org/https://doi.org/10.1016/S0065-2423\(08\)60372-8](https://doi.org/https://doi.org/10.1016/S0065-2423(08)60372-8).
- [20] T. Okumura, Inductively Coupled Plasma Sources and Applications, *Phys. Res. Int.* 2010

(2010) 164249. <https://doi.org/10.1155/2010/164249>.

- [21] A. Goncalves, J.R. Domínguez, J. Alvarado, Determination of Pd, Pt and Rh in vehicles escape fumes by GF-AAS and ICP-OES, *Talanta*. 75 (2008).
<https://doi.org/10.1016/j.talanta.2007.11.055>.
- [22] C.F. Wang, J.Y. Yang, C.H. Ke, Multi-element analysis of airborne particulate matter by various spectrometric methods after microwave digestion, *Anal. Chim. Acta*. 320 (1996).
[https://doi.org/10.1016/0003-2670\(95\)00534-X](https://doi.org/10.1016/0003-2670(95)00534-X).
- [23] S. Yatkin, M. Gerboles, A. Borowiak, Corrigendum to “Evaluation of standardless EDXRF analysis for the determination of elements on PM10 loaded filters” [*Atmos. Environ.* 54 (2012) 568-582], *Atmos. Environ.* 77 (2013).
<https://doi.org/10.1016/j.atmosenv.2013.06.049>.
- [24] R.J.C. Brown, K.E. Jarvis, B.A. Disch, S.L. Goddard, E. Adriaenssens, N. Claeys, Comparison of ED-XRF and LA-ICP-MS with the European reference method of acid digestion-ICP-MS for the measurement of metals in ambient particulate matter, *Accredit. Qual. Assur.* 15 (2010). <https://doi.org/10.1007/s00769-010-0668-7>.
- [25] J. Niu, P.E. Rasmussen, A. Wheeler, R. Williams, M. Chénier, Evaluation of airborne particulate matter and metals data in personal, indoor and outdoor environments using ED-XRF and ICP-MS and co-located duplicate samples, *Atmos. Environ.* 44 (2010).
<https://doi.org/10.1016/j.atmosenv.2009.10.009>.
- [26] Y. Kayser, J. Osán, P. Hönicke, B. Beckhoff, Reliable compositional analysis of airborne particulate matter beyond the quantification limits of total reflection X-ray fluorescence, *Anal. Chim. Acta*. 1192 (2022). <https://doi.org/10.1016/j.aca.2021.339367>.
- [27] K. Wadinga Fomba, N. Deabji, S. El Islam Barcha, I. Ouchen, E. Mehdi Elbaramoussi, R. Cherkaoui El Moursli, M. Harnafi, S. El Hajjaji, A. Mellouki, H. Herrmann, Application of TXRF in monitoring trace metals in particulate matter and cloud water, *Atmos. Meas. Tech.* 13 (2020). <https://doi.org/10.5194/amt-13-4773-2020>.
- [28] K.J. Hay, V.M. Boddu, B.E. Johnsen, J.A. Cooper, X-Ray Fluorescence-Based Multi-Metal Continuous Emission Monitor, (2005) 126.
- [29] R. Noll, C. Fricke-Begemann, S. Connemann, C. Meinhardt, V. Sturm, LIBS analyses for industrial applications-an overview of developments from 2014 to 2018, *J. Anal. At. Spectrom.* 33 (2018) 945–956. <https://doi.org/10.1039/c8ja00076j>.

- [30] L. Radziemski, D. Cremers, A brief history of laser-induced breakdown spectroscopy: From the concept of atoms to LIBS 2012, *Spectrochim. Acta - Part B At. Spectrosc.* 87 (2013) 3–10. <https://doi.org/10.1016/j.sab.2013.05.013>.
- [31] C. Duan, J. Li, Y. Zhang, K. Ding, X. Geng, Y. Guan, Portable instruments for on-site analysis of environmental samples, *TrAC - Trends Anal. Chem.* 154 (2022). <https://doi.org/10.1016/j.trac.2022.116653>.
- [32] R.T. Wainner, N.F. Aubut, K. Galbally-Kinney, M. Aviram, D. Gamliel, J. Grimble, M.B. Frish, S.-J. Chen, Portable LIBS for field analysis of trace metals in fuels, (2023) 29. <https://doi.org/10.1117/12.2663611>.
- [33] R.P. McLaughlin, G.S. Mason, A.L. Miller, C.B. Stipe, J.D. Kearns, M.W. Prier, J.D. Rarick, Note: A portable laser induced breakdown spectroscopy instrument for rapid sampling and analysis of silicon-containing aerosols, *Rev. Sci. Instrum.* 87 (2016). <https://doi.org/10.1063/1.4949506>.
- [34] J. Sipich, C. L'Orange, J. Volckens, A. Yalin, In-Situ Elemental Composition Analysis of Large Inhalable Aerosol Using Laser Induced Breakdown Spectroscopy, *Appl. Spectrosc.* 77 (2023) 261–269. <https://doi.org/10.1177/00037028221146804>.
- [35] G. Kim, K. Kim, H. Maeng, H. Lee, K. Park, Development of aerosol-LIBS (Laser induced breakdown spectroscopy) for real-time monitoring of process-induced particles, *Aerosol Air Qual. Res.* 19 (2019) 455–460. <https://doi.org/10.4209/aaqr.2018.08.0312>.
- [36] P. Diwakar, P. Kulkarni, M.E. Birch, New approach for near-real-time measurement of elemental composition of aerosol using laser-induced breakdown spectroscopy, *Aerosol Sci. Technol.* 46 (2012) 316–332. <https://doi.org/10.1080/02786826.2011.625059>.
- [37] D. Cremers, L. Radziemski, *Handbook of Laser-Induced*, 2013.
- [38] F.J. Fortes, J. Moros, P. Lucena, L.M. Cabalín, J.J. Laserna, Laser-induced breakdown spectroscopy, *Anal. Chem.* 85 (2013) 640–669. <https://doi.org/10.1021/ac303220r>.
- [39] L.J. Radziemski, From LASER to LIBS, the path of technology development, *Spectrochim. Acta - Part B At. Spectrosc.* 57 (2002) 1109–1113. [https://doi.org/10.1016/S0584-8547\(02\)00052-6](https://doi.org/10.1016/S0584-8547(02)00052-6).
- [40] V. Palleschi, Forty Years of Laser-Induced Breakdown Spectroscopy and Laser and Particle Beams, *Laser Part. Beams.* 2023 (2023) 2502152. <https://doi.org/10.1155/2023/2502152>.

- [41] A.L. Schawlow, C.H. Townes, Infrared and optical masers, *Phys. Rev.* 112 (1958) 1940–1949. <https://doi.org/10.1103/PhysRev.112.1940>.
- [42] T.H. Maiman, © 1960 Nature Publishing Group, *Nature*. 187 (1960) 493–494.
- [43] T.H. Maiman, Optical and microwave-optical experiments in ruby, *Phys. Rev. Lett.* 4 (1960) 564–566. <https://doi.org/10.1103/PhysRevLett.4.564>.
- [44] Maker P.D., Terhune R.W., Study of Optical Effects Due to an Induced Polarization Third Order in the Electric Field Strength, *Phys. Rev.* 137 (1965).
- [45] J.P. Singh, S.N. Thakur, LASER-INDUCED BREAKDOWN SPECTROSCOPY (Second Edition), Second, Susan Dennis, 2020.
- [46] S. Yoon, H.-W. Choi, J. Kim, Analysis of Changes in Spectral Signal According to Gas Flow Rate in Laser-Induced Breakdown Spectroscopy, *Appl. Sci.* 11 (2021). <https://doi.org/10.3390/app11199046>.
- [47] R. Noll, *Laser-Induced Breakdown Spectroscopy*, 2012.
- [48] N. El Sherbiny, O. Aied Nassef, Wavelength dependence of laser induced breakdown spectroscopy (LIBS) on questioned document investigation, *Sci. Justice.* 55 (2015) 254–263. <https://doi.org/10.1016/j.scijus.2015.02.002>.
- [49] J.H. Choi, Y. Moon, S.H. Lee, J.H. In, S. Jeong, Wavelength dependence of the ablation characteristics of Cu (In, Ga) Se₂ solar cell films and its effects on laser induced breakdown spectroscopy analysis, *Int. J. Precis. Eng. Manuf. - Green Technol.* 3 (2016) 167–171. <https://doi.org/10.1007/s40684-016-0021-7>.
- [50] X. Li, Z. Wang, Y. Fu, Z. Li, W. Ni, Wavelength dependence in the analysis of carbon content in coal by nanosecond 266 nm and 1064 nm laser induced breakdown spectroscopy, *Plasma Sci. Technol.* 17 (2015) 621–624. <https://doi.org/10.1088/1009-0630/17/8/02>.
- [51] J. Ashkenazy, R. Kipper, M. Caner, Spectroscopic measurements of electron density of capillary plasma based on Stark broadening of hydrogen lines, *Phys. Rev. Lett.* 43 (1991) 5568–5574. <https://doi.org/https://doi.org/10.1103/PhysRevA.43.5568>.
- [52] H. Griem, *Spectral Line Broadening by Plasmas*, 1st ed., 1974.
- [53] R.W.P. McWhirter, *Plasma Diagnostic Techniques*, in: R.H. Huddleston, S.L. Leonard (Eds.), Academic Press, New York, 1965: pp. 201–264.

- [54] G. Cristoforetti, A. De Giacomo, M. Dell’Aglia, S. Legnaioli, E. Tognoni, V. Palleschi, N. Omenetto, Local Thermodynamic Equilibrium in Laser-Induced Breakdown Spectroscopy: Beyond the McWhirter criterion, *Spectrochim. Acta - Part B At. Spectrosc.* 65 (2010) 86–95. <https://doi.org/10.1016/j.sab.2009.11.005>.
- [55] National Institute of Standards and Technology, NIST Atomic Spectra Database - Lines Holdings, (n.d.). https://physics.nist.gov/cgi-bin/ASD/lines_pt.pl.
- [56] E. Grifoni, S. Legnaioli, G. Lorenzetti, S. Pagnotta, F. Poggialini, V. Palleschi, From Calibration-Free to Fundamental Parameters Analysis: A comparison of three recently proposed approaches, *Spectrochim. Acta Part B At. Spectrosc.* 124 (2016) 40–46. <https://doi.org/10.1016/J.SAB.2016.08.022>.
- [57] E. Tognoni, G. Cristoforetti, S. Legnaioli, V. Palleschi, Calibration-Free Laser-Induced Breakdown Spectroscopy: State of the art, *Spectrochim. Acta Part B At. Spectrosc.* 65 (2010) 1–14. <https://doi.org/10.1016/J.SAB.2009.11.006>.
- [58] Z. Hu, D. Zhang, W. Wang, F. Chen, Y. Xu, J. Nie, Y. Chu, L. Guo, A review of calibration-free laser-induced breakdown spectroscopy, *TrAC Trends Anal. Chem.* 152 (2022) 116618. <https://doi.org/10.1016/J.TRAC.2022.116618>.
- [59] G. Gallou, J.B. Sirven, G. Gallou, C. Dutouquet, O. Le Bihan, E. Frejafon, Aerosols analysis by libs for monitoring of air pollution by industrial sources, *Aerosol Sci. Technol.* 45 (2011) 918–926. <https://doi.org/10.1080/02786826.2011.566899>.
- [60] C. Dutouquet, G. Gallou, O. Le Bihan, J.B. Sirven, A. Dermigny, B. Torralba, E. Frejafon, Monitoring of heavy metal particle emission in the exhaust duct of a foundry using LIBS, *Talanta.* 127 (2014) 75–81. <https://doi.org/10.1016/j.talanta.2014.03.063>.
- [61] D. Girón, T. Delgado, J. Ruiz, L.M. Cabalín, J.J. Laserna, In-situ monitoring and characterization of airborne solid particles in the hostile environment of a steel industry using stand-off LIBS, *Meas. J. Int. Meas. Confed.* 115 (2018) 1–10. <https://doi.org/10.1016/j.measurement.2017.09.046>.
- [62] S. V Zakharchenko, L.P. Semenov, A.M. Skripkin, Low-threshold optical discharge in a disperse aerosol medium, *Sov. J. Quantum Electron.* 14 (1984) 1642–1645. <https://doi.org/10.1070/qe1984v014n12abeh006244>.
- [63] I Yu Borets-Pervak, V S Vorob’ev, Threshold for gas breakdown initiated by an interaction of laser light with aerosol particles, *Quantum Electron.* 23 (1993) 224.

<https://doi.org/10.1070/QE1993v023n03ABEH002980>.

- [64] D.E. Lencioni, Laser-induced air breakdown for 1.06- μm radiation, *Appl. Phys. Lett.* 25 (1974) 15–17. <https://doi.org/10.1063/1.1655259>.
- [65] D.E. Lencioni, L.C. Pettingill, The dynamics of air breakdown initiated by a particle in a laser beam, *J. Appl. Phys.* 48 (1977) 1848–1851. <https://doi.org/10.1063/1.323937>.
- [66] D.E. Poulain, D.R. Alexander, J.P. Barton, S.A. Schaub, J. Zhang, Interactions of intense ultraviolet laser radiation with solid aerosols, *J. Appl. Phys.* 67 (1990) 2283–2288. <https://doi.org/10.1063/1.345522>.
- [67] D.C. Smith, R.T. Brown, Aerosol-induced air breakdown with CO₂ laser radiation, *J. Appl. Phys.* 46 (1975) 1146–1154. <https://doi.org/10.1063/1.322215>.
- [68] D.C. Smith, Laser Radiation-Induced Air Breakdown And Plasma Shielding, *Opt. Eng.* 20 (1981) 206962. <https://doi.org/10.1117/12.7972843>.
- [69] J.E. Lowder, H. Kleiman, Long-pulse breakdown with 10.6- μm laser radiation, *J. Appl. Phys.* 44 (1973) 5504–5505. <https://doi.org/10.1063/1.1662185>.
- [70] C L M Ireland, C Grey Morgan, Gas breakdown by a short laser pulse, *J. Phys. D. Appl. Phys.* 6 (1973) 720. <https://doi.org/10.1088/0022-3727/6/6/314>.
- [71] X. Zhang, Y. Deguchi, Z. Wang, J. Yan, J. Liu, Sensitive detection of iodine by low pressure and short pulse laser-induced breakdown spectroscopy (LIBS), *J. Anal. At. Spectrom.* 29 (2014) 1082–1089. <https://doi.org/10.1039/C4JA00044G>.
- [72] J.E. Carranza, E. Gibb, B.W. Smith, D.W. Hahn, J.D. Winefordner, Comparison of nonintensified and intensified CCD detectors for laser-induced breakdown spectroscopy, *Appl. Opt.* 42 (2003) 6016–6021. <https://doi.org/10.1364/AO.42.006016>.
- [73] E. Vors, L. Salmon, Laser-induced breakdown spectroscopy (LIBS) for carbon single shot analysis of micrometer-sized particles, *Anal. Bioanal. Chem.* 385 (2006) 281–286. <https://doi.org/10.1007/s00216-006-0320-x>.
- [74] D.A. Cremers, L.J. Radziemski, Direct Detection of Beryllium on Filters Using the Laser Spark, *Appl. Spectrosc.* 39 (1985) 57–63. <https://doi.org/10.1366/0003702854249349>.
- [75] J.E. Carranza, D.W. Hahn, Assessment of the upper particle size limit for quantitative analysis of aerosols using laser-induced breakdown spectroscopy, *Anal. Chem.* 74 (2002)

5450–5454. <https://doi.org/10.1021/ac020261m>.

- [76] D. Diaz, D.W. Hahn, Aerosol measurements with laser-induced breakdown spectroscopy and conditional analysis, *Spectrochim. Acta - Part B At. Spectrosc.* 179 (2021) 106107. <https://doi.org/10.1016/j.sab.2021.106107>.
- [77] D.W. Hahn, W.L. Flower, K.R. Hencken, Discrete particle detection and metal emissions monitoring using laser-induced breakdown spectroscopy, *Appl. Spectrosc.* 51 (1997) 1836–1844. <https://doi.org/10.1366/0003702971939659>.
- [78] D.W. Hahn, M.M. Lunden, Detection and analysis of aerosol particles by laser-induced breakdown spectroscopy, *Aerosol Sci. Technol.* 33 (2000) 30–48. <https://doi.org/10.1080/027868200410831>.
- [79] J.E. Carranza, K. Iida, D.W. Hahn, Conditional data processing for single-shot spectral analysis by use of laser-induced breakdown spectroscopy, *Appl. Opt.* 42 (2003) 6022. <https://doi.org/10.1364/ao.42.006022>.
- [80] E. Abás, C. Marina-Montes, M. Laguna, R. Lasheras, P. Rivas, P. Peribáñez, J. del Valle, M. Escudero, A. Velásquez, J.O. Cáceres, L.V. Pérez-Arribas, J. Anzano, Evidence of human impact in Antarctic region by studying atmospheric aerosols, *Chemosphere.* 307 (2022). <https://doi.org/10.1016/j.chemosphere.2022.135706>.
- [81] S.D. Arnold, D.A. Cremers, Rapid Determination of Metal Particles on Air Sampling Filters Using Laser-Induced Breakdown Spectroscopy, *Am. Ind. Hyg. Assoc. J.* 56 (1995) 1180–1186. <https://doi.org/10.1080/15428119591016197>.
- [82] U. Panne, R.E. Neuhauser, M. Theisen, H. Fink, R. Niessner, Analysis of heavy metal aerosols on filters by laser-induced plasma spectroscopy, *Spectrochim. Acta Part B At. Spectrosc.* 56 (2001) 839–850. [https://doi.org/https://doi.org/10.1016/S0584-8547\(01\)00209-9](https://doi.org/https://doi.org/10.1016/S0584-8547(01)00209-9).
- [83] R.E. Neuhauser, U. Panne, R. Niessner, Utilization of Fiber Optics for Remote Sensing by Laser-Induced Plasma Spectroscopy (LIPS), *Appl. Spectrosc.* 54 (2000) 923–927. <https://opg.optica.org/as/abstract.cfm?URI=as-54-6-923>.
- [84] R.E. Neuhauser, U. Panne, R. Niessner, Laser-induced plasma spectroscopy (LIPS): A versatile tool for monitoring heavy metal aerosols, *Anal. Chim. Acta.* 392 (1999) 47–54. [https://doi.org/10.1016/S0003-2670\(99\)00053-7](https://doi.org/10.1016/S0003-2670(99)00053-7).

- [85] P. Kulkarni, S. Chellam, J.B. Flanagan, R.K.M. Jayanty, Microwave digestion-ICP-MS for elemental analysis in ambient airborne fine particulate matter: Rare earth elements and validation using a filter borne fine particle certified reference material, *Anal. Chim. Acta.* 599 (2007) 170–176. <https://doi.org/10.1016/j.aca.2007.08.014>.
- [86] J. Aldabe, C. Santamaría, D. Elustondo, E. Lasheras, J.M. Santamaría, Application of microwave digestion and ICP-MS to simultaneous analysis of major and trace elements in aerosol samples collected on quartz filters, *Anal. Methods.* 5 (2013) 554–559. <https://doi.org/10.1039/c2ay25724f>.
- [87] F.G. Pinto, R.E. Junior, T.D. Saint’Pierre, Sample Preparation for Determination of Rare Earth Elements in Geological Samples by ICP-MS: A Critical Review, *Anal. Lett.* 45 (2012) 1537–1556. <https://doi.org/10.1080/00032719.2012.677778>.
- [88] N.R. McQuaker, D.F. Brown, P.D. Kluckner, Digestion of environmental materials for analysis by inductively coupled plasma-atomic emission spectrometry, *Anal. Chem.* 51 (1979) 1082–1084. <https://doi.org/10.1021/ac50043a071>.
- [89] A. Favre, V. Morel, A. Bultel, G. Godard, S. Idlahcen, A. Benyagoub, I. Monnet, A. Sémérok, M. Dinescu, S. Markelj, P. Magaud, C. Grisolia, Double pulse laser-induced plasmas on W and Al by ps-LIBS: Focus on the plasma-second pulse interaction, *Fusion Eng. Des.* 168 (2021) 112364. <https://doi.org/10.1016/J.FUSENGDES.2021.112364>.
- [90] D. Diaz, D.W. Hahn, U. Panne, Chapter 22 - LIBS for aerosol analysis, in: J.P. Singh, S.N. Thakur, *Laser-Induced Breakdown Spectroscopy (Second Edition)*, Elsevier, Amsterdam, 2020: pp. 499–535. <https://doi.org/https://doi.org/10.1016/B978-0-12-818829-3.00022-8>.
- [91] D.A. Redoglio, N. Palazzo, F. Migliorini, R. Dondè, S. De Iuliis, Laser-Induced Breakdown Spectroscopy Analysis of Lead Aerosol in Nitrogen and Air Atmosphere, *Appl. Spectrosc.* 72 (2018) 584–590. <https://doi.org/10.1177/0003702817742314>.
- [92] N. Palazzo, F. Migliorini, R. Dondè, S. Maffi, S. De Iuliis, Influence of oxygen addition to the carrier gas on laser-induced breakdown spectroscopy measurements on aerosols, *Spectrochim. Acta - Part B At. Spectrosc.* 115 (2016) 1–7. <https://doi.org/10.1016/j.sab.2015.10.012>.
- [93] L.C.L. Borduchi, D.M.B.P. Milori, P.R. Villas-Boas, Study of the effects of detection times in laser-induced breakdown spectroscopy and missed variation of plasma parameters with gate width, *Spectrochim. Acta Part B At. Spectrosc.* 191 (2022) 106409.

<https://doi.org/https://doi.org/10.1016/j.sab.2022.106409>.

- [94] J.E. Carranza, D.W. Hahn, Sampling statistics and considerations for single-shot analysis using laser-induced breakdown spectroscopy, *Spectrochim. Acta - Part B At. Spectrosc.* 57 (2002) 779–790. [https://doi.org/10.1016/S0584-8547\(02\)00007-1](https://doi.org/10.1016/S0584-8547(02)00007-1).
- [95] S.G. Buckley, H.A. Johnsen, K.R. Hencken, A.D.W. Hahn, Implementation of laser-induced breakdown spectroscopy as a continuous emissions monitor for toxic metals, *Waste Manag.* 20 (2000) 455–462. [https://doi.org/10.1016/S0956-053X\(00\)00011-8](https://doi.org/10.1016/S0956-053X(00)00011-8).
- [96] M. Sabsabi, P. Cielo, Quantitative analysis of aluminum alloys by Laser-induced breakdown spectroscopy and plasma characterization, *Appl. Spectrosc.* 49 (1995) 499–507. <https://doi.org/10.1366/0003702953964408>.
- [97] W.T.Y. Mohamed, Improved LIBS limit of detection of Be, Mg, Si, Mn, Fe and Cu in aluminum alloy samples using a portable Echelle spectrometer with ICCD camera, *Opt. Laser Technol.* 40 (2008) 30–38. <https://doi.org/10.1016/J.OPTLASTEC.2007.04.004>.
- [98] A. Sarkar, D. Alamelu, S.K. Aggarwal, Gallium quantification in solution by LIBS in the presence of bulk uranium, *Opt. Laser Technol.* 44 (2012) 30–34. <https://doi.org/10.1016/J.OPTLASTEC.2011.05.010>.
- [99] C.A. D'Angelo, M. Garcimuño, D.M. Díaz Pace, G. Bertuccelli, Plasma diagnostics from self-absorbed doublet lines in laser-induced breakdown spectroscopy, *J. Quant. Spectrosc. Radiat. Transf.* 164 (2015) 89–96. <https://doi.org/10.1016/J.QSRT.2015.05.014>.
- [100] D. Bulajic, M. Corsi, G. Cristoforetti, S. Legnaioli, V. Palleschi, A. Salvetti, E. Tognoni, A procedure for correcting self-absorption in calibration free-laser induced breakdown spectroscopy, *Spectrochim. Acta Part B At. Spectrosc.* 57 (2002) 339–353. [https://doi.org/10.1016/S0584-8547\(01\)00398-6](https://doi.org/10.1016/S0584-8547(01)00398-6).
- [101] A.M. El Sherbini, T.M. El Sherbini, H. Hegazy, G. Cristoforetti, S. Legnaioli, V. Palleschi, L. Pardini, A. Salvetti, E. Tognoni, Evaluation of self-absorption coefficients of aluminum emission lines in laser-induced breakdown spectroscopy measurements, *Spectrochim. Acta Part B At. Spectrosc.* 60 (2005) 1573–1579. <https://doi.org/10.1016/J.SAB.2005.10.011>.
- [102] V. Lazic, R. Barbini, F. Colao, R. Fantoni, A. Palucci, Self-absorption model in quantitative laser induced breakdown spectroscopy measurements on soils and sediments, *Spectrochim. Acta Part B At. Spectrosc.* 56 (2001) 807–820. [https://doi.org/10.1016/S0584-8547\(01\)00211-7](https://doi.org/10.1016/S0584-8547(01)00211-7).

- [103] F. Bredice, F.O. Borges, H. Sobral, M. Villagran-Muniz, H.O. Di Rocco, G. Cristoforetti, S. Legnaioli, V. Palleschi, L. Pardini, A. Salvetti, E. Tognoni, Evaluation of self-absorption of manganese emission lines in Laser Induced Breakdown Spectroscopy measurements, *Spectrochim. Acta Part B At. Spectrosc.* 61 (2006) 1294–1303. <https://doi.org/10.1016/J.SAB.2006.10.015>.
- [104] J. Bengoechea, J.A. Aguilera, C. Aragón, Application of laser-induced plasma spectroscopy to the measurement of Stark broadening parameters, *Spectrochim. Acta Part B At. Spectrosc.* 61 (2006) 69–80. <https://doi.org/10.1016/J.SAB.2005.11.003>.
- [105] G. Cristoforetti, E. Tognoni, Calculation of elemental columnar density from self-absorbed lines in laser-induced breakdown spectroscopy: A resource for quantitative analysis, *Spectrochim. Acta Part B At. Spectrosc.* 79–80 (2013) 63–71. <https://doi.org/10.1016/J.SAB.2012.11.010>.
- [106] T. Takahashi, B. Thornton, Quantitative methods for compensation of matrix effects and self-absorption in LIBS signals of solids, *Spectrochim. Acta - Part B At. Spectrosc.* 138 (2017) 31–42. <https://doi.org/10.1016/j.sab.2017.09.010>.
- [107] L.A. Currie, Nomenclature in evaluation of analytical methods including detection and quantification capabilities¹Adapted from the International Union of Pure and Applied Chemistry (IUPAC) document “Nomenclature in Evaluation of Analytical Methods including Detection”, *Anal. Chim. Acta.* 391 (1999) 105–126. [https://doi.org/https://doi.org/10.1016/S0003-2670\(99\)00104-X](https://doi.org/https://doi.org/10.1016/S0003-2670(99)00104-X).
- [108] C. Maury, J.-B. Sirven, M. Tabarant, D. L’Hermite, J.-L. Courouau, C. Gallou, N. Caron, G. Moutiers, V. Cabuil, Analysis of liquid sodium purity by laser-induced breakdown spectroscopy. Modeling and correction of signal fluctuation prior to quantitation of trace elements, *Spectrochim. Acta Part B At. Spectrosc.* 82 (2013) 28–35. <https://doi.org/https://doi.org/10.1016/j.sab.2012.12.005>.
- [109] D.C. Zhang, Z.Q. Hu, Y.B. Su, B. Hai, X.L. Zhu, J.F. Zhu, X. Ma, Simple method for liquid analysis by laser-induced breakdown spectroscopy (LIBS), *Opt. Express.* 26 (2018) 18794–18802. <https://doi.org/10.1364/OE.26.018794>.
- [110] G.L. Long, J.D. Winefordner, Limit of Detection: A Closer Look at the IUPAC Definition, *Anal. Chem.* 55 (1983) 713A-724A. <https://doi.org/10.1021/ac00258a724>.
- [111] R.E. Neuhauser, U. Panne, R. Niessner, G. Petrucci, P. Cavalli, N. Omenetto, On-line and in

situ detection of lead in ultrafine aerosols by laser-excited atomic fluorescence spectroscopy, *Sensors Actuators, B Chem.* 39 (1997) 344–348. [https://doi.org/10.1016/S0925-4005\(97\)80231-6](https://doi.org/10.1016/S0925-4005(97)80231-6).

- [112] B.T. Fisher, H.A. Johnsen, S.G. Buckley, D.W. Hahn, Temporal gating for the optimization of laser-induced breakdown spectroscopy detection and analysis of toxic metals, *Appl. Spectrosc.* 55 (2001) 1312–1319. <https://doi.org/10.1366/0003702011953667>.
- [113] European Council, Directive 2010/75/EU Industrial Emissions, *Off. J. Eur. Union.* L334 (2010) 17–119. https://doi.org/10.3000/17252555.L_2010.334.eng.
- [114] W. Wang, L. Sun, P. Zhang, T. Chen, L. Zheng, L. Qi, Study of matrix effects in laser-induced breakdown spectroscopy by laser defocus and temporal resolution, *J. Anal. At. Spectrom.* 36 (2021) 1977–1985. <https://doi.org/10.1039/d1ja00179e>.
- [115] B.C. Windom, P.K. Diwakar, D.W. Hahn, Dual-pulse Laser Induced Breakdown Spectroscopy for analysis of gaseous and aerosol systems: Plasma-analyte interactions, *Spectrochim. Acta - Part B At. Spectrosc.* 61 (2006) 788–796. <https://doi.org/10.1016/j.sab.2006.06.003>.
- [116] R.L. Gleason, D.W. Hahn, The effects of oxygen on the detection of mercury using laser-induced breakdown spectroscopy, *Spectrochim. Acta - Part B At. Spectrosc.* 56 (2001) 419–430. [https://doi.org/10.1016/S0584-8547\(01\)00169-0](https://doi.org/10.1016/S0584-8547(01)00169-0).
- [117] S.G. Buckley, Laser-Induced Breakdown Spectroscopy for Toxic Metal Emission Measurements: Experimental Considerations and Oxygen Quenching, *Environ. Eng. Sci.* 22 (2005) 195–204. <https://doi.org/10.1089/ees.2005.22.195>.
- [118] A. Molina, C.R. Shaddix, S.M. Sickafoose, P.M. Walsh, L.G. Blevins, Effect of temperature and CO₂ concentration on laser-induced breakdown spectroscopy measurements of alkali fume, *Spectrochim. Acta - Part B At. Spectrosc.* 60 (2005) 1103–1114. <https://doi.org/10.1016/j.sab.2005.06.005>.
- [119] P.K. Diwakar, P.B. Jackson, D.W. Hahn, The effect of multi-component aerosol particles on quantitative laser-induced breakdown spectroscopy: Consideration of localized matrix effects, *Spectrochim. Acta Part B At. Spectrosc.* 62 (2007) 1466–1474. <https://doi.org/10.1016/J.SAB.2007.10.001>.
- [120] E.J. Judge, J. Colgan, K. Campbell, J.E. Barefield, H.M. Johns, D.P. Kilcrease, S. Clegg, Theoretical and experimental investigation of matrix effects observed in emission spectra of

binary mixtures of sodium and copper and magnesium and copper pressed powders, *Spectrochim. Acta - Part B At. Spectrosc.* 122 (2016) 142–148.
<https://doi.org/10.1016/j.sab.2016.06.004>.

- [121] B.C. Windom, D.W. Hahn, Laser ablation—laser induced breakdown spectroscopy (LA-LIBS): A means for overcoming matrix effects leading to improved analyte response, *J. Anal. At. Spectrom.* 24 (2009) 1665–1675. <https://doi.org/10.1039/B913495F>.
- [122] D.A. Gonçalves, G.S. Senesi, G. Nicolodelli, Laser-Induced Breakdown Spectroscopy applied to environmental systems and their potential contaminants. An overview of advances achieved in the last few years, *Trends Environ. Anal. Chem.* 30 (2021).
<https://doi.org/10.1016/j.teac.2021.e00121>.
- [123] P.K. Diwakar, K.H. Loper, A.M. Matiaske, D.W. Hahn, Laser-induced breakdown spectroscopy for analysis of micro and nanoparticles, *J. Anal. At. Spectrom.* 27 (2012) 1110–1119. <https://doi.org/10.1039/c2ja30012e>.
- [124] E.R. Wainwright, C.J. Miller, L. Giri, R.A. Pesce-Rodriguez, C.C. Wu, J.L. Gottfried, Influence of silicon particle morphology on laser-induced plasma properties, *Spectrochim. Acta Part B At. Spectrosc.* 199 (2023) 106597. <https://doi.org/10.1016/J.SAB.2022.106597>.
- [125] D.J. Palásti, L.P. Villy, A. Kohut, T. Ajtai, Z. Geretovszky, G. Galbács, Laser-induced breakdown spectroscopy signal enhancement effect for argon caused by the presence of gold nanoparticles, *Spectrochim. Acta Part B At. Spectrosc.* 193 (2022) 106435.
<https://doi.org/10.1016/J.SAB.2022.106435>.
- [126] D. Ciniglia, F. Migliorini, R. Dondé, P. Diwakar, S. De Iuliis, Loading effect of matrix compounds in aerosol LIBS measurements, *Spectrochim. Acta Part B At. Spectrosc.* 208 (2023) 106784. <https://doi.org/10.1016/J.SAB.2023.106784>.
- [127] P.K. Diwakar, S. Groh, K. Niemax, D.W. Hahn, Study of analyte dissociation and diffusion in laser-induced plasmas: implications for laser-induced breakdown spectroscopy, *J. Anal. At. Spectrom.* 25 (2010) 1921–1930. <https://doi.org/10.1039/C0JA00063A>.
- [128] M.E. Asgill, S. Groh, K. Niemax, D.W. Hahn, The use of multi-element aerosol particles for determining temporal variations in temperature and electron density in laser-induced plasmas in support of quantitative laser-induced breakdown spectroscopy, *Spectrochim. Acta - Part B At. Spectrosc.* 109 (2015) 1–7. <https://doi.org/10.1016/j.sab.2015.04.005>.
- [129] K.S. Latty, K.C. Hartig, Elemental fractionation in aerosol laser-induced breakdown

spectroscopy with nanosecond and femtosecond laser ablation, *Spectrochim. Acta Part B At. Spectrosc.* 202 (2023) 106648. <https://doi.org/10.1016/J.SAB.2023.106648>.

- [130] C. Goueguel, D.L. McIntyre, J. Jain, A.K. Karamalidis, C. Carson, Matrix effect of sodium compounds on the determination of metal ions in aqueous solutions by underwater laser-induced breakdown spectroscopy., *Appl. Opt.* 54 (2015) 6071–6079. <https://doi.org/10.1364/AO.54.006071>.
- [131] A.S. Eppler, D.A. Cremers, D.D. Hickmott, M.J. Ferris, A.C. Koskelo, Matrix Effects in the Detection of Pb and Ba in Soils Using Laser-Induced Breakdown Spectroscopy, *Appl. Spectrosc.* 50 (1996) 1175–1181. <https://doi.org/10.1366/0003702963905123>.
- [132] J.L. Todolí, L. Gras, V. Hernandis, J. Mora, Elemental matrix effects in ICP-AES, *J. Anal. At. Spectrom.* 17 (2002) 142–169. <https://doi.org/10.1039/B009570M>.
- [133] G.C.Y. Chan, W.T. Chan, X. Mao, R.E. Russo, Investigation of matrix effects in inductively coupled plasma-atomic emission spectroscopy using laser ablation and solution nebulization — effect of second ionization potential, *Spectrochim. Acta Part B At. Spectrosc.* 56 (2001) 77–92. [https://doi.org/10.1016/S0584-8547\(00\)00295-0](https://doi.org/10.1016/S0584-8547(00)00295-0).
- [134] G. Wang, C. Xu, W. Kong, G. Englmaier, J. Fan, G. Wei, S. Furbo, Review on sodium acetate trihydrate in flexible thermal energy storages: Properties, challenges and applications, *J. Energy Storage.* 40 (2021) 102780. <https://doi.org/10.1016/J.EST.2021.102780>.
- [135] CRC Handbook of Chemistry and Physics, 84th Edition Edited by David R. Lide (National Institute of Standards and Technology). CRC Press LLC: Boca Raton. 2003. 2616 pp. \$139.95. ISBN 0-8493-0484-9., *J. Am. Chem. Soc.* 126 (2004) 1586. <https://doi.org/10.1021/ja0336372>.
- [136] Y.T. Li, D.J. Yan, Y.F. Guo, S.Q. Wang, T.L. Deng, Studies on Magnesium Chloride Hexahydrate as Phase Change Materials, *Appl. Mech. Mater.* 71–78 (2011) 2598–2601. <https://doi.org/10.4028/www.scientific.net/AMM.71-78.2598>.
- [137] M. Dong, X. Mao, J.J. Gonzalez, J. Lu, R.E. Russo, Time-resolved LIBS of atomic and molecular carbon from coal in air, argon and helium, *J. Anal. At. Spectrom.* 27 (2012) 2066–2075. <https://doi.org/10.1039/C2JA30222E>.
- [138] K.A. Hadidi, P.P. Woskov, G. Flores, K. Green, P. Thomas, Effect of Oxygen Concentration on the Detection of Mercury in an Atmospheric Microwave Discharge, *Jpn. J. Appl. Phys.* 38 (1999) 4595–4600. <https://api.semanticscholar.org/CorpusID:95488050>.

- [139] R. Saad, D. L'Hermite, B. Bousquet, Unexpected temporal evolution of atomic spectral lines of aluminum in a laser induced breakdown spectroscopy experiment, *Spectrochim. Acta Part B At. Spectrosc.* 101 (2014) 330–334.
<https://doi.org/https://doi.org/10.1016/j.sab.2014.09.017>.
- [140] X. Mao, S. bor Wen, R.E. Russo, Time resolved laser-induced plasma dynamics, *Appl. Surf. Sci.* 253 (2007) 6316–6321. <https://doi.org/10.1016/j.apsusc.2007.01.053>.
- [141] Q.L. Ma, V. Motto-Ros, W.Q. Lei, M. Boueri, X.S. Bai, L.J. Zheng, H.P. Zeng, J. Yu, Temporal and spatial dynamics of laser-induced aluminum plasma in argon background at atmospheric pressure: Interplay with the ambient gas, *Spectrochim. Acta - Part B At. Spectrosc.* 65 (2010) 896–907. <https://doi.org/10.1016/j.sab.2010.08.005>.
- [142] K. Park, G. Cho, J.H. Kwak, Development of an Aerosol Focusing-Laser Induced Breakdown Spectroscopy (Aerosol Focusing-LIBS) for determination of fine and ultrafine metal aerosols, *Aerosol Sci. Technol.* 43 (2009) 375–386.
<https://doi.org/10.1080/02786820802662947>.
- [143] National Institute of Standards and Technology, NIST LIBS database, (n.d.).
https://physics.nist.gov/cgi-bin/ASD/lines1.pl?composition=Si%3A60%3BFe%3A40&mytext%5B%5D=Si&myperc%5B%5D=60&spectra=Si0-2%2CFe0-2&mytext%5B%5D=Fe&myperc%5B%5D=40&low_w=245&limits_type=0&upp_w=275&show_av=2&unit=1&resolution=3000&temp=1&eden=1e17&maxcharg.
- [144] D. Ciniglia, P. Cirelli, F. Bilo, A. Zanoletti, A. Cornelio, S. De Iuliis, L.E. Depero, E. Bontempi, M.G. Perrone, P. Lopinto, M. Zonca, L. Borgese, Characterization of nebulization generated aerosol particles dispersion and deposition by total reflection X-ray fluorescence, *Aerosol Sci. Technol.* 57 (2023) 165–174. <https://doi.org/10.1080/02786826.2022.2155104>.

APPENDIX

A1 NEBULIZERS

In this work two different nebulizers were employed, the TSI Constant Output Atomizer and the medical nebulizer (HUDSON UP-DRAFT Nebulizer). In Figure 71 a picture of these two nebulizers is shown.

The choice of these two nebulizers was based on their different applications in the LIBS measurements. The TSI nebulizer was used in preliminary LIBS measurements, since the employment of a nebulizer with well controlled size and number of particles production was mandatory for preliminary tests. Once the LIBS set-up configuration was optimized, the TSI nebulizer was substituted with the medical one, being this last lighter and more practical to be used for on-site measurements. This last also offers greater efficiency in terms of size and cost for field tests and calibrations. The working conditions of the two nebulizers are also different.

- The TSI nebuliser is used with an air flow rate of 3 l/min generating droplets with a medium diameter of 0.3 μm .
- The Hudson nebuliser is operated with a 5 l/m flow rate generating droplets with a mean diameter of 5 μm .

Due to these different conditions and the different solution consumption of the two nebulizers, although working with solutions having the same molar concentrations, different aerosol concentrations are obtained in the two cases.



Figure 71. left) TSI Constant Output Atomizer; right) HUDSON UP-DRAFT Nebulizer.

Preliminary measurements were carried out in order to investigate the stability and repeatability of the consumption of both nebulizers. In fact, this is a fundamental parameter for calculating the concentration of the aerosol used for calibration. In Figure 72 examples of the consumption evaluated in different measurement tests are reported for the two nebulizers. Each point refers to measurements

performed in a wide range of times, starting from 2 minutes, the shortest one, up to 260 minutes the longest one, with a large number of tests performed in a narrower range of times, between 10 minutes and 30 minutes.

The consumption analysis was performed on 80 measurements, which are spread in time during the year. As it can be seen, the two nebulizers work with different solution consumption rates, which is due to different geometry and the working carrier gas flow rate. Considering a simple analysis of the mean and standard deviation, a consumption values of 0.05 ± 0.01 g/min for the TSI nebuliser and 0.13 ± 0.03 g/min for the HUDSON nebuliser are obtained, which also prove the different variability for the two nebulizers. In Figure 73 the consumption values and the relative error are reported for the two nebulizers.

Analysing the consumption trend, a central peak is visible in the consumption trend obtained with the TSI nebulizer, corresponding to the summer months. It is likely that higher temperatures affect the evaporation of the solution, leading to a higher overall consumption. The difference between the minimum consumption period and the maximum is about 40 % respect to the mean value, so this difference is valuable above the spreading of the data. Considering the HUDSON nebuliser, there is no evident trends in the consumption measurements.

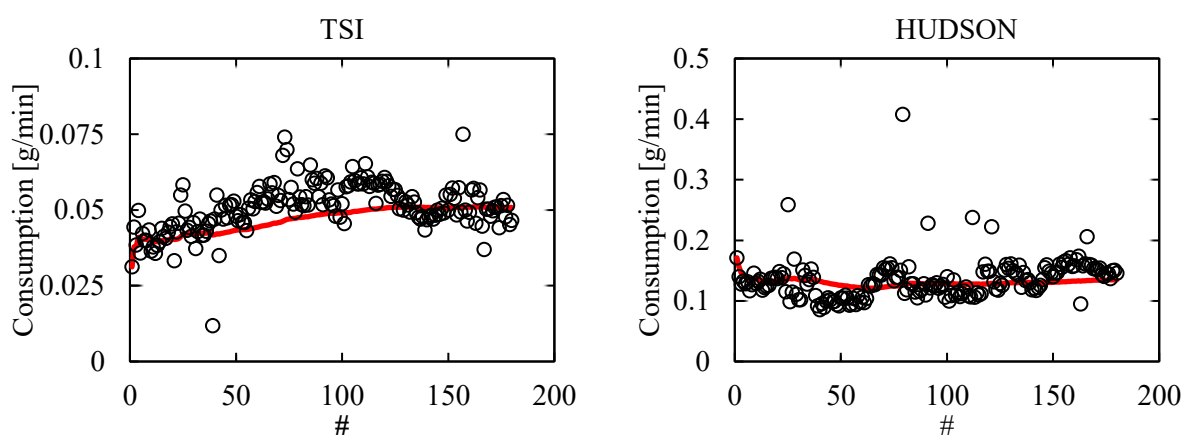


Figure 72. 180 repetitions of solution consumption measured during the nebulization; TSI (left) and HUDSON (right).

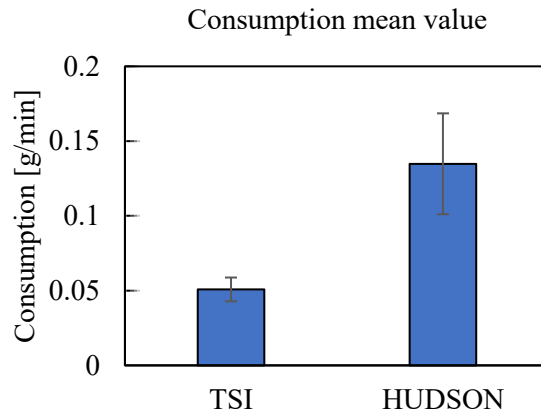


Figure 73. Mean consumption value calculated over the 180 repetitions and related standard deviation.

A2 NEBULIZATION ANALYSIS VIA TXRF

As a preliminary analysis, in order to develop a proper LIBS apparatus for real time heavy metals aerosol emission measurement, a proper study on the aerosol generation is carried on. In this context, the creation of properly characterized aerosols for calibrating online analysis methodologies, in this case LIBS, is of great interest, together with the creation of reference and calibration samples with known amounts of deposited PM. The deposited samples can be used for calibration of offline analysis methodologies considering the matrix effect due to the substrate used for the aerosol particles deposition. This would represent an interesting new approach to produce reference materials. As a proof of concept for the use of an aerosol generator to realize aerosol for calibrating online LIBS and particulate deposition for offline TXRF and LIBS on filters, we designed a model experiment to study aerosol particles dispersions and depositions. The obtained results have been published on the journal “Aerosol Science and Technology” in 2023 [144].

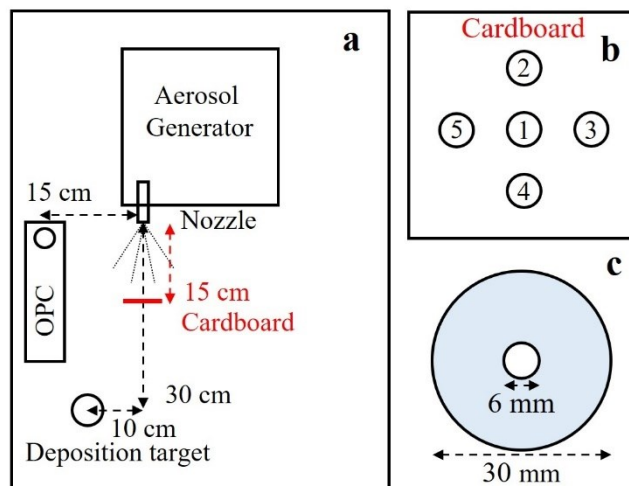


Figure 74. Experimental set-up for aerosol nebulization study.

Concentration and size distribution of aerosol particles created by nebulization of Cu salt aqueous solutions are determined by using an optical particle counter (OPC), changing the flow rate of the aerosol production unit. The experimental set-up is reported in Figure 74. The best experimental conditions to obtain a stable aerosol particles concentration in the system are retrieved and used for further investigation of the radial distribution of the particles across the aerosol. On this purpose particulate is collected on reflectors positioned at five different locations at a fixed distance from the generator nozzle. Quantitative analysis of the Cu mass of particulate is performed by TXRF using Ga as internal standard for calibration, loaded on the reflectors before starting the experiment.

It is observed that deposition increases with the flow rate, with the average flow rate (4 L/min) resulting in a steady concentration that balance aerosol particles production and deposition. This setting is selected for studying the aerosol spatial distribution by collecting the particulate at a fixed position and using a radial geometry. A leftward asymmetry of the aerosol particles flow with respect to the nozzle is evident by measuring the Cu mass deposited on reflectors, which linearly increases with exposure time to the aerosol. Small deviations from linearity observed at higher times are probably due to the shadowing internal standard effect by the deposited particulate. Well characterized aerosols can be used to calibrate online LIBS instruments though, due to the asymmetry detected in the mass distribution across the aerosol, care must be taken in considering the concentration calculated from the solution consumption as the one measured online in a specific point of the aerosol. A proper experimental arrangement must be considered to ensure a homogeneous aerosol suitable for calibration purposes. For this reason, in LIBS experimental procedure, the generated aerosol passes through a mixing chamber, in which the addition of clean air has two main purposes. The first one is to dry the droplets and let flow only the metal particulate through the measurement chamber, the second one is to mix droplets with air and create a uniform aerosol concentration.

These data are part of a paper published in a peer review journal, *Aerosol Science and Technology*.

A3 SUSPENSIONS

A further different method for generating specific aerosol for LIBS analysis in the laboratory always involves a nebulisation process, but instead of using a chemical solution can be used a suspension, in which the target particulate matter is suspended without undergoing any chemical-physical transformation. This procedure is adopted when the analyte cannot be dissolved in distilled water or need to be analysed in its original form. There are some special cases where it is useful, if not even necessary, to use this procedure, for example when the target particulate matter has been previously collected on a filter matrix and the objective is to perform a measurement on the analyte in aerosol

form. As an example, this could be the case of powders produced during braking, for which the construction of a LIBS apparatus suitable for online aerosol measurement is complex, so powders are collected on a filter matrix and then analysed. A more detailed analysis will be described later as a case study. As usual for other techniques, such as ICP, it would be possible to carry out a digestion process of the filter using a strong acid as a solvent and bring all the constituent elements into solution and produce aerosol with the usual procedure. In this particular case, it is not possible to use such an acid solution, because both in the instrumental configuration implemented with the TSI atomizer and with the medical nebulizer, damage would be done to the instrument. The TSI atomizer would be damaged at the micro-hole used to break the solution flow and would cause loss of control over the size of the droplets generated and also over the consumption of solution. The medical nebulizer, being made of plastic, would undergo to general damage on all the parts in contact with the solution. In addition, by dissolving the particles, information about the real aerosol would be lost. The elemental chemical information would be retained, but the LIBS signal would be uncorrelated with the particle size and elemental distribution within them. These are very variable characteristics within a real aerosol that would lead to significantly different signals from each other, unlike a homogeneous solution. This different behaviour is reflected in a different matrix effect, a different evaluation of the limits of detection and also in the greater probability of saturation and incomplete vaporization for the larger particles of the real aerosol. Characteristics that must be taken into account for the study of these types of aerosols.



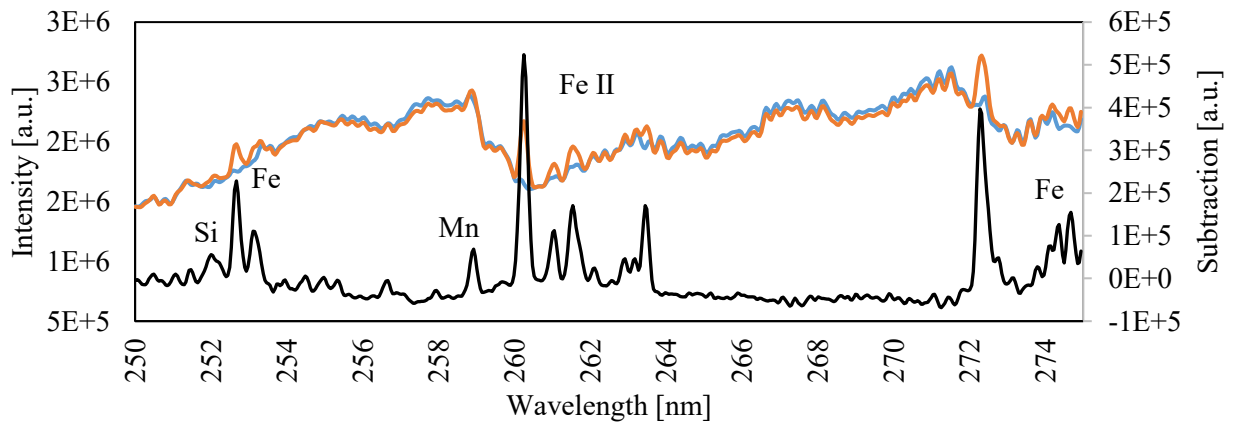
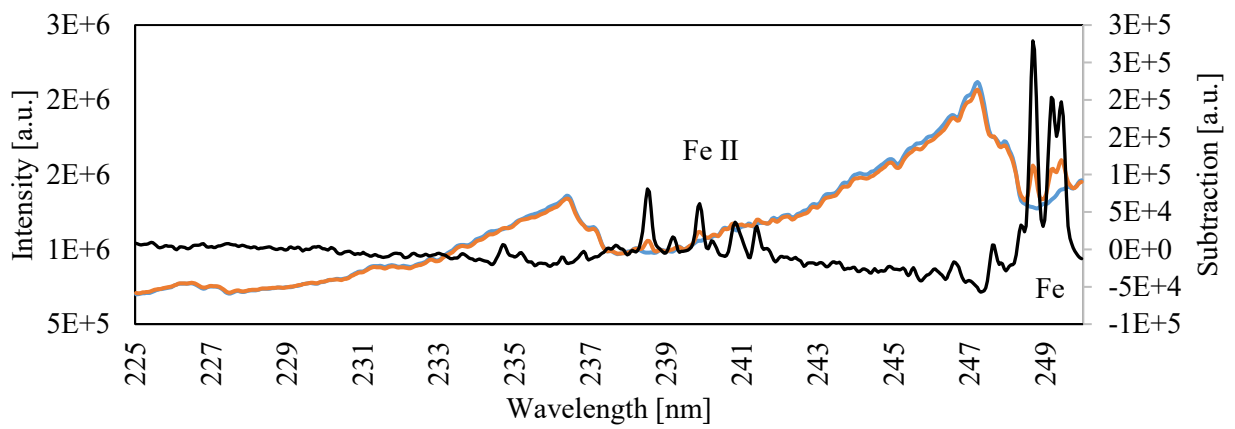
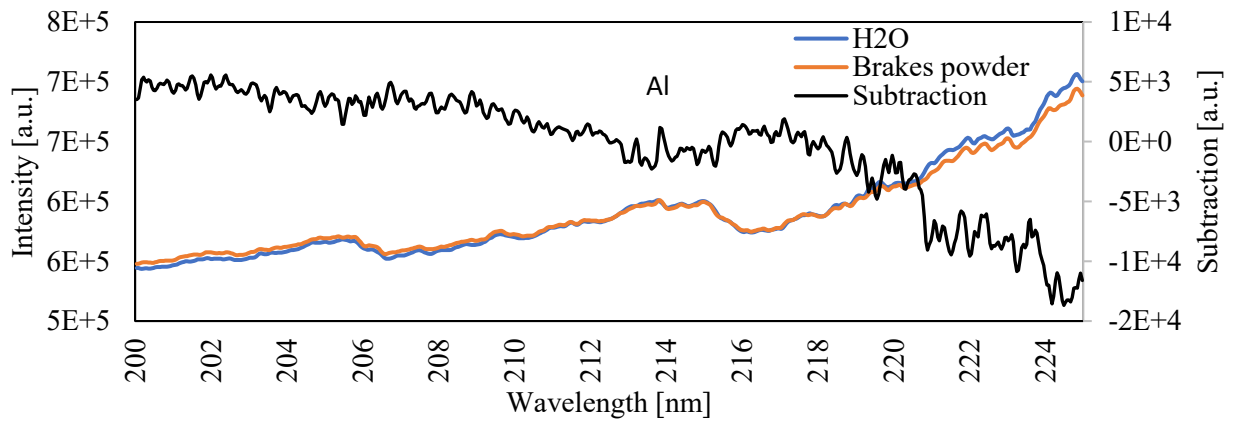
Figure 75. Procedure steps for suspension production. 1) loaded filter; 2) filter immersion in pure water; 3) ultrasonic bath for particles detachment and suspension; 4) suspension; 5) nebuliser tank filling; 6) aerosolization in ultrasonic bath.

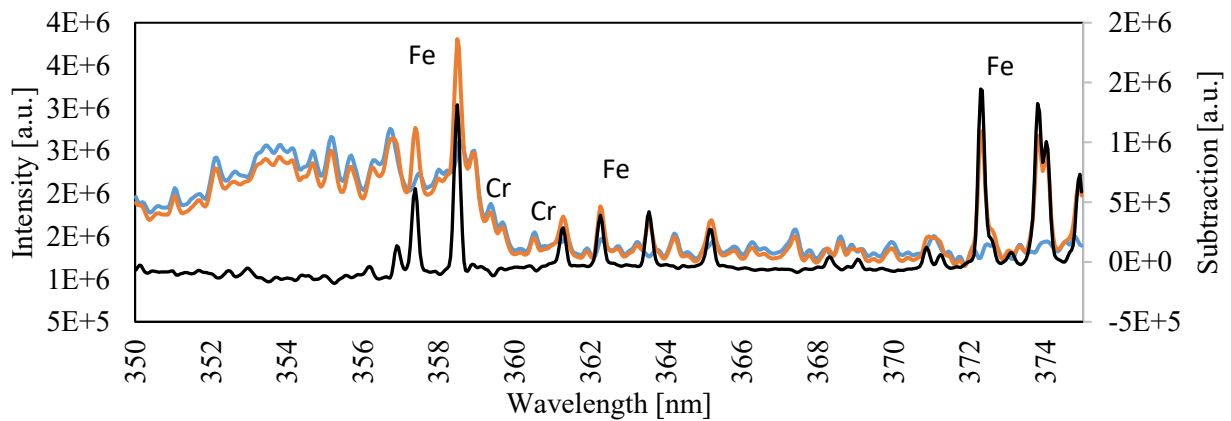
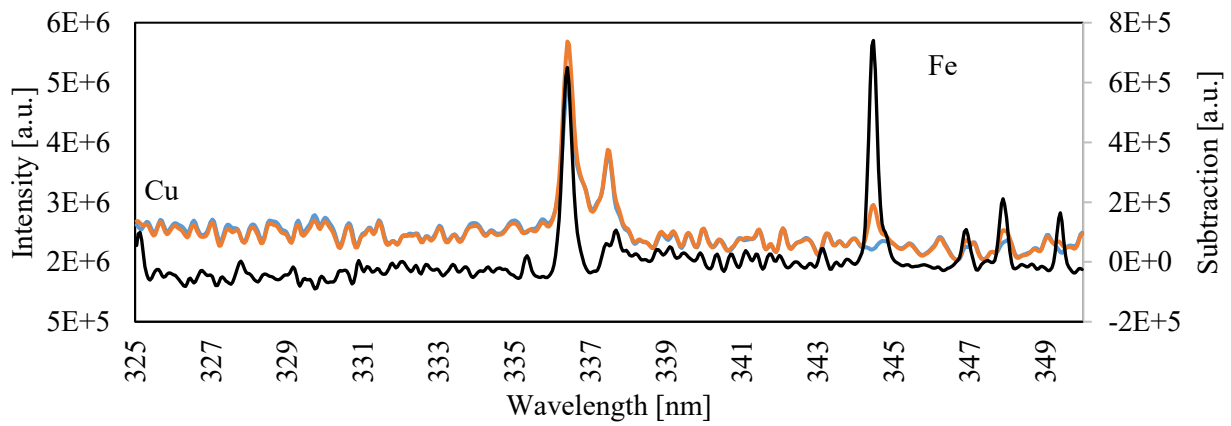
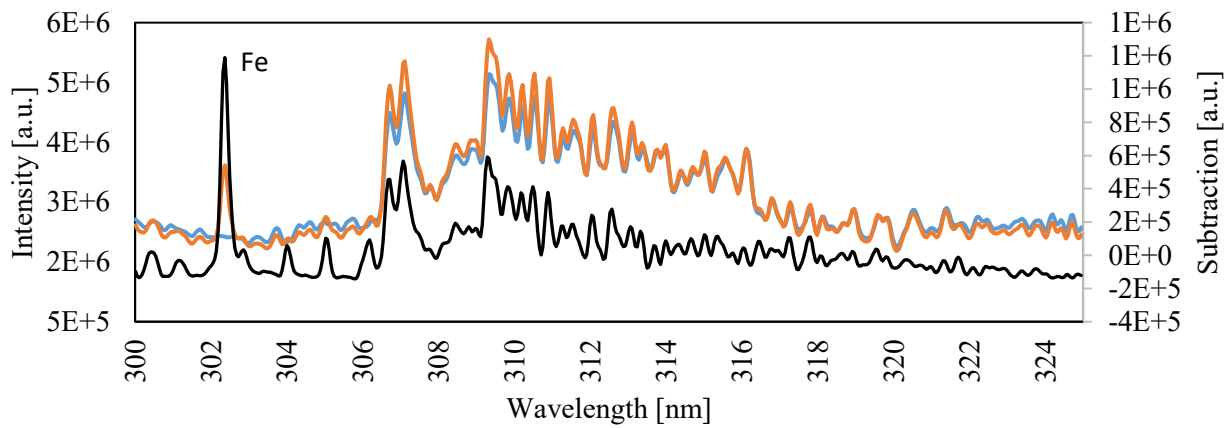
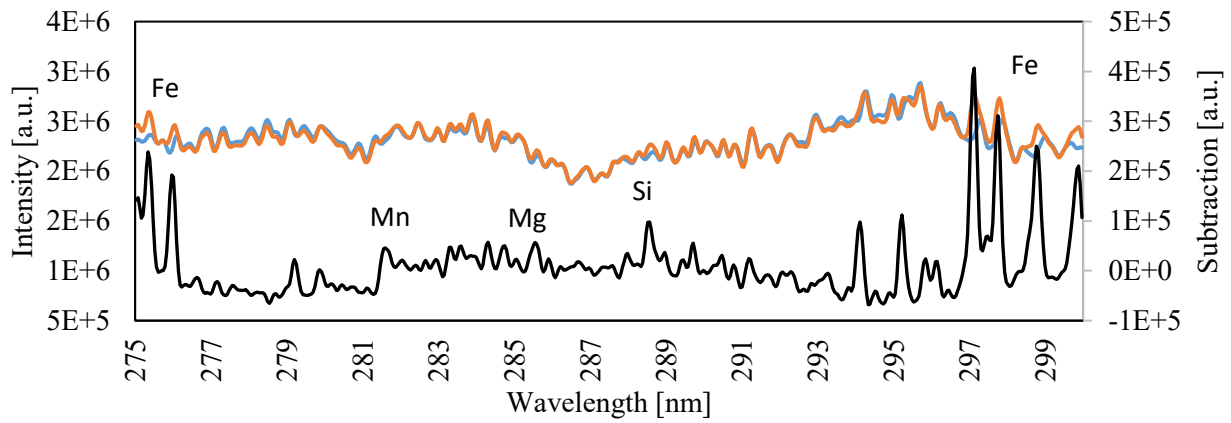
For these reasons, when the aerosol was filtered, the particle-loaded filters were immersed in ultra-pure distilled water and placed in an ultrasonic bath to allow the almost complete detachment of the deposited particles. Once the filter is cleaned, it is removed from the water and the suspension undergoes an additional ultrasonic bath process in order to keep the particles in suspension. Depending on the size of the particles, it is possible to recreate more or less stable suspensions. To overcome the problem of suspension instability, during the nebulization process, the tank used to contain the suspension is kept immersed in an ultrasonic bath, in order to have a suspension as stable and homogeneous as possible and not lose a good part of the particulate matter by deposition. This procedure is schematically reported in Figure 75. The limit of this procedure is the impossibility to have a complete detachment of particles from the filter and that the bigger particles will be difficultly nebulised due to their dimensions and due to their facility to deposit on the bottom instead of remaining in suspension.

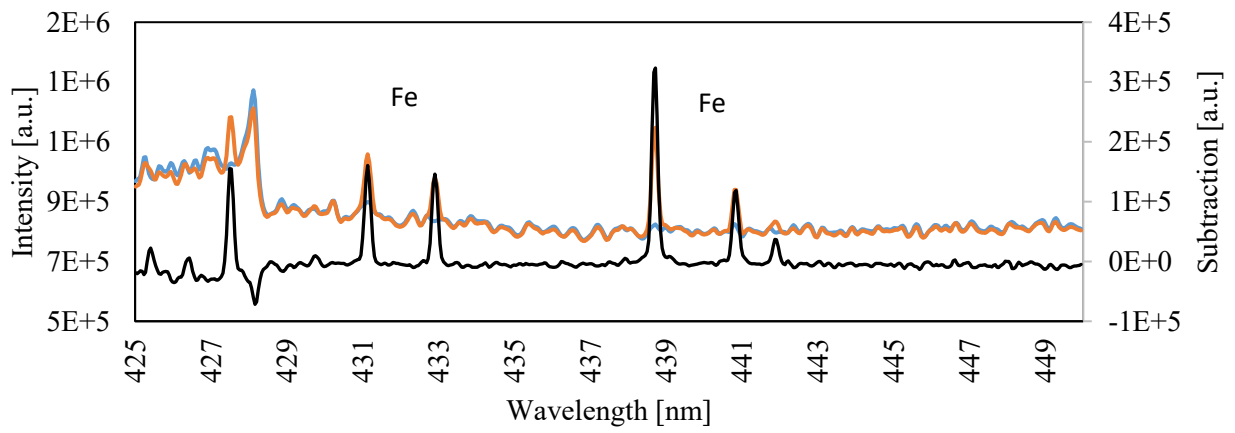
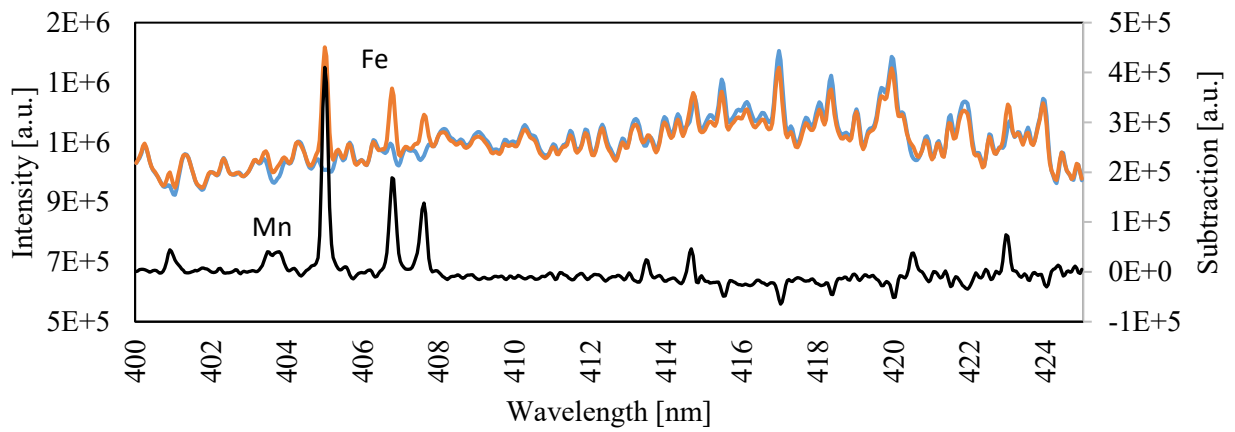
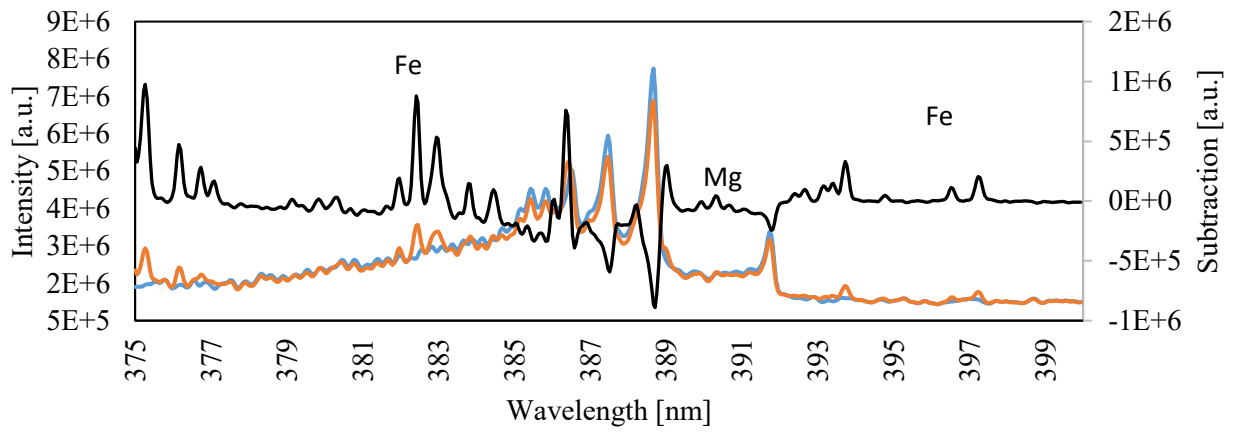
A4 BRAKE POWDER QUALITATIVE ANALYSIS SPECTRA

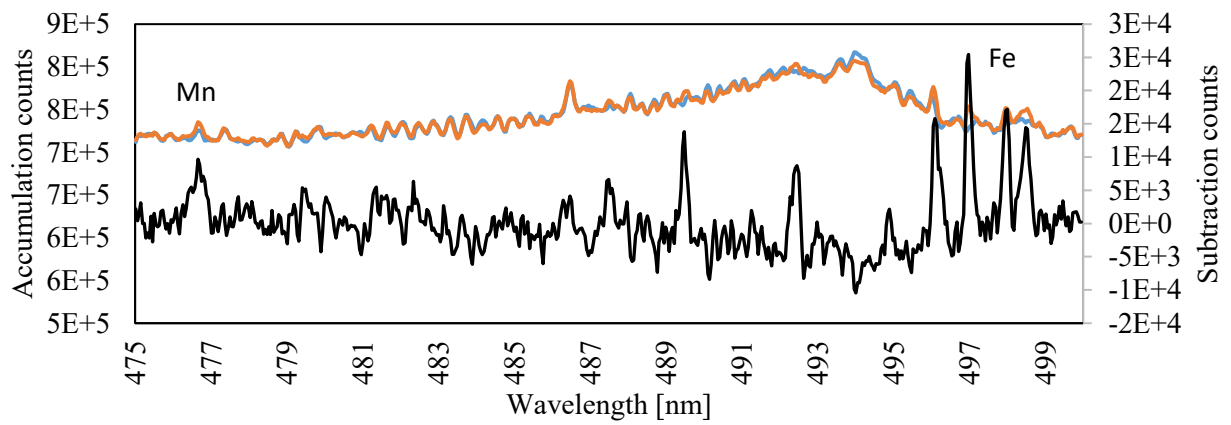
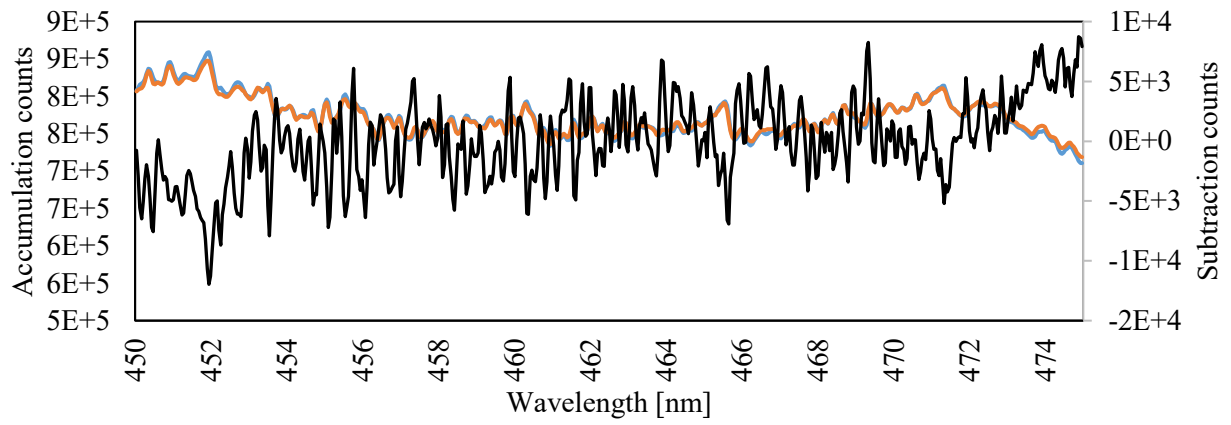
Acquired spectra from 200 nm to 500 nm, in 12 different windows with a range of 25 nm each (Figure 76) are reported. For each spectrum an accumulation of 10000 spectra is recorded. In each of the graph the emission spectrum of powders (orange) is reported, the emission spectrum of pure water (blue), used for background reference, and the signal obtained by the subtraction of the two (black). The subtraction is obtained by subtracting for each channel the water signal to the powder signal, in order to emphasize the presence of some emission lines.

Figure 76. Brakes powder qualitative spectra.











Loading effect of matrix compounds in aerosol LIBS measurements

D. Ciniglia^{a,b}, F. Migliorini^b, R. Dondé^b, P. Diwakar^c, S. De Iuliis^{b,*}

^a *INSTM & Chemistry for Technologies Laboratory, Department of Mechanical and Industrial Engineering, University of Brescia, Brescia, Italy*

^b *CNR ICMATE, Institute of Condensed Matter Chemistry and Technologies for Energy, Milano, Italy*

^c *Department of Mechanical Engineering, South Dakota School of Mines and Technology, 501 East Saint Joseph Street, Rapid City, SD 57701, United States of America*

ARTICLE INFO

Keywords:

LIBS
Aerosol
Matrix effect

ABSTRACT

In this work the effect of concomitant mass present in the probe volume on the Cu I LIBS signal in aerosol is studied for a correct interpretation in the quantitative analysis. Mg, Cr and Na are considered as matrix elements and the effect on the emission line is investigated increasing the loading of the elements with respect to copper concentration. Moreover, the role of the specific matrix compounds employed is also analyzed comparing Na chloride and Na acetate. The peak and base of Cu I LIBS signals as well as their corresponding peak/base ratios are detected increasing the concentration of the matrix compounds under analysis. To explore this matrix effect on the plasma, the temporal analysis of the peak and base of the Cu I emission line is performed with and without chromium in the highest concentration under analysis. Finally, temperature measurements are carried out in the different matrix conditions at relatively short delay time considering nitrogen neutral lines. The results obtained highlight the effect of the concomitant mass present in the probe volume, essentially related to the physical properties of the compounds considered. These properties can affect plasma conditions changing the temperature and the plasma temporal evolution, and ultimately affecting the LIBS signal.

1. Introduction

In recent decades, Laser-Induced Breakdown spectroscopy (LIBS) has been widely studied as a diagnostic tool for qualitative and quantitative elemental concentration measurements in different applications [1,2].

In this context, an important issue to face for the interpretation of the LIBS signal is the matrix effect, which is essentially related to the specific matrix considered (e.g. the presence of other solid/gas-phase elements in the probe volume) or also the different experimental conditions under analysis (e.g. temperature) [3–13]. These specific parameters are responsible for a modification in the line intensity of the analyte under study, which affects its calibration curve. Concerning LIBS analysis on aerosol, the presence of a gaseous matrix makes these measurements more suitable to be performed, being the matrix effect in gas phase significantly lower than in solid [14]. However, even in this case, the change in the line intensity due to specific matrix effects has to be considered for a correct interpretation of LIBS signals in the quantitative analysis.

Different works are reported in the literature concerning the study of matrix effects in LIBS measurements performed on aerosol particles or gas phase [3–11,15,16].

In particular, the role of the concomitant mass present in the probe volume on the physics of the particle vaporization as well as on the plasma conditions has been investigated, which results in a change in the response of the analyte under analysis. In this perspective, an interesting work was performed by Diwakar et al. [10], where changes in sodium or magnesium analyte emission response were investigated with the addition of concomitant mass to the aerosol. Adding copper, zinc, or tungsten the authors detected a 50% enhancement in analyte emission, which became negligible at a longer delay time. Furthermore, by measuring plasma temperature in the vicinity of the aerosol particles, a difference in bulk and local temperature was observed, probably related to the plasma energy required for vaporization and ionization of aerosol particle mass. Similar work was performed in ref. [11], where the matrix effect of copper in sodium and magnesium LIBS measurements was investigated. In particular, an enhancement of the neutral lines and a reduction in the ionic lines were observed. Such behavior was related to the increased electron density observed with copper addition, which promotes an enhancement in the recombination of ions with electrons, consequently increasing the neutral state population.

It is evident that for a deep comprehension of the matrix effects, the chemical and physical processes occurring in the plasma must be

* Corresponding author.

E-mail address: silvana.deiuliis@cnr.it (S. De Iuliis).

<https://doi.org/10.1016/j.sab.2023.106784>

Received 5 June 2023; Received in revised form 4 August 2023; Accepted 4 September 2023

Available online 9 September 2023

0584-8547/© 2023 Elsevier B.V. All rights reserved.

considered [17]. For example, the heat and mass diffusion rates within laser-induced plasma could be responsible for the presence of locally perturbed areas (in correspondence with the analyte) inside the bulk plasma. In this context, interesting work was performed by Asgill et al. [18], where bulk plasma and local (i.e., analyte-rich regions) temperatures were measured to detect plasma non-uniformity. As a result, a difference in these temperatures was observed, which was more significant at about 20–40 μs the delay time.

Latty and coworkers [19] recently investigated Cs and Na atomic emissions in a binary particle matrix with Cu using nanosecond and femtosecond lasers. An enhancement in the Na emission line and a reduction in the Cs emission line were detected with Cu present in the probe volume. This behavior was attributed to changes in the temperature induced by different aerosol compositions and perhaps to the upper energy levels involved. In particular, an enhancement of the signal was obtained in the case of higher upper energy levels, while a reduction corresponds to lower upper energy levels. Moreover, fs-LIBS significantly reduced this enhancement in the LIBS signals.

The works reported in the literature and the interpretation of the data obtained underlined the complexity of the processes involved in the laser-induced plasma, which are strictly related to the chemical and physical properties of the elements present in the probe volume and their combinations.

In this context, the role of the specific compounds present in the probe volume should be considered, as also suggested in the works of Gouegel and Eppler [20,21]. In these works, LIBS measurements were performed on soil and underwater conditions. In both cases, a significant difference was observed in the calibration curves and, consequently, in the detection limit of the analytes under analysis concerning the different chemical speciation of the compound considered. In particular, the analyte emission line intensity was proved to vary considering sulfate, chloride, or nitrate compounds. However, to our knowledge, no similar data are reported in the literature regarding the influence of chemical speciation on LIBS measurements performed on aerosol.

This work aims to further investigate the effects of concomitant mass present in the probe volume on the Cu I emission line to stress the role of the physical properties of the elements involved in the plasma. To this purpose, Mg, Cr, and Na were used as matrix elements. The effect on the signal was investigated by increasing the loading of these elements with respect to copper concentration. Moreover, the effect on Cu I emission line was investigated due to the specific matrix compounds. Moreover, it was investigated the effect on Cu I emission line due to the specific matrix compounds. To this purpose, Na chloride and Na acetate were used, and the effect was evaluated by increasing their loading in the probe volume. Changes in the LIBS signal and base were detected, varying the concentration of the matrix compounds. Combining the loading analysis with temperature measurements, the matrix effect observed under the different conditions is discussed in relation to the physical properties of the compounds used.

2. Experimental

The experimental setup employed for LIBS measurements is schematically represented in Fig. 1.

The fundamental beam of an Nd: YAG laser (1064 nm), working at 10 Hz repetition rate and energy of 370 mJ/pulse, is focused, using a 20 mm focal length lens, in the center of the measuring chamber to generate the plasma directly in the aerosol flow. The atmospheric pressure sample chamber comprises a PTFE six-way cell equipped with four optical windows. The chamber internal volume is 15 cm^3 , and the aerosol inlet and outlet have a diameter of 4 mm. LIBS signal is collected at 90° and focused using an 80 mm lens on an optic fiber. The radiation is analyzed with a spectrometer (Shamrock 500i spectrograph, coupled with an iStar 320 T, Andor Technology ICCD). The intensified CCD detector is synchronized with the Q-switch laser to change the delay time of the detector gate with respect to the laser shot. To detect atomic lines, a high-

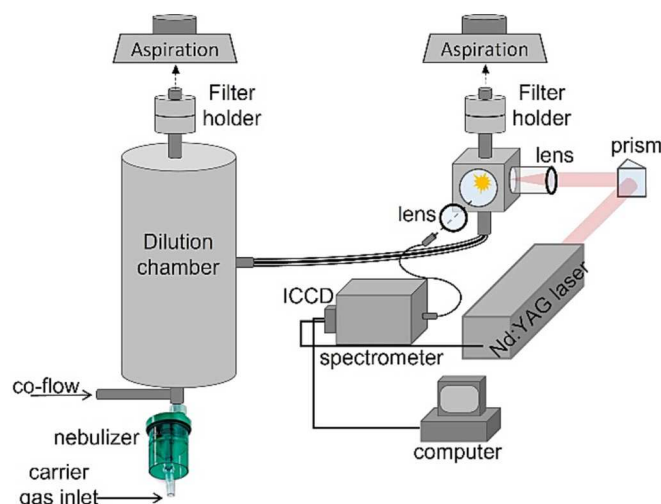


Fig. 1. Experimental setup for LIBS measurements.

resolution spectrograph grating is used (1200 grooves/mm) resulting in a 25 nm spectral window. Aerosol particles are produced by nebulizing solutions of salts (listed in Table 1), which are dissolved in ultra-purified deionized water. A medical nebulizer (HUDSON UP-DRAFT Nebulizer) filled with 15 ml solution is used to produce aerosol particles with a filtered air flow rate of 5 l/min. Under these conditions, droplets of about 3 μm in diameter are obtained. The droplets are then dried in a dilution chamber (40 l volume) connected to the nebulizer outlet. Here 5 l/min wet aerosol flow is mixed with 20 l/min dry air flow obtained by pumping at 25 l/min with an aspiration system (Edwards, E2M2) for LIBS measurements, by using another pumping system (DDS Aero, Tecora), 1 l/min flow rate of aerosol is isokinetically sampled from the dilution chamber and sent into the measuring chamber. The particles are then collected on a glass fiber filter positioned before the pump.

The role of Cr, Na, and Mg on Cu analyte LIBS signal was investigated to analyze the matrix multi-component effects. These elements were obtained from different salt solutions: nitrate, chloride, and acetate.

Then, samples were prepared by mixing 7.5 ml Cu 0.001 M solution with 7.5 ml matrix solution of different molar concentrations. This resulted in 400 $\mu\text{g}/\text{m}^3$ Cu concentration and varied matrix mass concentrations in the measuring chamber. The molar concentrations of the matrix solutions were properly prepared in order to obtain the mass concentration ratios reported in Table 1. In particular, 1:1, 1:3, and 1:5 refer to the Cu: (Mg, Cr, Na) mass concentration ratio. Moreover, in the case of Na, the role of the original compound was also investigated, namely chloride and acetate. In Table 1, the wavelengths of the emission lines used in the present work are also reported for each analyte, which were chosen as a compromise between the highest LIBS signal and reduced background structures interference.

3. Results

In Fig. 2, LIBS spectra corrected for the instrumental factor are

Table 1

For each element, the related compound used for the solutions, the wavelength of the analyzed emission line, and the concentration ratio with respect to Cu in the measuring chamber are reported.

	Compound	Wavelength [nm]	Element mass concentration Ratio
Cu	$\text{Cu}(\text{NO}_3)_2 \cdot 3\text{H}_2\text{O}$	324.7	
	NaCl	589	
Na	$\text{C}_2\text{H}_3\text{NaO}_2$	285.2	1:1–1:3–1:5
Mg	$\text{MgCl}_2 \cdot 6\text{H}_2\text{O}$	428.9	
Cr	C_6HCrO_6		

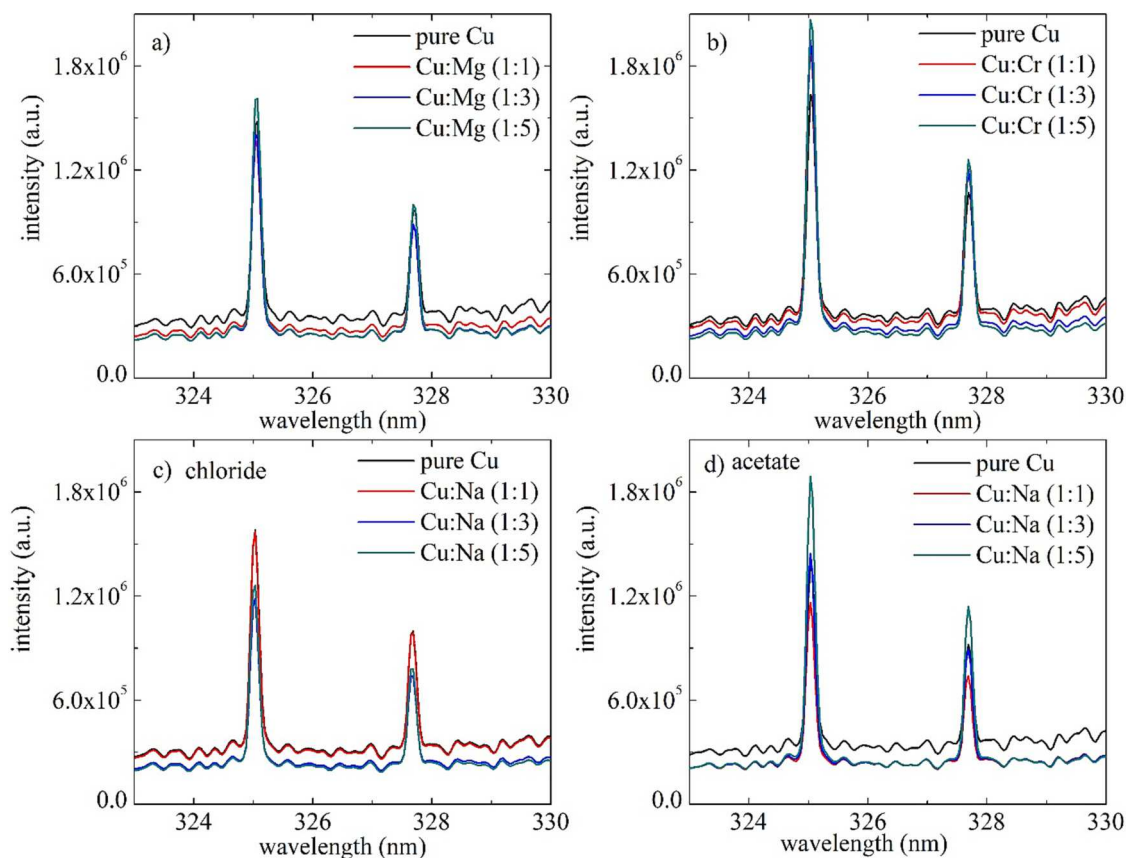


Fig. 2. Cu I emission spectra (delay = 30 μ s; gate = 100 μ s) with the addition of Mg chloride (a), Cr acetate (b), Na chloride (c), and Na acetate (d). In each plot, the curves refer to different concentration ratios (with respect to Cu) of the added element.

reported referring to Cu emission lines in the presence of different concentrations of Mg (a), Cr (b), and Na obtained from chloride (c) and acetate (d) salts. Spectra were collected with a detection gate of 100 μ s and a delay time of 30 μ s with respect to the laser occurrence, and result from an average over 3000 single shots. The temporal acquisition is set based on previously maximization of the signal. As it can be seen, a change in the peak and base is detected with the presence of other elements added to copper. As an overall trend, a decrease in the base is detected, while the emission line intensity exhibits different trend with element addition as described in the following.

The Peak-to-Base (P/B) of the 324.7 nm Cu emission line was considered to evaluate the matrix effect on the analyte signal. For the peak, the maximum value of the emission line was taken, and for the base, the root mean square (RMS) of the signal over 100 channels located half on the left and half on the right of the emission line was calculated. In Fig. 3, the P/B enhancement is reported as obtained from the ratio of Cu P/B with and without the matrix elements (Mg, Cr, and Na). As an overall trend, a significant loading effect of matrix elements is evident on P/B Cu values. A progressive enhancement is obtained increasing the concentration, which, however, is strictly related to the element and compound considered. In this context, the addition of chromium acetate exhibits the highest matrix effect on the Cu P/B value, starting from a 1:1 concentration ratio and reaching an enhancement of 75% with 1:5 loading. Moreover, from a direct comparison of Na Chloride and Na acetate matrix compounds, we can see that the addition of Na acetate is more effective in the enhancement produced.

To assess the impact of the Cu peak and base on P/B enhancement values shown in Fig. 3, the two values are separately reported versus the Cu:matrix concentration ratio in Fig. 4 (Cu:M in the figure). In this case, the peak is always the maximum value of the emission line, while the base is the root mean square value of the signal in the spectral region

between 326 and 327 nm. This choice is taken to be more representative of the plasma evolution. The uncertainties of our measurements were evaluated considering the semi-dispersion of five Cu line intensities obtained in pure Cu aerosol. In this way, the variabilities due to the laser energy, the nebulization, and dilution flow rate conditions are considered. As a result, a relative error of 9.6% for the line intensities and 4.2% for the base is obtained and reported as error bars in Fig. 4.

As already seen from the spectra in Fig. 2, the base (Fig. 4a) exhibits a global decreasing trend with loading, which is different for the matrix elements under analysis. However, close Cu base signals are reached at 1:5 Cu:M ratio in all cases. On the contrary, Cu peak values (Fig. 4b) are differently affected by each matrix element. It is worth noticing that Cr addition always promotes an enhancement of the Cu LIBS signal with loading.

Therefore, the increase in P/B with Cu:M shown in Fig. 3 is mostly due to the decrease in the base, although the entity of the enhancement is dependent on the matrix element.

To further explore the impact of matrix compounds on plasma conditions, the temporal analysis of the Cu line emission was performed for pure Cu and 1:5 Cu:Cr (Fig. 5), which corresponds to the highest enhancement. As shown in the figure, the base with Cr addition is lower than pure Cu, especially at early delay times (from 10 μ s to 20 μ s). This behavior is consistent with the previous analysis reported in Fig. 2. As for the peak, with Cr addition, an increase in the Cu emission line is detected, with the maximum shifted from 40 μ s delay time (for pure Cu) to 30 μ s delay time (with Cr addition). The behavior observed, namely the decrease in the background and the corresponding increase of the emission line at short delay times, accounts for a change in plasma conditions essentially due to plasma cooling.

Interestingly, at 60 μ s, the peak values are close, suggesting that the matrix effect can be considered negligible at long delay time.

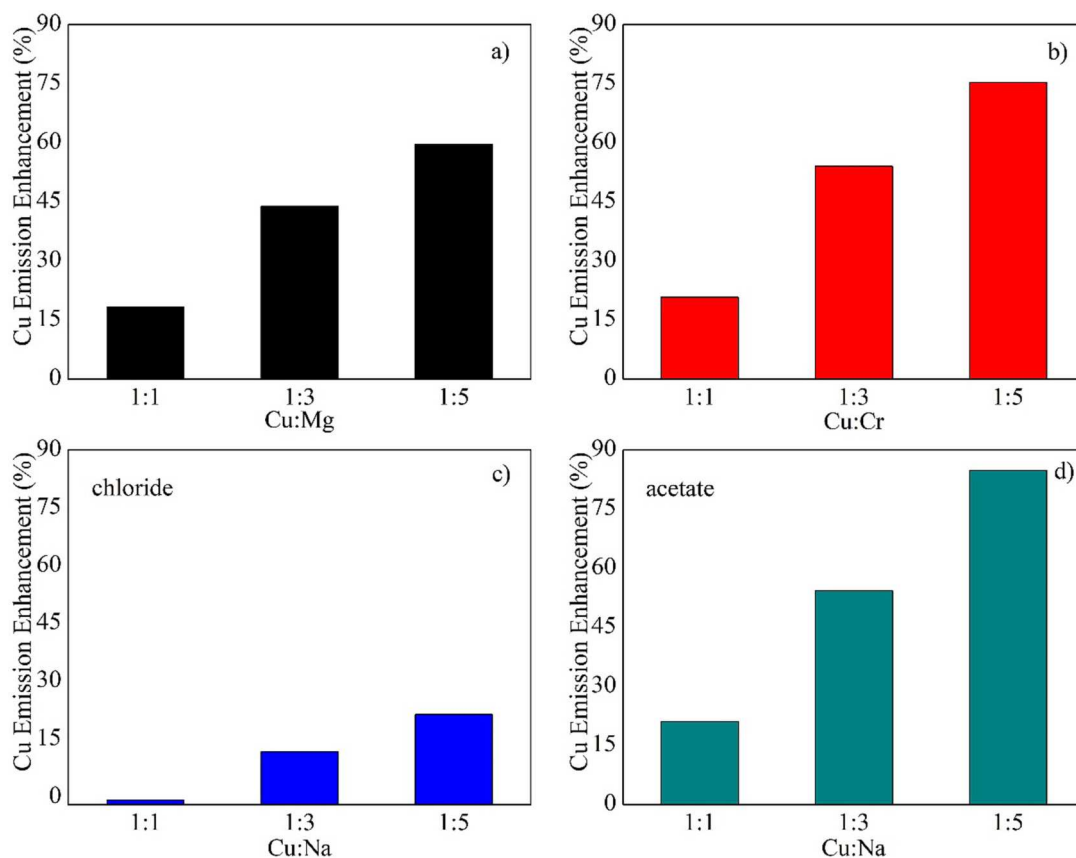


Fig. 3. Enhancement of the 324.7 nm Cu I emission signal with the addition of Mg chloride (a), Cr acetate (b), Na chloride (c), and Na acetate (d).

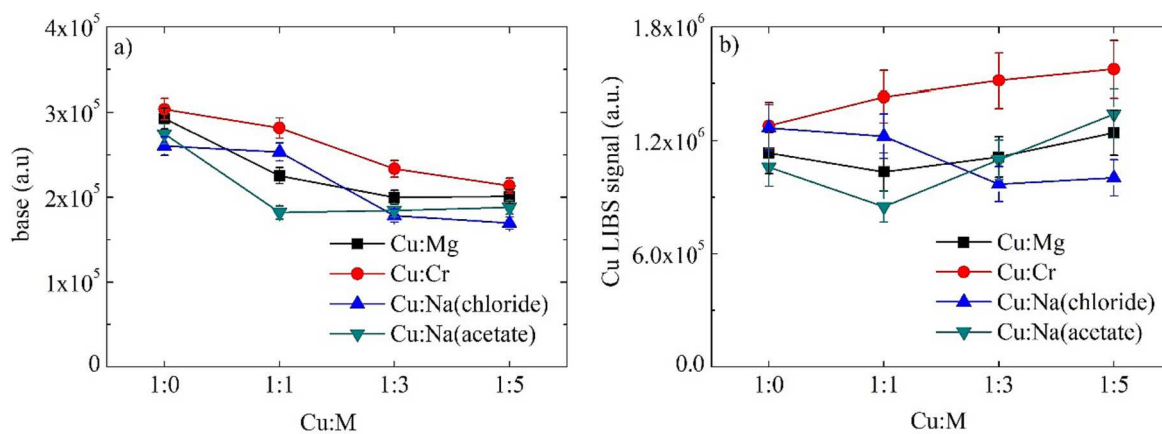


Fig. 4. Base intensity (a) and Cu I emission line (b) varying Cu:M ratio. Error bars are added at each point.

The plasma temperature is evaluated from the slope of the Einstein-Boltzmann equation. [20–24]. The analysis was performed on pure Cu and 1:5 Cu:M condition. Unfortunately, with our experimental set-up only two Cu lines can be detected, which are not sufficient for temperature measurements. Therefore, Ni I lines are considered, namely 410.0, 410.9, 746.8, 821.1 and 821.6 nm. Due to the substantial decrease of Ni I lines with delay, these measurements are carried out from 5 to 15 μ s delays. In Fig. 6, temperature measurements versus delay time (a) and an example of the Boltzmann plot (b) are reported. It can be seen that in presence of matrix elements, a decrease in plasma temperature is detected at a short delay time, consistently with the base behavior previously reported in Fig. 4, although data are collected in different time windows.

The decrease in plasma temperature is related to an enhancement in collisions and subsequent recombination between electrons and ions. As a result of these processes, an increase in Cu LIBS neutral lines can be obtained. Such behavior is strictly related to the chemical and physical properties of the elements and/or compounds involved [25,26]. The combination of the heat of vaporization (HV), binding energy (BE), and ionization energy (IE), these last related to the volatility, can play a role in the comprehension of the different behavior observed. For example, the similar trend of MgCl₂ and Na acetate, both in the base and the LIBS peak signal, can be attributed to their close heat of vaporization (of the compounds and atoms) and volatility (HVMg(chloride) = 33 kJ/mol [27]; HVNa(acetate) = 34 kJ/mol [28]; HVMg = 128 kJ/mol [29]; HVNa = 98 kJ/mol [29]). Comparing the two sodium compounds

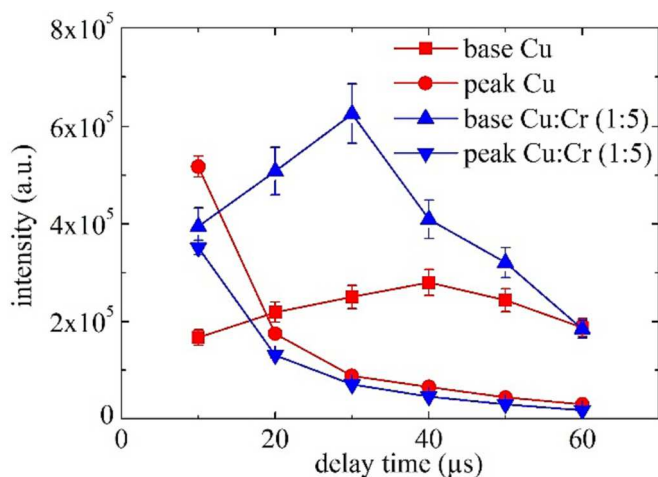


Fig. 5. Temporal analysis of the 324.7 nm Cu I emission line from 10 μ s to 60 μ s delay time, with a detection gate aperture of 10 μ s.

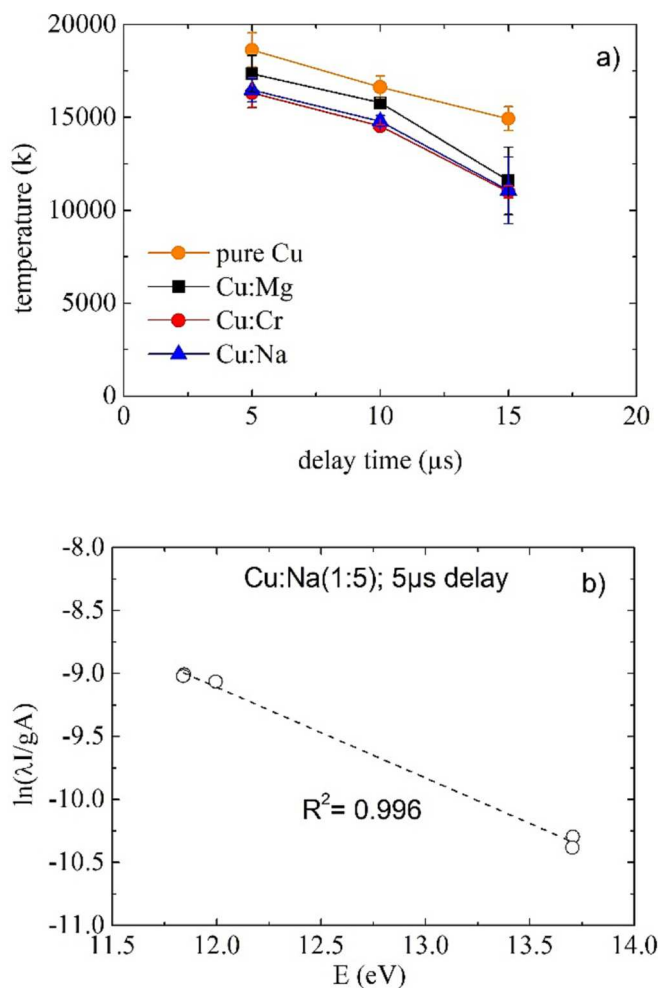


Fig. 6. a) Temperature versus delay time. Temperature values are obtained using N I emission lines (delay: 5–15 μ s; gate: 5 μ s) for pure Cu and 1:5 Cu:M. Na chloride was used for these measurements. b) Example of Boltzmann plot (Na:Cu(5:1)).

(chloride vs acetate), the relative binding energy and heat of vaporization accounts for the different effect on Cu LIBS signal. In fact, although both the compounds have similar binding energies (BE_{Na}

(chloride) = 7.98 eV [29]; $BE_{Na(acetate)}$ = 8.58 eV [29]) Na acetate has $HV = 34$ kJ/mol [28], which is much lower than the value of NaCl ($HV = 284$ kJ/mol [29]). In this case, a large part of the energy is needed to break the molecular bond and only a small quantity is left for ionization ($IE_{Na} = 8.92$ eV [29]). Therefore, few free electrons are available for the recombination with Cu ions, resulting in a slight change in the atomic line intensity. Considering Chromium acetate, to our knowledge few physical properties are available in the literature, and it is not possible to relate them to the enhancement observed.

These measurements highlight the complex mechanisms at the basis of the matrix effect. Matrix physical properties affect plasma conditions, changing temperature and plasma temporal evolution, substantially affecting the LIBS signal. However, the relation between the LIBS enhancement and the matrix physical properties cannot be a priori predicted at this stage, considering that only few compounds/analytes are here investigated. As a final remark, in line with these observations, performing LIBS measurements at a relatively long delay time, when these chemical and physical processes triggered by matrix effects are quenched, could be a possible strategy to be adopted.

4. Conclusions

In this work, the effect of the concomitant mass present in the probe volume on the Cu LIBS emission line was investigated. To this purpose, Mg, Na and Cr were added to Cu aerosol changing the loading.

Increasing the matrix concentration, a decrease in the LIBS signal base is detected independently from the matrix element, which however plays an important role in the entity of the Cu P/B enhancement. Such effect is more pronounced for Cr addition. In this case, the analysis of the temporal behavior of both base and Cu peak reveals a change in the plasma conditions with the presence of concomitant mass in the probe volume. In fact, the decrease in the base, especially in the first micro-seconds delay and a shift of the Cu peak towards short delay times confirms a decrease in the plasma temperature probably due to quenching processes. Physicochemical matrix properties, such as heat of vaporization, binding energy, and ionization energy help in understanding the mechanism occurring in the probe volume but affect the plasma conditions in a not predictable way. On a final note, at high matrix loading, it is suggested performing LIBS measurements at long delay time, when the chemical and physical processes triggered by matrix effects are quenched.

Declaration of Competing Interest

The authors declare that they have no known competing financial interests or personal relationships that could have appeared to influence the work reported in this paper.

Data availability

Data will be made available on request.

Acknowledgments

The authors would like to acknowledge the financial support by F.A. N.G.H.I project, an innovation project in the framework of European funding ROP ERDF 2014–2020.

The authors would like also to acknowledge the financial support from CNR in the framework of the Short-Term Mobility (STM) Program.

References

- [1] Z. Yang, J. Ren, M. Du, Y. Zhao, K. Yu, Enhancement laser-induced breakdown spectroscopy for heavy metal detection in agriculture: a review, *Sensors* 22 (2022) 5679, <https://doi.org/10.3390/s22155679>.

- [2] Q. Zhang, Y. Liu, Review of in-situ online LIBS detection in the atmospheric environment, *At. Spectrosc.* 43 (2) (2022) 15–185, <https://doi.org/10.46770/AS.2021.609>.
- [3] W. Wang, L. Sun, P. Zhang, T. Chen, L. Zheng, L. Qi, Study of matrix effects in laser-induced breakdown spectroscopy by laser defocus and temporal resolution, *J. Anal. At. Spectrom.* 36 (2021) 197, <https://doi.org/10.1039/d1ja00179e>.
- [4] B.C. Windom, P.K. Diwakar, D.W. Hahn, Dual-pulse laser induced breakdown spectroscopy for analysis of gaseous and aerosol systems: plasma-analyte interactions, *Spectrochim. Acta Part B* 61 (2006) 788–796, <https://doi.org/10.1016/j.sab.2006.06.003>.
- [5] R.L. Gleason, D.W. Hahn, The effects of oxygen on the detection of mercury using laser-induced breakdown spectroscopy, *Spectrochim. Acta Part B* 6 (2001) 419–430, [https://doi.org/10.1016/S0584-8547\(01\)00169-0](https://doi.org/10.1016/S0584-8547(01)00169-0).
- [6] G. Buckley, Laser-induced breakdown spectroscopy for toxic metal emission measurements: experimental considerations and oxygen quenching, *Environ. Eng. Sci.* 22 (2) (2005) 195–204, <https://doi.org/10.1089/ees.2005.22.195>.
- [7] N. Palazzo, F. Migliorini, R. Dondè, S. Maffi, S. De Iulii, Influence of oxygen addition to the carrier gas on laser-induced breakdown spectroscopy measurements on aerosols, *Spectrochim. Acta Part B* 115 (2016) 1–7, <https://doi.org/10.1016/j.sab.2015.10.012>.
- [8] D.A. Redoglio, N. Palazzo, F. Migliorini, R. Dondè, S. De Iulii, Laser-induced Breakdown spectroscopy analysis of Lead aerosol in nitrogen and air atmosphere, *Appl. Spectrosc.* 72 (4) (2018) 584–590, <https://doi.org/10.1177/0003702817742314>.
- [9] A. Molina, C.R. Shaddix, S.M. Sickafoose, P.M. Walsh, L.G. Blevins, Effect of temperature and CO₂ concentration on laser-induced breakdown spectroscopy measurements of alkali fume, *Spectrochim. Acta Part B* 60 (2005) 1103–1114, <https://doi.org/10.1016/j.sab.2005.06.005>.
- [10] P.K. Diwakar, P.B. Jackson, D.W. Hahn, The effect of multi-component aerosol particles on quantitative laser-induced breakdown spectroscopy: consideration of localized matrix effects, *Spectrochim. Acta Part B* 62 (2007) 1466–1474, <https://doi.org/10.1016/j.sab.2007.10.001>.
- [11] E.J. Judge, J. Colgan, K. Campbell, J.E. Barefield II, H.M. Johns, D.P. Kilcrease, S. Clegg, Theoretical and experimental investigation of matrix effects observed in emission spectra of binary mixtures of sodium and copper and magnesium and copper pressed powders, *Spectrochim. Acta Part B* 122 (2016) 142–148, <https://doi.org/10.1016/j.sab.2016.06.004>.
- [12] B.C. Windom, D.W. Hahn, Laser ablation-laser induced breakdown spectroscopy (LA-LIBS): a means for overcoming matrix effects leading to improved analyte response, *J. Anal. At. Spectrom.* 24 (12) (2009), <https://doi.org/10.1039/b913495f>.
- [13] D.A. Goncalves, G.S. Senesi, G. Nicolodelli, Laser-induced breakdown spectroscopy applied to environmental systems and their potential contaminants. An overview of advances achieved in the last few years, *Trend. Environ. Analyt. Chem.* 30 (2021), e00121, <https://doi.org/10.1016/j.teac.2021.e00121>.
- [14] P.K. Diwakar, K.H. Loper, A.-M. Matiaske, D. Hahn, Laser-induced breakdown spectroscopy for analysis of micro and nanoparticles, *J. Anal. At. Spectrom.* 27 (2012) 1110–1119, <https://doi.org/10.1039/C2JA30012E>.
- [15] E.R. Wainwright, C.J. Miller, L. Giri, R.A. Pesce-Rodriguez, C.-C. Wu, J.L. Gottfried, Influence of silicon particle morphology on laser-induced plasma properties, *Spectrochim. Acta Part B* 199 (2023), 106597, <https://doi.org/10.1016/j.sab.2022.106597>.
- [16] D.J. Palasti, L.P. Villy, A. Kohut, T. Ajtai, Z. Geretovszky, G. Galbacs, Laser-induced breakdown spectroscopy signal enhancement effect for argon caused by the presence of gold nanoparticles, *Spectrochim. Acta Part B* 193 (2022), 106435, <https://doi.org/10.1016/j.sab.2022.106435>.
- [17] P.K. Diwakar, S. Groh, K. Niemax, D.W. Hahn, Study of analyte dissociation and diffusion in laser-induced plasmas: implications for laser-induced breakdown spectroscopy, *J. Anal. At. Spectrom.* 25 (2010) 1921–1930, <https://doi.org/10.1039/C0JA00063A>.
- [18] M.E. Asgill, S. Groh, K. Niemax, D.W. Hahn, The use of multi-element aerosol particles for determining temporal variations in temperature and electron density in laser-induced plasmas in support of quantitative laser-induced breakdown spectroscopy, *Spectrochim. Acta Part B* 109 (2015) 1–7, <https://doi.org/10.1016/j.sab.2015.04.005>.
- [19] K.S. Latty, K.C. Harting, Elemental fractionation in aerosol laser-induced breakdown spectroscopy with nanosecond and femtosecond laser ablation, *Spectrochim. Acta Part B* 202 (2023), 106648, <https://doi.org/10.1016/j.sab.2023.106648>.
- [20] C. Goueguel, D.L. McIntyre, J. Jain, A.K. Karamalidis, C. Carson, Matrix effect of sodium compounds on the determination of metal ions in aqueous solutions by underwater laser-induced breakdown spectroscopy, *Appl. Opt.* 54 (19) (2015) 6071–6079, <https://doi.org/10.1364/AO.54.006071>.
- [21] A.S. Eppler, D.A. Cremers, D.D. Hickmott, M.J. Ferris, A.C. Koskelo, Matrix effects in the detection of Pb and Ba in soils using laser-induced breakdown spectroscopy, *Appl. Spectrosc.* 50 (9) (1996) 1175–1181, <https://doi.org/10.1366/0003702963905123>.
- [22] B. Bousquet, V. Gardette, V. Motto Ros, R. Gaudioso, M. Dell'Aglio, A. De Giacomo, Plasma excitation temperature obtained with Boltzmann plot method: significance, precision and accuracy, *Spectrochim. Acta Part B* 204 (2023), 106686, <https://doi.org/10.1016/j.21b.2023.106686>.
- [23] A. De Giacomo, R. Gaudioso, M. Dell'Aglio, A. Santagata, The role of continuum radiation in laser induced plasma spectroscopy, *Spectrochim. Acta Part B* 65 (2020) 385–394, <https://doi.org/10.1016/J.SAB.2010.03.016>.
- [24] G. Cristoforetti, A. De Giacomo, M. Dell'Aglio, S. Legnaioli, E. Tognoni, V. Palleschi, N. Omenetto, Local thermodynamic equilibrium in laser-induced breakdown spectroscopy: beyond the McWhirter criterion, *Spectrochim. Acta Part B* 65 (2010) 86–95, <https://doi.org/10.1016/j.sab.2009.11.005>.
- [25] J.S. Todoli, L. Gras, V. Hernandez, J. Mora, Elemental matrix effects in ICP-AES, *J. Anal. At. Spectrom.* 17 (2002) 142–169, <https://doi.org/10.1039/B009570M>.
- [26] G.C.-Y. Chan, W.-T. Chan, X. Mao, R.E. Russo, Investigation of matrix effects in inductively coupled plasma-atomic emission spectroscopy using laser ablation and solution nebulization - effect of second ionization potential, *Spectrochim. Acta Part B* 56 (1) (2001) 77–92, [https://doi.org/10.1016/S0584-8547\(00\)00295-0](https://doi.org/10.1016/S0584-8547(00)00295-0).
- [27] Y. Li, D. Yan, Y. Guo, S. Wang, T. Deng, Studies on magnesium chloride hexahydrate as phase change materials, *Appl. Mech. Mater.* 71-78 (2011) 2598–2601, <https://doi.org/10.4028/www.scientific.net/AMM.71-78.2598>.
- [28] G. Wang, C. Xu, W. Kong, G. Englmair, J. Fan, G. Wei, S. Furbo, Review on sodium acetate trihydrate in flexible thermal energy storages: properties, challenges and applications, *J. Energy Storag.* 40 (2021), 102780, <https://doi.org/10.1016/j.est.2021.102780>.
- [29] D.R. Lide, CRC handbook of chemistry and physics, 84th Edition, *J. Am. Chem. Soc.* 126 (5) (2004) 1586, <https://doi.org/10.1021/ja0336372>.



Characterization of nebulization generated aerosol particles dispersion and deposition by total reflection X-ray fluorescence

Davide Ciniglia, Paola Cirelli, Fabjola Bilo, Alessandra Zanoletti, Antonella Cornelio, Silvana De Iuliis, Laura Eleonora Depero, Elza Bontempi, Maria Grazia Perrone, Paolo Lopinto, Marco Zonca & Laura Borgese

To cite this article: Davide Ciniglia, Paola Cirelli, Fabjola Bilo, Alessandra Zanoletti, Antonella Cornelio, Silvana De Iuliis, Laura Eleonora Depero, Elza Bontempi, Maria Grazia Perrone, Paolo Lopinto, Marco Zonca & Laura Borgese (2022): Characterization of nebulization generated aerosol particles dispersion and deposition by total reflection X-ray fluorescence, Aerosol Science and Technology, DOI: [10.1080/02786826.2022.2155104](https://doi.org/10.1080/02786826.2022.2155104)

To link to this article: <https://doi.org/10.1080/02786826.2022.2155104>



Published online: 15 Dec 2022.



Submit your article to this journal [↗](#)





View related articles [↗](#)



View Crossmark data [↗](#)



Characterization of nebulization generated aerosol particles dispersion and deposition by total reflection X-ray fluorescence

Davide Ciniglia^{a,b,c}, Paola Cirelli^d, Fabjola Bilo^{a,e}, Alessandra Zanoletti^a, Antonella Cornelio^a, Silvana De Iulii^b, Laura Eleonora Depero^{a,e} , Elza Bontempi^{a,e}, Maria Grazia Perrone^c, Paolo Lopinto^c, Marco Zonca^c, and Laura Borgese^{a,d} 

^aINSTM & Chemistry for Technologies Laboratory, Department of Mechanical and Industrial Engineering, University of Brescia, Brescia, Italy; ^bCNR ICMATE, Institute of Condensed Matter Chemistry and Technologies for Energy, Milano, Italy; ^cTCR Tecora® Srl, Cogliate, Italy; ^dDepartment of Information Engineering, University of Brescia, Brescia, Italy; ^eSMART SOLUTIONS s.r.l., Brescia, Italy

ABSTRACT

To prevent air pollution and achieve air quality regulations, it is essential to develop analytical techniques that can determine the concentration of metals in aerosol particles, both in the gas phase and after collection onto filters. Total reflection X-ray fluorescence spectroscopy (TXRF) and laser-induced breakdown spectroscopy (LIBS) are emerging as complementary techniques for determining the elemental composition of aerosol particles. The accuracy of their results relies on calibration methods based on aerosol and multi-element filters representative of the on-line measurement conditions and particulate collection for off-line measurement, respectively. In this paper we propose a novel methodology for characterizing nebulization generated aerosol particles dispersion and deposition by means of TXRF to assess the use of an aerosol generator to produce calibration samples for LIBS and TXRF analysis. Particles concentration and size distribution of the aerosol produced by nebulizing a Cu salt aqueous solution are measured inside a glove box modifying the production parameters and collecting the corresponding particulate deposited on reflectors. The most stable conditions are observed at average flow rate and selected for studying the aerosol spatial distribution. The Cu mass collected on reflectors positioned at a fixed distance and radial geometry with respect to the nozzle exit is measured by TXRF and increases linearly with time. Results suggest that this experimental configuration could be used to realize calibration samples for TXRF analysis representative of particulate deposition. The use of these aerosols as LIBS calibration samples could lead to significant errors due to the observed flow asymmetry.

ARTICLE HISTORY

Received 9 August 2022
Accepted 24 November 2022

EDITOR

Mark Swihart

1. Introduction

Air pollution represents a major health, environmental, societal, and economic burden, caused by natural (volcanoes, dust winds) and anthropogenic (industry, transportation, agricultural, household) sources. Although over recent decades air quality in Europe has improved, air pollution levels in many places still exceed EU standards and World Health Organization guidelines (European Commission 2017; WHO Global Air Quality Guidelines 2021). Particulate matter (PM) is among the six primary pollutants in air, which thresholds are set by the European Air Quality standards (European Parliament; European Council 2008). Chemical composition, particle size, and absolute particle mass density all vary significantly depending on the origins of the PM emissions as well as the

surrounding environment and transport conditions. The monitoring of toxic metals, especially Pb, Hg, As, Cd, and Ni, which are parts of long-range transboundary air pollution (Taurino et al. 2020; European Parliament; European Council 2008), is especially crucial to avoid the negative impact those metals have on human health and ecosystems. Additionally, some air pollution information systems include other metals classified as hazardous, persistent, or bio-accumulative (e.g., Cr, Cu, Zn, Pt, Rh) (Briffa, Sinagra, and Blundell 2020). The chemical analysis of PM is typically done using regulated analytical techniques like Atomic Absorption (AAS) or Inductively Coupled Plasma (ICP) Spectrometry (Kapiamba et al. 2022; Kashani and Mostaghimi 2010; Maestre, Todolí, and Mermet 2004; EU 2004). PM is collected onto membrane

filters made of different materials like quartz, PTFE, PC, cellulose (Goncalves, Domínguez, and Alvarado 2008), which are then solubilized in strong acids in a labor- and energy-intensive process that could lead to contamination and material loss (Wang, Yang, and Ke 1996). These methods are supported by several standards for workplaces and environment air (ISO 15202, EN14902) and they enable accurate analysis with very low limit of detection (ng/m^3). These are not sustainable or environmentally friendly methods, and they cannot provide information on short time polluting emissions. Therefore, methods and approaches that enable complementary quantitative elemental measurement both directly at the emission and indirectly on filters or other collection media are desirable.

Laser Induced Breakdown Spectroscopy (LIBS) is a promising simultaneous multi-elemental technique which allows to measure PM online directly in the aerosol and offline after collection on air filtering media or impactor stages. If the elements concentration in the air volume is higher than the detection limit, quick information about it can be obtained when utilizing LIBS for online aerosol analysis. Since significant enrichment can be accomplished with the collecting time, lower concentration can be found by analyzing PM offline (Fortes et al. 2013). Only few studies compare the analytical performance of these two approaches (Gallou et al. 2011). Although LIBS application at the exhaust of combustion systems is demonstrated (Hahn and Omenetto 2012), its extension to air quality monitoring is still challenging since the detection limits achieved are above the regulatory limits (Diaz and Hahn 2021; Carranza, Iida, and Hahn 2003; Carranza and Hahn 2002). The availability of controlled and well characterized aerosols and the implementation of specific quantification procedures are fundamental to perform LIBS instrumental calibration (Redoglio et al. 2018; Palazzo et al. 2016; Dutouquet et al. 2014).

Another promising alternative multi-element technique is X-Ray Fluorescence (XRF), which is quicker and less expensive than the regulated aforementioned procedures while also being more environmentally friendly, sustainable, and nondestructive (Yatkin, Gerboles, and Borowiak 2012; Brown et al. 2010; Niu et al. 2010). Despite this, its applications to PM are still scarce, especially in Europe, due to a lack of standardized methods and reference materials, while the American Environmental Protection Agency developed a method (U.S. EPA 1999) for XRF analysis of 44 elements on filters with quantification limits in the ng/m^3 . Total reflection XRF (TXRF) and XRF

under grazing incidence (GI) are known for achieving higher sensitivities, thanks to the instrument geometrical configuration enhancing the fluorescence emissions and collection. These techniques showed high potential for the analysis of PM collected on quartz reflector (Kayser et al. 2022) and quartz fiber filters (Wadinga Fomba et al. 2020). All the commercial TXRF instruments can be used to analyze PM filters treated with a procedure codenamed SMART STORE®, which consists in laminating the filter between two sheets of adhesive polymer and cutting it to the correct shape and size, while preserving the PM composition preventing contamination and loss and simplifying handling (Bacon et al. 2021).

Any analytical technique relies on instrumental calibration and development of quantitative analysis methods based on reference materials and calibration samples. A few certified reference materials (CRMs) of PM used in XRF spectrometry are available: NIST 2783, NIST RM 8786 from the National Institute of Standards & Technology (Gaithersburg, MD 20899, USA), and CRM SL-MR-2-PSF-01 from the Laboratoire National de Métrologie et d'Essais (LNE) (1 Gaston Boissier, 75724 Paris Cedex 15, France) Currently, there is a lack of CRM for PM and it doesn't exist any fit-for-purpose for LIBS, TXRF, and XRF under GI. Reference materials and calibration samples are used to determine the linear calibration relationship between the element signal and the concentration for quantification purposes, as demonstrated in recent studies of XRF under GI (Cirelli et al. 2022; Borgese et al. 2020). The need for this kind of material is also stressed for metrology reasons. The recent European EMPIR (European Metrology Program for Innovation and Research) project AEROMET (www.aerometproject.com/about), is indeed aiming to improve the measurements of particulate mass, size, and concentration of atmospheric aerosol particles by TXRF. Among the project main objectives there is the establishment of traceable validated methods to determine major components of PM collected directly on X-ray reflectors by means of cascade impactors and, on this purpose, reference materials are required. Indeed, the stages of a cascade impactor typically contain arrays of nozzles and thus produce test samples where PM is non homogeneously distributed over a large surface, and in such conditions a correct quantification is a difficult task. In TXRF analysis, quantification is mostly performed by internal standard (IS) calibration and rarely by external calibration. Yttrium is commonly used as IS element for quantification (Wastl et al. 2013), as not widely present in the atmospheric PM. To ensure a uniform IS element

distribution, a nanoliter deposition unit is sometimes used and the spot patterns produced by the cascade impactor are re-pipetted (Prost, Wobrauschek, and Strelt 2017).

In this context, the creation of properly characterized aerosols for calibrating online analysis methodologies as well as for the creation of reference and calibration samples with known amounts of deposited PM is of great interest. The latter samples can be used for calibration of offline analysis methodologies considering the matrix effect due to the substrate used for the aerosol particles deposition. This would represent an interesting new approach to produce reference materials. As a proof of concept for the use of an aerosol generator to realize aerosol for calibrating online LIBS and particulate deposition for offline TXRF, we designed a model experiment to study aerosol particles dispersions and depositions. Concentration and size distribution of aerosol particles created by nebulization of Cu salt aqueous solutions are determined by using an optical particle counter (OPC), changing the flow rate of the aerosol production unit. The best experimental conditions to obtain a stable aerosol particles concentration in the system are retrieved and used for further investigation of the radial distribution of the particles across the aerosol. On this purpose particulate is collected on reflectors positioned at five different locations at a fixed distance from the generator nozzle. Quantitative analysis of the Cu mass of particulate is performed by TXRF using Ga as internal standard for calibration, loaded on the reflectors before starting the experiment.

2. Materials and methods

The 400 L-sized glove box (dimensions 90 cm × 64 cm × 71 cm, L × W × H) contains the experimental setup. The arrangement is as illustrated in Figure 1 and roughly scales the actual distribution of the apparatus's parts.

In the center of the glove box is the aerosol generator (Aerosol Generator 7.811 GRIMM Aerosol Technick GmbH & Co). A solution of copper nitrate hydrate salt ($\text{Cu}(\text{NO}_3)_2 \times \text{H}_2\text{O}$) in ultra-pure deionized water with a molar concentration of 0.01 yields 0.64 g/L is nebulized to create the aerosol. An optical particle counter (OPC) is used to measure the size distribution and production of aerosol particles (OPC model EDM 107 GRIMM Aerosol Technick GmbH & Co) If you're looking at the aerosol generator from the back, the OPC is inserted inside the chamber glove box, 15 cm to the right of the aerosol generator's output (see Figure 1). With a measurement frequency

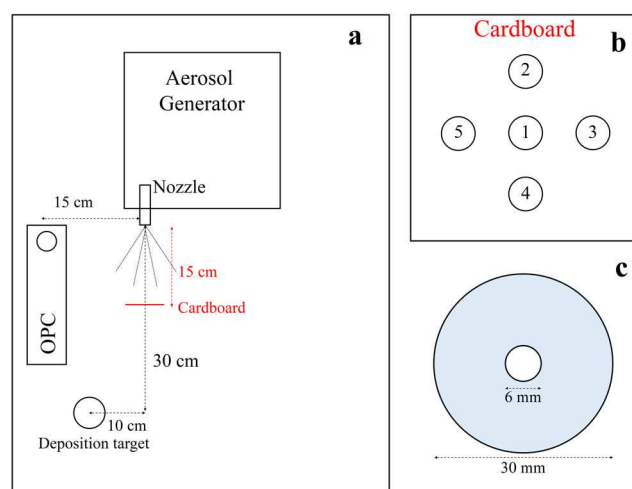


Figure 1. (a) Experimental set-up for generation and collection of aerosol particles, located inside a glovebox; (b) samples position on the cardboard, with number 1 positioned at the same height as the exit nozzle; (c) samples masks (light blue), with the central area available for deposition and TXRF analysis.

of 6 seconds, the OPC samples aerosol particles at 1.2 L/min and splits them into 31 dimensional classes ranging in diameter from 0.25 μm to >32 μm .

Three flow rate values of the aerosol nebulizer are tested: 2.5, 4 and 5.5 L/min, respectively. These values are chosen in accordance with the manufacturer's recommended flow rate range. In the provided flow rate range, 4 L/min is selected as the average value, while the minimum and maximum flow rate values are 2.5 L/min and 5.5 L/min, respectively, which are inferred from the flow rate vs. pressure graph in the instrumental manual. One may anticipate that the flow rate under study would increase as the particle concentration increased. In each condition, 90 min measurements are carried out consisting into three sets of 30 min each, namely: with the aerosol generator switched on, with the aerosol generator switched off and the particulate let deposit, and finally with the aspiration system under operation to clean the glove box before the following test. For the first two parts, the aspiration in the glove box is turned off. It was confirmed that the particle concentration in the glove box was lower than the background level following each 90-min testing. Because the goal of these tests was to determine the aerosol nebulizer settings to utilize in the study of the radial distribution, the experiment was run just once for each flow rate. The experiment's goal was not to find average or median values, therefore repeating it would simply have confirmed the trends that were already established under the three flow rate settings.

Details of the experimental conditions are reported in Table 1.

Table 1. Aerosol generator setting conditions investigated: pressure, air flow and nebulized solution in 30 min.

	Low	Medium	High
Pressure (mbar)	160	340	660
Air flow rate (l/min)	2.5	4	5.5
Nebulized solution (ml)	0.25	1.0	2.5

Table 1 displays the flow rates, pressure, and amount of solution nebulized in 30 min. The aerosol particles generation, deposition and aspiration are continuously analyzed through the OPC, monitoring the number of particles per unit volume (N/l) present in the measurement glove box and for each dimensional class.

To monitor the particulate deposition after dispersion in the glove box without being influenced by the largest droplets or the coagulated droplets departing from the nozzle and dropping down along the axis, the reflector was placed 30 cm in front of the nebulizer and out of the axis 10 cm lateral from the nozzle exit. The polycarbonate reflector is covered with a Parafilm mask to select the deposition area with a diameter of 6 mm (see Figure 1), which is the active area for TXRF measurements. A standard gallium solution with a Ga mass of 87 ng is deposited on the TXRF measurement region of the reflector. Particles rebounding is thought to be minor, thus nothing further is put to the surface to prevent it.

The radial distribution of the particulate in the glove box at 15 cm from the exit nozzle of the aerosol generator is investigated, assuming a cone distribution of the aerosol particles coming out from the nozzle (Beale and Reitz 1999). Figure 1a depicts the location of the 5 reflectors on a cardboard piece that was positioned perpendicular to the aerosol flow. Figure 1b depicts the collection's relative position. The four additional reflectors are on the left, above, to the right, and below the center one. The central reflector is positioned at the same height as the nebulizer nozzle. By gathering the particulate for impact to the surface of reflectors in this manner, the radial distribution of the aerosol particles may be determined. To sample at 30 s, 60 s, 90 s, 120 s, 240 s, and 360 s, the same reflectors are employed. The samples are set up on the cardboard to catch the particulate for 30 s. The samples are taken out for TXRF measurements and then put back in place for another 30 s. This process is cumulatively repeated for the other collecting times (for a total exposure of 60 s).

For TXRF analysis a S2 Picofox Bruker is used, equipped with a Mo anode x-ray tube operating at 50 kV and 750 μ A, multilayer monochromator, silicon drift detector (SDD) with 30 mm² area and energy

resolution was 165 eV at 5.9 keV. Samples were irradiated for 120 s for the radial distribution investigation and for 600 s for the deposition studies. Qualitative analysis and spectra deconvolution are performed with the spectrometer software (Spectra 4.0, Bruker). The software database is used to manually identify elements.

3. Results and discussion

Figure 2 shows the evolution of the total number of aerosol particles for the various flow rates under consideration, 2.5 (low), 4.5 (medium) and 5.5 (high) L/min, over the whole 31-dimensional classes.

The three conditions of generation (a), deposition (b) and aspiration (c) are highlighted. The background mean value of $(3.93 \pm 0.42) \cdot 10^5$ N/L was determined outside the glove box before the experiment began and is displayed in the same figure for comparison.

It is clear from analyzing the three plots shown in Figure 2 that the medium and high flow rates exhibit the same trend in time with a marked increase in the concentration of aerosol particles during the generation stage, in contrast to the trend seen with the low flow rate. At the medium flow rate of 4 L/min, the concentration grows in the production region and reaches a plateau value of 2×10^6 N/L. It may be inferred that with these settings it is possible to have a constant aerosol particles concentration in the glove box. A noticeable reduction in concentration is observed during deposition and aspiration, being more pronounced with the latter. There is evidence that it is impossible to achieve stable concentration conditions in the glove box when the aerosol generator operates at its maximum flow rate of 5.5 L/min because a steep increase in the number concentration of the aerosol particles (from 5×10^5 N/L to 5×10^6 N/L) is observed until the generator is turned off at 30 min. When it comes to the medium flow rate, it is seen that the concentration decreases significantly during the deposition and aspiration stages, becoming much more pronounced during the aspiration. It is difficult to say whether aerosol particles are produced at the low flow rate. Once the glove is closed, the aerosol particle concentration does indeed fall below the background level. This might be as a result of the effect of deposition persisting into the experiment's second phase. Finally, a portion of the deposited particulate was re-suspended by the aspiration system, slightly increasing the concentration of total aerosol particles.

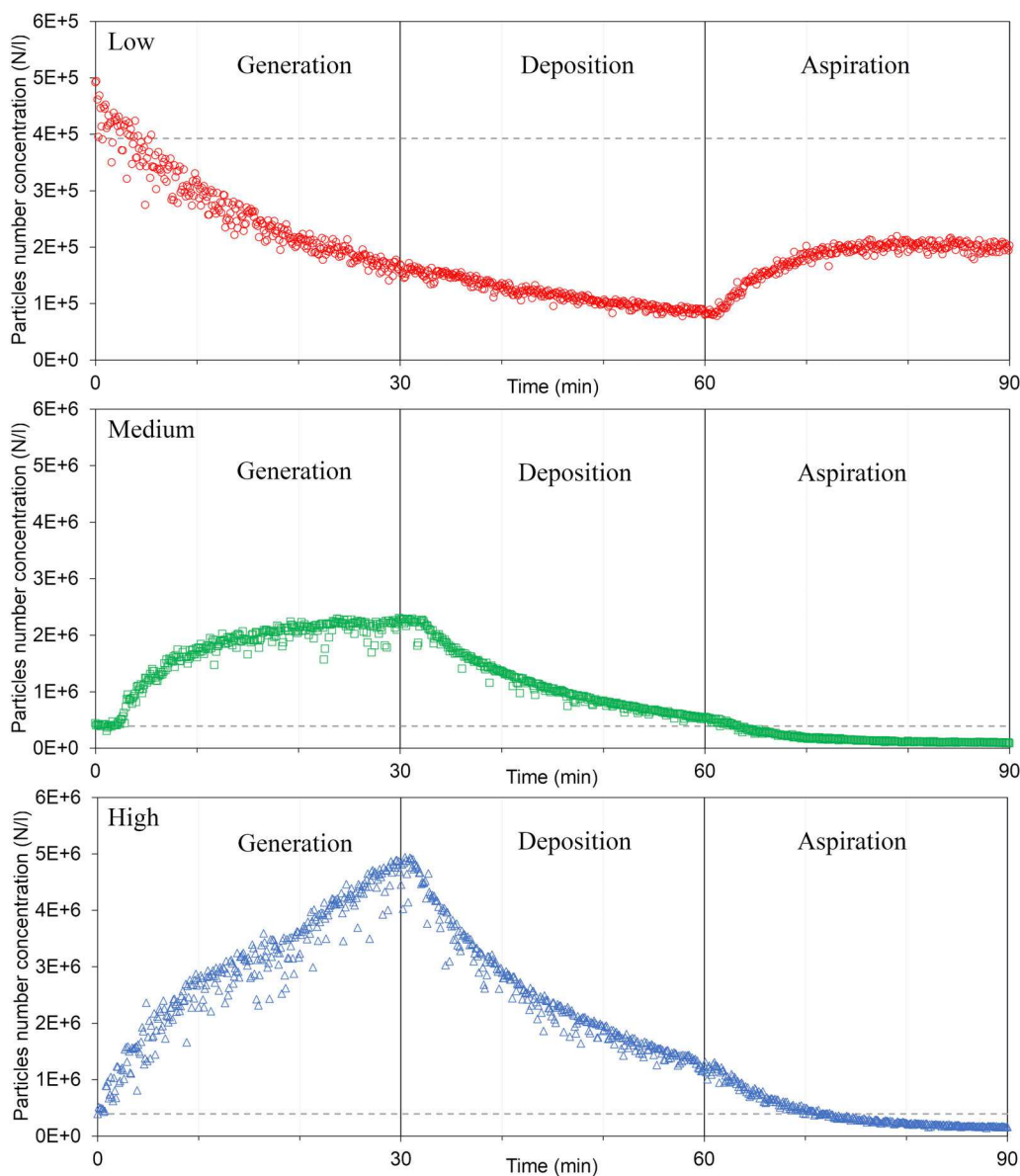


Figure 2. Aerosol particles number concentration versus time during the generation, deposition, and aspiration for the low, medium, and high flow rates (see Table 1). The dashed line represents the external background mean value.

Figure 3 depicts the aerosol particle size distribution for the three flow rate tests during the experiment's generation phase. In all the size ranges under consideration, except for those larger than $1\ \mu\text{m}$, which invariably go to zero, a size distribution with three clearly defined band modes is found for medium and high flow rates. The medium flow rate presents the smallest mode shifted at lower diameters. The low flow rate exhibits a single mode with a center frequency of $0.28\ \mu\text{m}$, supporting the idea that no aerosol particles would be produced under these circumstances. These results are consistent with the size distribution provided by the manufacturer for a specific salt concentration in the solution as described in the user manual. In fact, even if the three modes detected for medium and high

flow rates are not given in the size distribution provided by the manufacturer, the maximum at $0.3\ \mu\text{m}$ is obtained in both sets of measurements.

Figure 4 depicts the TXRF spectra of the particles deposited on the reflectors. Qualitative analysis reveals the presence of Ca, Ti, Fe, Cu, Zn, Ga (added as IS) and the scattering of Mo -X-ray source. The contamination of disposable reflectors is likely the cause of elements other than Cu as examination revealed no evidence of Cu contamination in the solution. They do not match the Cu signal proportionally, in fact. After a 90-min experiment, the total amount of Cu that had accumulated on the reflectors in the bottom of the glove box was measured. For low, medium, and high flow rates, the deposited masses were,

respectively (0.08 ± 0.03) ng, (1.6 ± 0.2) ng and (10.8 ± 0.8) ng. The error bars, represent extended uncertainties, pertaining to three TXRF measurements

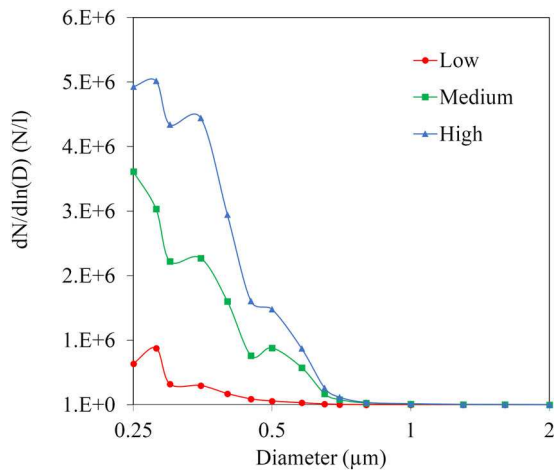


Figure 3. Aerosol particle size distribution for low, medium, and high flow rates. Dimensional classes above $2\mu\text{m}$ are excluded as no particles are detected.

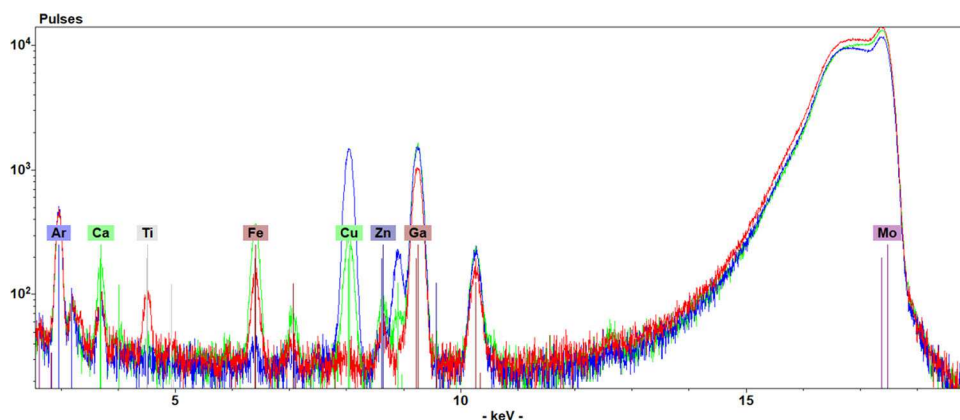


Figure 4. TXRF spectra of aerosols collected by deposition at the bottom of the glovebox at low (red), medium (green), and high (blue) flow rate.

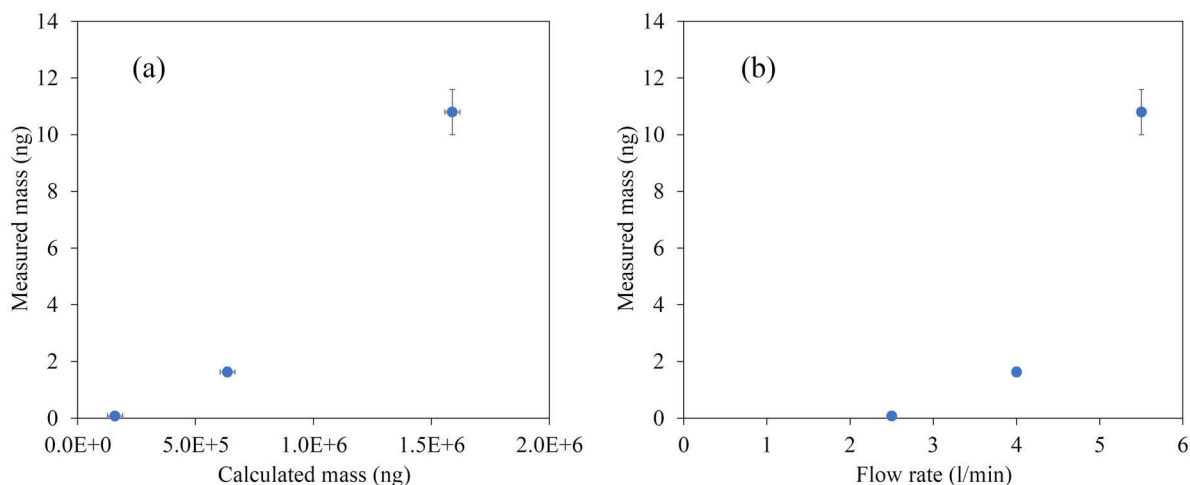


Figure 5. Comparison between the deposited Cu mass on the reflector measured by TXRF (y-axis) and (a) the nebulized Cu mass, and (b) the flow rate on the (x-axis).

made on the same sample while it was rotated around its axis. The contributions of the internal standard concentration uncertainty, sample preparation uncertainty, and instrumental repeatability uncertainty were considered while calculating the values.

As can be seen, while a decrease of one order of magnitude in the Cu mass is observed going from high to medium flow rates, a significant decrement of Cu mass is observed at low flow rates, confirming the hypothesis of the formation of minor amounts of aerosol particles. Starting with the concentration of Cu in the solution and the volume of the nebulized metal, it is possible to calculate the mass of the produced aerosol particles. Figure 5 depicts the relationship between the Cu mass calculated for 30 min nebulization and the Cu mass measured by TXRF on the deposited reflector.

There is a difference of five orders of magnitude between these values, which is likely caused by the limited deposition and the small region on the

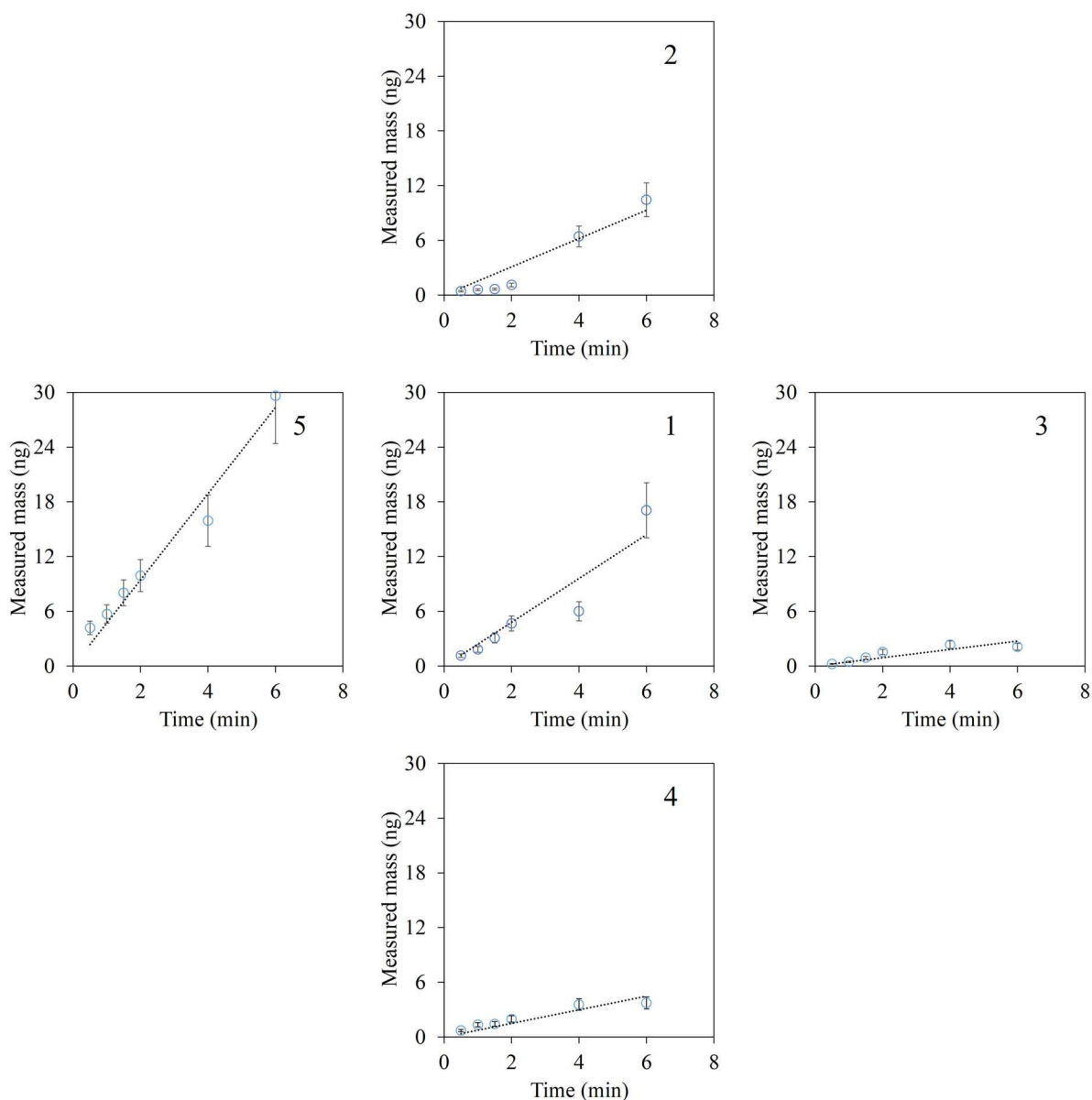


Figure 6. Cu mass with respect to deposition time and dotted line represents linear fitting. Error bars represents expanded uncertainties.

masked reflector (6 mm diameter), though a positive correlation is observed. The same trend is seen between the Cu mass measured by TXRF and the flow rate, showing that the deposited increases with the aerosol particle formation.

To investigate the distribution of radial aerosol particles, the medium flow rate is used. Indeed, as was already said, under these circumstances, the concentration of aerosol particles gradually stabilizes. The Cu mass measured by TXRF with respect to the deposition time are shown in Figure 6.

The plots are spatially structured to reflect the actual radial distribution of the aerosol particles at each place. This simple model experiment is built on the assumption that all liquid aerosol particles will

deposit onto the reflector upon impact, supported by the observed linearly increasing Cu mass deposits over time on the reflector at constant deposition rate. Based on the geometry of the nozzle itself, the flow rate, and the viscosity of the utilized solution, the results demonstrate how Cu aerosol spreads out from the nozzle in a cone geometry (Beale and Reitz 1999). The linear fittings shown in Figure 6 are obtained imposing the intercept to zero, after verifying statistically that the intercepts are compatible to zero within 3 standard errors, and R^2 values lie between 0.92 and 0.99. The linearity of the curves demonstrates the repeatability of particulate deposition by impact on the reflector surface and the validity of the measurement based on TXRF, with higher deviation with

increasing mass, particularly at the lower times. The center of the flow, or point 1, on the vertical axis, has the greatest amount of deposition. When looking at the horizontal distribution, position 5 (to the left of the aerosol generator exit) has the highest value of Cu mass, and position 3 (to the right of the nebulizer nozzle) has the lowest value of Cu mass. We can draw the conclusion that, in this configuration, the aerosol particles cone is not uniform, showing a stronger flow to the exit's left.

Considering the residuals from linear fitting, data above 4 min show higher deviation. Indeed, as it can be seen in Figure 6, an overestimation of Cu mass results, which is more significant for the most loaded position. The possible presence of absorption effects causing a decrease in the fluorescence intensity, is investigated. Indeed, in TXRF analysis it is important to ensure that the mass of the sample under study is limited, to avoid strong selective X-ray absorption of the matrix for the analyte element (Klockenkämper and von Bohlen 2015). The intensity deficit caused by the absorption remains below a permissible level (usually 5%) if the mass deposition [$\mu\text{g}/\text{cm}^2$] is lower than a maximum depending on the layer matrix here represented by the copper nitrate salt. Following the approach reported by Cirelli et al. (2022) it is possible to calculate the maximum mass loading to ensure negligible absorption effects equal to $2.84 \mu\text{g}/\text{cm}^2$, corresponding to $0.802 \mu\text{g}$ for the exposed area of the carrier. This value is much higher than the loading of the sample under study, ensuring that the thin-film approximation is respected for all our samples. Thus, the variation of data may be due to the other effects such as crystals aggregations, resulting in higher mass deposition. In addition, Cu mass overestimation may be also due to the non uniform shadowing effect of the deposited gallium internal standard by the deposited particulate and a resulting lower accuracy for quantitative determination (Fittschen et al. 2006).

4. Conclusions

In this paper, we provide a novel method for characterizing nebulization-generated aerosols by TXRF analysis. An OPC measures the size distribution and particle concentration of the aerosol produced by nebulizing a Cu salt aqueous solution inside a glove box. Three nebulizers flow rate were tested to assess differences in particulate deposition at the bottom of the glove box, analyzing the Cu mass on reflectors by TXRF. It is observed that deposition increases with the flow rate, with the average flow rate (4 L/min)

resulting in a steady concentration that balance aerosol particles production and deposition. This setting is selected for studying the aerosol spatial distribution by collecting the particulate at a fixed position and using a radial geometry. A leftward asymmetry of the aerosol particles flow with respect to the nozzle is evident by measuring the Cu mass deposited on reflectors, which linearly increases with exposure time to the aerosol. Small deviations from linearity observed at higher times are probably due to the shadowing internal standard effect by the deposited particulate. These results confirm that it is possible to study the spatial distribution of aerosol particles generated by nebulization from salt-based water solutions, and particulate depositions by means of TXRF, thanks to its incredible sensitivity to very low mass amounts. In addition, being the concentration detected on the aerosol axis the most reliable in terms of deposition versus time, this can be used to realize calibration samples for TXRF analysis representative of particulate deposition, modulating the deposited mass amount with exposure time. Well characterized aerosols can be used to calibrate online LIBS instruments though, due to the asymmetry detected in the mass distribution across the aerosol, care must be taken in considering the concentration calculated from the solution consumption as the one measured online in a specific point of the aerosol. A proper experimental arrangement must be considered to ensure a homogeneous aerosol suitable for calibration purposes.

ORCID

Laura Eleonora Depero  <http://orcid.org/0000-0001-7818-3212>

Laura Borgese  <http://orcid.org/0000-0003-3486-2656>

References

- Bacon, J. R., O. T. Butler, W. R. L. Cairns, O. Cavoura, J. M. Cook, C. M. Davidson, and R. Mertz-Kraus. 2021. Atomic spectrometry update - A review of advances in environmental analysis. *J. Anal. At. Spectrom.* 36 (1): 10–55. doi:10.1039/D0JA90074E.
- Beale, J. C., and R. D. Reitz. 1999. Modeling spray atomization with the Kelvin-Helmholtz/Rayleigh-Taylor hybrid model. *Atomiz. Spr.* 9 (6):623–50. doi:10.1615/AtomizSpr.v9.i6.40.
- Borgese, L., F. Bilo, A. Zacco, S. Federici, A. W. Mutahi, E. Bontempi, K. Trzepla, N. Hyslop, S. Yatkin, P. Wobrauschek, et al. 2020. The assessment of a method for measurements and lead quantification in air particulate matter using total reflection X-ray fluorescence spectrometers. *Spectrochim. Acta - B At. Spectrosc.* 167: 105840. doi:10.1016/j.sab.2020.105840.

- Briffa, J., E. Sinagra, and R. Blundell. 2020. Heavy metal pollution in the environment and their toxicological effects on humans. *Heliyon* 6 (9):e04691. doi:10.1016/j.heliyon.2020.e04691.
- Brown, R. J. C., K. E. Jarvis, B. A. Disch, S. L. Goddard, E. Adriaenssens, and N. Claeys. 2010. Comparison of ED-XRF and LA-ICP-MS with the European reference method of acid digestion-ICP-MS for the measurement of metals in ambient particulate matter. *Accred. Qual. Assur.* 15 (9):493–502. doi:10.1007/s00769-010-0668-7.
- Carranza, J. E., and D. W. Hahn. 2002. Sampling statistics and considerations for single-shot analysis using laser-induced breakdown spectroscopy. *Spectrochim. Acta - B At. Spectrosc.* 57 (4):779–90. doi:10.1016/S0584-8547(02)00007-1.
- Carranza, J. E., K. Iida, and D. W. Hahn. 2003. Conditional data processing for single-shot spectral analysis by use of laser-induced. *Appl. Opt.* 42 (30):6022–8. doi:10.1364/AO.42.006022.
- Cirelli, P., F. Bilo, K. Tsuji, T. Matsuyama, G. Siviero, L. Pisani, A. Zacco, L. E. Depero, D. Eichert, and L. Borgese. 2022. Assessment of calibration methods for Pb-loaded aerosol filters analysed with X-ray fluorescence under grazing incidence. *Spectrochim. Acta B At. Spectrosc.* 192:106414. doi:10.1016/j.sab.2022.106414.
- Diaz, D., and D. W. Hahn. 2021. Aerosol measurements with laser-induced breakdown spectroscopy and conditional analysis. *Spectrochim. Acta - B At. Spectrosc.* 179:106107. doi:10.1016/j.sab.2021.106107.
- Dutouquet, C., G. Gallou, O. L. Bihan, J. B. Sirven, A. Dermigny, B. Torralba, and E. Frejafon. 2014. Monitoring of heavy metal particle emission in the exhaust duct of a foundry using LIBS. *Talanta* 127:75–81. doi:10.1016/j.talanta.2014.03.063.
- EU. 2004. Directive 2004/107/EC of the European Parliament and of the Council of 15/12/2004 relating to arsenic, cadmium, mercury, nickel and polycyclic aromatic hydrocarbons in ambient air. *Off. J. Eur. Union L.* 23 (3):3–16.
- European Commission. 2017. Central mediterranean route: Commission proposes Action Plan to support Italy, reduce pressure and increase solidarity. https://ec.europa.eu/commission/presscorner/detail/en/IP_17_1882.
- European Parliament; European Council. 2008. Directive 2008/50/EC on ambient air quality and cleaner air for Europe. *Off. J. Eur. Commun.* 152:1–44.
- Fittschen, U. E. A., S. Hauschild, M. A. Amberger, G. Lammel, C. Strel, S. Förster, P. Wobrauschek, C. Jokubonis, G. Pepponi, G. Falkenberg, et al. 2006. A new technique for the deposition of standard solutions in total reflection X-ray fluorescence spectrometry (TXRF) using pico-droplets generated by inkjet printers and its applicability for aerosol analysis with SR-TXRF. *Spectrochim. Acta - B At. Spectrosc.* 61 (10–11):1098–104. doi:10.1016/j.sab.2006.09.009.
- Fortes, F. J., J. Moros, P. Lucena, L. M. Cabalín, and J. J. Laserna. 2013. Laser-induced breakdown spectroscopy. *Anal. Chem.* 85 (2):640–69. doi:10.1021/ac303220r.
- Gallou, G., J. B. Sirven, G. Gallou, C. Dutouquet, O. L. Bihan, and E. Frejafon. 2011. Aerosols analysis by libs for monitoring of air pollution by industrial sources. *Aerosol Sci. Technol.* 45 (8):918–26. doi:10.1080/02786826.2011.566899.
- Goncalves, A., J. R. Domínguez, and J. Alvarado. 2008. Determination of Pd, Pt and Rh in vehicles escape fumes by GF-AAS and ICP-OES. *Talanta* 75 (2):523–7. doi:10.1016/j.talanta.2007.11.055.
- Hahn, D. W., and N. Omenetto. 2012. Laser-induced breakdown spectroscopy (LIBS), part II: Review of instrumental and methodological approaches to material analysis and applications to different fields. *Appl. Spectrosc.* 66 (4):347–419. doi:10.1366/11-06574.
- Kapiamba, K. F., W. Hao, S. Adom, W. Liu, Y. W. Huang, and Y. Wang. 2022. Examining metal contents in primary and secondhand aerosols released by electronic cigarettes. *Chem. Res. Toxicol.* 35 (6):954–62. doi:10.1021/acs.chemrestox.1c00411.
- Kashani, A., and J. Mostaghimi. 2010. Aerosol characterization of concentric pneumatic nebulizer used in inductively coupled plasma-mass spectrometry (ICP-MS). *Atomiz. Spr.* 20 (5):415–33. doi:10.1615/AtomizSpr.v20.i5.40.
- Kayser, Y., J. Osán, P. Hönicke, and B. Beckhoff. 2022. Reliable compositional analysis of airborne particulate matter beyond the quantification limits of total reflection X-ray fluorescence. *Anal. Chim. Acta.* 1192:339367. doi:10.1016/j.aca.2021.339367.
- Klockenkämper, R., and A. von Bohlen. 2015. *Total-reflection X-ray fluorescence analysis and related methods*. 2nd ed. New Jersey: John Wiley & Sons, Inc.
- Maestre, S. E., J. L. Todolí, and J. M. Mermet. 2004. Evaluation of several pneumatic micronebulizers with different designs for use in ICP-AES and ICP-MS. Future directions for further improvement. *Anal. Bioanal. Chem.* 379 (5–6):888–99. doi:10.1007/s00216-004-2664-4.
- Niu, J., P. E. Rasmussen, A. Wheeler, R. Williams, and M. Chénier. 2010. Evaluation of airborne particulate matter and metals data in personal, indoor and outdoor environments using ED-XRF and ICP-MS and co-located duplicate samples. *Atmos. Environ.* 44 (2):235–45. doi:10.1016/j.atmosenv.2009.10.009.
- Palazzo, N., F. Migliorini, R. Dondè, S. Maffi, and S. De Iulii. 2016. Influence of oxygen addition to the carrier gas on laser-induced breakdown spectroscopy measurements on aerosols. *Spectrochim. Acta - B At. Spectrosc.* 115:1–7. doi:10.1016/j.sab.2015.10.012.
- Prost, J., P. Wobrauschek, and C. Strel. 2017. Quantitative total reflection X-ray fluorescence analysis of directly collected aerosol samples. *X-Ray Spectrom.* 46 (5):454–60. doi:10.1002/xrs.2752.
- Redoglio, D. A., N. Palazzo, F. Migliorini, R. Dondè, and S. De Iulii. 2018. Laser-induced breakdown spectroscopy analysis of lead aerosol in nitrogen and air atmosphere. *Appl. Spectrosc.* 72 (4):584–90. doi:10.1177/0003702817742314.
- Taurino, E., A. Bernetti, A. Caputo, M. Cordella, R. De Lauretis, I. D'Elia, E. Di Cristofaro, A. Gagna, B. Gonella, and F. Moricci. 2020. Italian Emission Inventory 1990–2018. Informative Inventory Report 2020. Report 319/2020, Institute for Environmental Protection and Research Environmental Assessment, Rome, Italy.
- US-EPA. 1999. *Compendium of methods for the determination of inorganic compounds in ambient air, compendium method IO-3.4: Determination of metals in ambient particulate matter using inductively coupled plasma (ICP)*

- spectroscopy*. Center for Environmental Research Information. Office of Research and Development, U.S. Environmental Protection Agency Cincinnati, OH: 45268. EPA/625/R-96/010a).
- Wadinga Fomba, K., N. Deabji, S. E. Islam Barcha, I. Ouchen, E. Mehdi Elbaramoussi, R. Cherkaoui El Moursli, M. Harnafi, S. El Hajjaji, A. Mellouki, and H. Herrmann. 2020. Application of TXRF in monitoring trace metals in particulate matter and cloud water. *Atmos. Meas. Tech.* 13 (9): 4773–90. doi:10.5194/amt-13-4773-2020.
- Wang, C. F., J. Y. Yang, and C. H. Ke. 1996. Multi-element analysis of airborne particulate matter by various spectrometric methods after microwave digestion. *Anal. Chim. Acta* 320 (2–3):207–16. doi:10.1016/0003-2670(95)00534-X.
- Wastl, A., F. Stadlbauer, J. Prost, C. Horntrich, P. Kregsamer, P. Wobrauschek, and C. Strelt. 2013. Nanoliter deposition unit for pipetting droplets of small volumes for Total Reflection X-ray Fluorescence applications. *Spectrochim. Acta - B At. Spectrosc.* 82:71–5. doi:10.1016/j.sab.2013.01.006.
- WHO Global Air Quality Guidelines. 2021. Particulate matter (PM_{2.5} and PM₁₀), ozone, nitrogen dioxide, sulfur dioxide and carbon monoxide. Coastal and Estuarine Processes. Geneva: World Health Organization. <https://apps.who.int/iris/handle/10665/345329>.
- Yatkin, S., M. Gerboles, and A. Borowiak. 2012. Evaluation of standardless EDXRF analysis for the determination of elements on PM₁₀ loaded filters. *Atmos. Environ.* 54: 568–82. doi:10.1016/j.atmosenv.2012.02.062